CRANFIELD UNIVERSITY

Jan Roman Hönnige

Thermo-Mechanical Control of Residual Stress, Distortion and Microstructure in Wire + Arc Additively Manufactured Ti−6Al−4V

School of Aerospace, Transport and Manufacturing
Welding Engineering and Laser Processing Centre

PhD Thesis
2015 - 2018

Supervisor: Dr. Paul Colegrove
Associate Supervisor: Prof. Stewart Williams

CRANFIELD UNIVERSITY

School of Aerospace, Transport and Manufacturing
Welding Engineering and Laser Processing Centre

PhD Thesis
2015 - 2018

Jan Roman Hönnige

Thermo-Mechanical Control of Residual Stress, Distortion and Microstructure in Wire + Arc Additively Manufactured Ti–6Al–4V

Supervisor: Dr. Paul Colegrove
Associate Supervisor: Prof. Stewart Williams

This thesis is submitted in partial fulfilment of the requirements for the degree of Doctor of Philosophy

© Cranfield University 2018. All rights reserved. No part of this publication may be reproduced without the written permission of the copyright owner.

Acknowledgements

Es ist nichts schrecklicher als eine tätige Unwissenheit.

Wenn man alle Gesetze studieren sollte, so hätte man gar keine Zeit, sie zu übertreten.

- Johann Wolfgang von Goethe

Coming to and working at the WELPC / Cranfield University was certainly one of the most fortunate decisions in my life. What I was allowed to learn exceeded by far the content of this work. I am thankful to everyone who allowed this research to exist in the first place, the AMAZE project (no 313781) for funding it and Stewart Williams, who trusted me to do a PhD at this University and who supported me as my associate supervisor.

Paul, your principal supervision was a well-balanced path between direction and freedom of action. This supported my personal development, as well as the comprehension of academic and methodological approaches, more than anything else. I very much respect the strength, energy and moral you showed in the past years.

I wish to express my gratitude to my subject adviser Supriyo Ganguly, who had fundamental impact on the planning and conduction of the extensive residual stress experiments. Furthermore the technical support of John, Nisar and especially Flemming Nielsen has been overwhelming. They were the backbone of the technical achievements of the department. Also without amazing friends and colleagues in the WELPC, this research would have been a lot harder. I also would like to thank all my friends of the Cranfield University football team. We shared great adventures, victories and now fantastic memories.

Ein ganz besonderer Dank gilt meinen Eltern, Kirsten Petersen und Andreas Hönnige. Was ihr mir von Horkheim bis Amelinghausen auf den Weg gegeben habt waren die Werkzeuge für diese Errungenschaft. Durch eure unterschiedliche und besondere Art der Erziehung habe ich die Kraft gehabt die hohen Anforderungen zu erfuellen und konnte das technische und persoenliche Vertrauen meiner Kollegen gewinnen.

Danke an Lara, Ilka und Kay. Ihr seid meine sozialen Vorbilder an denen ich mich im Umgang mit Menschen orientiert habe. Danke Jürgen für dein Interesse an mir, für deine konstruktive und objektive Ehrlichkeit und danke an meine Grosseltern, dir mir alle wertvolle Dinge mit auf den Weg gaben. Durch euch habe ich gelernt, bei wichtigen Entscheidungen Herz und Kopf abzuwägen. Danke an meinen besten Freund, Johannes Rörup und seine Frau Jana fuer die vielen Erfahrungen, Abenteuer, Erinnerungen, Bodenstaendigkeit, Bescheidenheit und Humor. Ich seid das Beispiel dafuer, dass Familie, Freundschaft und Heimat über Allem steht.

Debora, la tua energia e la tua forza, il tuo amore ed il tuo sostegno morale sono stati fondamentali. Ho trovato in te un supporto incredibile. Tu arricchisci la mia vita. Ammiro le tue qualità sia come persona e sia come ingegnere. Spero di poterti restituire tutto quello che mi hai dato. Ti amo.

Declaration

A large part of the work described in this thesis is based on articles which have been submitted or published elsewhere:

The content of chapter 3 was submitted to the journal Materials and Design on 17th December 2017 (JMAD-S-17-11440) with the title "Residual Stress and Stress Relief in Ti–6Al–4V Wire + Arc Additively Manufactured Intersections". The contour method performed in this work was conducted by Bilal Ahmed from Coventry University. Partial content of chapter 4 was published in the conference proceedings of the 10th International Conference in Residual Stresses (ICRS) 2016 in Sydney with the title "Residual Stress Characterisation and Control in the Additive Manufacture of Large Scale Metal Structures". The contour method performed in this work was conducted by Matthew Roy from the University of Manchester. Partial content of chapter 5 were submitted to the conference proceedings of the 9th International Conference on Materials for advanced Technologies (ICMAT) 2017 in Singapore with the title "Improvement of microstructure and mechanical properties of Wire + Arc Additively Manufactured Ti–6Al–4V with Machine Hammer Peening". The content of chapter 6 and 7 will both be submitted to Journals after the completion of this thesis. Jefferson Oliveira from StressMap at the Open University Milton Keynes performed the contour method in this work. Alistair Ho from the University of Manchester performed the EBSD β-reconstruction and produced the strain maps. Masoud Abbaszadeh from Helmholtz Zentrum Geesthacht performed the numerical simulations. The candidate (Jan Roman Hönnige) contributed principally to all chapters in this thesis described above. This thesis is submitted on the conditions contained in the Regulations, and has not been submitted for any other academic or professional award. All of the work described was carried out as part of the course of study at Cranfield University and not previously or subsequently

Abstract

Wire + arc additive manufacturing (WAAM), unlike most other additive techniques, targets the manufacture of near-net-shape parts for large-scale structural components with medium complexity. WAAM is of special interest for the aerospace industry for reducing lead-time, material and process costs. Ti–6Al–4V is one alloy that could potentially benefit most from the advantages of WAAM, due to high material and process costs, and is therefore the main scope of this research. The manufacture of critical-use components for civil aviation requires a high process control to provide consistently strong and isotropic mechanical properties, as well as the elimination of residual stresses.

Cold work can manipulate and counteract residual stresses caused by the additive process. When applied between two layers (i.e. between the deposition passes → inter-pass) it was found to refine the microstructure and thereby significantly improve the mechanical properties. So far it was only understood that it can theoretically control both residual stress and microstructure, but the science behind the process and how different parameters influence the effectiveness was only proposed. The present research demonstrates how cold work can be used effectively to address both issues, by identifying the process-relevant mechanisms.

Before manipulating residual stresses, their development needed to be investigated Behaviour that had only been predicted using numerical simulations was measured for the first time using neutron diffraction and contour method stress determination techniques. This behaviour includes the development of residual stress during the deposition of straight walls and intersections, stress redistribution upon distortion after unclamping and the potential of thermal stress relief. Analogies to previous findings on steel helped explain the findings. The knowledge of stress development finally helped the development of an analytical model to predict residual stress and distortion, as well as stress redistribution upon unclamping.

The performance and parameters of plastic deformation strategies were investigated using various characterisation techniques. Those include hardness mapping, residual

stress measurements using hole-drilling and the contour method, electron-backscatter-diffraction (EBSD) plastic strain mapping, heat treatment, as well as numerical simulations to compare against the respective measurement techniques. The methodology allowed the development of parameters that produce the required amount of plastic deformation into the required depth of the material, for different thermal histories. Even though 6 % to 8 % of plastic strain can allow reorientation and the development of finer grains, 12 % of plastic strain or more is probably required to achieve a desired grain size. This value is equivalent to 4° lattice misorientation using an EBSD strain mapping technique and it is equivalent to an increase of hardness by at least 20 HV.

Different rolling and one alternative cold working techniques were investigated to address both individual issues, residual stress and microstructure. Side rolling was found to be far more effective on controlling residual stress and distortion than vertical inter-pass rolling. Profiled vertical inter-pass rolling on the other hand is far more effective to refine the microstructure and improve mechanical properties than flat rolling. Machine Hammer Peening is an alternative cold working techniques that offers a much higher degree of freedom compared to rolling. The proof of concept to integrate peening into additive manufacturing was successful. However, available machine hammer peening tools do not supply the impact energy required to be at eye level with rolling. It is estimated that approximately 5000 mJ would be required to be as effective as rolling with 70 kN.

The fast thermal cycle within the heat affected zone during the additive deposition was measured for the first time at different locations, which allowed conclusions regarding the respective and local development of the microstructure. It furthermore helped to better understand the grain refinement mechanism, and the influence of thermal cycles on subsequent undesired grain growth. The research findings can be applied to develop effective inter-pass cold work strategies for arbitrary thermal cycles and they are sufficient to validate numerical simulations to design better process parameters more efficiently.

Table of Contents

Acknowledgements i

Declaration iii

Abstract v

Table of Contents viii

List of Acronyms xii

List of Symbols xiii

Chapter 1 Literature Review 1

1.1 Metal Additive Manufacturing 1
1.1.1 Powder Bed Fusion 3
1.1.2 Directed Energy Deposition 4
1.1.3 Wire + Arc Additive Manufacturing 5

1.2 Titanium and the alloy Ti–6Al–4V 8
1.2.1 Crystal Structure 8
1.2.2 Crystal Mechanics during Plastic Deformation 11
1.2.3 Microstructure and Mechanical Properties of Ti–6Al–4V 12

1.3 Microstructure and Mechanical Properties of Ti–6Al–4V WAAM 18
1.3.1 Development of Microstructure 18
1.3.2 Crystallographic slip in WAAM 20
1.3.3 Mechanical Properties in WAAM 21
1.3.4 Mechanical Property Comparison to other AM techniques 22
1.3.5 Summary 23

1.4 Development of Residual Stress and Distortion in Metal AM 24
1.4.1 Thermal Residual Stress Development 24
1.4.2 Residual Stress and Distortion in Welding 25
1.4.3 Residual Stress in WAAM 26

1.5 Control of Microstructure and Properties of Ti–6Al–4V AM 28
1.5.1 Thermal Techniques 28
1.5.2 Mechanical Techniques 31
1.5.3 Alloying 38
1.5.4 Summary 40

1.6 Control of Residual Stress & Distortion in Welding and AM 41
1.6.1 Thermal Techniques 42
1.6.2 Mechanical Techniques 44

1.7 Pertinent Residual Stress Measurement Techniques 50
1.7.1 Non-destructive Diffraction Techniques 51
1.7.2 Contour Method 53

1.8 Conclusion 54

1.8.1 Summary of microstructure and residual stress development in WAAM 54
1.8.2 Summary of mitigation techniques 54
1.8.3 Gaps in Literature 57
1.8.4 Aims, Objectives and Thesis outline 58

Chapter 2 Bending Beam Theory – Residual Stress & Distortion 61

2.1 Calculations 61
2.1.1 Residual Stress 63
2.1.2 Euler-Bernoulli Beam Theory 64
2.1.3 Timoshenko Beam Theory 65
2.1.4 Sector of a circle 67
2.1.5 Redistributed Stress Field 68

2.2 Case Study 69

2.3 Verification 72

2.4 Conclusion 74

Chapter 3 Residual Stress and Texture Control in Intersections by Stress Relief and Rolling 77

3.1 Introduction 77

3.2 Methodology 78
3.2.1 Production of Specimen 78
3.2.2 Neutron Diffraction Residual Stress Measurement 80
3.2.3 Contour Method 84
3.2.4 Microstructure 85

3.3 Results 85
3.3.1 Microstructure 85
3.3.2 Neutron Diffraction 86
3.3.3 Contour Method 90

3.4 Discussion 91
3.4.1 Neutron Diffraction 91
3.4.2 Stress Development in intersections 92
3.4.3 Contour Method 94

3.5 Conclusions 96

Chapter 4 Residual Stress and Distortion Control by Side-Rolling 99

4.1 Introduction 99

4.2 Methodology 99
4.2.1 Sample production 99
4.2.2 Neutron Diffraction 101
4.2.3 Contour Method 101
4.2.4 Microstructure 104

4.3 Results 105
4.3.1 Layer dimensions 105
4.3.2 Distortion 106
4.3.3 Residual Stress 106

4.3.4 Wall geometry 110
4.4 Discussion 110
4.4.1 Measurement Accuracy 110
4.4.2 As-Deposited RS & D 112
4.4.3 Effectiveness of Side Rolling 113
4.5 Conclusions 115
Chapter 5 Machine Hammer Peening as Alternative to Rolling 117
5.1 Introduction 117
5.2 Methodology 118
5.2.1 MHP Tool Characterisation 118
5.2.2 Inter-Pass MHP for Grain Refinement 123
5.2.3 Post-Process MHP for Distortion Control 124
5.3 Results 125
5.3.1 MHP Tool Characterisation 125
5.3.2 Post-Process MHP for Distortion Control 129
5.3.3 Inter-Pass MHP for Grain Refinement 130
5.4 Discussion 131
5.4.1 MHP Tool Characterisation 131
5.4.2 Inter-Pass MHP for Grain Refinement 132
5.4.3 Post-Process MHP for Distortion Control 135
5.4.4 Ideal Stress Measurement Technique 135
5.4.5 Ideal Plastic Strain Induction and Measurement 137
5.4.6 Practical Summary 138
5.5 Conclusion 138
Chapter 6 Parametric Plastic deformation Study 140
6.1 Introduction 140
6.2 Methodology 142
6.2.1 Topography Measurement 144
6.2.2 Residual Stress Measurement 144
6.2.3 EBSD Plastic Strain Mapping 147
6.2.4 Hardness Mapping 147
6.2.5 Numerical Rolling Simulation 148
6.2.6 Heat Treatment and Microstructure Analysis 149
6.3 Results Section A: Rolling Experiments 150
6.3.1 Topography 150
6.3.2 Residual Stress Maps 151
6.3.3 EBSD Strain Maps 152
6.3.4 Hardness Maps 153
6.3.5 Numerical Simulation 156
6.3.6 Grain Refinement after Heat Treatment 157
6.4 Results Section B: MHP Experiments 158
6.4.1 Topography 159
6.4.2 Residual Stress Maps 159
6.4.3 EBSD Strain Maps 162

6.4.4 Grain Refinement after Heat Treatment 162
6.5 Discussion 162
6.5.1 Accuracy and Comparison of Characterisation Techniques 162
6.5.2 Influence of Rolling Parameters 166
6.5.3 Influence of MHP Parameters 169
6.5.4 Practicality 171
6.6 Conclusion 175
Chapter 7 Thermal History and the impact on the Microstructure ..177
7.1 Introduction 177
7.1.1 Microstructure 177
7.1.2 Challenges to measuring the relevant temperatures 178
7.1.3 Refinement by inter-pass cold work 179
7.2 Methodology 180
7.2.1 Temperature History in the HAZ 180
7.2.2 Machine Hammer Peening and Grain Refinement 182
7.3 Results 183
7.3.1 Thermal History 183
7.3.2 Machine Hammer Peening and Grain Refinement 188
7.4 Discussion 192
7.4.1 Temperature/time history and resulting microstructure 192
7.4.2 Machine Hammer Peening and grain refinement 195
7.4.3 The effect of repeated heat cycles in WAAM and α-plate size in refined β grains 197
7.5 Conclusion 199
Chapter 8 Conclusions and Future Research 201
8.1 Residual Stress Control in WAAM 201
8.2 Microstructure Control in Ti–6Al–4V WAAM 202
8.3 Practical Advice 204
8.4 Future Research 205
Bibliography 207
Appendix A Contact Mechanics: Rolling and MHP I
Appendix B Crystal Structure and hcp orientation VII
Appendix C EBSD Investigation of Strain Distribution in a Rolled WAAM Component XIII
Appendix D Compression test XXI
Appendix E Inter-pass Rolling Trials XXIII

List of Acronyms

AM	Additive Manufacturing
BCC	Body Centred Cubic
BCT	Body Centred Teragonal
BOR	Burgers Orientation Relationship
BTF	Buy-to-Fly (ratio)
CAD	Computer Aided Design
CNC	Computerised Numerical Control
CM	Contour Method
CMT	Cold Metal Transfer
CRSS	Critical Resolved Shear Stress
DED	Directed Energy Deposition
EBSD	Elektron Backscatter Diffraction
EDM	Electron Discharge Machining
FE	Finite Element
GMT	Global Mechanical Tensioning
HD	Hole Drilling
HCF	High Cycle Fatigue
HCP	Hexagonal Close Packed
HIP	Hot Isostatic Pressing
LCF	Low Cycle Fatigue
LSP	Laser Shock Peening
MHP	Machine Hammer Peening
MIG	Metal Inert Gas
ND	Neutron Diffraction
NDT	Non-Destrictive Testing
OLM	On-Line Monitoring
RS & D	Residual Stress and Distortion
SEM	Scanning Electron Microscope
SLM	Selective Laser Melting
TIG	Tungsten Inert Gas
TOF	Time-of-Flight
TRL	Technology Readiness Level
UIT	Ultrasonic Impact Treatment
UTS	Ultimate Tensile Strength
WAAM	Wire + Arc Additive Manufacturing
YS	Yield Strength

List of Symbols

α	room temperature titanium phase (HCP)	
α'	titanium martensite (HCP)	
α''	heavily oversaturated titanium martensite (orthorhombic)	
α_{GB}	Grain boundary α	
α_T	Thermal expansion coefficient	[1/K]
β	high temperature titanium phase (BCC)	
ε	Strain	[µm/m]
θ	Reflection angle (neutron diffraction)	[°]
θ	Timoschenko deviation of beam cross section	[rad]
κ	Timoschenko coefficient	[-]
λ	wavelength of neutron beam	[Å]
λ	wavelength of artefact propagation	[mm]
ν	Poisson's ratio	[-]
ρ	Curvature radius of bending beam	[m]
σ	Stress	[MPa]
τ	Shear Stress	[MPa]
φ	Rotation of beam cross-section	[rad]
χ	Curvature	[1/m]
a	amplitude	[mm]
a, c	Lattice parameter	[Å]
a_0, c_0	Stress-free lattice parameter	[Å]
d, d_0	Crystallographic plane spacing, stress free plane spacing	[Å]
d	MHP step distance	[mm]
E, E_{hkl}	Elastic (Young's) modulus of material and {hkl} plane	[GPa]
E	MHP impact energy	[mJ]
f	frequency	[Hz]
F	Force	[N]
h	Planck constant (= 6.626×10^{-34})	[Js]
h, k, l	Millier indice	
I_{yy}	Second moment of area	[mm^4]
m_n	mass of neutron = (1.675×10^{-27})	[kg]
h, L, v	wall height, length, width	[mm]
t	time	[s]
t	indent distance	[mm]
v	neutron velocity	
u, v, w	Displacement in x, y and z	
x, y, z	Cartesian coordinates	

Chapter 1 Literature Review

The scope of this research is Wire + Arc Additive Manufacturing (WAAM) of metals and in particular the titanium alloy Ti–6Al–4V. This chapter reviews the technical aspects and business case for WAAM against other additive manufacturing (AM) techniques. It also shows typical target parts, recent developments and finally the industrial requirements to this alternative manufacturing technique. After introducing additive manufacturing and the standard material characteristics of Ti–6Al–4V, the WAAM-specific material properties will be presented. The two main challenges, which are anisotropic and inferior material behaviour, as well as residual stresses, will be described in more detail. Based on the introduction of concurrent techniques to control both, the aim, the objectives and the research route will be justified.

1.1 Metal Additive Manufacturing

Agarwala et al. [1] described in 1995 direct selective laser sintering (SLS) as a rapid prototyping technique for polymers, plastics and metals for direct functional use. Some of the issues discussed are still present today, such as the definition of process windows for a stable deposition or limited material density. In the same year the Fraunhofer Institute Aachen patented Selective-Laser-Melting (SLM) [2]. Commonly known as 3D-printing, the term additive manufacturing (AM) is commonly used in industry and academia and is therefore used in this work. ASTM International acknowledged AM in 2009 with the first specific standard [3], where it is described as a technique based on "computer-aided design (CAD) to build objects layer by layer", which is in contrast to conventional subtractive techniques, such as cutting or machining. The industrial drivers for sectors, such as automotive, medicine, aerospace and defence are for example cost and lead time reduction in large scale AM. Moreover, the tool-less technique enables the production of features that are impossible to manufacture with any other conventional technique [3]. In 2010 Gibson [4] described the AM techniques in a comprehensive book and recently Yilmaz [5] published a review paper about the state of art of AM. An example of a typical AM part is shown in Figure 1, which is a seat bracket

used on the Airbus A350 that was topologically optimised (-30 wt.%) and manufactured additively with features that cannot be built by casting or machining. In a similar case study it was shown that a topology optimised design provided the same stiffness, as the original part, but reduced the maximum stress by more than 50 % and the weight by 64 % [6]. Topological optimisation can be diploid to design free-form parts to build components with improved material usage. Reddy et al. [7] recently summarised concurrent topological optimisation techniques. Manufacturing net-shape or near-net-shape components also minimises machining effort and reduces material waste. The buy-to-fly (BTF) ratio represents hereby the mass of the raw material compared to the mass of the final part in service. AM can theoretically reduce the BTF to the optimum of 1, as opposed to more than 10 or 20 using conventional processes [8].

Figure 1: A conventional and additively manufactured titanium bracket for the Airbus A350 XWB [9].

According to ISO/ASTM 52900:2015 several general principles of AM techniques exist that also include the processing of non-metal material in different forms, such as liquids or plastics. Powder bed fusion and directed energy deposition (DED) are the two most widespread principles for metal deposition. Other AM techniques include binder jetting, extrusion, material jetting, sheet lamination and vat photo-polymerisation. While powder bed fusion selectively fuses regions of a powder bed using focused laser or electron beams, DED comprises a wider field: The heat source can be either a laser, an

electron beam or a welding arc and the feed stock can be either a wire (usually welding wire) or a metal powder that is blown into the molten pool.

1.1.1 Powder Bed Fusion

Regardless of whether the heat source is a laser [10] or an electron beam [9], both powder bed systems operate in the same fashion, as shown in Figure 2, which shows the electron beam melding (EBM) and the selective laser melting (SLM) process. In each case, a thin layer of metal powder is provided in the build chamber on a vertical axis platform. The beam melts the powder selectively, which then solidifies almost instantly and forms a slice of the part, which is called layer. The platform moves downwards by the thickness of the layer and the new volume is filled with new powder for the next layer. This sequence is repeated until the part is finished inside the build chamber, surrounded by non-melted powder. The final part is therefore built of many 2D slices that make a 3D free-form component that can theoretically be used without processing i.e. it is net-shaped.

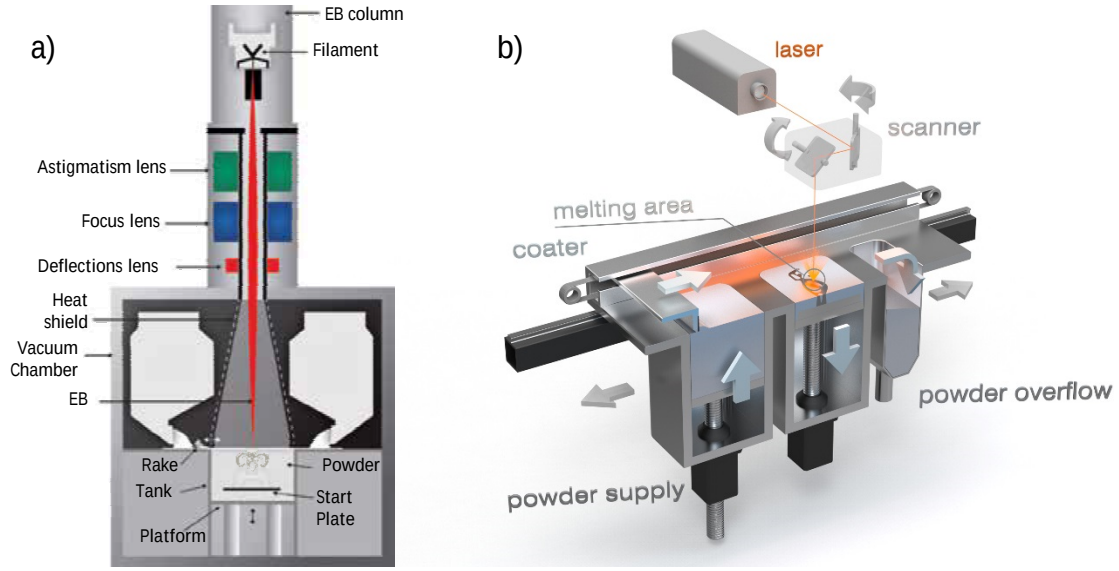

Figure 2: Concept of both powder-bed AM systems: (a) EBM [9] and (b) SLM [10].

The Swedish manufacturer Arcam AB offers three EBM machines specialised for medical implants and small aerospace components. They deposit metal powders of the alloys Ti–6Al–4V, TiAl, Ti Grade 2, Cobalt Chrome and Inconel 718 [11]. The researcher who patented SLM in Germany founded the company SLM Solutions GmbH in Lübeck [12], which are a competitor to the two Bavarian brands Concept-Laser [10] and EOS [13] that

all work with the same principle, as well as Renishaw [14] and the powder bed system of Trumpf [15]. The laser-based powder bed fusion systems offer the same material range used for EBM, plus several steels and aluminium alloys. In 2016 General Electric bought both, Concept-Laser and Arcam AB along with the market-leading Canadian material supplier for metal powder AP&C [16] and incorporated them into a subsidiary GE Additive [9].

The downside of metal powder bed fusion are the slow deposition rates (< 0.17 dm^3/h), limited build volumes (50 dm^3 in SLM and 14 dm^3 in EBM), high acquisition, raw material and running costs, as well as the vulnerability for defects. Furthermore building costs only account for approximately 35 % of the total part costs, while post-processing, testing and qualification makes up the other 65 %, which also requires substantial additional processing time. These aspects are often not mentioned. Powder bed systems might be the most mature AM technology, but are rather unsuitable for the cost-effective manufacture of large-scale components for dynamic structural applications.

1.1.2 Directed Energy Deposition

Blown powder systems are classified as DED and do not provide the powder in the bed, but deliver it instead straight into the molten pool with the target to use all of the fed powder. A laser-metal deposition (LMD) torch with three powder feeding nozzles is shown in Figure 3 (a). The build volume is limited by the size of the manipulator, i.e. build chamber. LMD systems for example can deposit 3.6 kg/h Ti–6Al–4V in a 4 x 3 x 2 m build volume [17], making them more suitable for large-scale components than powder bed fusion. Lasers are the typical heat source for this larger scale process, but other methods, such as plasma arcs exist as well [18]. Nevertheless, the blown powder method is also relatively prone to produce defects, like pores or voids, which are fatal for dynamic properties [19], [20].

Equivalent to blown powder DED, the metal can be fed into the molten pool in form of a wire. Heat sources can be laser beams [21], electron beams (EB) [22] or welding arcs [23]. EB-based wire AM systems can have very high deposition rates up to 20 kg/h at the expense of the accuracy and a poor surface finish. The deposited near-net-shape then requires finish machining, which increases the BTF. Another important difference is that

the EB requires a vacuum atmosphere, which results in expensive equipment and it influences the heat loss of the component. This results in a very slow or a very hot process, reducing the tensile properties significantly. In 1996 the US-company Sciaky started the development of their wire-based EBAM® technique. The EBAM®-300 series deposits up to 9 kg/h and is currently their largest near-net-shape deposition unit with a working envelope of 5.8 x 1.2 x 1.2 m^3 [24]. Vacuum chamber, side-fed wire supply and machining requirement limit the flexibility and process integrity of the process shown in Figure 3 (b).

a) b)

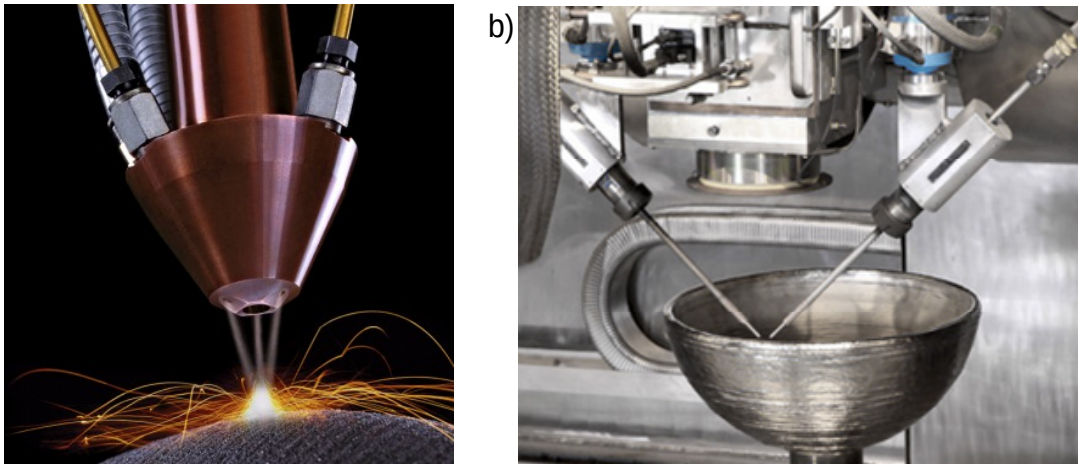

Figure 3: (a) LMD nozzle [15] and (b) Sciaky's EBAM 300 Series metal 3D printer [24].

1.1.3 Wire + Arc Additive Manufacturing

The use of arc welding equipment for rapid prototyping was investigated by Ribeiro [25] in 1995 at Cranfield University. Wire + arc additive manufacturing (WAAM) was mentioned first by Sequeria Almeida et al. [26] in 2010. It is a high-deposition-rate additive manufacturing process, which can be used for the manufacture of large-scale structural parts of medium complexity. Commercial welding torches are manipulated by a robotic or computerised-numerical-control (CNC) systems to deposit metal wire on a substrate [27], as shown in Figure 4. The manufactured part displayed is the near-net-shape of a Bombardier landing gear rib. Metal Inert Gas (MIG) and Cold Metal Transfer (CMT), Tungsten Inert Gas (TIG) and Plasma power sources can be used to deposit a wide range of metals including steel, Ti–6Al–4V and aluminium alloys [26]–[30]. The deposited near-net-shape component then needs finishing, such as machining [27] or forging [31]. A case study to manufacture an aluminium wing rib structure showed a

reduction of the BTF from 45 to 2.7 [32]. Other research institutes and Universities, such as IK4 Lortek in Spain [33], the University of Wollongong in Australia [34], University of Firenze in Italy [35], Katholieke Universiteit Leuven in Belgium [23] and others in the US and Asia have followed Cranfield's lead.

Several companies have been set up to exploit the technology: The Norwegian manufacturer Norsk Titanium uses Plasma WAAM systems since 2004, which they call Rapid Plasma Deposition (RPD^{TM}) [36] and the German company Gefertec, established in 2015, markets MIG-based WAAM systems, which they call 3DMP®, using 3-axis and 5-axis gantries at 750,000 € per unit and deposit aluminium and steel with a limited working envelope of 3 m^3 [37]. This all shows the recent and vast industrial awareness and demand from several sectors for the WAAM technology.

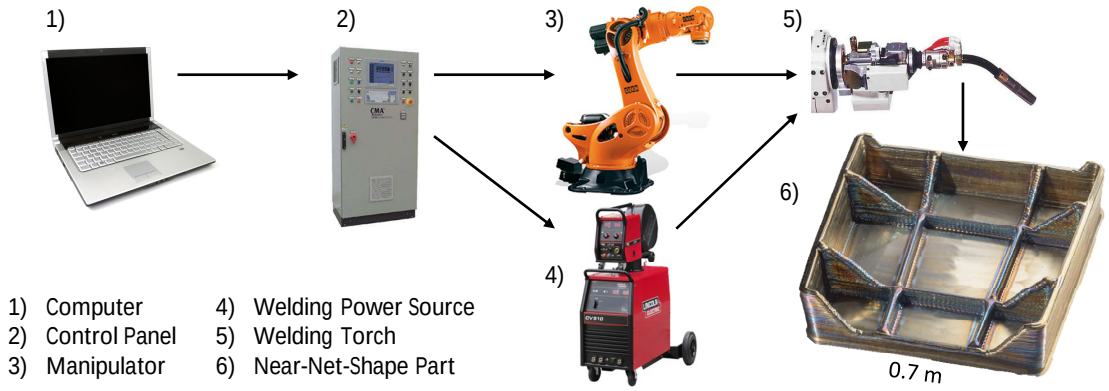

Figure 4: Components of a WAAM System.

1.1.3.1 Technical Readiness and Qualification

Figure 5 shows a Ti–6Al–4V component from Norsk after finish machining. This part is used on Boeing's Dreamliner 787 and was the first structural part to be FAA-approved in 2017 [38]. This is an important milestone for WAAM. However, it was the part that was qualified, rather than the process, which would be the key to fully exploit the commercial and industrial benefits of WAAM. Otherwise every single part would have to go through a complex, expensive and long qualification process, making WAAM inflexible and slow. Non-destructive testing (NDT) and online monitoring (OLM) are required to qualify the WAAM process [27]. Identifying defective depositions on-line allows the direct repair for example by machining the faulty material and redepositing it again.

Figure 5: Norsk's FAA-approved component installed on the Boeing 787 Dreamliner [38].

1.1.3.2 Business Case and Process Integration

WAAM techniques provide a high deposition rate at the expense of resolution and minimum feature size. It is proposed to integrate WAAM into the manufacturing chain of serial production, rather than using it as a rapid prototyping technique only. It is intended to replace other conventional manufacturing techniques, such as machining from solid, casting and forging fabrication and it is thereby expected to improve efficiency and value generation. The strength of WAAM is its' flexibility and robustness of open-frame assembly lines, process integrity, the reduction of part count, workspace, process steps, lead time, material waste and thereby costs, as well as the use of topologically optimised and lighter components [27], [39]. An attractive attribute is that a typical WAAM system is assembled from low-priced and off-the-shelf robotic systems and welding equipment. The comparison of technical performance of WAAM components against other techniques is based upon mechanical properties, build tolerance, BTF, residual stress, distortion and costs. The alloy Ti–6Al–4V is probably the material to benefit most from the advantages of WAAM, due to commonly high material and processing costs. The main AM competitor to WAAM is Sciaky's electron beam + wire system with slightly higher deposition rates, but lower mechanical properties [24].

The future target is a self-contained and independent operational manufacturing line with increased design freedom that can manufacture finished parts. Figure 6 shows the concept of the modular hybrid machine using WAAM combined with machine tools. Robots can deposit free-form structures in open frame and perform multidirectional on-line machining or cold work. The development of hybrid AM systems is not confined to

WAAM. Laser-AM processes have been developed that incorporate machining to produce finished parts [40], [41] to avoid additional post-processing steps.

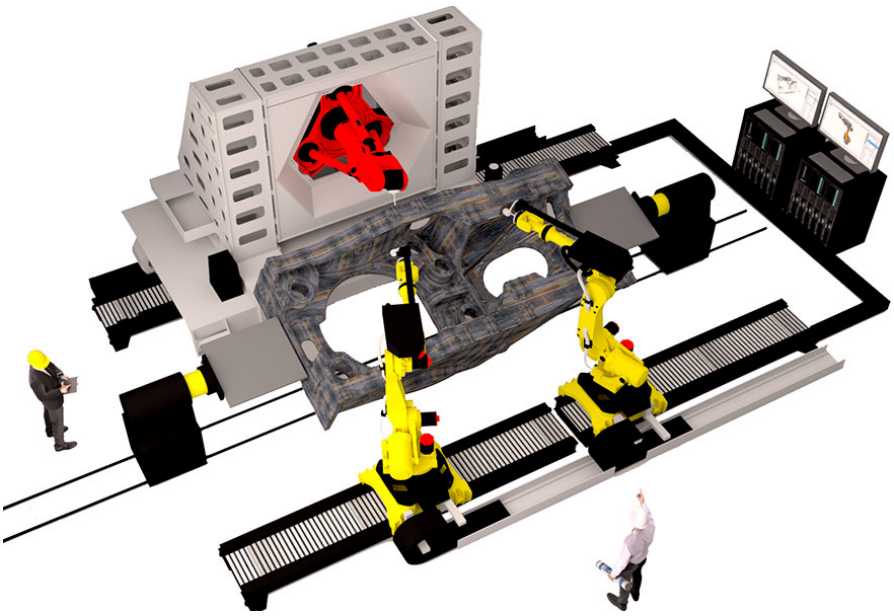

Figure 6: Concept for large scale hybrid manufacturing using additive technologies and integrated machining [42].

1.2 Titanium and the alloy Ti–6Al–4V

Titanium and its alloys are characterised by high strength (> 1000 MPa) even at high temperatures, moderate melting point (1600 °C) low density (< 4600 kg/m^3), corrosion resistance, weldability and forming behaviour . It is mainly used in aerospace, defence, chemical and medical applications. Its high material and processing costs prevent more widespread usage in the automotive industry. 20 – 30 % of titanium utilised in the US is as commercially pure (CP) titanium, while more than 50 % is in its' most popular alloy Ti–6Al–4V (short Ti64). The airframe of a Boeing 777 for example contains roughly 10 % titanium by weight. Comprehensive information regarding applications, history, commercial and political aspects can be found elsewhere [43], [44]. This chapter focusses on the relevant aspects for the present work only, which are the thermo-mechanical properties and microstructure.

1.2.1 Crystal Structure

Titanium can occur in two crystallographic structures, depending on the alloying elements and temperature. The transition point of pure titanium is at 882 ± 2 °C. Above this temperature it appears as a body-centred cubic (bcc) β phase. Below this

temperature it transforms into the hexagonal close-packed (hcp) α phase. Both unit cells are shown in Figure 7 (a).

The phase transformation of the bcc to the hcp unit cell happens on the $\{110\}_\beta$ plane, which transforms into the basal $\{0002\}_\alpha$ plane of the hexagon [45]–[47], which also makes the $\langle 111\rangle_\beta$ plane parallel to the $\langle 1120\rangle_\alpha$ plane. This relationship was first observed by Burgers in single crystals of zirconium [48], which is why it is named the Burgers Orientation Relationship (BOR) (Figure 6 (b)). At room temperature, the hcp unit cell has anisotropic Young's- and shear modulus between $E = (100 \dots 145)\, GPa$ and $G = (34 \dots 46)\, GPa$, depending on the angle of the applied force in respect to the basal plane. The elastic constants of a hcp-α single crystal was described by Flowers et al. [49] and more recently by Stapleton et al. [50]. With increasing temperature, both Young's and the shear modulus decrease linearly to the β-transus. [43].

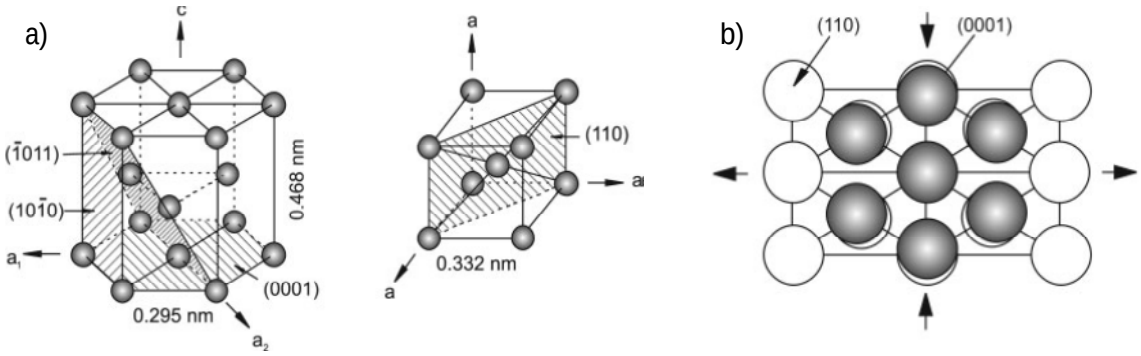

Figure 7: Titanium unit cells: (a) low temperature HCP unit cell and high temperature BCC; (b) the phase transformation according to the BOR [44].

When alloyed, the phase diagram changes. Alloying elements can be either α or β stabiliser, meaning they increase or decrease the transition temperature. Figure 8 shows qualitatively the change of phase transition temperatures in titanium vs. the amount of added elements. Examples for α stabiliser are Al, O, N and C. Aluminium is the most common alloying element for titanium because it strengthens the α-phase, reduces the density, has complete solubility and is the only metal among all α stabilisers [51]. When hot processing titanium in open environment it reacts with atmospheric oxygen, which can enter 200 µm into the surface [52], leading to an increase in the β-transus for example to over 1100 °C at 1 wt.% oxygen content [53] The group of β stabilisers is subdivided in β isomorphous- and β eutectoid forming elements. The β isomorphous

forming elements, such as V, Mo and Nb, have the opposite effect of an α-stabiliser. These elements can allow the alloy to form a stable α+β-phase or a complete β-phase at room temperature, which facilitates hot working [51]. The β eutectoid forming elements create alloys with a eutectoid transition temperature at 300°C; the most common examples are the metals Fe, Cr and Si. Other elements, such as Zr, Sn (belonging like Ti to the IV subgroup) or Hf (IV main group) have hardly any effect on the transition temperature or the effect is different at low or high concentrations. However, alloyed together with other elements they may turn these neutral elements into an α- or β-stabiliser, which shows the difficulty in describing the effect of multiple alloys in titanium.

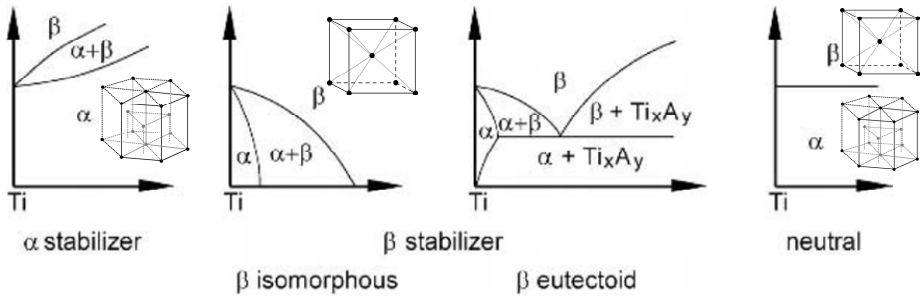

Figure 8: Effects of Alloying Elements on Phase Transformation Temperature [44].

Ti−6Al−4V contains stabilising elements for both phases and forms both phases at room temperature, which labels it an α + β alloy. Its' specific transition temperature is 995 °C [44]. At room temperature Ti−6Al−4V typically contains between 3% and 9% of the high temperature β-phase [45], [54], [55]. Non instantaneous cooling allows the diffusion of Al and V to remain in the phase they stabilise in a greater magnitude (partitioning) [55]. This in turn can change the local transition temperatures, as shown in the phase diagram if Ti−6Al−xV in Figure 9 (a) [44]. Figure 9 (b) shows the bcc β-volume fraction in the material for different temperatures, which is constant up to approximately 700 °C and then increases to 100 % bcc at the β-transus of 995 °C [55]. The nominal composition in wrought material can differ in both phases. There can be up to 7% Al and less than 1% V in the α-phase, but less than 3% Al and more than 16% V in the β phase for example [55], [56]. Kherrouba et al. [57] discussed the relevant diffusion kinetics during the β → α transformation at different cooling rates together the resulting

microstructure. Different compositions can also affect unit cell size and micro elastic properties [58]. Thermal expansion of α and β phase was reported by Elmer et al. [59].

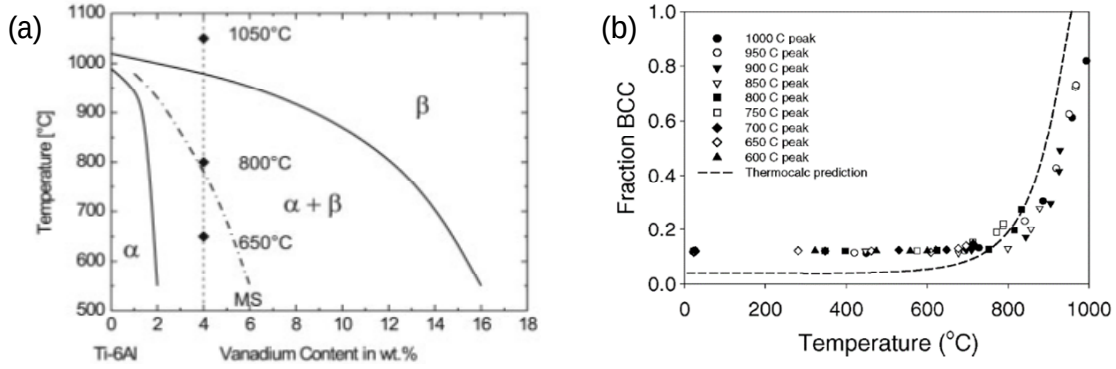

Figure 9: (a) Schematic phase diagram of Ti-6Al-V [44] and (b) β-volume fraction at different temperatures [55].

1.2.2 Crystal Mechanics during Plastic Deformation

Plastic deformation in metals causes distortion in the crystallographic lattice. Cold Rolling can cause plane slipping and twinning of the unit cells. Unlike plane slipping, twinning changes the orientation of a unit cell or can even result in phase transformation [60]. In general a large variety of possible hcp slip systems can be observed [50], [61]. A typical deformation mode in the hcp lattice is slipping of the basal $\{0002\}$ plane in $\langle 11\bar{2}0\rangle$ direction [62], requiring 92 MPa critical resolved shear stress (CRSS) [63]. The preferred one is the prismatic $\{10\bar{1}0\}\langle 11\bar{2}0\rangle$ slip system with a CRSS of 23.5 MPa. Pyramidal slip systems exist as well, but at a much higher CRSS. Changing the temperature [43], [64] or composition [61] can also influence the preferred slip systems [43]. Sole slipping however cannot accommodate the large strain in ductile titanium. Localised stress accumulation on grain boundaries that would result in discontinuity [65] require twinning for compensation [62], especially at high strain rates [66]. The most common primary twins (type I) are $\{10\bar{1}2\}\langle 10\bar{1}1\rangle$ tensile twinning and $\{11\bar{2}2\}\langle 11\bar{2}3\rangle$ compression twinning [67]. Figure 10 (a) shows which twin systems are activated by extension and contraction in a hcp zirconium unit cell [63]. The twins in some of the equiaxed grains in pure titanium, activated by compression, are shown in the inverse pole figure (IPF) in Figure 10 (b) [61]. Note that grains of similar orientation (colour) contain a similar amount of twins. Some of them contain a lot (red) and some contain none (yellow). This highlights the sensitivity of the strain induction orientation to

activate certain twin systems. The twinning behaviour in Ti−6Al−4V Widmannstätten was very recently characterised by Ma et al. [68].

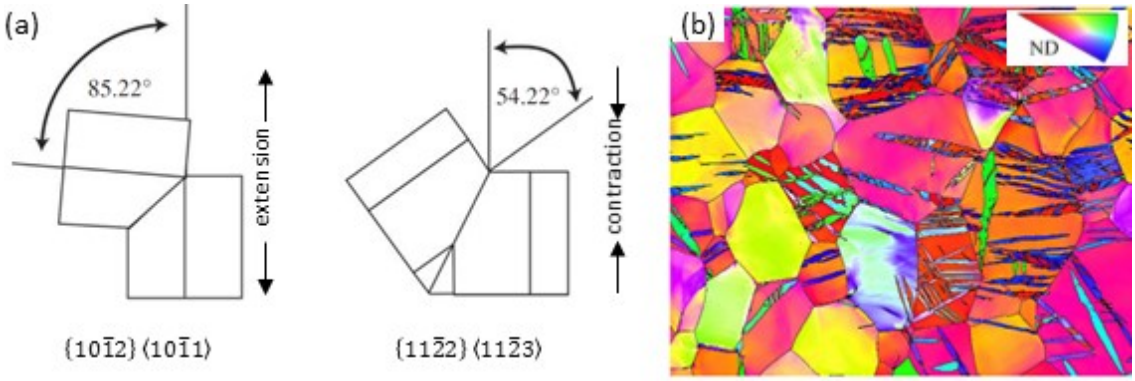

Figure 10: (a) Type I twin systems in a hcp-Zr (c/a = 1.593) on extension and contraction [63]; (b) IPF map of cold rolled CP titanium (c/a = 1.588) with deformation twins in equiaxed α-grains at 8.1 % compressive strain [61].

Bcc twinning was found in metastable β-titanium alloy Ti-25Ta-24Nb on mechanical loading. The two observed bcc twin systems are the $\{112\}\langle 111\rangle$ and the $\{332\}\langle 113\rangle$ system [69]–[71], resulting in a misorientation of 60° and 50° respectively. The twinning variant is again a function of the direction of the applied plastic strain. Ti−6Al−4V contains both, hcp α and bcc β phases at room temperature, but twinning of the bcc unit cell of the β-phase was reported to be not favourable in this particular alloy [71]. Donoghue [72] however suggests that twinning of the bcc lattice of the β-phase within the an α-plate can be possible, if the β-phase is sufficiently small. For other materials it was observed that if a grainsize is below a critical value, then the CRSS drops [73]. This could explain unexpected bcc twinning in lamellar Ti−6Al−4V, where bcc misorientation angles of 60° and 51° were found after β-twinning [72].

Thermal processing of plastically deformed grains with imparted strain energy can trigger structural refinement due to recovery and recrystallisation [44]. However this should not be confused with the grain refinement mechanism in Ti−6Al−4V WAAM by rolling, which is explained in section 1.5.2.1

1.2.3 Microstructure and Mechanical Properties of Ti−6Al−4V

1.2.3.1 Formation at different Cooling Rates

Depending on the processing route that can involve thermal and deformation processes, Ti−6Al−4V can occur in three different microstructures, shown in Figure 11. There is the

fully equiaxed microstructure, the fully lamellar microstructure or a bi-modal (duplex) microstructure [43]. This review addresses mainly the microstructure most relevant the present work, the fully lamellar microstructure. The fully lamellar microstructure is often called "β annealed", as it forms upon cooling from above the β-transus [43], [51], [74], which of course includes cooling from liquid (>1600 °C) in the case of AM to room temperature. Figure 11 (a) shows the fully lamellar microstructure, obtained by air-cooling from the β-phase field.

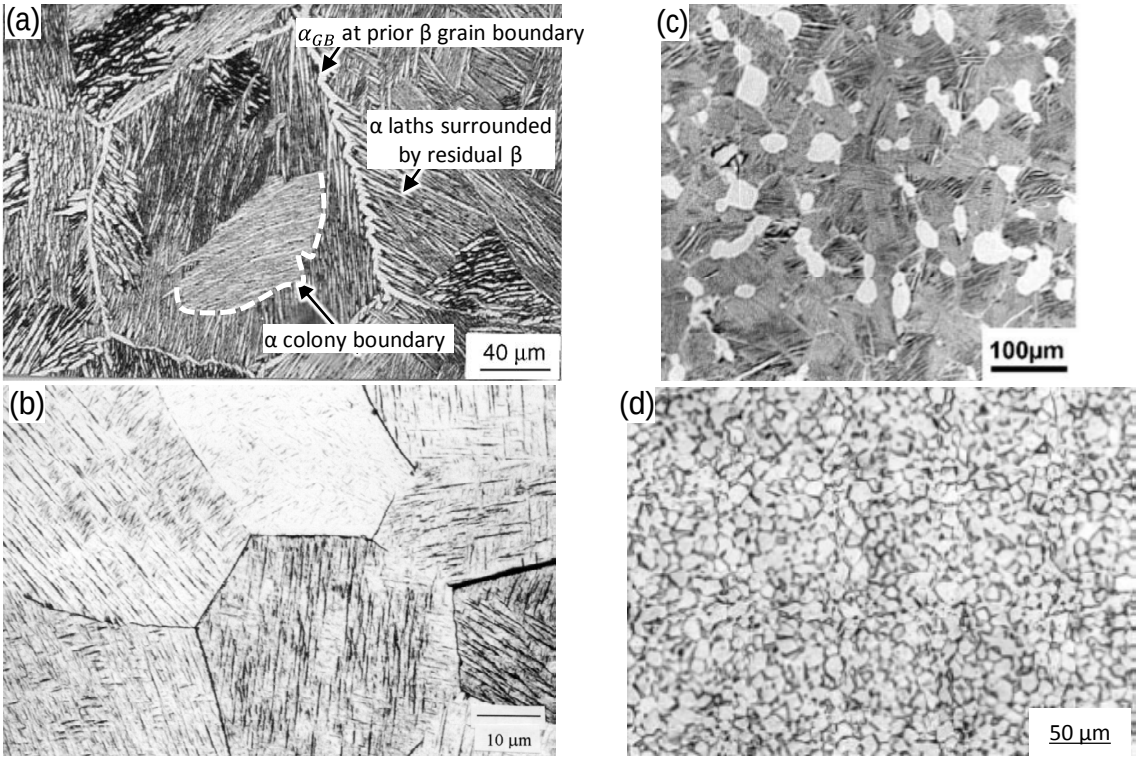

Figure 11: (a) fully lamellar microstructure of Ti–6Al–4V after air-cooling from the β-field [74]; (b) martensitic α'(α'') plates after water quenching [75]; (c) the Bi-modal microstructure of the IMI 834 alloy [43] and (d) fully equiaxed Ti–6Al–4V microstructure after very slow cooling.

The α-phase appears bright and the β-phase dark. A thick α-phase can be found at the prior-β grain boundary, which is why it is called grain boundary α (α_{GB}). Thin α-plates grow from the boundary into the β grain and can form colonies. The length and width of both, α-plate and α-colony decrease with higher cooling rates [44], [47], [57], [74]. The phase transformation at cooling rates that form the lamellar microstructure is diffusion based, but doesn't result in extreme element partitioning [47], which is why a local composition is closer to the nominal one, as opposed to wrought material [56], [76]. It should be noted that due to the densely packed atoms, the diffusion in the hcp

α is between one and two orders of magnitude lower than in the β-phase [44]. The diffusion kinetics were discussed elsewhere [57]. Slow cooling rates below 2 °C/s result in the formation of stable α-colonies surrounded by the residual β-matrix without any martensitic traces [51].

Figure 12 a) shows a CCT diagram of Ti−6Al−4V taken from Ahmed and Rack [76]. At cooling rates above 410 °C/s (defined at 900 °C) the β-phase transforms into a fully martensitic microstructure, oversaturated with β-stabiliser. It appears with orthonogal α' plates (Figure 11 (b)), containing dislocations, stacking faults and sometimes twins. With increasing amount of oversaturated β-stabiliser, the closed packed hexagon of the α' distorts into an orthorhombic α'' unit cell [43]. Slower cooling rates result into α massive microstructure, which appears only in dilute alloys and becomes acicular with higher solute content. It is graduately being replaced by diffusion controlled formation of Widmann-stätten α [43], [76]. The temperature of completed transformation increases to 780 °C at 20 °C/s and further to the β-transus during quasistatic cooling. Kherrouba et al. [57] reported more recently the calculated and measured volume fraction of β→α transformed phase fraction in Ti−6Al−4V at different moderate cooling rates (Figure 12 (a)). These rates are comparable to those expected inside the heat-affected-zone (HAZ) during the WAAM deposition of this alloy [77].

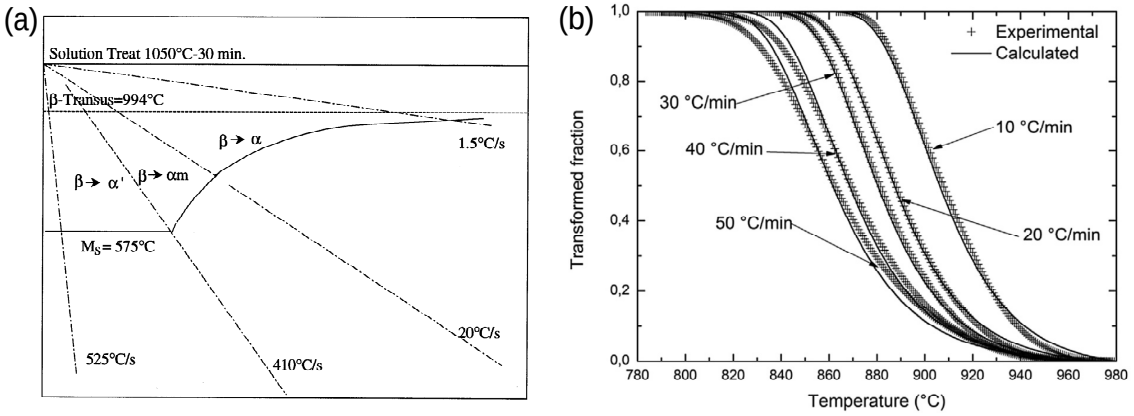

Figure 12: (a) CCT Diagram of Ti−6Al−4V [76] and (b) β → α transformed volume fractions during cooling [57].

Examples for a bi-modal (duplex) microstructure and fully equiaxed microstructure are presented for comparison in Figure 11 (c) and (d) respectively. They are excluded from this review, but would be produced by annealing below the β-transus.

Since the martensitic α'-phase has an hcp structure as well, it is difficult to distinguish it from the normal α-phase using X-Ray Diffraction (XRD). As mentioned above, the element partitioning below the martensitic cooling rate changes the hcp lattice size compared to the diffusionless martensitic transformation, which determines the peak location the XRD pattern of the α-phase [58] and can help to distinguish between α and α'. The appearance of a microstructure that contains traces of α' martensite can range from Figure 11 (a) to (b). The orthorombic α'' martensite however can be identified more easily. The typical orientation of the nanoscopic hcp unit cell in respect to the microscopic α-plate orientation, which can depend on the global orientation in the macroscopic deposit was investigated by Mathisen et al. [65] and Eriksen et al. [78] on Ti−6Al−4V plasma WAAM material. Figure 13 shows the alignment of the hcp cell in the grain boundary α_{GB} and the coherency of the growing α-colony and the surrounding parent and residual β-matrix respecting BOR.

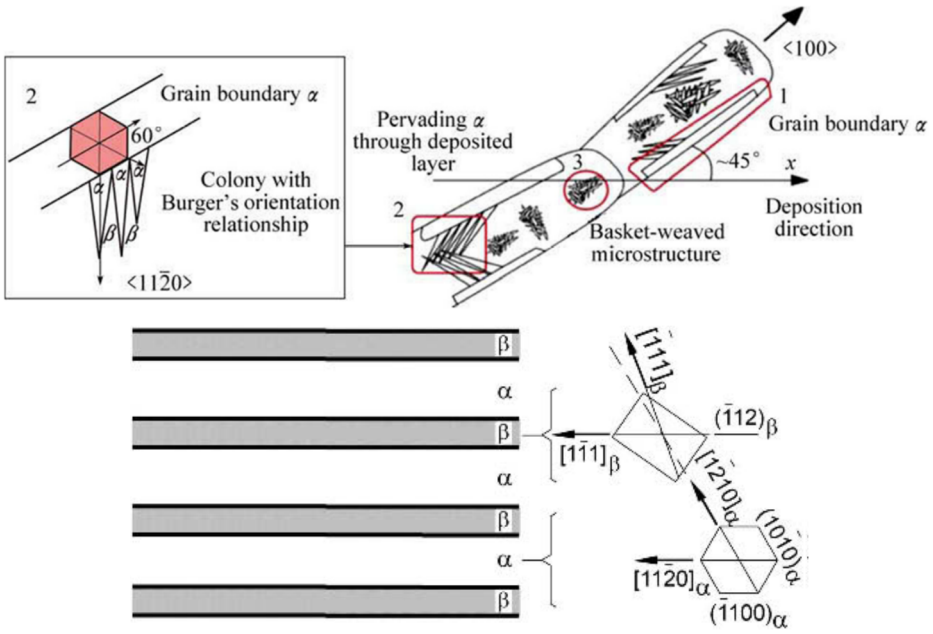

Figure 13: (a) Schematic of the hcp orientation in the grain boundary αGB and in subsequently formed lamellar microstructure [65], [78]; (b) Schematic representation of the crystallographic relationship between α plates and β matrix in α colonies [43].

1.2.3.2 Static Mechanical Properties

The morphology of the phases in Ti−6Al−4V strongly influence the mechanical properties [51]. Figure 14 visualises the strength relevant features in a fully lamellar microstructure.

The features are the prior-β grain size D, the α-colony size d and the α-plate size t [51]. Their dimensions are very sensitive to the cooling rate that ultimately determines the mechanical properties [47]. An increase in cooling rate decreases the size of all three of them. Table 1 shows the yield strength and elongation of a fully lamellar microstructure with respect to the α-plate size t [44]. However, the main driver for mechanical properties is the α-colony size t, as it represents the slip length [47], [75].

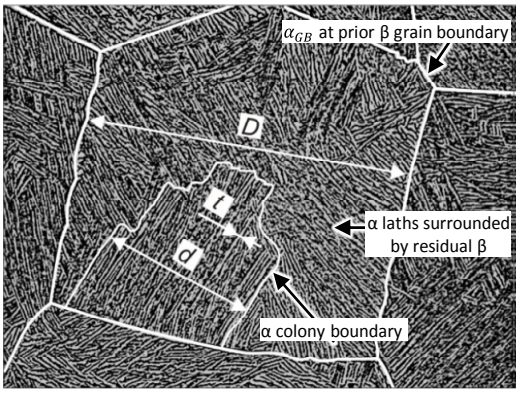

Figure 14: Feature definition relevant for mechanical properties in lamellar microstructure [51]

Smaller α-colonies, which are limited to the prior-β grain size, result from a higher cooling rate from the β-phase field and have in general both, an increased yield strength and ductility. Figure 15 shows the influence of the cooling rate on both properties, taken from four authors. The authors are in good agreement in strength and in moderate agreement in elongation, apart from Gil et al. [75], who reported values at cooling rates at an order of magnitude lower than the others.

Table 1: mechanical properties of Ti–6Al–4V depending on the α-plate thickness [44].

Thickness t of α-plate [μm]	Yield Strength [MPa]	Elongation [%]
0.5 (fine)	1040	20
1	980	25
10 (coarse)	935	15

At cooling rates above 8 °C/s or 18 °C/s the strength dramatically increases due to the formation of martensitic microstructures, where the colony size (slip length) becomes equal to the individual α-plate [47], [51], [74]. The highest cooling rates above 410 °C/s [79] result in a fully martensitic microstructure and can achieve a yield strength of more than 1100 MPa. The martensitic microstructure however drastically decreases the ductility, as the fracture mechanism changes from ductile trans-crystalline through the

α-colonies to inter-crystalline along the soft grain boundary α_{GB}. Comparing Figure 15 with Figure 14 (b) suggests that α-plate around 1 µm width can contain traces of martensite and indicate the transition point from ductile to brittle.

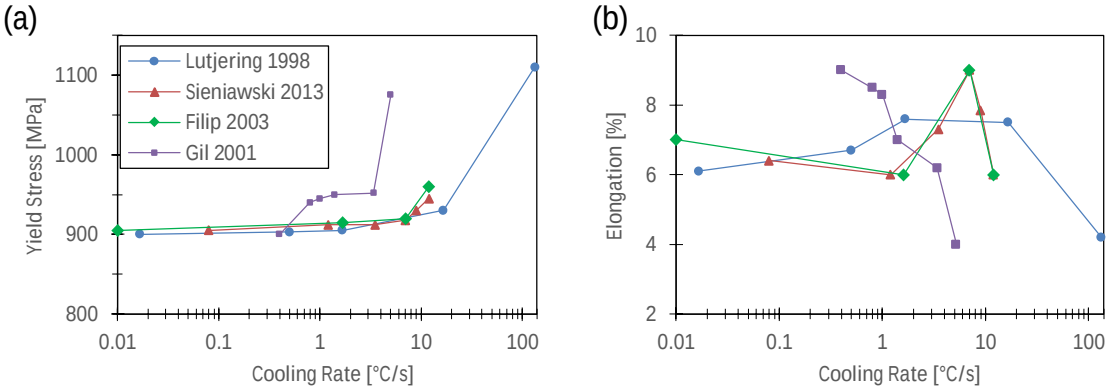

Figure 15: Comparison of static mechanical properties relative to the cooling rate taken from [47], [51], [74], [75][1]: (a) strength and (b) maximum elongation.

Without the presence of α_{GB} it could be possible to better exploit the high strength of the martensitic grain with less loss of ductility. Without the presence of martensite it might be possible to achieve high strength and good ductility, if colonies of thin α-plate can be produced in a different way (other than by controlling the cooling rate). Environmental oxygen, that can be solutionised during hot processing not only changes the β-transus.

The strength of titanium also increases significantly with higher oxygen content, as the CRSS of both preferred slip systems increases from 20 MPa and 60 MPa for the prismatic and basal slip system respectively to approximately 120 MPa with 0.8 at% (0.3 wt%) of equivalent oxygen content (O_{eq} = O + 2*N + 0.75*C (in at%)) [63], while it still remains ductile [80]. The allowable limits for commercially pure titanium grades 1 to 4 increases from 0.18 wt% to 0.4 wt% [43]. Also the alloy Ti–6Al–4V embrittles dramatically above 0.4 wt% oxygen [81]. According to AMS 4911L, Ti–6Al–4V sheets have therefore an allowed oxygen and nitrogen content of 0.2 and 0.05 at% respectively.

[1] The publications from Sieniawski et al. 2013 and Filip et al. 2003 were produced 10 years apart, but both by Rzeszów University of Technology, hence the similar values.

1.2.3.3 Fatigue

The first dislocation motion during fatigue is determined by the slip length (α-colony size) and correlates with the yield strength. Resistance against the first motion is equivalent to the resistance against crack nucleation and therefore determines the high-cycle-fatigue (HCF) strength. High cooling rates that form small α-colony improve the fatigue life [47]. Figure 16 (a) shows the improved fatigue life for a finer lamellar microstructure that also has an improved yield strength, achieved by higher cooling rates. Figure 16 (b) is a micrograph of an initiated crack during fatigue loading.

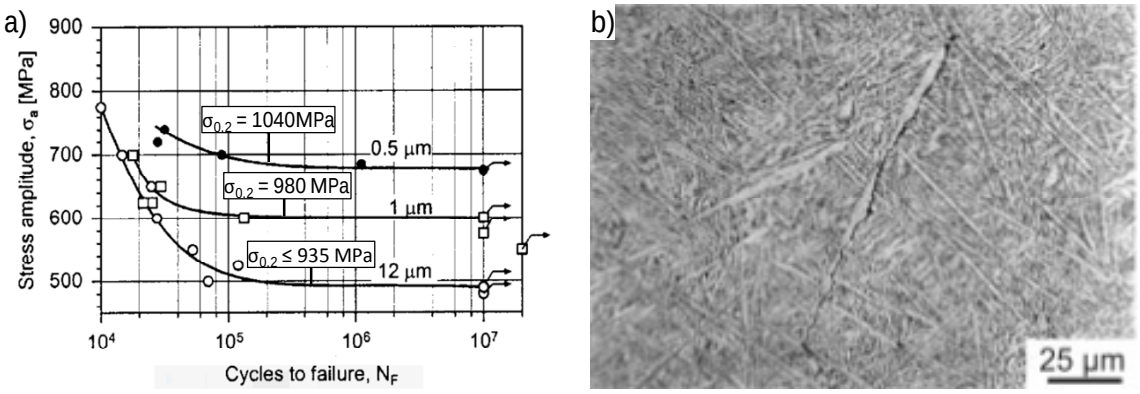

Figure 16: (a) HCF behaviour depending on the α-plate width t at R=-1 of Ti–6Al–4V and (b) the fatigue crack initiation within the plate using σa = 775 MPa [44].

For low-cycle-fatigue (LCF) behaviour not only the nucleation, but also the nature of the crack propagation is relevant. Both, martensitic plates and α-colonies boundaries are strong obstacles for the propagation, so their presence due to high cooling rates also improve the LCF [47]. Fracture surfaces of ductile and brittle Ti–6Al–4V, produced at different cooling rates can be observed elsewhere [74], [82].

1.3 Microstructure and Mechanical Properties of Ti–6Al–4V WAAM

1.3.1 Development of Microstructure

A side view of the molten pool in Ti–6Al–4V AM is shown in Figure 17, which actually shows a schematic of the SLM process, but the principle is similar to WAAM. Macrographs using different welding heat sources are presented in Figure 18 (a-c), showing side and cross sections using Tungsten Inert Gas (TIG) [77], Cold Metal Transfer (CMT) [26] and Plasma Arc Welding (PAW) heat sources. Visible in all three of them are

large columnar grains that grow from the substrate and can extend the height of the deposited wall. Their appearance is illustrated in Figure 17 and Figure 18 (d)[83].

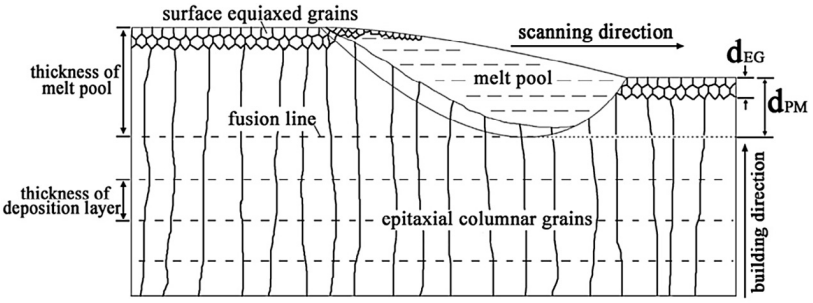

Figure 17: Schematic illustration for the side-sectional formation of large columnar prior-β grains for titanium AM components during the layer-by-layer laser melting deposition [17].

Depositing on a fully equiaxed substrate, results in the typical columnar microstructure: The high temperature bcc β-grains of the deposit grow epitaxially from the existing grains, which impart their crystallographic orientation. During continuous deposition, solid state grain growth and growth during solidification of the added material typically favours the orientation of the $\{001\}_{bcc}$ fibre parallel to the maximum thermal gradient [84]. The result is strong $\{100\}_{bcc}$ texture, as grains of this orientation steadily supplants grains with other orientations until finally only large grains with the dominant orientation co-exist. The inverse pole figure (IPF-z) [85] in Figure 18 (e) shows according to this that the crystallographic orientation of all large columnar prior-β grains is the dominant $\{001\}_{bcc}$ fibre [30], [86], resulting in the mechanical anisotropy. The microstructure inside the large prior-β grains of Ti−6Al−4V using WAAM is the bespoke lamellar microstructure [87]. The cooling rate not only influences the size of the α-plate, but also the β-morphology. High cooling rates, which go along with increased deposition rates and scanning speed, can decrease β-grain size and change the morphology in LMD from being primary columnar into equiaxed [17]. Reduced α and β sizes increase the materials strength. The horizontal lines in Figure 18 (a-c) are the so called layer bands. They are not the fusion boundary shown in Figure 17, but the border of the HAZ of each deposit. Their distance apart is equivalent to the layer height. Initially it was believed that these bands refer to the β-transus temperature [29] of 995 °C [44], but measurements of more recent work suggests that these lines probably represent the α-dissolution temperature [77], which is 748 °C for Ti−6Al−4V [88]. The size and

morphology of the α-plate within the β-grains depends also on the location between two layer bands: The finest α-plate can be found just above one layer band. They grow almost linearly in size with increasing distance from the band until the next layer band, from where the pattern repeats [54]. The size can range between 0.3 µm and 1 µm [77]. The α morphology transition from the parent material microstructure to the deposit (Figure 18 (d)) can also be found in EB welding of Ti–6Al–4V [89] for example, and the fusion zone contains the AM typical lamellar microstructure.

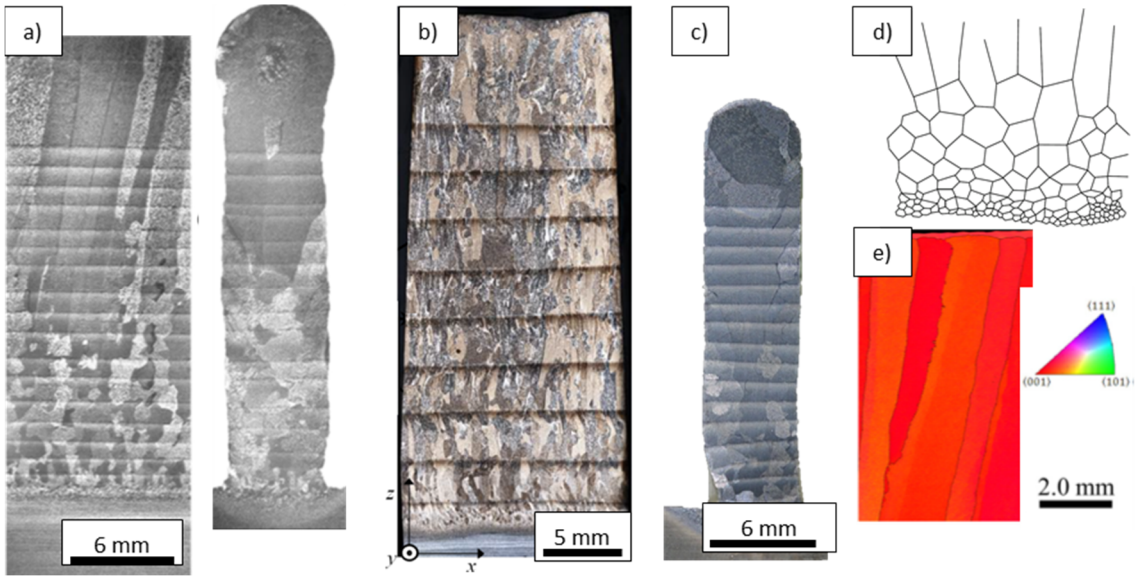

Figure 18: Macrographs of Ti–6Al–4V AM: (a) side and cross section deposited using TIG [77]; (b) side section using CMT [26]; (c) cross section using PAW; (d) a schematic of the epitaxial grain grow [83] and (e) the IPF-z orientation coloured EBSD map of the reconstructed parent β phase [86].

Charles et al. [90] developed a thermal model for TIG-WAAM that included phase transformation in each heat cycle, as well as diffusion and instantaneous events. The grain evolution equation can account for individual local thermal histories. The model also considered α dissolution to β, martensitic transformation, as well as β-grain size and α-plate width [91].

1.3.2 Crystallographic slip in WAAM

Mathisen et al. [65] investigated the crystallographic strain response in Ti–6Al–4V WAAM material including preferred slip systems and dislocation compensation in the matrix to maintain structural continuity and intergranular interactions. They show local stress accumulation at prior-β grain boundaries and within the different α-colonies and

Widmannstätten during mechanical loading and the role of the crystal orientation in combination with the CRSS of the hcp unit cell. Slip planes are typically restricted to the longest dimension of the α-plate and grain boundary α_{GB} was not found to be significantly weaker compared to coarse α-colonies.

1.3.3 Mechanical Properties in WAAM

Since the microstructure and therefore the mechanical properties depend mostly on the thermal history (e.g. cooling rate from the β-phase field), which changes significantly with varying deposition parameters and strategies, the standard properties achieved cannot be determined for any AM process. Ti–6Al–4V WAAM using a plasma heat source however can achieve deposits without pores that diminish mechanical performance [29]. Thermal histories can be predicted by simulations to determine desired material characteristics, as done by Nikam et al. [18] for plasma deposition of Ti–6Al–4V. The yield and ultimate strength can reach 835 MPa and 930 MPa respectively in a single pass wall using plasma or TIG heat sources with maximum elongations up to 20 % [87], [92]. These properties however are typically anisotropic, due to the bespoke texture: in vertical build direction, normal to the substrate, the strengths are roughly 5 % lower and the elongation 40 % higher compared to the longitudinal direction [87], [92]. Wang et. al [87] furthermore investigated the HCF behaviour ($R = 0.1$ at 30 Hz) of the TIG deposited Ti–6Al–4V WAAM, where most of the specimen in both directions reached the fatigue life of 10^7 cycles at 600 MPa with a higher run-out rate for the vertical specimen. A few specimens however contained pores, causing early failure. The crack growth behaviour was investigated by Zhang et al. [93], [94]. The deposit has a better crack growth resistance compared to the wrought substrate with fine equiaxed microstructure, causing the crack path to deviate into the substrate. Xie et al. [95] recently investigated the anisotropic influence of the α-regime and grain boundary α_{GB} on the crack path selection and growth rate. The fatigue crack in the vertical build direction tends to deviate away from the grain boundary α_{GB}. In longitudinal direction, the fatigue crack deviated towards the α-colony and away from the basket weaved microstructure. Different deposition strategies, thermal management and other factors can influence and improve these properties and will be discussed in section 1.5.

Apart from the mechanical properties of deposited material, the component performance can also be influenced negatively by pores and voids, which are common problems using aluminium alloys [27], [96] or Ti−6Al−4V and CMT as the WAAM heat source. Lack of fusion and key-holes however can occur especially at intersections using wrong deposition parameters. These defects must be avoided to exploit the material properties, but they are uncommon for depositing Ti−6Al−4V with plasma heat sources.

1.3.4 Mechanical Property Comparison to other AM techniques

All AM processes typically have a fully lamellar and/or martensitic Ti−6Al−4V microstructure with comparable morphological features, such as α-colonies, basket weaved Widmanstätten, martensitic structures, large and columnar prior β-grains and grain-boundary α_{GB}.

1.3.4.1 Powder AM

The laser-powder-bed system SLM produces the highest strengths reported for AM. The high cooling rate produces strong martensitic α'' Ti−6Al−4V [97], which can reach 1140 MPa yield and 1245 MPa ultimate strength with only 4.7 % elongation [98]. The strength of electron beam melted powder can have yield and ultimate strengths of 1025 MPa and 1100 MPa respectively with 12 % elongation [99], [100]. The fatigue strength however is symptomatically low at 250 MPa [99], due to typical powder defects, like voids and pores. The blown-powder based processes can have yield and ultimate strength of 950 MPa and 1025 MPa respectively with 5% to 12% anisotropic elongation [101].

1.3.4.2 Other Wire-based AMs

The properties of other wire-based HDR Ti−6Al−4V AM processes, like EBAM® or RPD™ are comparable to those of WAAM, due to similar heat input and cooling rates: The yield and ultimate strength of Norsk Titaniums Ti−6Al−4V using their RPD™, are 835 MPa and 910 MPa respectively [36]. The electron beam and wire-based deposited strength of Sciaky inc. is comparable, but slightly less due to even higher deposition rates. The 3DMP® process of Gefertec GmbH is a MIG-based AM process, who recently started depositing titanium, but didn't report any properties yet. The private research company IK4-Lortek uses the CMT process and achieved 890 MPa and 990 MPa ultimate and yield strength [102], due to a colder process and higher cooling rates. Laser + Wire deposited

Ti–6Al–4V can have yield and ultimate strengths from 800 MPa to 925 MPa and from 900 MPa to 975 MPa at elongations between 5% and 15% [82]. The values are mostly driven by the amount of grain-boundary α_{GB}. Brandl et al. [103] and Baufeld et al. [23] directly compared the performance of laser-deposited Ti–6Al–4V wire with WAAM.

1.3.5 Summary

In summary, the as-deposited properties of Ti–6Al–4V using all AM techniques are generally good, but it cannot be said that one process produces higher strength and better ductility than others. The direct comparison of mechanical properties between processes can be misleading, as different technologies can be used with a range of parameters that determine the deposition rate, and therefore heat input and cooling rates. Agius et al. [20] for example summarises the wide range of static and dynamic mechanical properties reported by various authors using different powder-bed fusion parameters. Figure 19 shows qualitatively the anisotropy and the influence of deposition rate and cooling rate on the as-deposited properties of two arbitrary AM processes. Increasing the deposition rate often increases the heat input, therefore decreases the cooling rate. This results in reduced strength with increased ductility.

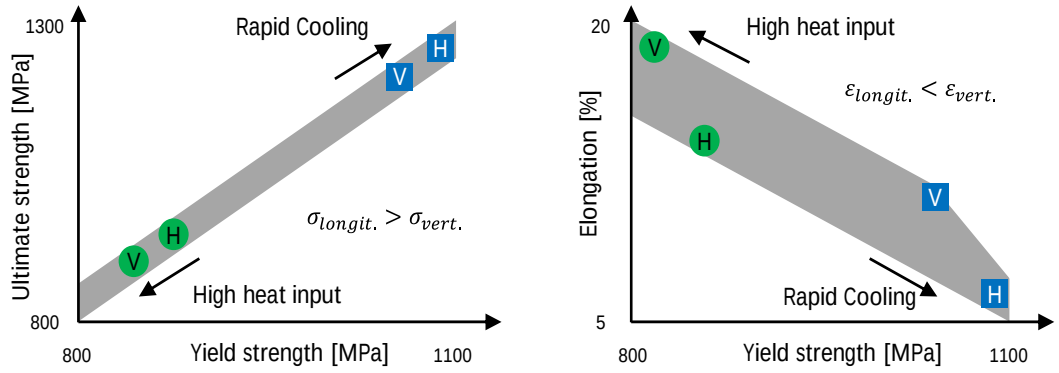

Figure 19: Qualitative Influence of deposition rate and cooling rates on static mechanical properties in vertical (V) and horizontal (H) direction of two arbitrary AM processes with high and low cooling or deposition rates.

While the horizontal direction features a slightly higher strength, the vertical direction typically comes with a much better ductility, which is due to texture, rather than the thermal history. Powder-based systems however often show issues with pores and voids, decreasing the ductility and fatigue strength significantly in this alloy, popular for aircraft structural components. Therefore wire-based systems are favoured for critical structural and dynamically loaded components, since defects are far less likely.

1.4 Development of Residual Stress and Distortion in Metal AM

Common causes for residual stress development in solids can be deformation with unbalanced local plastic deformation, machining, chemical treatment or phase transformation processes with volume changes [104]. The most prominent cause however is thermally induced stresses, which will be focused on in this review.

1.4.1 Thermal Residual Stress Development

Due to thermal shrinkage, residual stresses occur with large magnitudes in metal welding and additive manufacturing and are often accompanied by distortion. An infinitesimal weld nugget in a solid environment can be considered as a bar clamped in non-deformable brackets, which is figurative for the idealised model of Deplus et al. [105], who explain the stress development using the diagram in Figure 20: The sequence shows the stress development in a constrained bar during heating and cooling.

$$\frac{\Delta\sigma}{\Delta T} = E(T) * \alpha_T(T) \tag{1}$$

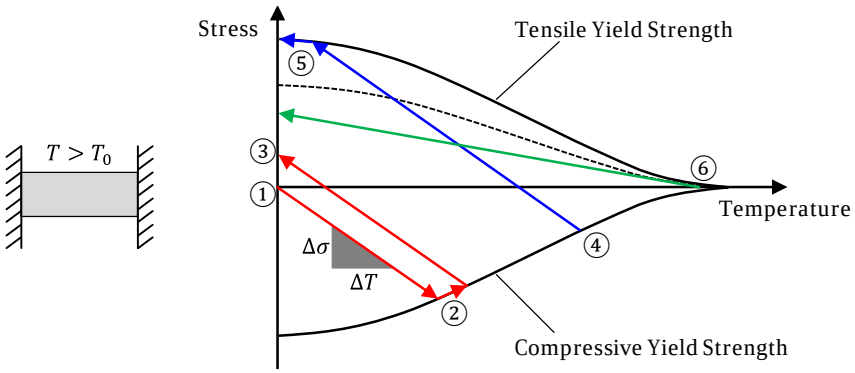

Figure 20: Residual stress development in a constrained bar during heating and cooling (adpt. [105]).

The bell curve represents the characteristic yield value over the temperature. With an increasing temperature, both the tensile and compressive yield strength decrease until reaching zero at the melting point. Before heating, the bar does not contain any stress (1). With rising temperature, the compressive stress increases linearly with the temperature, according to eq. (1), where the Young's modulus *E* and the coefficient of thermal expansion α_T can be slightly temperature dependent. At the same time the compressive yield strength of the material decreases until the increasing stress reaches the compressive yield curve. Further increasing the temperature finally causes plastic

flow (2), i.e. shortening the nominal stress-free length. When cooled to the initial temperature, the bar contains tensile residual stress (3). If the bar during the first heating step would have been heated further (4), the residual stress could even reach the tensile strength curve before coming back to the initial temperature, leaving tensile residual stress equal to the yield strength in the bar (5). The slopes $\Delta\sigma/\Delta T$ and the bell curve are independent thermo-mechanical material properties. Therefore cooling from liquid (6) can result in tensile residual stresses between 0 % and 100 % from the yield stress. If the stress developing gradient $\Delta\sigma/\Delta T$ is equal to or higher than the degree in which the yield stress drops with the temperature, then the residual stress reaches yield stress in point (5). If the gradient is lower, then is residual stress will be below the yield strength. The gradient $\Delta\sigma/\Delta T$ for Ti−6Al−4V for example is 0.980 MPa/K, while the yield stress drops with approximately 1.2 MPa/K [Guo 2008], thus this alloy should in theory develop residual stresses at about 80 % of the yield strength at room temperature in rigid brackets. If the brackets, i.e. the solid environment, are also affected by thermal expansion, which is the case in welding, then the stress development can be mitigated. The gradients $\Delta\sigma/\Delta T$ for pure aluminium and some steels for example are with roughly 1.69 MPa/K and 1.89 MPa/K respectively higher than for the titanium alloy and result in theoretical residual stresses that reach 100 % of the respective yield stress, even if the environment is heated.

1.4.2 Residual Stress and Distortion in Welding

Welding is a classic and comprehensively investigated engineering example where residual stresses occur. The development follows the principle from Figure 20, as the weld seam and the two components to be welded represent the thermally loaded bar and the surrounding clamps respectively. Masubuchi [106] explains the development of residual stresses in linear welds with the help of the schematic in Figure 21 (a) showing process temperatures and resulting residual stress. With the thin sheet assumption, any residual stresses do not balance through thickness, but through the surrounding material. The four stages represent the temperature and stress field before welding, in the cross-section of the weld pool, in the cross-section after solidification during cooling and the established stress field. The maximum residual stresses can even exceed the

parent material's yield strength, if the filler material has a higher strength than the joined sheets [107], [108]. The welding process however influences the size of the plastically deformed region, processes that involve larger heat input generate a greater plastically deformed region, resulting in larger distortion [108]. Using low-heat-input solid state butt welding, such as friction stir welding (FSW), the maximum tensile residual stresses can be kept below 30 % of the parent material's yield strength [109], [110], which also reduces the distortion. Peak stresses in Ti–6Al–4V butt welds using EB welding can reach 600 MPa and even yield stress at the very surface, measured with XRD, ESPI and contour method [89].

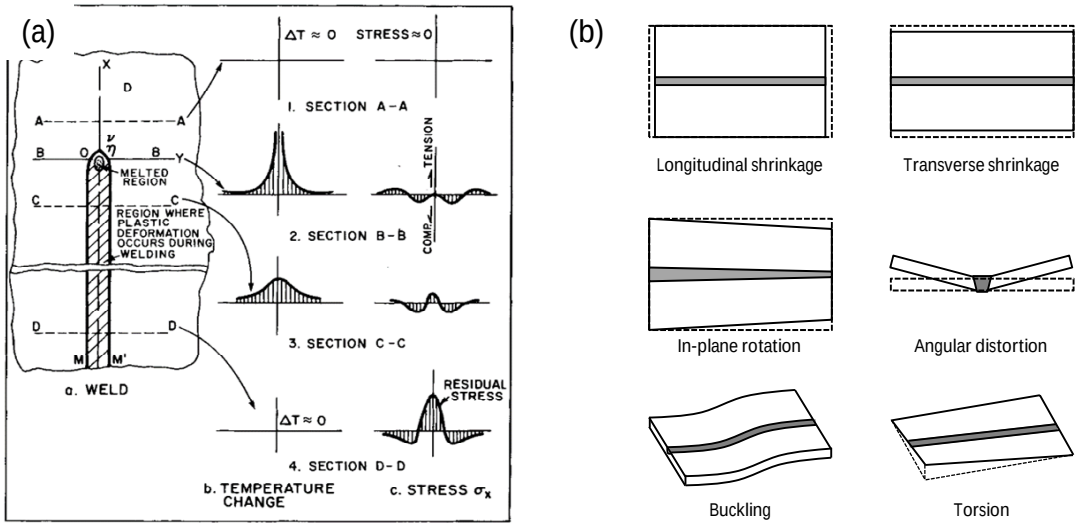

Figure 21: (a) Schematic of the temperature and stress history during welding [106] and (b) types of distortion.

The cross-hatched area indicates the region where plastic flow occurred, which is the region that finally exhibits longitudinal tensile residual stresses. The surrounding material balances that tensile stress and compressive stress develops. The plane stress field can cause distortion, which involves stress redistribution. Figure 21 (b) gives an example of the different distortion types that can occur.

1.4.3 Residual Stress in WAAM

Because WAAM uses arc-welding heat sources, the stress development is comparable to welding, as the first deposited layer is effectively a bead-on-plate weld. Figure 22 shows the qualitative residual stress development in a free-standing WAAM wall and the redistribution upon distortion upon after unclamping, proposed by Colegrove et al. [111], who performed the first residual stress measurement in a steel WAAM wall. A

free standing WAAM wall forms a T-shaped cross section with the substrate (Figure 22 (a)).

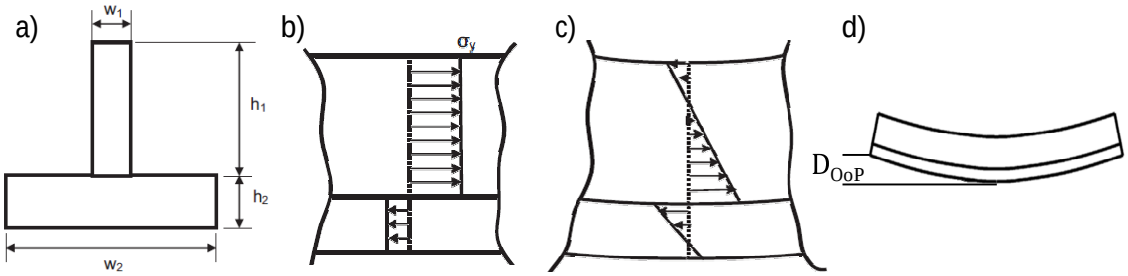

Figure 22: (a) WAAM cross-section with the deposit on the substrate; (b) Constant longitudinal tensile stresses in the deposit and balancing compressive stresses in the substrate; (c) redistributed stress field after unclamping and (d) schematic out-of-plane distortion D_OoP [111].

The wall develops large tensile residual stresses that are supposedly constant along the wall height and are balanced by compressive stresses in the substrate (Figure 22 (b)), while the structure remains clamped rigidly. After unclamping, the unbalanced stress field redistributes to a self-equilibrium state (Figure 22 (c)) by distorting upwards out of plane (Figure 22 (d)). The stress profiles before unclamping (Figure 22 (b)) were modelled, but not measured. The measurement of the residual stresses in WAAM is difficult and time consuming. Four stress measurements on Ti–6Al–4V WAAM before the beginning of the present thesis were performed [112]–[116]. The stress state before and after unclamping, i.e. stress development during the process, was investigated with the help of numerical simulations [39], [117]–[119]. Other numerical models comprehensively describe the development of the stresses in WAAM and stress relaxation during the deposition depending on part temperature or the effect of clamping [120]–[124]. The predicted longitudinal residual stress during deposition reached the yield strength for steel [39], [118], [119]. After unclamping the peak stress in the wall near the substrate drops to approximately 60 % of the initial peak stress before unclamping [39], [113]–[119]. Mehnen et al. [39] modelled the stress development in steel intersections, but did not present the results in great detail. The stress state in the centre of the intersection seems anisotropic and can be compressive under certain conditions. Other processes, such as SLM, are more widely investigated regarding RS & D [125]. Mukherjee et al. [117] for example predicted almost 1000 MPa

tensile residual stress in Ti–6Al–4V SLM, which is approximately 80 % of the SLM yield strength [98], representing the theoretical maximum according to Deplus et al. [105].

In summary the stress development is widely investigated in other AM processes using numerical simulations. However, actual measurements are rare and limited to straight single pass Ti–6Al–4V and steel walls.

1.5 Control of Microstructure and Properties of Ti–6Al–4V AM

Since the microstructure that develops in Ti–6Al–4V WAAM and the resulting mechanical properties are very sensitive to the processing route (Chapter 1.2.3 & 1.3), there is a variety of techniques to influence the development. The biggest influences on the microstructure are the thermal history, the composition of the alloy, deformation processes or a combination of these. Both the technical feasibility and the practicality of these methods will be discussed.

1.5.1 Thermal Techniques

Thermal techniques can be either the modification of the cooling rate during deposition or thermal post-processing after building the completed part.

1.5.1.1 Thermal Management and Building Strategy

The cooling rate in homogeneous material is driven by the thermal properties, the heat input and the heat sink. The heat sink is the capability of the environment to extract heat from the deposit and is determined by the temperature and the thermal mass. The thermal mass is given by the geometry of the part. Without deploying active thermal management techniques, the heat input and heat sink can practically only be influenced by the deposition strategy. The heat input is the energy per unit length of the wall and therefore the power $\dot{Q}$ divided by the travel speed v. Examples of the different deposition strategies are the single pass strategy, or for larger features the parallel pass strategy and the oscillating pass strategy shown in Figure 23 (a-c) respectively [92]. The heat input of the single pass strategy is determined by the deposition parameters that define the geometry. It still should be noted that different parameters and heat input can produce identical bead shapes [126]. For the parallel wall the heat input is determined by the parameters for depositing each pass. Note however that due to the

thickness of the deposit there is a large heat sink that assists cooling [92]. For the oscillating strategy there is considerable heat accumulation, since the actual travel speed *v* along the length of the wall is relatively slow, which impedes the cooling rate.

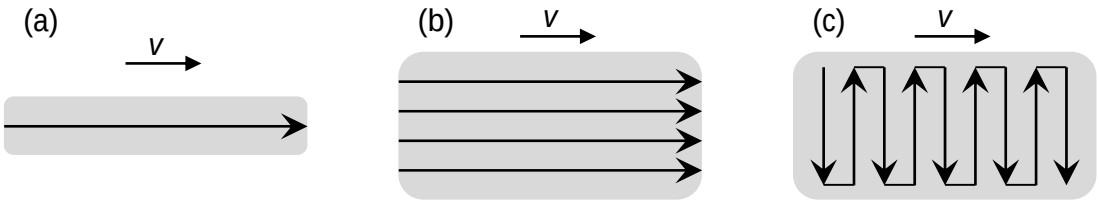

Figure 23: Deposition Strategies: (a) single pass; (b) parallel pass; (c) oscillating pass.

Antonysamy et al. [127] reported the influence of geometrical features on the α and β morphology using EBM, where more surrounding material acted as a larger heat sink and increased the cooling rate. Often the deposition strategy is chosen based on other characteristics, such as the higher deposition rate of the oscillating strategy or its' capability to vary the wall width during a layer [32]. Furthermore increasing the inter-layer dwell time between two passes allows the previous deposit to cool to a lower temperature providing a greater heat sink for the subsequent layer [128]. Figure 24 shows the Ti–6Al–4V DED-AM (Laser + blown powder) microstructure at a deposition rate of 0.96 kg/h, which is comparable to WAAM.

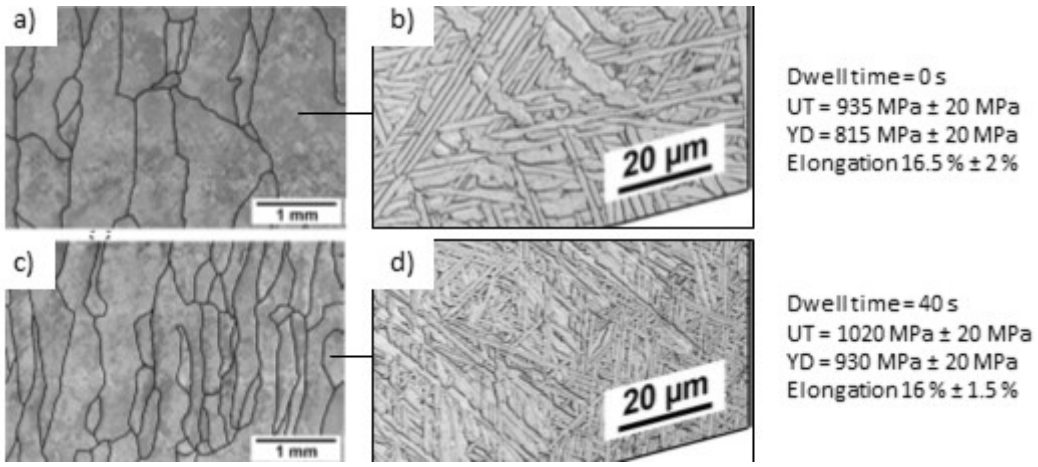

Figure 24: DLD-AM Ti–6Al–4V Microstructure (a) large β grains and (b) α-plate without inter-layer dwell time compared to (c) finer β grains and (d) α-plate with 40 s inter-layer dwell time (adpt. from [128]**).**

Without inter-layer dwell time both the prior β and α grains (Figure 24 (a) and (b)) are larger compared to those with an interlayer dwell time (Figure 24 (c) and (d)). The longer dwell time allows cooling and provides a lower starting temperature, which increases

cooling rate. The increased yield and ultimate strength from 815 MPa and 935 MPa respectively to 930 MPa and 1020 MPa, did not suffer from sacrificing the ductility [128]. However, allowing the structure to cool by providing inter-layer dwell time decreases the productivity. Deploying a trailing heat sink through cryogenic cooling can increase the cooling rate through the transformation field. Active inter-pass cooling allows to reach a lower starting temperature to be established sooner [129].

A pulsing laser beam can also be used for thermal management to increase strength of laser additively deposited Ti−6Al−4V and improve the homogeneity through the build. The short interaction time results in less redundant re-heating of surrounding material and therefore more rapid cooling [130]. CMT power sources are the WAAM equivalent for pulsed deposition, which is used for many materials. However, initial studies showed that Ti−6Al−4V is not very compatible with CMT, as it produces very unstable depositions, poor deposit quality and defects.

1.5.1.2 Heat treatment

Improving Ti−6Al−4V microstructure by heat treatment was discussed in section 1.2.3. Treatment above the β-transus would solutionise the alloy completely and eliminate any traces of the α-morphology. Treatment below the β-transus allows diffusion and modifies microstructural features. Galarraga et al. [79] report the comprehensive effects of different heat treatment parameters, such as cooling rate after solution treatment, aging temperature and time on the phase composition, microstructure, strength and elongation in Ti−6Al−4V EBM, which is fully lamellar in the as-deposited condition. Increasing the aging time and/or the temperature increases the α-plate size, forms grain boundary α_{GB} and improves ductility at the expense of the strength. Faster cooling rates after solution treatment or near-β-transus treatment form martensitic phases, improving the strength at the expense of ductility. The highest achieved strength was a UTS of 1352 MPa, but with less than 5 % elongation. The highest ductility achieved with a heat-treatment was 12 % which is still lower than the 13 % of the as-deposited condition. Longhitano et al. [131] reported in 2018 how the ductility in tension and compression can be recovered at the expense of the strength using different heat treatment temperatures near and above the β-transus, as shown in Figure 25.

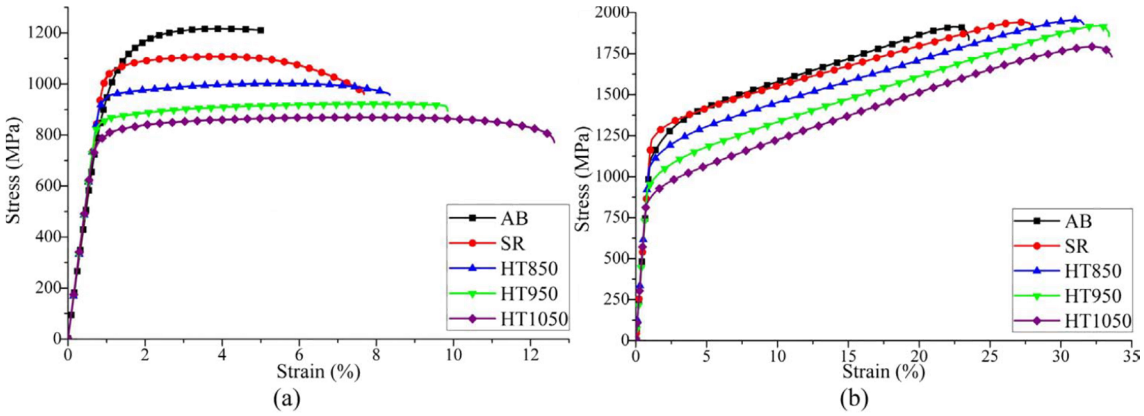

Figure 25: (a) tensile and (b) compressive behaviour of as-built (AB), stress relieved (SR) at 650 °C, and heat treated (HT) at 850 °C, 950 °C and 1050 °C Ti–6Al–4V (SLM) [131].

However, unlike active cooling or a trailing heat sink, post-deposition heat treatment would constitute an additional process step to the manufacturing chain, rather than a process-integrated technique. Furthermore for those heat treatments that require rapid cooling, the low heat-transfer coefficient of titanium limits the cooling rate in thick features, produced in WAAM.

1.5.1.3 HIPing

Hot isostatic pressing (HIP or HIPing) is high temperature heat treatment applied under environmental pressure. It can be used to increase the density of powder additively manufactured Ti–6Al–4V parts that contain pores or voids produced with EBM [100]. Like normal heat treatment, it improves the ductility at the expense of the strength, compared to the as-deposited and stress relieved material. The elimination of defects can drastically improve the fatigue life from 250 MPa to over 550 MPa [99]. Due to the absence of defects with WAAM of Ti–6Al–4V, HIPing becomes.

1.5.2 Mechanical Techniques

As established in section 1.2.2 deformation induced twinning changes the crystal orientations inside a single grain, while maintaining full coherency, but increases slip resistance and therefore increases the material's strength. Inter-pass cold work triggers a more complicated sequence of phenomena, involving phase transformation of twinned crystals, which allows strengthening at relatively low levels of plastic deformation.

1.5.2.1 Rolling

Cold Rolling is a local plastic deformation technique that was initially developed to eliminate RS & D after butt-welding (Figure 26 (a)) [132]–[136]. Colegrove et al. [111] was the first article to investigate its application to steel by rolling the deposit after each layer. Figure 26 (b)) shows the schematic of a WAAM wall deposited on a clamped substrate. After the deposition a roller deforms the deposit plastically, usually after it has cooled to room temperature. Inter-pass rolling enhances the grain refinement of the ferrite in low-carbon steel deposits, but it does not increase the strength [111].

Martina et al. [113] applied rolling on Ti–6Al–4V WAAM walls and found that inter-pass rolling produced in significant β-grain refinement and increased mechanical properties [137]. This was the start for a broad research programme on inter-pass cold work on Ti–6Al–4V WAAM (and aluminium WAAM [96], [138]) at Cranfield University [27], [72], [77], [86], [114], [139], [140].

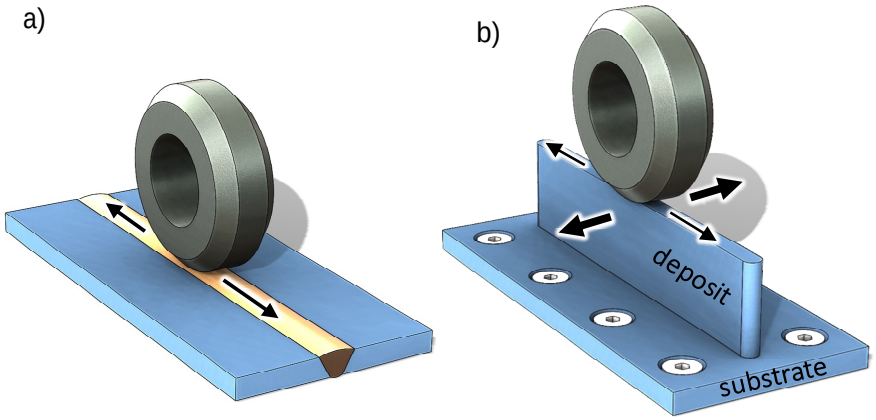

Figure 26: (a) Rolling of butt welds; (b) vertical rolling and (c) pinch rolling of deposited walls [141].

Figure 27 (a) shows the reference microstructure in a Ti–6Al–4V WAAM cross section with the typical large columnar prior-β grains. The inverse-pole-figure respective to the z-direction (IPF-z) shows the strong texture of the reconstructed β-grains and the SEM image shows the size of the α-plate. Figure 27 (b) shows the improved microstructure when deploying inter-pass rolling with a rolling load of 50 kN. The z-IPF shows the refined and equiaxed prior-β grains with random orientation that contain smaller α-plates compared to the unrolled condition. Inter-pass rolling can achieve comparable improvement of the mechanical properties compared to thermal techniques. The

improved properties are shown in Figure 28 (a-c), where it is evident that the improvement in strength does not come reduced ductility and it decreases the characteristic anisotropy, as the horizontal (H) and vertical (V) values converge.

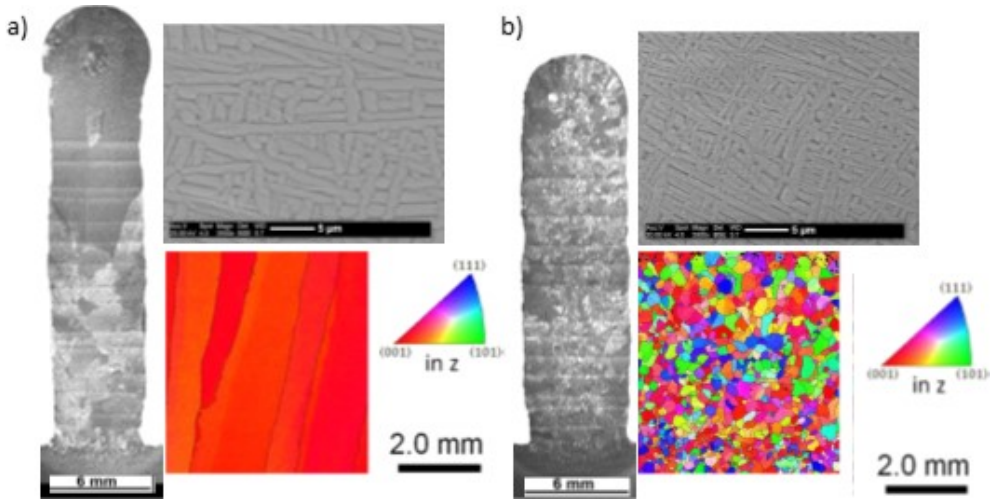

Figure 27: Microstructure, IPF and SEM images of a Ti–6Al–4V WAAM cross-section (a) in the as-deposited reference sample and (b) after inter-pass rolling (adpt. from [77], [86]).

Increasing the rolling load yields greater grain refinement and higher strength. However, the actual microstructural process is not completely understood. Martina et al. [77] investigated how the as-deposited microstructure behaves, when a single rolling step is induced followed by a final deposition step. They showed that the refinement did not appear after a single rolling pass, but the process heat of the subsequent layer raised the temperature of the plastically deformed region, which finally triggered the refinement. Donoghue et al. [86] investigated reasons for the refinement and why a surprisingly low level of plastic deformation is required. Donoghue [72] finally rebutted the initial belief that hcp α-twinning, followed by α→β phase transformation with the new orientation, was responsible for the refinement. Instead he found evidence that the {112} <111> bcc system can be twinned twice during rolling, even though it is understood to be not favourable compared to hcp twinning in Ti–6Al–4V [71]. However he proposed that unexpected bcc twinning becomes possible if the residual β-phase size falls below a critical, but unknown value, which could reduce the CRSS. The rapid cooling rate in WAAM is expected to form very thin β-layers between the α-plates, which could enable this to occur [72]. The following explanation is therefore the concurrent explanation for β-grain refinement in inter-pass rolling. Without plastic deformation, the

residual β-shells that embed the α-plate all have the same crystallographic orientation, because they stem from the same large prior β-grain.

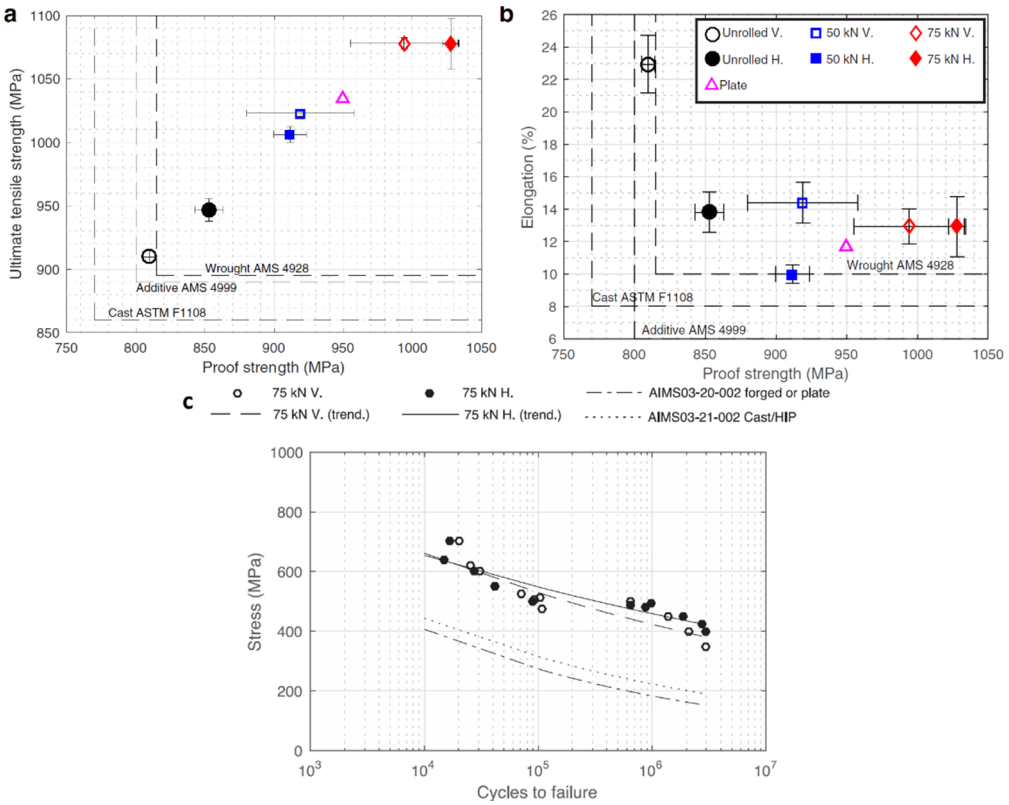

Figure 28: Effect of inter-pass rolling on static properties showing (a) ultimate strength and (b) elongation against proof strength and in comparison with wrought and cast properties; (c) fatigue properties after inter-pass rolling [139].

The process heat of the subsequent layer elevates the temperature and stimulates the α→β phase transformation, which lets the retained β-phase grow before new β-grains could nucleate in pure α-grains [72]. They therefore maintain orientation and re-unite to either form a single β-grain or at least allow α-plate growth, if the material does not transform completely. It is believed that rolling causes bcc twinning inside the residual β-shells and bcc twinning causes misorientations of 51° or 60° [72], so neighbouring residual β-phases cannot grow coherently anymore. Instead they form individual grain, when reheated. During their growth, they absorb the orientation memory of the α-plates on heating and enforce the development of new orientations of α-plates on cooling according to BOR, described in section 1.2.1. Figure 29 shows this microstructural development during the inter-pass rolling process after rolling (a, b) and after the subsequent deposition (c, d). The typical as-deposited microstructure is shown

in Figure 29 (a) and does not change by investigating it with an optical microscope. The EBSD strain map in Figure 29 (b) shows significant misorientation in neighbouring α-plates, which supposedly suggests β-twinning as well.

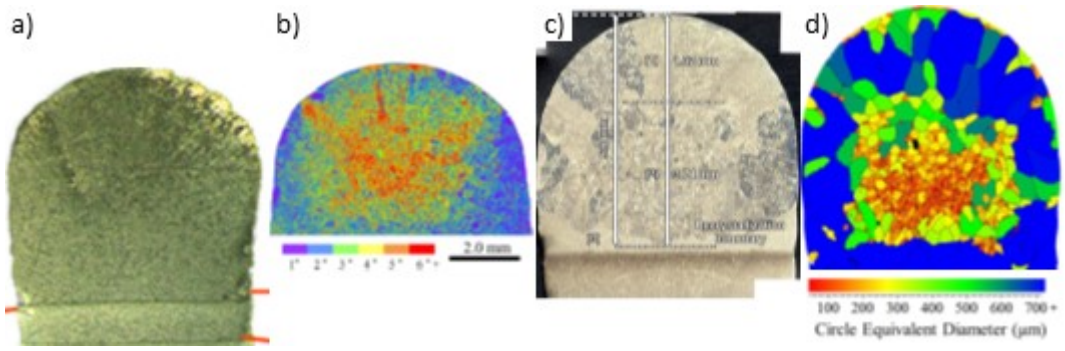

Figure 29: Microstructural development in a Ti–6Al–4V WAAM cross section during inter-pass rolling: (a) as-deposited wall after it was rolled; (b) EBSD strain map of plastic strain distribution; (c) subsequent layer deposited on top of rolled deposit; (d) EBSD map showing reconstructed prior-β grain size (adpt. from [77], [86]).

The way these EBSD strain maps are obtained can be found in the appendix. The refinement after depositing the subsequent layer can be observed in Figure 29 (c), which was taken using an optical microscope. It can be seen that the region that contains large plastic strain prior to deposition now contains very fine prior-β grains, which is quantified with the EBSD map in Figure 29 (d). The deposition serves as the heat treatment of the previously rolled material. An alternative that triggers refinement of plastically deformed material can be active and controlled techniques, such as laser post-processing [142].

Figure 30 shows the High Value Engineering (HiVE) machine, which is a hybrid WAAM system with integrated rolling. The original friction stir welding CNC machine was modified by Cranfield University to study the feasibility of process integrated applications, such as machining or cold working [27]. The HiVE can deposit multidirectional vertical walls using WAAM and can also perform machining or cold rolling on the component [143], [144]. Rolling however is inflexible, has limited applications and can only be used on vertical walls. This limits the application to the most simple features and components and therefore eliminating the design freedom of this AM technique. The required equipment (HiVE) is cumbersome and slow. The full exploitation of WAAM therefore requires faster and more flexible techniques.

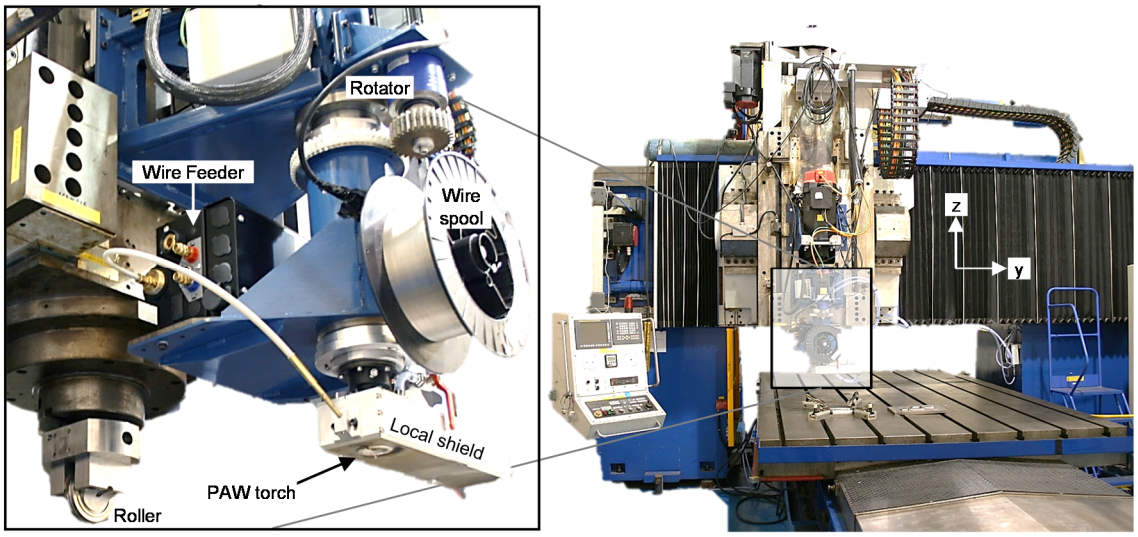

Figure 30: The "HiVE" build platform: WAAM deposition unit retrofitted with a rotator to the z-axis of a FSW machine; the FSW tool is replaced by a customised roller unit.

1.5.2.2 Peening

An alternative local deformation technique is peening. There are a number of alternatives including laser-shock peening [145]–[148], shot peening [149], [150], ultrasonic impact peening [151], piezo peening [152] or Machine Hammer Peening (MHP) [153]–[161]. Kulekci and Esme [162] summarised the application and effects of difference concurrent peening techniques. Peening is widely deployed to improve component behaviour. It is used for example to increase wear resistance and tribological behaviour by surface smoothing and hardening [155], [159], [160] and to induce surface residual stress, which is generally beneficial to improve fatigue life, as it prevents crack initiation and decreases propagation [145]–[147]. Maawad et al. [145] describes the improvement of surface residual stress induced into titanium alloys and Zhou et al. [163] reported that nanocrystalline phase transformation and recrystallisation in duplex Ti–6Al–4V is possible with peening without thermal post-processing. Cold-phase transformation near the surface is an effect that can also be found after MHP of X5CrNi18-10 [164].

The difficulty in process integration with WAAM depends on the technique. LSP for example is typically used on coated surfaces and a layer of rinsing water further increases the shock wave energy density into the material [148], which is not very practicable with WAAM, as it is applied between passes and the material needs to be

clean and dry for the next deposited layer. SP and PP have individual constraints as well that impede the automated process integration. MHP tools however can be manipulated by robotic equipment, which enables easy process integration. UIT can be used as well, however only hand-held tools are currently available.

Figure 31 shows three different types of MHP tools. Figure 31 (a) shows the electromagnetically driven tool Accuradur by the company Accurapuls [154], [158], [161]. Figure 31 (b) is the pneumatically driven FORGEfix (Air) by KWM tools [153], [160] and Figure 31 (c) shows the prototype ECOpeen, which is not on the market yet, but was presented to the community recently [164], [165]. All of these tools can be mounted on an industrial robot or CNC-machine, which makes them compatible for an open process integration like WAAM as an inter-pass or surface finishing tool. Despite the very different technology, the three tools share similar characteristics, such as a tool speed between 200 Hz and 400 Hz, as well as a maximum indenter amplitude of 1 mm to 4 mm at impact energies up to 750 mJ. Therefore unlike the quasi-static rolling, very high strain rates can be expected in Ti–6Al–4V and should be taken into account [66].

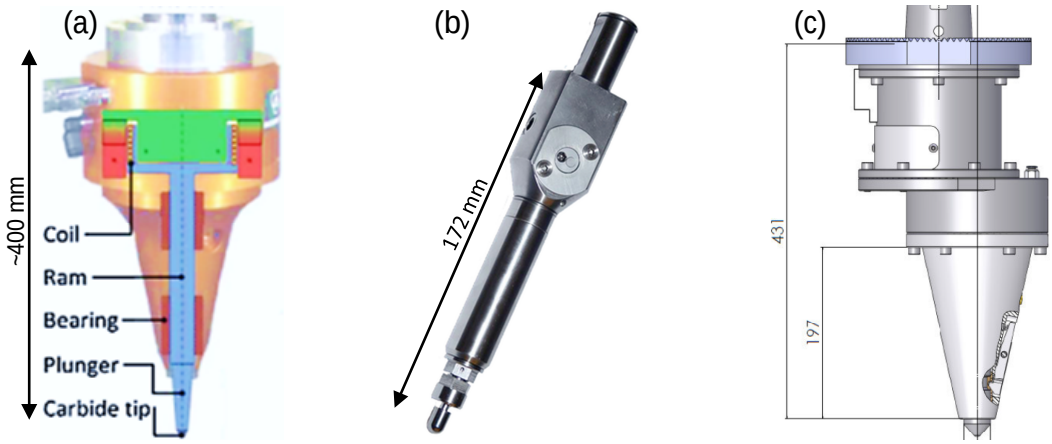

Figure 31: Machine Hammer Peening tools: (a) Accuradur; (b) FORGEfix; (c) ECOpeen [153], [159], [166].

Donoghue et al. [167] showed the first application of inter-pass peening to AM, where it effectively induced grain refinement on Ti–6Al–4V WAAM using a hand-held UIT tool, without describing the capability of the tool or the actual methodology of peening. Byun et al. [168] recently reported grain refinement by inter-pass MHP on Ti–6Al–4V WAAM, as well as improvement in the mechanical properties. The paper is written in the Korean language and does not mention the actual MHP tool used, or any characteristics or

fundamental tool parameters apart from it being applied after every layer. The yield strength of the refined microstructure was 875 MPa and the ultimate strength was 950 MPa, which is an improvement to the otherwise relatively poor as-deposited mechanical properties of the ERTi-5 wire, which has a yield strength of less than 800 MPa [92], [168]. The influence of the alloy and the wire quality is discussed in the following chapter.

1.5.3 Alloying

The chemical composition threshold of Ti–6Al–4V according to ASTM F136 standard [169] allows an aluminium content between 5.5 % and 6.5 % and between 3.5 % and 4.5 % of Vanadium. This chapter briefly discusses the influence of composition and metal feedstock quality on the mechanical properties, as well as the concurrent research about the development of AM-specific alloys.

1.5.3.1 Feedstock quality and AM alloy research

The most commonly used titanium alloy Ti–6Al–4V is typically chosen in AM, as no AM optimised titanium alloy is commercially available. However, even using Ti–6Al–4V wire from different suppliers can result in significant variations in mechanical properties [92], [168]. The chemical specification of Ti–6Al–4V ELI (extra low interstitials) of the powder-bed additive manufacturing machine supplier Arcam EBM for example is voluntarily more constrained than the ELI powder according to ASTM standard [11], [169]. This shows the sensitivity of the alloy to interstitials and the high quality requirement. The development of AM-optimised titanium alloys is limited. No literature was available that discusses deliberately modified compositions of titanium alloys for AM purposes. Zopp et al. [170] investigated the deposition of a different commercially available alloy other than Ti–6Al–4V, which is the metastable β-alloy Ti-5Al-5V-5Mo-3Cr (Ti5553). Using SLM the Ti5553 deposits appeared to have disproportional more issues with porosity compared to the standard Ti–6Al–4V. Ma et al. [34] alloyed titanium aluminide in-situ using WAAM (TIG) with a double-wire system, which is a simple setup to investigate changes in alloy composition. Other investigations of titanium alloy optimisation do not seem to be available yet.

More advances were made with aluminium based alloys. The first alloy to be developed and optimised for an AM process is Scalmalloy® (Al-Mg-Sc) [171]. The as-deposited properties of the low density (2.7 g/cm^3) alloy are 450 MPa yield strength with 8 % elongation at break. More recently Martin et al. [172] reported the successful deposition of heat treatable high strength aluminium alloy (AA7075) without cracks, which is normally considered un-weldable by fusion techniques. This was possible by using powder with nanoparticles, which promoted heterogeneous nucleation and equiaxed grain growth, as opposed to columnar growth of dendrites in normal powder, which results solidification strain and cracking.

1.5.3.2 Addition of elements

The addition of boron is used in Ti−6Al−4V casting, where trace amounts of 0.1 wt.% can decrease the β-grain size by an order of magnitude to 200 µm, which also reduces the size of the α-plate and changes their morphology from large colonies to a basket-weave structure [173]. The formation of TiB was supposedly the strengthening mechanism. Mahbooba et al. [174] report similar reduction in prior β-grain size after trace boron addition into Ti−6Al−4V using EBM, but unlike casting they remained columnar. The increase of TiB phases also act as undesired crack initiation sites and decrease the overall ductility [174]. Bermingham et al. [175] investigated the effect of trace boron addition in Ti−6Al−4V WAAM (TIG) including post-deposition heat treatment. They also report the effectiveness on eliminating grain boundary α_{GB} and colonies, combined with a general α-grain reduction with a smaller aspect ratio length/width. TiB needles serve as nucleation of more and isotropic α-grains. The reason is that TiB needles form during eutectic segregation around the dendrites during solidification. During the β→α phase transformation, α does not nucleate on the β-grain boundary to form α_{GB} or colonies anymore, but on the TiB needles, which prevents the formation of colonies and promotes more equiaxed α-grains. Unlike the previously mentioned EBM process [174], the as-deposited trace-boron-added Ti−6Al−4V WAAM material actually showed an improvement in compressive strain, which also was improved by post-depositional heat treatment [175].

Hydrogen is partially soluble in Ti–6Al–4V. The solubility increases dramatically at temperatures above 650 °C. This effect is used with 2-step thermo-hydrogen-processing (THP), which is the hydrogenation at high temperatures between 550 °C and 850 °C, by keeping the part in Hydrogen/Argon environment, followed be dehydrogenation [98]. The infusion with hydrogenation slowly refines the Ti–6Al–4V AM microstructure, which remains, when the hydrogen is removed in the dehydrogenation step. The extraction of hydrogen is conducted in vacuum atmosphere at similar temperatures below the β-transus to prevent grain growth and the formation of grain boundary α_{GB}. The elongation in SLM parts can be doubled by THP from 4.7 % to 9.8 %, while the yield strength decreased from 1140 MPa 1035 MPa.

At elevated temperatures, the alloy becomes susceptible to oxygen. Environmental oxygen can easily be picked up during the deposition and sensitively influence strength and ductility [52], [176], but it can be used to deliberately increase the strength [80]. Ti–6Al–4V with 1 wt.% oxygen for example can reach a yield strength of 1260 MPa, when aged at 550 °C. As this strength was derived by hardness measurements, no statements regarding the ductility could be made [80].

Small tungsten powder particles (0.7 µm – 2 µm) can almost fully dissolve (96.5 % - 99.2 %) in the Ti–6Al–4V matrix, while larger particles up to 250 µm form second phase composites. A weight percent up to 10 wt.% was added with different particle sizes by Choe et al. [177], who observed an increase of the tensile strength above 1100 MPa. The fully dissolved alloys maintained the same elongation at failure of 14.5 % compared to the unalloyed Ti–6Al–4V.

1.5.4 Summary

The static yield strength of any Ti–6Al–4V material, depending on the various process routes, ranges roughly between 800 MPa and 1200 MPa and the maximum elongation between 5 % and 20 %. Unfortunately the highest strength is typically accompanied by the lowest ductility and vice versa. The typical stress/strain behaviour of differently processed Ti–6Al–4V alloy is illustrated in Figure 32. The three techniques to control the microstructure and mechanical properties discussed in this section increase strength or ductility typically at the expense of the other. Faster heat cycles yield a stronger material

(A), which is influenced by the deposition parameters. Several heat cycles, caused by subsequent depositions, promotes further grain growth of the as-deposited microstructure, making the alloy more ductile (B). Inter-pass rolling allows the absorption of α-grains by the growing twinned β-grains, which not only eliminates the orientation memory, but also the α-plate size of the initially deposited material. The α-microstructure of inter-pass rolled Ti–6Al–4V WAAM appears therefore smaller, as if the material experienced faster or less heat cycles, resulting in higher strength (A). Indeed in some cases it can appear more martensitic.

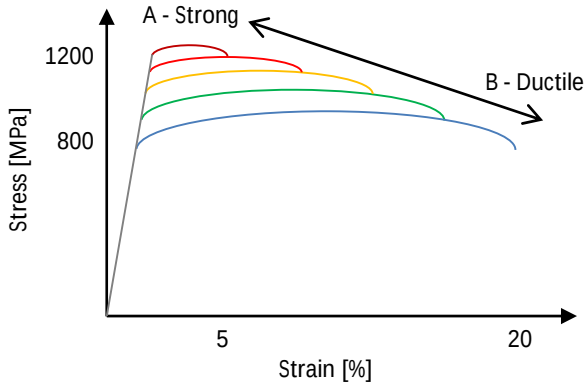

Figure 32: Scheme of possible stress strain characteristics of differently processed Ti–6Al–4V.

Interstitials, such as oxygen, can act as obstacles for dislocation slippage, decrease the slip length and therefore increase the strength as well (A). High energy input results in thermal history of longer elevated temperatures, allowing diffusion and α-grain growth, resulting in more ductile material (B), as long as the material still forms α-plate and not the bi-modal microstructure. The same can be said for several heat cycles, active aging, HIPing and sometimes stress relief. For most applications a compromise of both is desired, which is a strength of 1000 MPa and an elongation of 10 %. However often the material fails at relatively low elongations due to internal defects or low wire quality. It should be noted that the anisotropic microstructure in Ti–6Al–4V AM results in material that is stronger in longitudinal direction (A) and more ductile in vertical direction (B).

1.6 Control of Residual Stress & Distortion in Welding and AM

The development of residual stresses and distortion (RS & D) in AM, as discussed in chapter 1.4, is typically due to constrained thermal shrinkage caused by temperature

mismatch with the cooler substrate (or previous deposit) during the deposition. Per experience, removing (i.e. cutting) the deposit from the substrate breaks the load path between the tensile loaded deposit from the balancing compressive substrate, which can eliminate most of the RS & D. In WAAM the substrate is typically integrated into the final component, which does not allow the removal of the deposit from the substrate [27]. A simple approach to prevent distortion is the symmetrical deposition on both sides of the substrate [32], as it produces balanced stresses, however they are still present and large. To mitigate and control RS & D is widely investigated in the related field of welding. Contemporary approaches to reducing residual stresses in welds have been summarized by Coules [178] and Weman [179] and can be applied to AM as well. The successful control of stresses can be achieved by adequate post-deposition treatment or by the prevention of their development in the first place. Both, prevention and post-processing treatments can be either thermal or mechanical. Prevention of stresses addresses the elimination of the mismatch between the deposit and the substrate. Post-processing involves relaxation by crystallographic plane slipping, either induced thermally by reducing the flow strength or mechanically by straining the material above the flow strength. Both, thermal and mechanical techniques are also used to manipulate the microstructure and mechanical properties, as described in the previous section 1.5. This chapter describes the same techniques and their potential to manipulate the stresses during AM.

1.6.1 Thermal Techniques

1.6.1.1 Stress Relief + Heat Treatment

Thermal stress relief is the post-depositional treatment of the entire component. The flow strength of a material decreases with increasing temperature and internal stresses cannot exceed it. Figure 33 (a) shows the yield strength of Ti–6Al–4V at different temperatures [180]–[182]. While the room temperature strength can reach 1000 MPa, it drops to approximately 400 MPa at 650 °C. Temperatures above 700 °C further decrease the flow strength to nearly zero, which eliminates the residual stress in Ti–6Al–4V FSW [183]. However, these temperatures promote diffusion, α-grain growth and phase transformation into bcc-β, as discussed in chapter 1.2.1 (Figure 9 (b)). From

this stage the cooling rate matters not only for the residual stress formation, but also for the final established microstructure, which is why stress relieving temperatures are not recommended to exceed 700 °C [184], [185].

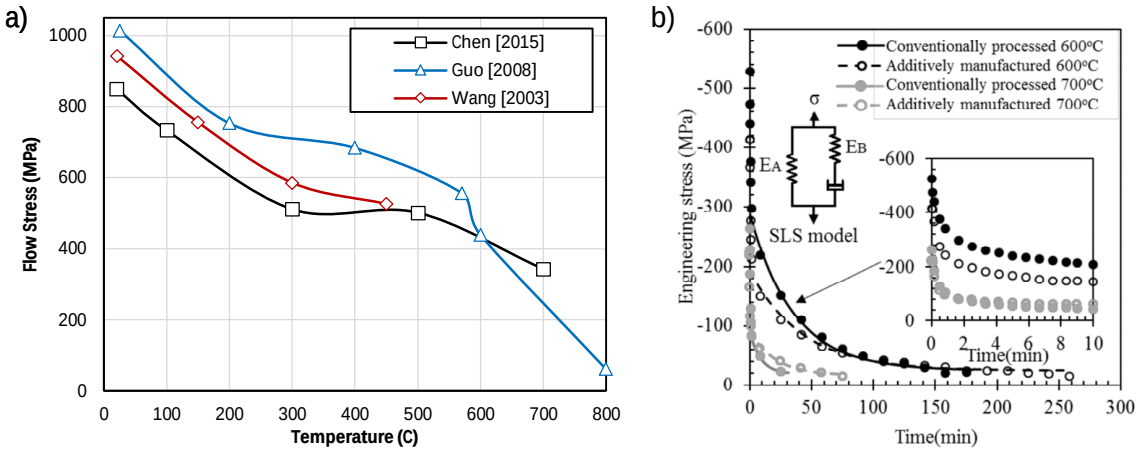

Figure 33: Ti–6Al–4V flow stress: (a) flow stress vs. temperature [180]–[182] and (b) residual stress vs. time during stress relief [185].

To demonstrate the time dependence, Wang et al. [185] stress relieved commercially and additively manufactured (DED) Ti–6Al–4V material and observed the internal stress using in-situ neutron diffraction. Figure 33 (b) shows the residual stress of two stress relieving temperatures within 4.5 h of treatment. The duration at high temperatures allows further stress relaxation by promoted creep [184]. Microstructural heat treatment [79], [131] and HIPing of AM components [99], [100] happen at temperatures between 850 °C and 1100 °C. This exceeds the typical stress relieving temperatures [184] and thereby relaxes the residual stresses automatically. Ti–6Al–4V WAAM does not require heat treatment or HIPing, but only the lower temperature stress relief. However, no publications about stress relieving it are available.

1.6.1.2 Thermal Management

The building strategy [92], active pre-heating [186] and varying the inter-layer dwell time [120], [121] are three AM-process-integrated techniques that reduce the thermal mismatch between deposit and substrate by raising the temperature prior to deposition. A higher substrate temperature can prevent the development of RS & D. Increasing the inter-layer dwell time during the deposition (DED) of Ti–6Al–4V decreases the initial temperature of the previous layer, which finally results in higher residual

stresses and distortion, which is not generally the case for all metals. The material Inconel®625 for example showed the exact opposite effect in the same study [120]. To further increase the initial temperature, the component can be heated actively during the deposition of Ti–6Al–4V (WAAM) to prevent thermal stresses and cracking during the build [186]. This solution however is in conflict with the control of the Ti–6Al–4V microstructure, because the resulting reduction in cooling rates decreases the strength, which was explained in section 1.5.1. An in-situ active cooling system that follows the heat source on the other hand is a different heat management approach to reduce RS & D [187], which reduced the residual stresses in aluminium FSW by more than 50 %..

1.6.2 Mechanical Techniques

According to Mordfin [188] three mechanical stress relieving processes can be distinguished, namely stress relaxation by cold working, vibratory stress relief and relaxation during fatigue, of which the latter will be disregarded in this review. Cold working can be applied locally, for example by rolling or peening, or globally by stretching the entire component. They can be, together with vibratory stress relief, post-deposition or inter-pass treatments. Pre-tensioning techniques are process-integrated techniques that prevent the development of residual stresses.

1.6.2.1 Rolling

Rolling can also be used to mitigate RS & D in WAAM. Applied to steel [111] and Ti–6Al–4V [115] WAAM it was found to be limited, as the plastic deformation occurs mostly in the transverse, rather than the longitudinal direction where the stretch is required to eliminate the residual stresses. Figure 34 shows the longitudinal residual stress changes from the unrolled condition (a), as well as vertical-inter-pass rolled samples Ti–6Al–4V WAAM using (b) 50 kN and (c) 75 kN [115]. The results were measured using the contour method [189]. It can also be seen that inter-pass rolling decreases the layer height and increases the wall width [115]. These results were confirmed using neutron diffraction. A comparison of the longitudinal residual stresses are shown in Figure 35 (a), which shows the large compressive region at the top of the rolled walls, after the last rolling step. Rolling can eliminate residual distortion entirely in butt welds [132]–[136] and stiffened aluminium panels manufactured by FSW [190].

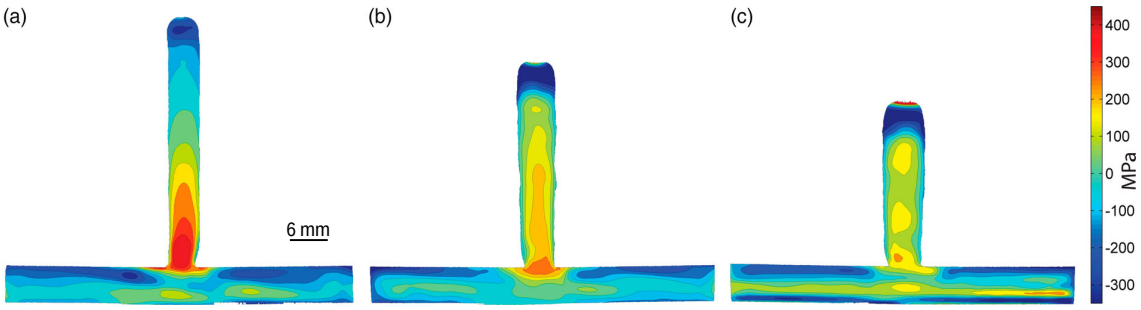

Figure 34: Longitudinal residual stress normal to the cross-section in (a) and unrolled Ti–6Al–4V WAAM wall and wen inter-pass rolling is applied using (b) 50 kN and (c) 75 kN [115].

Figure 35 (b) shows the limited effect of vertical inter-pass rolling on the distortion Ti–6Al–4V WAAM, where it was reduced, but not eliminated. Further increasing the rolling load caused in the failure of the deposit [115]. Constraining the lateral deformation during vertical rolling with the use of a slotted roller eliminated distortion [111]. Xie et al. [191] investigated the effect of a trailing pinch-rolling mechanism behind the torch to control the geometry of a WAAM steel deposit.

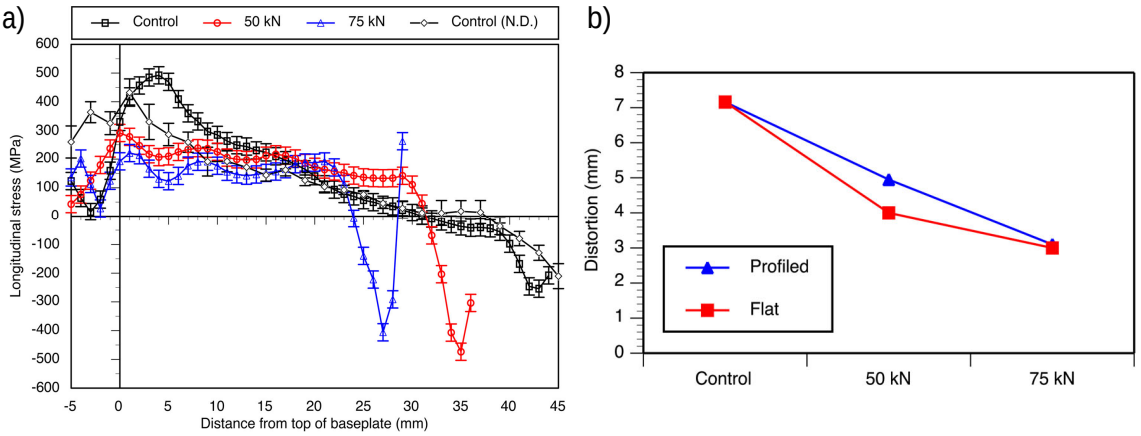

Figure 35: (a) Neutron diffraction stress measurement of longitudinal stresses after inter-pass rolling and (b) the resulting out-of-plane distortion [115].

They also observed microstructural modification, similar to those in vertical rolling [111]. In WAAM however this will significantly constrain the design freedom, because it is difficult to apply to small deposits, wide deposits, deposits with changing wall width, curvature or intersections. Burnishing uses a small roller ball with a high hydrostatic pressure of up to 400 bar on a surface. It is used to smooth a surface or to induce compressive stress [192], [193]. However the penetration is less deep than the previously mentioned MHP devices [164].

1.6.2.2 Peening

Different peening techniques were introduced in section 1.5.2.2, with most emphasis on machine hammer peening (MHP). Initially the tools that were developed had low energy and were used for improving surface roughness. More recently these tools became heavier and can now induce compressive stresses up to a few mm [194], which can cause an out-of-plane distortion in sheets [162]. Low-frequency hand-held tools, like the rivet hammer RRH06P can be used on-site to eliminate residual stresses in bead-on-plate repairs [194], butt welds [195] and multi-pass welds [196]. MHP is also used to induce compressive stress at the weld toe to prevent crack initiation [197]. These tools can be mounted on CNC machines and therefore be integrated in WAAM (Figure 36 (a))

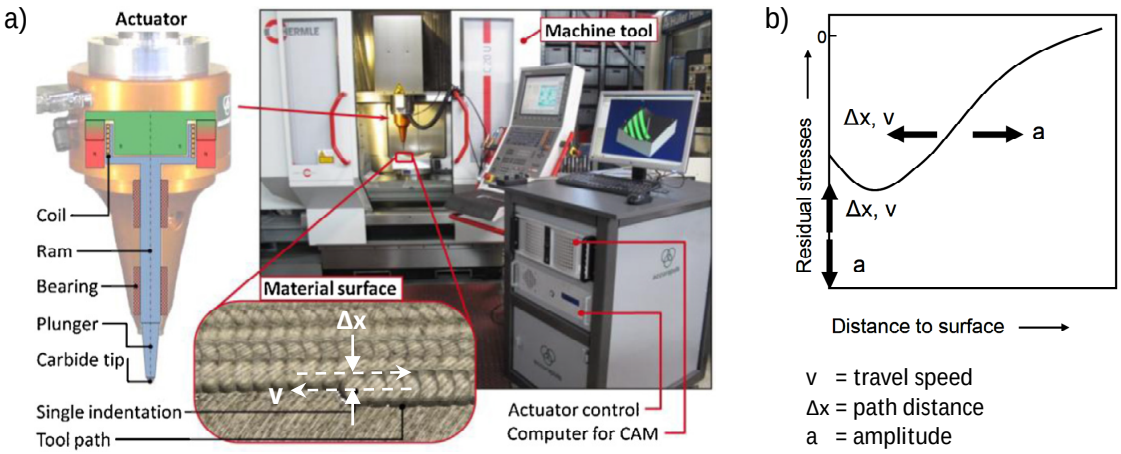

Figure 36: (a) Accurapuls system mounted to a CNC machine [159] and (b) how peening parameters influence a stress profile [152].

A typical compressive peening profile is shown in Figure 36 (b), which is a result of a mixed behaviour of plastic stretch, static Hertz' pressure [198] and Johnsons' dynamic contact [199]: The resulting residual stress, which increases with the distance from the surface is compressive and it decreases with greater distance from the surface and is zero or slightly tensile in the far field [162]. Lienert et al. [152] investigated how the peening parameters influence the stress profile using an in-house built piezo peening tool. Decreasing the travel speed *v* (at a given frequency) and the path distance both increase the density of single impacts per unit area. Increasing the impact density can increase the peak compressive stress and the penetration depth, as shown in shown in Figure 36 (b). However saturation behaviour can be observed for both. It should also be noted that the residual stress maximum in the direction transverse to the tool travel

direction is usually larger than in the parallel direction, while the penetration depth is identical for both. The piezo amplitude *a* also increases the maximum compressive stress and penetration depth, but this is a unit unique for piezo peening. For the tool characterisation the energy threshold recently established, which is the sum of the required elastic and plastic energy and to produce one indent [199]. The energy threshold replaced the impact force [158] as a comparative value between MHP tools, as tools with similar impact forces can produce different stress profiles and indent diameters [164].

1.6.2.3 Vibratory Stress Relief

Vibratory stress relief (VSR) is typically used in welding and casting. The development of portable VSR systems happened from the 60's to the 80's, started with DC systems, but AC systems were developed due to their more robust nature [200]. Figure 37 (a) shows the AC VSR system "VCM90" (£10,000 in 1991), which supplies up to 220 Hz and 25 *g*-force at 25 A (240 V; 6 kW) electrical consumption.

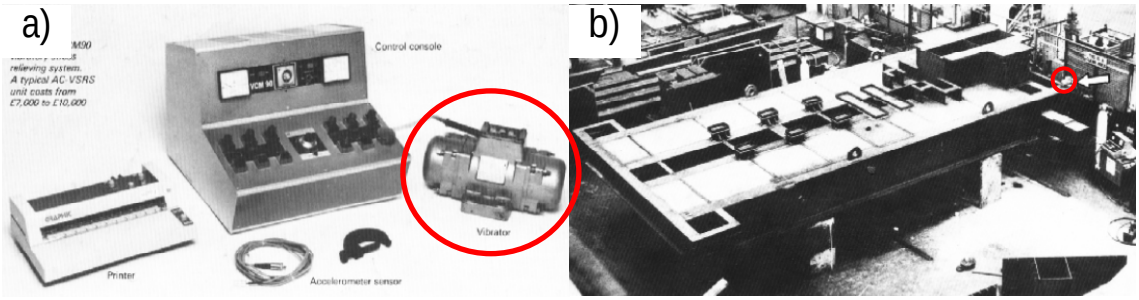

Figure 37: (a) The VSR system "VCM90" and (b) its' application on a 18 t bed plate [200].

The vibrator of the unit weights 50 kg and is mounted on the workpiece, which can be an 18 t bed plate, as shown in Figure 37 (b). Jurcius et al. [201] used a 350 kg force inducer with 35 % eccentricity at 86 Hz to stress relieve a 140 mm long butt weld of 30 mm thick steel sheets, as shown in Figure 38 (a). They showed that VSR can be applied on steel welds in-situ or after welding, where the first can relieve the stresses to same degrees as PWHT (Figure 38 (b)), without softening the welded material. There was no literature available that reported the application to WAAM or a different AM process. Post-processing is probably more suitable in this case, as in-situ vibrations would influence the sensitive weld pool. It was finally not chosen for this research either, but it is worth being considered in the future.

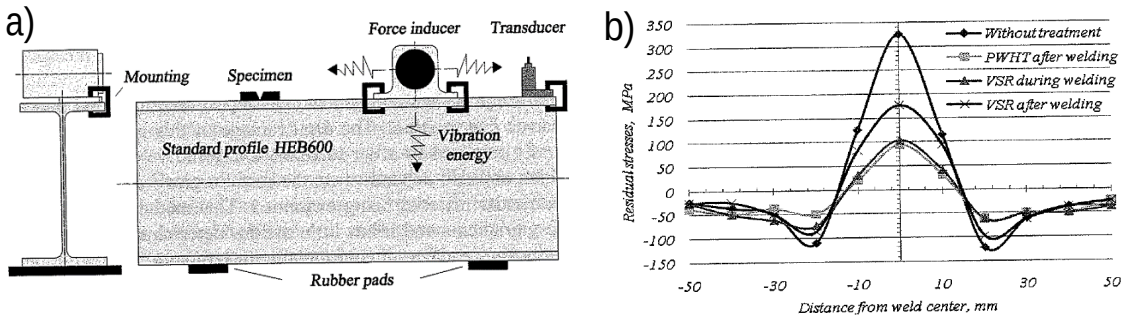

Figure 38: (a) Work desk for VSR treatment and (b) longitudinal residual stresses after VSR treatment [201].

1.6.2.4 Acoustic Softening

Prieb [202] proposed ultrasonic treatment in 2001, which may be used to reduce residual stresses in metallic workpieces. Relaxation occurs if the internal stresses plus the ultrasonically induced shear stresses τ_{US} exceed the temperature dependent flow stress. This decrease in effective flow strength is called acoustic softening [203]. The ultrasonic excitation operates around 20 kHz and also causes rapid local temperature increase, which decreases the flow strength locally and further improves the effect of this technique [202]. Commercially available systems have around 3 kW electrical power. Krajewski et al. [204] used ultrasonic vibration (2.5 kW) during aluminium (AA2017 and AA5056) welding by exciting the plates, which had a significant impact on the weld-pool behaviour and resulting shape and microstructure. It also eliminated pores. Zhou et al. [205] and He et al. [206] reduced the residual stresses in aluminium butt welding by in-situ ultrasonic treatment using a trailing ultrasonic tool behind the welding torch, as shown in Figure 39.

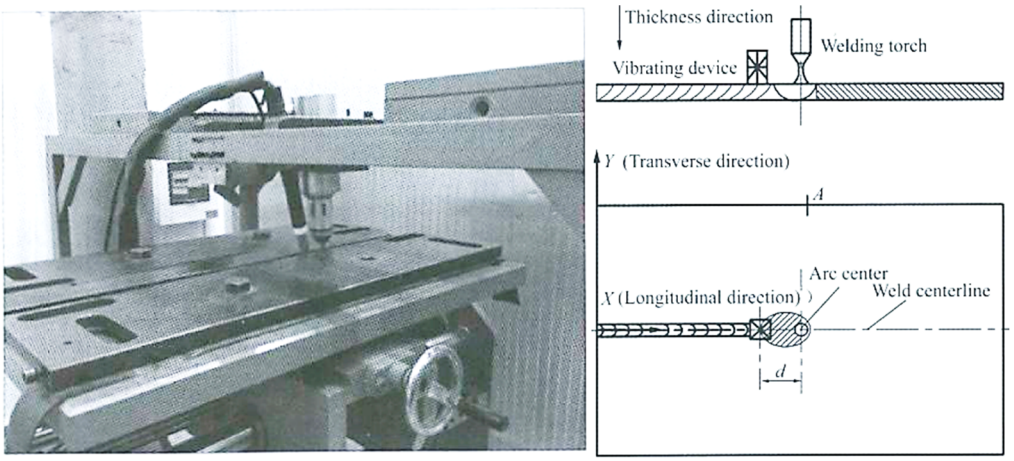

Figure 39: Setup of the welding with in-situ ultrasonic vibration method [205].

They found that an ideal distance of the tool near the torch is required for a successful application. Fartashvand et al. [207] recently investigated the acoustic softening behaviour in Ti–6Al–4V alloy. Only 0.34 kW ultrasonic longitudinal excitation (25 kHz) decreased the flow strength from 890 MPa to 800 MPa during tensile testing without an increase in temperature and without observing acoustic hardening. To achieve this it was necessary to locate the transmitters in a fashion that the nodes of vibrational waves are located in the centre of the specimen, where plastic flow is anticipated. Acoustic softening was not reported to be combined with WAAM or any other AM technique either, but like vibratory stress relief, it represents a promising candidate.

1.6.2.5 Pre-Tensioning

Global mechanical Tensioning (GMT) is a pre-tensioning technique that attempts to pre-load the substrate to a stress level that is expected to develop during welding. Figure 40 shows the experimental setup used by Altenkirch et al. [208], who investigated the effect of the pre-load (in % of YD) on RS & D in aluminium FSW (AA7449).

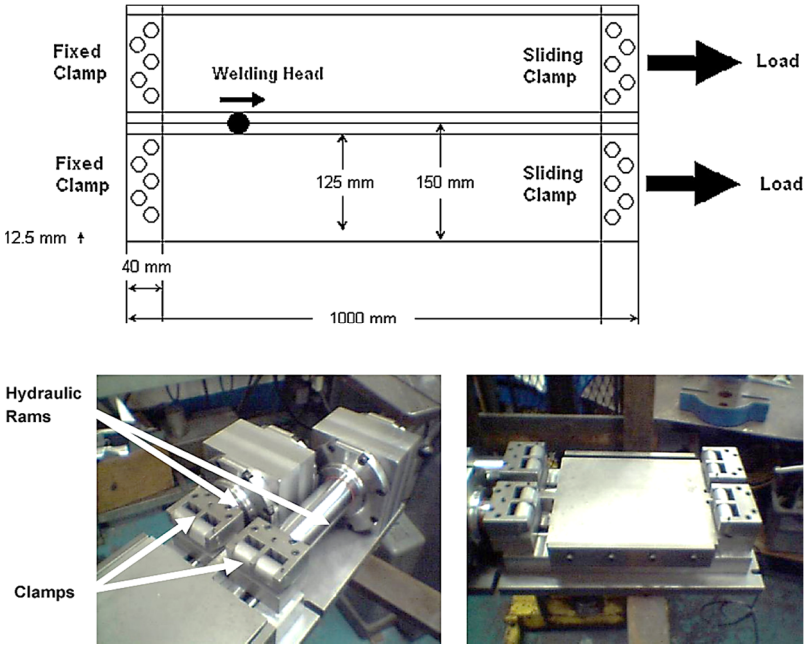

Figure 40: Mechanical Tensioning Method and Equipment [208]

Both joining components are clamped on one side, while hydraulic rams apply a tensile force on the other side. FSW is then conducted while the two sheets are under tension. The residual stress in the joined region that develops due to the FSW process is equivalent to conventional FSW. However, the use of GMT also maintains tensile stress

in the parent material, which ultimately eliminates the mismatch in stress between bead and sheet. Unloading the pre-tension allows a homogeneous contraction of both and prevents the development of tensile stresses. Staron et al. [209] reported that aluminium (AA2024) plates that are tensioned to 70 % of their yield strength during FSW produced compressive stress in longitudinal direction in the weld zone, rather than tensile stresses. A variety of 2xxx and 7xxx series alloys were investigated and needed to be loaded to 30-35 % of initial yield stress, which is approximately 115 MPa or 175 MPa for the respective series [208]–[210]. This is equivalent to the untreated yield strength after welding. Other preventive techniques are pre-setting [179] or pre-bending [211].

1.7 Pertinent Residual Stress Measurement Techniques

The measurement of residual stresses are usually not trivial. They can be time consuming, expensive, destructive and inaccurate with low penetration and resolution. Withers et al. [212] in 2008 and Rossini et al. [104] in 2012 published review papers and Proulx [213] a book in 2001 about concurrent and recent advances in residual stress measurement. Figure 41 classifies the different techniques regarding their penetration and spatial resolution [212].

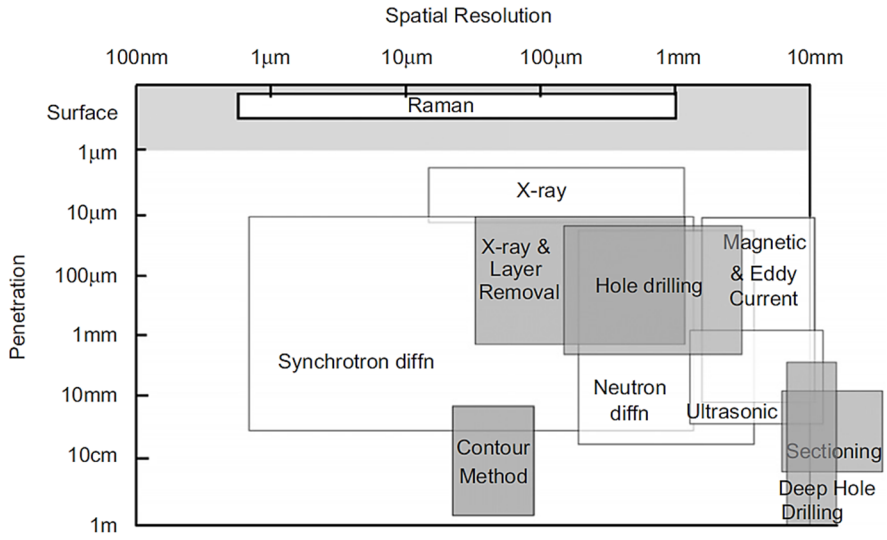

Figure 41: Working Envelope of some Stress Measurement Techniques after regarding Penetration Depth and Spatial Resolution. The Target Envelop and Strain Gauges have been added manually [212].

These techniques can be either non-destructive, semi-destructive or destructive. Fast, easy and low cost non-destructive techniques are the Ultrasonic Method and the magnetic Barckhausen Noise Method. However both have a poor spatial resolution and the latter only works on ferromagnetic materials [104]. X-ray diffraction (XRD) and the $\sin^2\psi$ method only penetrates the material a few µm [214]. Layer removal by electro-discharge machining (EDM) can be used to increase the measurement depth of XRD. Easy and low cost hole-drilling methods (HD) are considered semi-destructive. Both, XRD and HDM are the most commonly used RS measurement techniques, but they can only measure in-plane stresses along a profile perpendicular to an accessible surface. Facing the feature dimensions and geometries typical for WAAM, the requirement for RS measurement techniques is a penetration between 1 mm and 1000 mm with a spatial resolution of ideally less than 1 mm (compare Figure 41). This excludes most techniques and limits the options to the non-destructive neutron diffraction (ND) and synchrotron strain scanner, of which the latter is basically high energy XRD. A destructive candidate is the relatively young and contour method.

1.7.1 Non-destructive Diffraction Techniques

Detailed information about diffraction techniques for stress measurement can be found in several books [215]–[217] on which the content of this section is based on. ND and XRD are based on measuring inter-planar spacing *d* within the crystallographic lattice, while the lattice is aligned normal to the measuring direction. The comparison of the lattice spacing with a stress-free reference lattice represents the strain, which yields the engineering stress according to Hooke's law using the Young's modulus *E* and Poisson ratio ν. The crystallographic lattice spacing *d* is determined by the help of Bragg's law in eq. (2), which is visualised in Figure 42, where θ is the angle of the incident beam and reflected beam with the plane and λ is the wavelength of the incoming neutron or electron beam, which is the magnitude of atomic distances.

$$2d * \sin\theta = n\lambda \tag{2}$$

Depending on the diffraction angle, the diffracted parallel beams can have either a destructive or constructive interference (Figure 42 (a) or (b)). The lattice spacing *d* can

now be determined by measuring the diffracted angle that yields interference, if the wavelength of the incoming beam is fixed and known (monochromatic). A second way of measuring lattice spacing *d* is the use of a polychromatic "white" beam with a range of wavelengths and a fixed scattering angle θ.

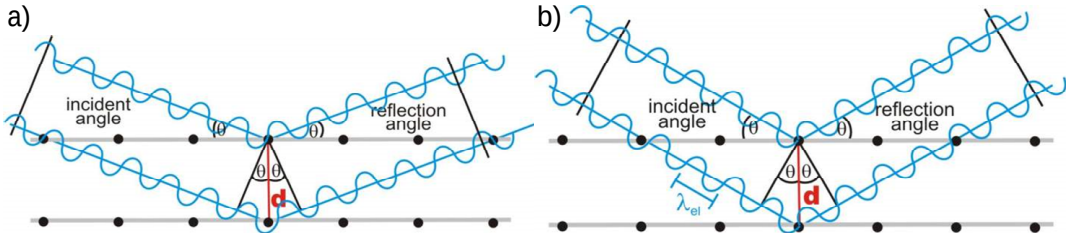

Figure 42: (a) destructive and (b) constructive interference at different diffraction angles at a wavelength λ.

The detector can measure several diffraction peaks at a fixed diffraction angle. In pulsed neutron sources, the wavelength of the beam that diffracted successfully can now be determined by the time-of-flight condition in eq. (3), where *h* is the Planck constant, m_n the mass of a neutron and *v* their velocity. The plane spacing can be determined using eq. (2) and (3) together, which yields eq. (4).

$$\lambda = \frac{h}{m_n v} = \frac{h}{m_n} * \left(\frac{t}{L_1 + L_2}\right) \tag{3}$$

$$d_{hkl} = \frac{h}{2 \sin\theta \, m_n (L_1 + L_2)} t_{hkl} \tag{4}$$

L_1 and L_2 are the distances from the source to the sample and from the sample to the detector respectively. Now the time-of-flight (TOF) t_{hkl}, which is around 13 µs, can be measured easily. However, Neutron and synchrotron radiation facilities are rare. The following selection of European instruments was eligible for such measurements:

- "ENGIN-X" at the ISIS Facility near Oxford [218] (polychromatic neutron beam)
- "STRESS-SPEC" at FRM II in Munich [219] (monochromatic neutron beam)
- "SALSA" at the ILL in Grenoble [220] (monochromatic neutron beam)
- "HEMS" beamline on PETRA III at the DESY in Hamburg [221] (X-Ray Synchrotron)

In order to conduct an experiment, an application for “beam time” is required, in which a scientific and industrial benefit of the proposed experiment needs to be stated. A proposal must be submitted 6 month prior to the experiment and beam time of 2-3 days may be granted on average and the proposals can also be rejected (which happened to half of the proposed experiments during this research). Unfortunately, these are the only non-destructive stress measurement techniques suitable for this research.

1.7.2 Contour Method

The contour method is a relatively new residual stress measurement technique, invented by Mike Prime [189] that involves carefully cutting the specimen using wire EDM (electro-discharge machining), measuring the surface profile of the newly created cut faces, filtering out experimental noise and averaging the profiles from the two cut parts [222], and finally applying the reverse of the averaged profile as nodal displacement boundary conditions in an FE (finite element) model of the cut part [223]. The stress calculated at the simulated cut surface is a true representation of the residual stress in the component acting normal to the cut plane, which was present in the sample before the cut was conducted. Performing the EDM cut can be a source of error, as wire entry and exit can create artefacts, which can be controlled by the use of sacrificial material [224] or other correction procedures [225]. Plasticity while the EDM wire is removing material that contains stresses close to the yield strength is another issue that needs to be prevented [226]. In Europe, only three institutes perform the contour method, which are all located in the UK. These are the University of Manchester, Coventry University and the Open University in Milton Keynes, of which only the latter performes the method commercially with a spin-off company.

Due to the high resolution and penetration depth, the contour method is probably the most suitable to investigate longitudinal residual stresses in Ti–6Al–4V WAAM components (as in Figure 34). However, it is a relatively young and not well established technique. The community is also debating about errors caused by the EDM cut, and plasticity effects, which is why results obtained by this techniques are usually compared against another independent technique. When comparing stresses on the same

specimen, the comparative stress measurement needs to be non-destructive (chapter 1.7.1) and performed prior the contour method.

1.8 Conclusion

1.8.1 Summary of microstructure and residual stress development in WAAM

Both the residual stresses and the microstructure, as well as the consequent mechanical properties depend mostly on the thermal history of the entire component. Key aspect for the thermal history are the deposition parameters and the near-net shape geometry. A "cooler" process results in higher cooling rates and improves the mechanical properties, but also increase residual stresses. A pre-heated substrate mitigates residual stresses, but also results in weak mechanical properties, as the low consequent cooling rate produces large grains. Controlling the thermal history not only proves to be difficult, as the deposition parameters are pre-determined to produce a certain near-net shape geometry, but controlling one issue (residual stress or microstructure) typically worsens the other. It is therefore required to investigate mitigation techniques to address each individual issue.

1.8.2 Summary of mitigation techniques

Table 2 summarises the thermal and mechanical techniques that can control microstructure, mechanical properties and residual stresses in Ti–6Al–4V WAAM. Chapter 1.5 and 1.6 focus on the technical efficacy of the individual techniques. This chapter critically assesses their ability to fit into a WAAM manufacturing chain in terms of side effects, number of additional process steps, time and effort, applicability on typical WAAM components and other constraints. All techniques are not simple and come with technical limitations and challenges for process-integration, which makes it difficult to determine an ideal candidate.

Table 2: Effect of mitigation techniques on microstructure and residual stress in Ti–6Al–4V WAAM.

Effect of Process	Effect on Ti–6Al–4V WAAM microstructure		Effect on residual stress in Ti–6Al–4V WAAM		Assessment of process side effects and integration			
		Chapter		Chapter	possible negative effect	in-situ	post-proc	Ease of integration
Build strategy	Influences cooling rate	1.5.1.1	Influences temp. gradient	1.6.1.2	Changes bead shape	✓	✗	Easy
Active Cooling	Influences cooling rate	1.5.1.1	Influences temp. gradient	1.6.1.2	Can disturb deposition	✓	✗	Moderate
Stress Relief	Ideally none	-	Reduces stress significantly	1.6.1.1	Unexpected distortion during relief	✗	✓	Time consuming
Heat Treatment	New microstructure	1.5.1.2	Can eliminate stress	1.6.1.1	Inhomogeneous microstructure	✗	✓	Time consuming
HIP-ing	New microstructure	1.5.1.3	Can eliminate stress	1.6.1.1	Part shrinkage and inhomog. microstructure	✗	✓	Time consuming and difficult for large parts
Pre-Heating	Influences cooling rate	-	Reduces stress	1.6.1.2	Decreases strength	✓	✗	Moderate
Rolling	Twinning and Refinement	1.5.2.1	Can reduce significantly	1.6.2.1	Changes part geometry	✓	✓	Moderate
MHP	Twinning and Refinement	1.5.2.2	Can reduce	1.6.2.2	Changes geometry	✓	✓	Relatively Easy
Vibratory Relief	Unknown	-	Can reduce significantly	1.6.2.3	Can disturb the molten pool	✓	✓	Moderate
Acoustic Softening	Unknown, probably none	-	Can reduce	1.6.2.4	Unknown	✓	✓	Unknown
GMT	None	-	Can reduce significantly	1.6.2.5	Probably none	✓	✓	Extensive
Alloying	Endless options	1.5.3	Probably very little	-	Endless options	✓		Costly and time consuming

1.8.2.1 Thermal techniques

Thermal techniques are either post-processing or in-situ, but usually not both. Post-deposition heat treatment for microstructural or stress relieving purposes would require furnaces that can treat the large meter-scale components produced with WAAM, while they remain clamped to a backing bar that prevents distortion during treatment. Quenching of large sections results in inhomogeneous cooling rates during air or water cooling. In addition an inert atmosphere needs to be considered to prevent the alloy from reacting with atmospheric oxygen. Thermal post-processing is time consuming, difficult and constitutes an additional process step. In-situ techniques can be process integrated and therefore applied during deposition. Optimised deposition parameters and build strategy to control the cooling rate can be integrated without any additional tooling. The amount of improvement with these methods is limited. However, modifying them can change the sensitive molten pool and subsequently the final geometry, which has a highest priority. Active cooling to room temperature (and not in-situ cooling during the β-α transformation) can increase the productivity at the best. Pre-heating to control the residual stresses is possible, but it requires a stiff and thermal insulating clamping system. Otherwise the clamping could be distorted by the part. Negative side effects are very slow cooling rates that result in poor strength.

1.8.2.2 Mechanical techniques

All mechanical techniques can be applied in-situ, inter-pass or post-processing. In-situ or inter-pass can be applied on-line during the manufacture of the component. With the use of an individual manipulator for the cold work process, the loss of productivity can be reduced to a tolerable extent. Extensive research on on-line rolling is ongoing at Cranfield University with a variety of project partners. Inter-pass rolling constrains the building envelope and the design freedom of the otherwise open process. Nevertheless, the effort is worth the achievement of improved and isotropic mechanical properties and the incidental reduction of residual stress. It can furthermore be applied on-line and does not require additional post-processing. To overcome the constraints and the design limitations, machine hammer peening can be complementary or replace rolling as on-line cold work method. Commercially available MHP tools are not powerful enough to achieve the required penetration depth regarding plastic deformation, but recently developed prototypes appear promising. The special advantage of MHP tools is that they are compatible with CNC machine tools and industrial robots. Their application can easily be added to the manufacturing chain and the machine operator does not require extensive training, as it is simply an additional item in the tool changer. New generations of MHP tools that deliver sufficient impact energy to be competitive to rolling will be accompanied by a significant noise problem.

Vibratory stress relief works well for welding, as post-processing technique or in-situ, of which the latter is more effective. The sensitive molten pool in WAAM however might be influenced or could even collapse due to the vibrations, which impedes the process control for deposition. Nevertheless, it does not require additional manipulation of tooling and does not affect the productivity, as it can be implemented in-situ. Microstructural changes and elimination of pores were reported for other metals, which could also occur with Ti–6Al–4V. Similar things can be concluded for the less violent acoustic softening, which is more complicated to apply and requires scientific knowledge that doesn't seem to be available yet in the literature. Both, vibratory stress relief and acoustic softening can have a positive effect on mechanical properties and residual stress.

The most effective and theoretically easiest technique is GMT. The process integration would be independent from the deposition on the mechanically stretched substrate. In theory the substrate must be loaded close to yield value or to the value of the otherwise expected residual stresses, which is feasible for thin sheets. The high strength of Ti–6Al–4V and the typical dimensions of WAAM substrates complicate application of the technique. For example, the substrate of the Bombardier landing gear rib demonstrator (Figure 4) requires an estimated tensile pre-loaded of 8,500 kN in both directions of the substrate. Even though this would entirely eliminate residual stresses, the equipment required to produce this load would be substantial. Ultimately GMT would not improve the microstructure, which was one of the objectives of this research programme.

1.8.3 Gaps in Literature

Based on this literature review and the summary in Table 2, some gaps were identified in respect to control RS & D and microstructure in combination with Ti–6Al–4V WAAM, of which the following were pursued in this thesis:

The residual stresses during the deposition have only been simulated so far, but were never confirmed using stress measurements. These residual stresses were furthermore only investigated for straight single pass walls and not for more complex features, such as intersections for example. It was neither demonstrated that thermal stress relief is actually capable of eliminating the potentially complex multiaxial residual stresses in AM. Restraining the lateral deformation during rolling to improve the effectiveness of reducing residual stresses was still a hypothesis, but wasn't quantified or described in great detail yet.

A quantitative investigation to identify the influence of practical rolling parameters for microstructural control was not available and especially not for more realistic feature dimensions. It was simply assumed that larger loads yield larger strain and ultimately larger grain refinement. The required temperature history for a certain amount of plastic deformation to yield a desired degree of grain refinement was not quantified either, of which the precise thermal history in the relevant area – the HAZ – was completely speculative in WAAM.

Even though literature shows that MHP could potentially be used for microstructural control, similar to rolling, both techniques were not compared directly to assess the performance of the alternative cold working technique MHP.

Further gaps in the literature were identified, but exceeded the scope of this research and were hence not pursued. Based on those and on the new findings made during this research, section 8.4 suggests potential future research.

1.8.4 Aims, Objectives and Thesis outline

The aims of this thesis were addressed by the following objectives, summarised in this thesis outline:

1. Developing an analytical model to predict RS & D

Knowledge taken from previous experiments and numerical simulations will be used in chapter 2 to develop an analytical model, based on cantilever bending beam theory, to predict RS & D in WAAM. The model can consequently be used to evaluate the measurements performed in the following chapters.

2. Understanding the fundamental development of RS & D during WAAM

Residual stresses will be measured in straight WAAM walls before and after unclamping to validate what has only been simulated before. These measurements can be used to compare against the analytical model in chapter 2 using measurements in Ti–6Al–4V walls (chapter 4).

3. Understanding the development of RS in WAAM intersections

Joints and intersections are critical features. The measurement of residual stress development in intersections in chapter 3 will assess the criticality. It will also be identified if or to what extent thermal stress relieving and rolling is effective to control stresses in WAAM intersections.

4. Proving that lateral restraint improves the residual stress control

The effectiveness of side rolling will be investigated in chapter 4 on straight Ti–6Al–4V WAAM walls, which reveals how effective it is to prevent lateral expansion.

5. Evaluating the potential of machine hammer peening as alternative to rolling.

The proof of concept of MHP as alternative cold working technique will be conducted in Chapter 5, which shows the general application of MHP, as well as the potential for stress and microstructural control.

6. Understanding the relevant contact mechanics of Rolling and MHP.

Contact mechanisms and the influence of cold working parameters will be assessed using different elastic and plastic strain measurement techniques in chapter 6.

7. Understanding the thermal history within the HAZ during the Ti–6Al–4V WAAM deposition

The last chapter 7 will report the measured thermal history during the WAAM deposition, as well as the microstructural response to the heat cycle.

Chapter 2 Bending Beam Theory – Residual Stress & Distortion

Residual stresses are a one of the biggest challenges in additive Manufacturing. Their control requires the knowledge of their development during and after the deposition. Stress measurements are often difficult, expensive and time consuming, as explained in section 1.7. It is therefore common practise to blindly predict RS & D in WAAM with FE simulations, often without experimental validation. These transient simulations are also laborious and time-consuming to calculate the thermal history during deposition. In a second load step, the thermal history is used in a thermo-mechanical prediction of the internal residual stresses. The third load step involves removing the boundary conditions of the substrate, which simulates unclamping of the component that results in distortion and redistribution of the stress field. Ding et al. [118] proposed a numerical simulation procedure to reduce calculation time compared to full transient models [119]. However, even the reduced time is considerable [227] and requires detailed process information, such as heat input and material property data over the temperature. Therefore parametric studies to investigate the influence of various materials, substrate and wall geometries are often infeasible.

Before investigating the development of RS & D, as well as way to control them, the present chapter proposes an analytical model, which allows simple and fast predictions. This approach takes the investigation of Colegrove et al. [111], who have used standard bending beam equations, a step further by applying curvature, addressing the Timoshenko beam theory and analysing the effect for a range of parameters, rather than confirming only one condition. The model was validated against various measurements and simulations in literature, as well as the residual stress measurements performed in this thesis.

2.1 Calculations

Figure 43 (a) shows the parameterised problem of a distorted WAAM wall, presented with the annotation of an Euler-Bernoulli cantilever beam with the length L_0, where the tensile residual stresses in the deposit (red) represent internal forces that result in the

out-of-plane distortion *w(x)* of the substrate and the curvature radius *ρ*. The Cartesian coordinate system is aligned with its x-axis along the length of the deposit, while the y and z-direction represent the transverse and the build direction. The location z = 0 of the coordinate system is for the calculation not at the interface as usually [115], but at the neutral axis of the T-profile. The T-profile consists of the substrate (thickness *t*; width *s)* and the deposit (wall width *v*; wall height *h*), as shown in Figure 43 (b).

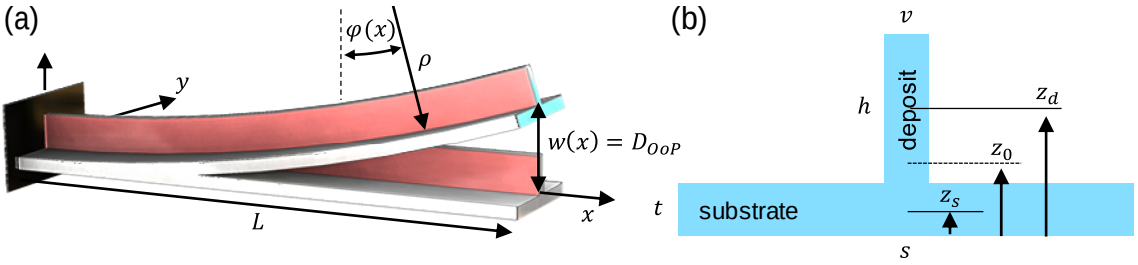

Figure 43: Out-of-plane distortion w(x) of substrate according to the Euler-Bernoulli beam with a T-cross section (in-plane distortion of the deposit)

The location of the neutral axis z_0 in the geometrical centre of the area can be calculated using eq. (1), where z_s and z_d are the individual geometrical centres of both areas with respect to the bottom of the substrate.

$$z_0 = \frac{\sum z_{s,i} A_i}{\sum A_i} = \frac{z_d A_d + z_s A_s}{A_d + A_s} \tag{5}$$

The cross section of the substrate is assumed to be constant along the length *L* and during the deposition of the wall, and so are the wall width *v* and height *h*. The height *h* increases with each layer, while the wall width *v* does not vary. The stiffness of the cross-section against any bending moment around the y-axis is E^*I_{yy}, where *E* is the Young's modulus of the material and I_{yy} the second moment of inertia, which is calculated with eq. (2) and more specifically with eq. (7) for rectangles, with Δz being the distance from the geometrical centre of the area to the neutral axis, referred to as Steiner's contribution. If a cross section consists of two different rectangles, the total second moment of inertia is the sum of both. The second moment of inertia of the present T-section is therefore eq. (8), where the total height *h* of course changes with number of deposits *n*, as well as the distances of the areas to the neutral axis z_0. The stiffness of the wall increases by the power of 3 with the height of the wall.

$$I_{yy} = \iint z^2 \, dy \, dz \; [m^4] \tag{6}$$

$$I_{yy} = \frac{1}{12} ab^3 + ab * \Delta z^2 \tag{7}$$

$$I_{yy}(n) = \frac{1}{12}(st^3 + vh(n)^3) + st\Delta z_s(n)^2 + vh(n)\Delta z_d(n)^2 \tag{8}$$

2.1.1 Residual Stress

With the addition of each layer, more material is added that contains tensile stresses in the longitudinal direction, while the substrate remains clamped. Additional tensile cross-sectional area increases the force and potential bending moment to some extent. Figure 44 shows the cross-sectional view of the internal stress assumption according to Colegrove at al. [111] and the consequent internal loads.

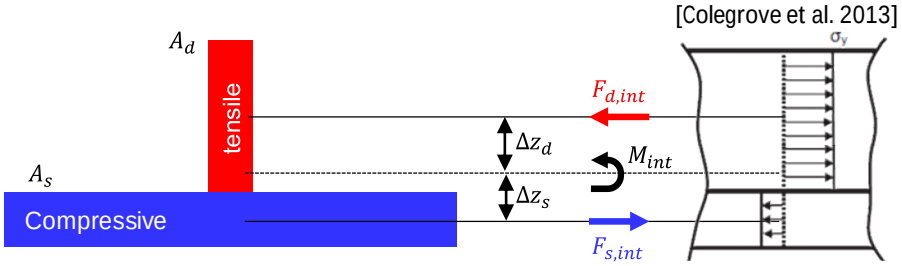

Figure 44: Internal residual stresses and resulting bending moment according to Colegrove et al. [111]

Before unclamping, it is assumed that the wall contains large tensile and constant residual stresses along the height and width. For simplification, boundary effects on the interface are neglected. The substrate contains the balancing compressive residual stresses. The total force on a cross section is a result of the internal stresses and can be calculated with eq. (9), acting in the centre of gravity of the integrated volume. With the stress being constant along height, width and length, the equation simplifies to eq. (10) that acts in the geometrical centre of the integrated volume. The change of sign is due to internal forces acting, rather than external ones. The compressive stress in the substrate must bring the longitudinal forces to equilibrium (eq. (11)), so they can be estimated with eq. (12). The stress in the substrate is limited to the material's yield value. Both internal forces act in the centre of their area (Figure 44), which is not aligned

to the neutral axis z_0, thus creating a bending moment $M_{int}\ (n)$ (eq. (13)), which is a function of wall the wall height only.

$$F_{d,int}(x,n) = -\iint \sigma_{xx,d}(x,y,z) * dA(n) \tag{9}$$

$$F_{d,int}(n) = -\sigma_{xx,d} * w * h(n) \tag{10}$$

$$F_{d,int}(n) = -F_{s,int}(n) \tag{11}$$

$$\sigma_{xx,d} = -\sigma_{xx,s} * \frac{vh}{ts} \tag{12}$$

$$M_{int}(n) = F_{d,int}(n)\Delta z_d(n) + F_{s,int}(n)\Delta z_s(n) = 2F_{d,int}(n)[\Delta z_d + \Delta z_s](n) \tag{13}$$

2.1.2 Euler-Bernoulli Beam Theory

The deflection w(x) in Figure 43 (a) must satisfy eq. (14), which is the standard Euler-Bernoulli beam differential equation, where q(x) would be a vertical load in z-direction, distributed along x. The present problem does neither have this distributed load (gravity is negligible), nor any other externally acting forces or moments. The double integration of eq. (14) yields eq. (15) without any constants due to boundary conditions.

$$q(x) = \frac{d^2}{dx^2}\left(EI_{yy} * \frac{d^2w}{dx^2}\right) = EI_{yy} * w''''(x) \tag{14}$$

$$M(x) = -EI_{yy} * w''(x) \tag{15}$$

In the present case, M is not a function of the length and therefore neither is $w''(x)$, so eq. (15) can also be solved to calculate the curvature χ and the reciprocal curvature radius ρ (eq. (16)). Rotations of the cross-section $\varphi(x)$ can now easily be calculated by further integrating eq. (15) to eq. (17), which doesn't have constants either (boundary condition $\varphi(x = 0) = 0$), but it is only valid for small rotations $\varphi(x)$, as translation $u(x)$ and shortening of the beam is not considered here. A final integration with the boundary condition $w(x = 0) = 0$ finally yields the eq. (18) to calculate the out-of-plane distortion $w(x)$. A parametric study is now possible with M and I_{yy} as a function of the number of layers n deposited. However, the constant curvature χ and radius ρ along the

length of the beam cannot perfectly be described for large deflections or beams with this quadratic equation that does not consider *u(x)*.

$$w'' = \frac{M_{int}}{EI_{yy}} = \chi = \frac{1}{\rho} \tag{16}$$

$$w'(x) = \frac{M_{int}}{EI_{yy}} x = \varphi(x) \tag{17}$$

$$w(x = L) = \frac{M_{int}(n)}{2EI_{yy}(n)} L^2 \tag{18}$$

2.1.3 Timoshenko Beam Theory

The Euler-Bernoulli beam theory is only valid for small deflections. For large deflections the Timoshenko beam theory also considers rotations *Θ(x)* of the cross-section against the neutral axis, as shown in Figure 45, as well as longitudinal translation *u(x)* (eq. (19)). In FEM Timoshenko beam elements are used when large deflections are expected, but they require more computational time.

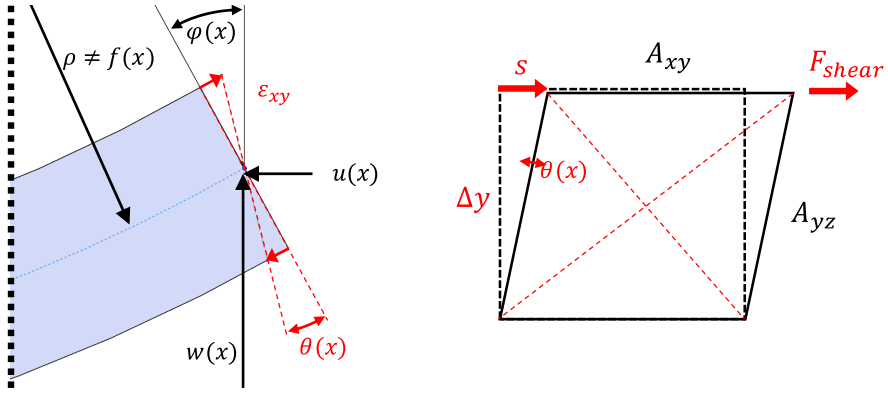

Figure 45: Out-of-plane distortion w(x) of a Euler-Bernoulli beam with a T-cross section.

Under these condition, eq. (17) is no longer valid. The deviation *Θ(x)* must satisfy the new differential eq. (20), where *A* is the shear area and *G* the shear modulus of the material. The Timoshenko shear coefficient *κ* depends on the cross section [228] and has always a value below 1. In general Timoshenko's differential equation must be used if eq. (21) applies. For values close to 1, the difference between Timoshenko and Bernoulli disappears. For extreme case, if the Timoshenko coefficient becomes 0, then the cross-section would not rotate at all during distortion. In WAAM values much smaller

than 1 can easily be reached, making Timoshenko a requirement. For solving eq. (20) the function $\varphi(x)$ must be known.

$$u(x) = -z * \varphi \tag{19}$$

$$\theta_{xy}(x) = w'(x) = \varphi(x) - \overbrace{\frac{EI_{yy}}{\kappa AG}\varphi''(x)}^{Timoshenko} \tag{20}$$

$$\frac{EI_{yy}}{\kappa L^2 AG} \ll 1 \tag{21}$$

To find *Θ(x)* the shear strain can be calculated from eq. (22) and the shear analogue to Hooke's law can be used to find the shear stress τ_{xz} or σ_{xz} (eq. (23)) with the shear force F and the area $A_{xy} = A_{zy}$. The stress tensor $\boldsymbol{\sigma}$ is assumed to be planar (24), with no component in y-direction, and with the important symmetry condition $\tau_{xz} = \tau_{xz}$.

$$2 * \varepsilon_{xz} = \theta_{xy} = \frac{s}{\Delta y} \tag{22}$$

$$\tau_{xz} = \sigma_{xz} = 2G * \varepsilon_{xz} = G * \theta_{xz} = \frac{F_{shear}}{A} \qquad \forall\, \theta(x) \ll 1 \tag{23}$$

$$\boldsymbol{\sigma} = \begin{pmatrix} \sigma_{xx} & \tau_{xz} \\ \tau_{zx} & \sigma_{zz} \end{pmatrix} \tag{24}$$

The present WAAM deposit is assumed to not have any vertical residual stress components σ_{zz} and since there are no external vertical forces in any direction either, the shear stress in the x-plane and z-direction ε_{xz} must be zero. Since no stress variations along the length in x-direction are assumed either, there cannot be any shear strain ($\tau_{xz} = 0$) that rotates the local cross section relative to the neutral axis.

As long as no shear strain is present that rotates the cross-section relative to the neutral axis, the Euler-Bernoulli beam theory is still valid, regardless of the Timoshenko condition (eq. (21)), because the deviation $\theta_{xy}(x) = \varphi(x)$. By differentiating the linear equation in eq. (17) twice, it becomes evident that $\varphi''^{(x)} = 0$, which makes the Timoshenko ratio (in eq. (20)) become zero, yielding mathematically the Euler-Bernoulli problem again. This is only the case for this very unique load case of a constant bending

moment applied to the cantilever beam. However, the Euler-Bernoulli problem still does not consider *u(x)* and still describes a circle with a quadratic equation, which is why a third approach is investigated that describes the sector of a circle.

2.1.4 Sector of a circle

The internal bending moment M_{int} and moment of inertia I_{yy} are constant along the length and therefore so are the curvature χ and curve radius ρ. The problem can therefore also be solved using the geometrical dependencies of the sector of a circle (Figure 46). The radius ρ is calculated using eq. (16), which can also be written as eq. (25). The initial length L_0 is given and eq. (26) yields the local angle of the cross section. The new shortened length L is then calculated using eq. (27) and the out of plane distortion *w (L)* finally with eq. (28).

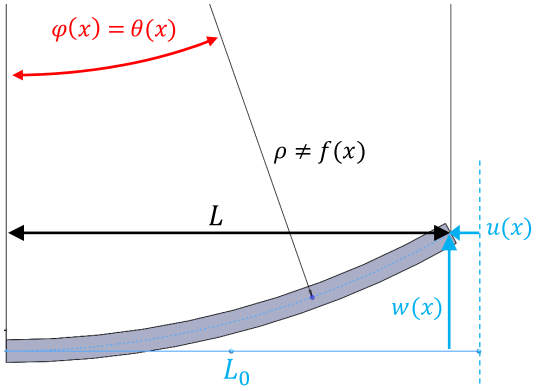

Figure 46: Sector of a circle

$$\rho(n) = \frac{EI_{yy}(n)}{M_{int}(n)} \tag{25}$$

$$\varphi(n) = 2 * \frac{L_0}{\rho(n)} \tag{26}$$

$$L(n) = 2\rho(n) * \sin\left(\frac{1}{2}\varphi(n)\right) \tag{27}$$

$$w(L_0, n) = \rho(n) * \left[1 - \cos\left(\varphi(n)\right)\right] = 2\rho(n) * \sin^2\left(\frac{1}{4}\varphi(n)\right) \tag{28}$$

For the case study in the next section 2.2, the Bernoulli beam theory (section 2.1.2) can be used to calculate the constant curvature along the cantilever beam, because

Timoshenko is not required for the reasons explained in section 2.1.3. The distortion will be calculated using eq. (28), as is represents the distorted WAAM part more realistically, including the displacement *u(x)* and not as a quadratic equation.

2.1.5 Redistributed Stress Field

The residual stress profile causes bending distortion around the neutral axis, as shown in Figure 47. The stress profile within a bent beam with constant bending moment is calculated using eq. (29). Note that the neutral axis must be located at $z = 0$ for this equation.

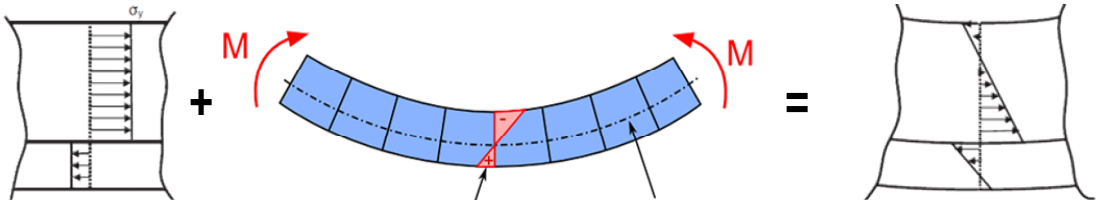

Figure 47: Redistribution theory [111]

With the principle of superposition, the bending stress overlays the residual stresses of additive manufacturing. Their sum is therefore the resulting residual stress field. This behaviour was first suggested by Colegrove et al. [111] (Figure 47) and is quantified in more detail in the present work. At the neutral axis, the stress does not change distortion. Above the neutral axis, the (tensile in the wall) stress drops linearly and below the neutral axis, the stress (compressive in the substrate) increases. The slope of the redistributed profile can be calculated with eq. (30).

$$\sigma_{xx,bend}(z) = \frac{M_{int}(n)}{I_{yy}(n)} * z \tag{29}$$

$$\frac{\Delta\sigma_{xx}}{\Delta z} = \frac{M_{int}(h)}{I_{yy}(h)} \tag{30}$$

This behaviour can be observed In small steel walls [119] and in medium high Ti–6Al–4V walls [141] (Figure 48). The location of the neutral axis is calculated over the geometry only (eq. (1)) and the measured and simulated residual stress before and after unclamping showed the exact same behaviour below and above the neutral axis (Figure

48). In Ding et al. [119] the neutral axis was well below the surface of the substrate and in Hönnige et al. [141] slightly above. Both plots show that the stress profiles pivot around the calculated position of the neutral axis. Colegrove et al. [111] already showed that the slope of their analytical model agrees with redistribution simulated by Ding et al. [119]. The slope of Hönnige et al. [141] agrees as well with the analytical model. This will be discussed in chapter 4, which contains the content of the publication.

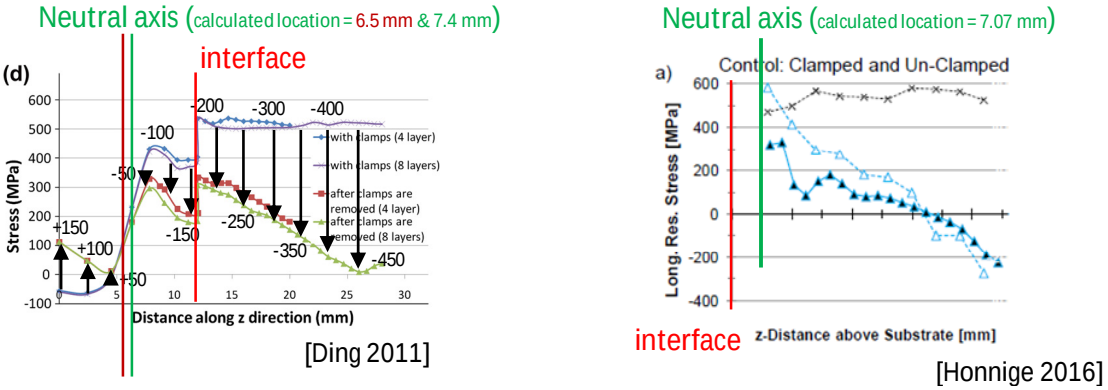

Figure 48: Neutral axis added to stress profiles from the literature [119], [141].

2.2 Case Study

The aim of this case study is to predict the out of plane distortion of the substrate and the curvature radius ρ for three different Ti–6Al–4V WAAM wall widths (v = 4 mm, 8 mm and 12 mm) and any height. It is assumed that the longitudinal residual stress before unclamping are constant across the cross-section of the wall at 550 MPa [141]. The balancing compressive residual stresses in the substrate are also constant in the cross-section and interface issues are neglected. The maximum stress in the substrate is furthermore limited to the yield strength of 815 MPa [92]. This unbalanced stress condition is virtually unclamped, allowing the substrate to distort out of plane with a constant curvature. A certain distortion is required for stress equilibrium, which can be plotted as a function of the wall height for each wall width.

The plot in Figure 49 shows an increase in distortion with increasing wall height for all three widths up to approximately 5 mm. This represents a very small deposit of 2 or 3 layers only, for which the 12 mm wide wall results the greatest distortion. Unclamping of higher walls results actually in less distortion. At 20 mm height, the 12 mm wide wall

has produced a cross-section large enough to cause yielding in the substrate, resulting in discontinuity of the slope, which happens as well for the thinner walls at greater heights. Above this critical value, the stress in the substrate is assumed to be constant at compressive yield.

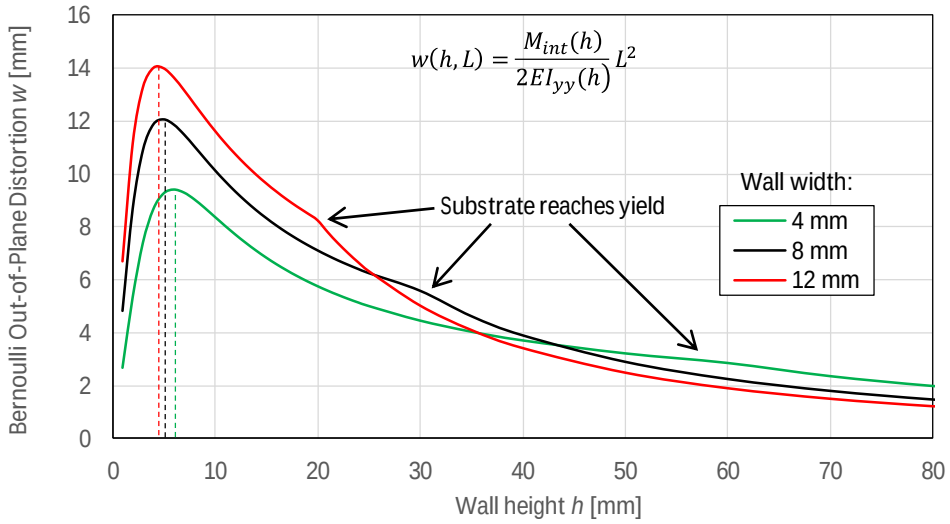

Figure 49: Calculated out-of-plane distortion of the substrate vs. the deposited wall height

It is also possible to plot the curvature radius *ρ(h)*, which is independent of the wall length. The graph in Figure 50 shows this value for the same parameters from Figure 49, showing the extreme values at the same wall height.

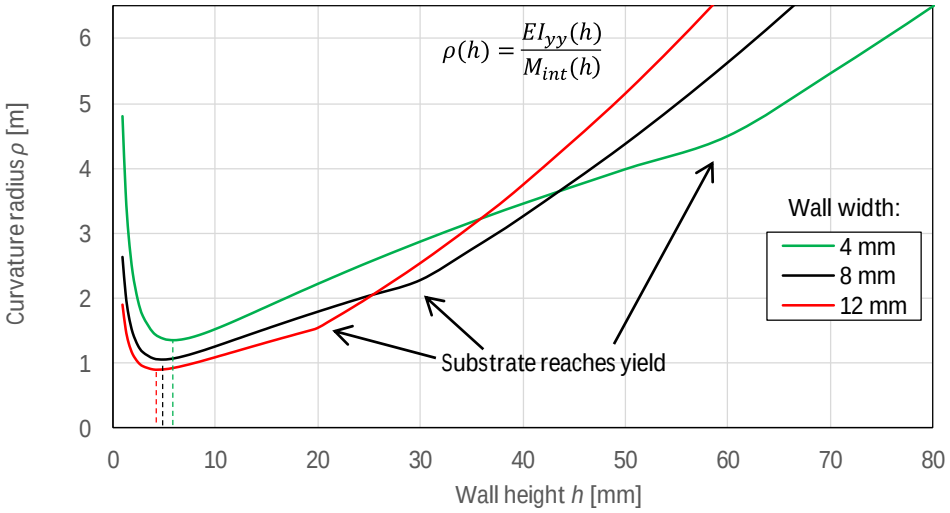

Figure 50: Calculated curvature Radius of the substrate surface vs. the deposited wall height

Even though it is a more comparative plot, the direct measurement of the large curvature radii is difficult. The critical wall height can be determined for any wall and

substrate geometry that produces the greatest distortion and the smallest curvature radius. Figure 51 shows the study, in which three walls with different heights and otherwise identical dimensions are investigated. The neutral axis for the three cases A (h = 4 mm), B (h = 16 mm) and C (h = 64 mm) is located within the substrate, just above and well above the surface of the substrate respectively. The critical wall height for maximum distortion for this geometry would be 5.95 mm and a wall height of 12.64 mm would set the neutral axis exactly into the interface between substrate and deposit. Using the properties of Ti–6Al–4V (E = 113 MPa [92]), Table 3 shows the calculated results for the three cases A, B and C. It shows that the bending moment increases a lot with the wall height, but because the moment of inertia increases disproportionally more, the curvature χ and stress gradient Δσ/Δh decrease.

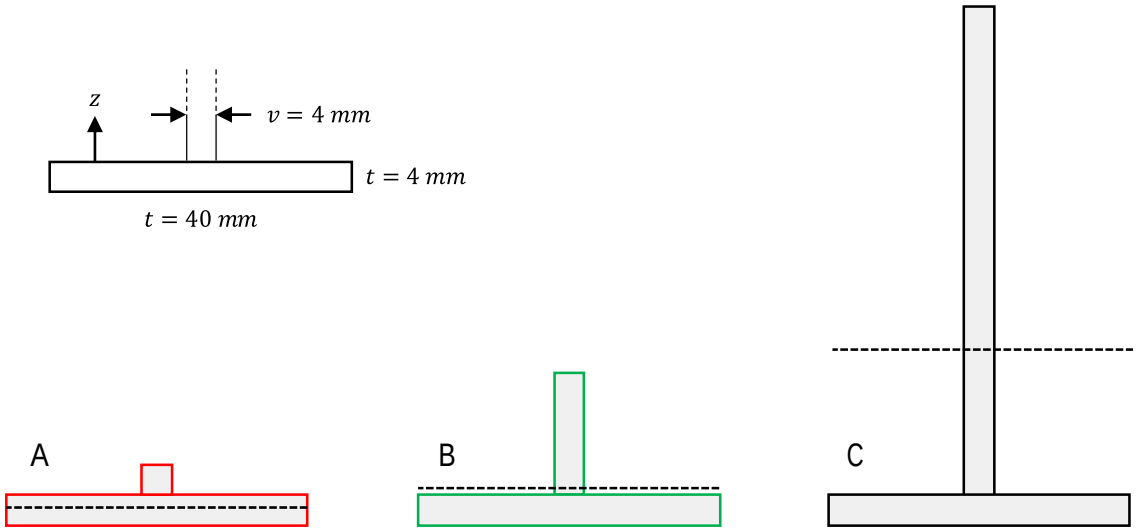

Figure 51: Three identical geometries with different wall heights and the neutral axis located (A) in the substrate, (B) just above the interface and (C) far above the interface.

The stress profiles for the three cases before and after unclamping are shown in Figure 52. As presupposed, the tensile stress in the wall is assumed to be the same regardless the height and is fixed at 500 MPa. However, the compressive stress in the substrate increases, when more material is deposited. Unclamping causes pivoting of the profiles around the neutral axis. The reduction in stress in the top of the small wall does not produce compressive stress, unlike the higher walls that even develop large compressive stress at the top. In the latter, the tensile residual stresses were increased below the neutral axis after the redistribution. So even though the maximum distortion decreases

at wall heights above the critical value, the tensile stresses in the wall are increased and become the largest near the interface with the substrate, which represents a critical feature.

Table 3: calculated values for the walls A, B and C in this case study

	A	B	C
h	4	16	64
z_neutr.ph. [mm]	-1.6	0.9	18.9
Iyy [mm^4]	467	6,450	201,416
σ_deposit [MPa] (def.)	520	520	520
σ_substr [MPa] (calc.)	52	208	832
M_int [Nm]	33.28	332.8	4526
Δσ/Δh [MPa/mm]	71.20	54.11	22.47
ρ [m]	1.6	2.1	5.1
χ [1/m]	0.62	0.47	0.20

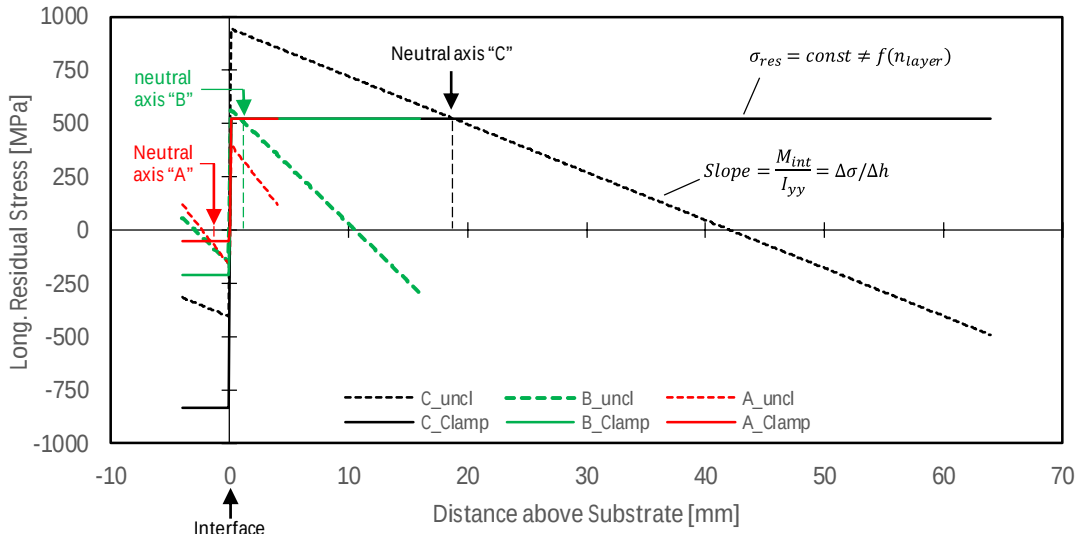

Figure 52: Initial and redistributed stress profiles of the three wall heights with the values from Table 3

2.3 Verification

The calculations above are based on a variety of assumptions and this analytical approach is only valid for a single free-standing straight wall with a constant geometry, the simplest feature in AM. For varying stresses or changing wall geometries [229] along the length, the Timoshenko differential equation must be satisfied and the circular calculation with a constant curvature is no longer valid. This can be addressed using numerical approaches [230]. However, this analytical approach reflects the measurements from the literature reasonably well, as shown in Table 4, which compares actual measurements and FE Simulations of stress and distortion in WAAM using different geometries and materials with the analytically predicted values. The

comparison of calculated distortion and stress redistribution with the predicted values are plotted in Figure 53. The analytical approach matches the measured distortion in Ti–6Al–4V walls from Martina et al. [115] reasonably well considering the difficulty to measure the distortion, for which the accuracy is estimated to be approximately ± 0.4 mm.

The definition of the stress gradient is even more difficult to determine, as the propagation of uncertainty from neutron diffraction, including texture, grain size and temperature variation, and the contour method needs to be considered. Other errors, such as insufficient friction of the clamping and slipping cannot be quantified with confidence. The uncertainty depends furthermore on the strength and the Young's modulus of the material. It is therefore reasonable that the deviation from the analytical prediction is more significant. Ding et al. [119] predicted RS & D for 8 mm and 16 mm steel walls using a FE model and the analytical approach is close to both distortion and the stress gradient. The simulated distortion of 3.2 mm would precisely match the stress gradient of 20 MPa/mm using the analytical approach. The analytical approach calculates a stress gradient for a 40 mm high wall that is slightly higher than the one predicted by the simulation.

Table 4: Comparison of numerical predictions and measurements with the analytical model

	Martina '16 [115]	Ding '11 [119]	Colegrove '13 [111]	Wang 2012 [87][2]	Montevecchi 2017 [227]	Hoye 2014 [112]
Material	Ti–6Al–4V	ER70S-6 steel	ER70S-6 steel	Ti–6Al–4V	ER70S-6 steel	Ti–6Al–4V
σ_{Res} [MPa]	570 (est.)	500	500 (est.)	570 (est.)	500 (est)	570
E [GPa]	115	210	210	115	210	115
s; t [mm]	60; 6.35;	60; 12	60; 12	60; 6.5;	150; 8	100; 12
V [mm]	5.75	5	5	4.5	6	5
h [mm]	23.4	8, 16, 40	40	100	8	36
2 x L_0 [mm]	405	500	490	660	150	178
ρ [m] Euler Bernoulli	2.9	13.3; 9.2; 11.4	9.50	8.16	10.11	5.79
w [mm] circular approach	7.08	2.4; 3.4; 2.7	3.29	6.68	0.278	2.74
w [mm] Experiment	7.2	3.3	5.5 and 7	6.4	0.25 ... 0.3[3]	-
Δσ/Δh [MPa/mm] Theory	-24.1	-16; -23; -18	18.4			-18.1
Δσ/Δh [MPa/mm] Exper.	-18.4	-20; -20; -15	15.8	N/A	N/A	-22

[2] Distortion not shown in the paper, but a specimen is still available

[3] Distortion was reported at a different location, the relevant value was taken from distorted FE model

Colegrove et al. [111] measured the residual stress in the stress profile, which matches moderately well with the simulation. The measured profile however is not linear, but slightly curved suggesting distortion of the substrate during the deposition. This was mentioned in the paper to be due to compromised clamping, which already showed discrepancies to Ding et al. despite the otherwise identical geometry and deposition parameters [119]. This would also explain the larger distortion of the experiment compared to the analytical approach. Also the clamping of Hoye et al. [112] was probably insufficient, as the few bolts allowed the development of a relatively curved residual stress profile. The distortion of the very large wall in Wang et al. [87] can also be predicted precisely by the analytical approach, where the model shows that the substrate just reached yield stress. Chapter 4 contains stress measurements before and after unclamping WAAM walls made of Ti–6Al–4V. This analytical approach predicts the distortion and the stress distribution well and is explained in detail in these chapters.

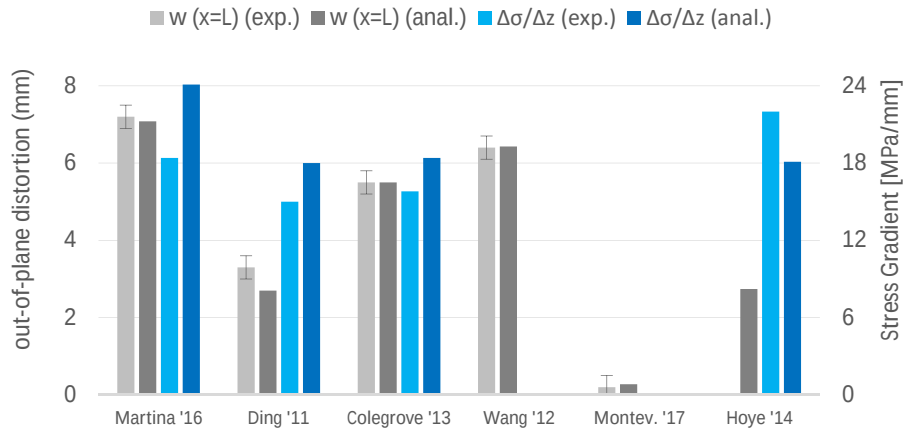

Figure 53: Comparison of experimental results taken from [87], [92], [111], [112], [119], [227] with predicted values.

2.4 Conclusion

When reporting stresses profiles, it is advantageous for understanding the redistributed stress to indicate the location of the neutral axis. The longitudinal stress at this location represents the constant as-deposited stress before unclamping. Also the stress gradient along the height after unclamping should be examined, because it is directly related to the curvature of the distorted section, which is a better way for comparing distortion than the out-of-plane displacement, because it is independent from the length of the

section. The relevant chapter 4 will respect these conclusions. If the measured stress gradient does not have a constant slope, then reasons for this should be discussed and there may be a number of potential causes: If the slope is a curve, it might be possible that the clamping was insufficiently rigid and the part gradually distorted during the build. Secondly a discontinuous slope with a sharp step or bend could suggest that the part released stresses abruptly during the deposition. However, other explanations can be possible

In summary, this simple analytical approach predicted the RS & D measurements and the results from complex numerical simulations surprisingly precisely. It can be used to efficiently estimate critical wall heights, possible distortion after unclamping and stress redistribution during distortion. It can also suggest the worst substrate geometry for determined wall geometries in terms of maximum stress and/or distortion. In some cases for example it might be advisable to use a smaller substrate for example to decrease residual stress or distortion.

Chapter 3 Residual Stress and Texture Control in Intersections by Stress Relief and Rolling

The content of this chapter was submitted to the journal Materials and Design on 17th Dec 2017 (JMAD-S-17-11440). The manuscript was reviewed and a revised version was resubmitted on 2nd Feb 2018.

3.1 Introduction

Before exploring residual stress mitigation techniques in AM, their development must be better understood. Few numerical simulations and measurements are available, however they often describe the stress in straight walls only, as mentioned in section 1.4.3. The manufacture of structural components requires more complex features than straight and free-standing walls, such as curves and intersections, as shown in a typical WAAM application in Figure 54, a near-net-shape Bombardier landing gear rib. To date, thermal stress relief is considered as the only method to reliably eliminate the entire residual stresses [185]. However, no measurements were performed to prove whether that is true. It is conceivable that tensile hydrostatic stress regions can develop in intersections.

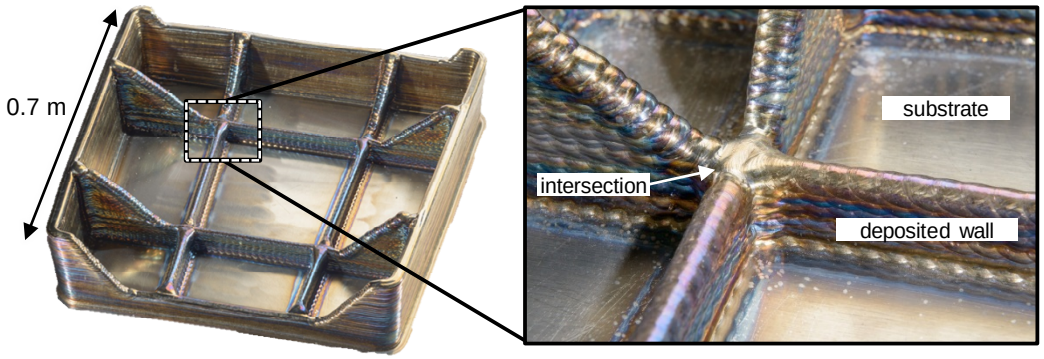

Figure 54: Typical WAAM application: Bombardier near-net-shape Ti–6Al–4V landing gear rib [141]

This chapter discusses the development of residual stresses in Ti–6Al–4V WAAM intersection for which no literature was available. Thermal stress relieving was applied to this potentially problematic feature to see whether or to what extent stresses can be relieved following the procedure from section 1.6.1.1. The effect of inter-pass rolling on both aspects, residual stress (1.6.2.1) and microstructure (1.5.2.1) is discussed as well,

to see if the effect on intersections is similar compared to free-standing single pass walls. The established neutron diffraction (ND) stress measurement technique was performed (1.7.1) to calculate the stress profiles in the three principal directions of the intersection, after which the destructive contour method (CM) was used (1.7.2) for a more detailed insight into the stress distribution within the entire component.

3.2 Methodology

3.2.1 Production of Specimen

Four Ti–6Al–4V intersecting walls were built with the deposition parameters from Table 5 using the in-house-built HiVE machine (High-Value Engineering). The HiVE (Figure 30) is a converted friction stir welding CNC gantry with a WAAM deposition unit retrofitted to the machine.

Table 5: Deposition Parameters

Current	210	[A]
Torch stand-off	8	[mm]
Travel speed	3.5	[m/min]
Plasma Gas	0.8	[l/min]
Plasma Shield	10	[l/min]
Trailing Shield	~200	[l/min]

The machine tool has been replaced by a customized roller device, which is capable of two-directional rolling with vertical rolling loads up to 100 kN. The deposition unit is attached to a rotator, allowing the coaxial rotation of the shield, wire feeder and wire spool around the plasma torch. A Fronius Plasma 10 model was used to deposit 1.2-mm-diameter Ti–6Al–4V wire on a 12-mm-thick Ti–6Al–4V substrate that was clamped during the deposition to a rigid steel backing block, which prevented distortion during the deposition. For the first three layers the current was increased by 10% to compensate for the heat sinking effect of the substrate. A laminar flow local trailing shield [231] attached to the torch was used to prevent the deposited material from oxidising [52]. The plasma gas was pure-shield argon, as was the plasma shielding gas and the trailing shielding gas. The oscillating path strategy, which is shown in the schematic in Figure 55, was used to produce the intersections:

For odd layers (a), a continuous wall (I) was deposited in the x-direction with 6 mm oscillating width and a 3 mm step size. Two shorter lateral walls (II) & (III) with identical parameters to the first wall were deposited from the outside towards the centre in positive and negative y-direction respectively, until they joined the continuous wall. At the intersection the oscillating width was increased from 6 mm to 10 mm to ensure a neat joint and provide enough material to machine a radius to finish the feature. After finishing one pass, the trailing shield remained above the sample for 45 s to prevent oxidation. Even layer numbers were deposited in the opposite direction: the continuous wall (I) was deposited in the negative x-direction and the discontinuous wall (II) & (III) from inside out in negative and positive y-direction respectively. The interlayer dwell time for all four specimens between each layer was 5 min. Two of these four specimens were inter-pass rolled with 75 kN using a H13 tool steel roller with 150 mm diameter and convex profile of 3 mm radius (Figure 55 c).

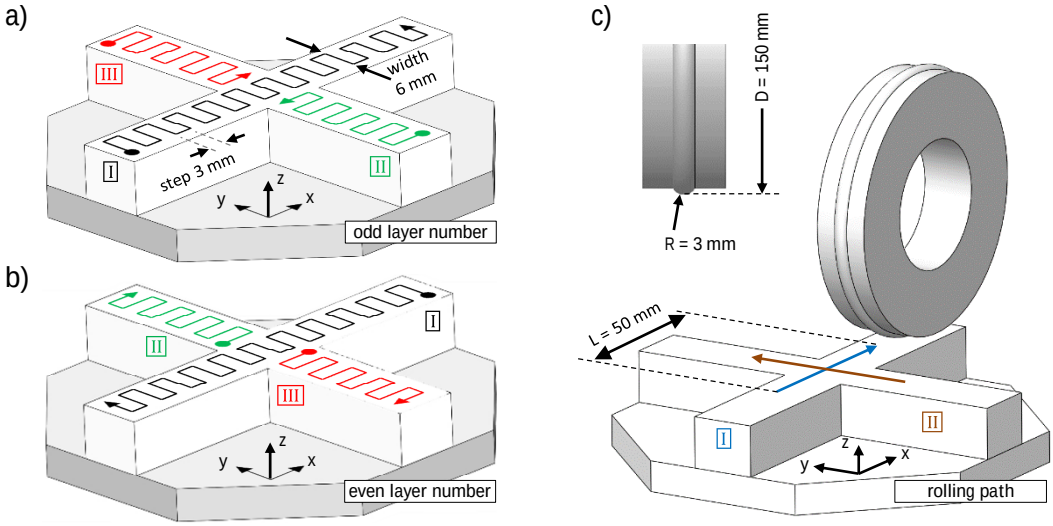

Figure 55: Path strategy for (a) odd and (b) even layers; (c) roller profile and pattern

The crossing rolling paths were performed after one intersection layer was completed. The total rolling lengths in both directions was 50 mm and were symmetrical across the intersection (Figure 55 c). Irrespective of whether rolling was applied or not, these deposition parameters produced a total wall width of approximately 10 mm. The build was stopped once the wall reached a height of 25 mm; the last layer had an even layer number. One intersection of each, with and without rolling, was thermally stress relieved, in an inert argon atmosphere at 640 °C for 4 h, while it remained clamped to

the backing block. Finally all four specimens were machined to identical geometries. From the top of the wall, a maximum of 2 mm was machined away to reduce the height to 24 mm. The wall width was machined from approximately 10 mm to 6 mm and the radius at the intersection to 2.5 mm (Figure 56). Residual stresses in additive manufacturing are typically measured without finishing processes that potentially influence the stress field, such as machining. Finish machining however resulted in a more representative specimen in the condition of operation. Another benefit was that it decreased the path length for the neutrons in the neutron diffraction strain scan.

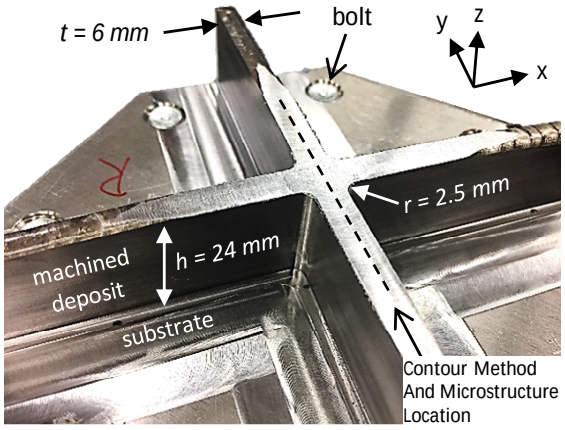

Figure 56: Specimen after Machining

3.2.2 Neutron Diffraction Residual Stress Measurement

Lattice plane spacing measurements for residual stress calculation were carried out at the ENGIN-X time-of-flight neutron diffractometer at the pulsed neutron source of the Rutherford Appleton Laboratory in Didcot, UK [218]. The "white beam" with a wide range of wavelengths close to atomic distances allows the counting of neutrons diffracted by multiple planes simultaneously. Gauge volumes of $3 \times 3 \times 3$ mm^3 were located along the vertical centreline of the specimen with steps of 3 mm. Based on the typical WAAM microstructure [77], [86], it was estimated that 1-10 prior-β grains can be incorporated in the gauge volume. Each of those can contain approximately 10^8 α plate, which are estimated to be roughly between 10 μm^3 and 100 μm^3 in size. Their actual size and orientation depend on the orientation and nature of the parent prior- β grain [65] and the cooling rate [128]. During the d_0 measurement to determine the strain-free lattice spacing, it was established that the texture and sample orientation did not influence the measurement [232]. The specimen was orientated accordingly to obtain

measurements in 3 orthogonal directions. Figure 57 (a) shows the setup for the z-scan during the measurement of the longitudinal directions using both detectors and Figure 57 (b) the measurement of the normal direction with the north detector. Here the south bank remains unused, because the orientation does not align with any of the measured orientations and the neutron path through the titanium substrate plus the thick steel backing bar does not allow the detection of peaks. The path length for the measurement of the longitudinal and transverse direction was 11 mm, while it was 15.5 mm for the normal direction. Electro-discharge machining was deployed to produce stress-free references, for all four specimens to establish the individual unstrained d_0. The d_0 gauge volumes were measured in all 4 orientations around the z-axis in the configuration of Figure 57 (c) to minimise texture effects and differences in both detectors.

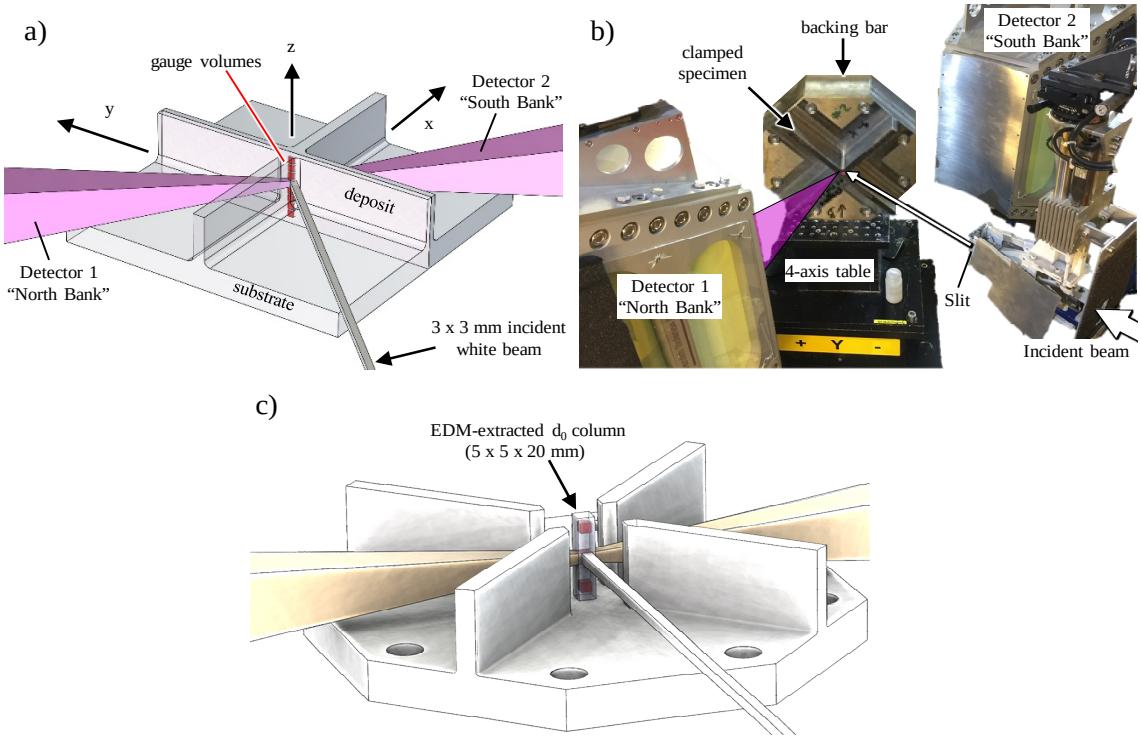

Figure 57: Setup at ENGIN-X: a) Schematic of the beam paths to detect the longitudinal and lateral directions; b) Image of the actual setup on the beam-line to detect the normal plane with the north detector, while the south detector is "dark"; c) location of the d_0 gauge volumes within the EDM-extracted centre column.

In the hexagonal-close-packed (hcp) α crystal, eight planes can be identified within the analysed TOF-range between 22000 µs and 47500 µs, which are the {2021}, {1122}, {1013}, {1120}, {1012}, {1011}, {0002} and {1010} planes. They were single-peak fitted to determine the plane spacings *d* and fitted in whole using Pawley refinement [233] to

directly determine the hcp lattice parameters a_{hcp} and c_{hcp}. When using monochromatic neutron sources, the {1011} and {1013} can be used to measure strains in Ti–6Al–4V additive manufacturing [116], [141], because they consistently provide good signal strength. The {1011} plane however is understood to be sensitive to intergranular strain and therefore unsuitable for stress calculation. The {1013} plane is therefore the only plane suitable for stress calculation in the textured as-deposited WAAM material. Donoghue *et al*. and Antonysamy *et al*. [86], [127], [167] performed electron-backscatter-diffraction (EBSD) measurements to determine the crystallographic α and reconstructed β-orientation in Ti–6Al–4V AM. The procedure to confirm the crystallographic orientation in neutron diffraction using the general materials diffractometer (GEM) at ISIS with EBSD has been performed previously on near-α-titanium [234]. During solidification, the basal $\{100\}_{bcc}$ plane of the high-temperature phase is known to align normal with the build direction z, in other words parallel to the substrate [86], [127], [167]. The Burgers Orientation Relationship (BOR) in Figure 58 (a) shows how the basal {0001} α-plane of the bespoke α-plate transforms on the $\{110\}_{bcc}$ plane [29] once the temperature drops below the β-transus.

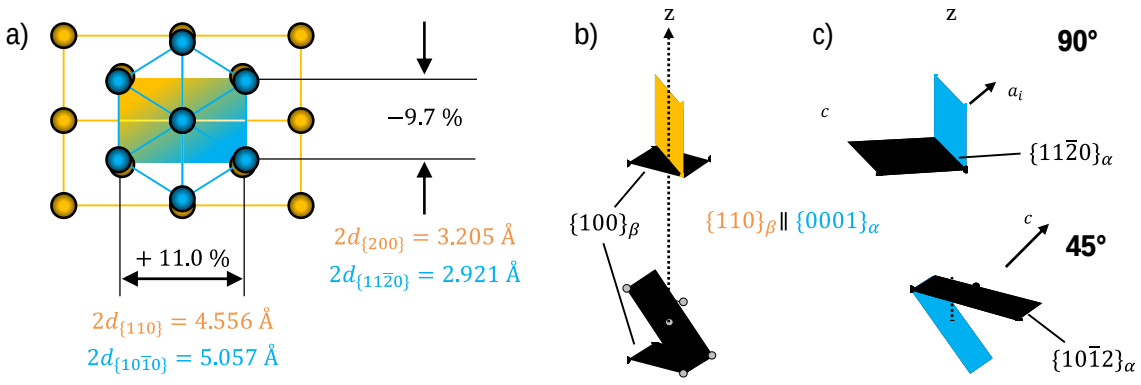

Figure 58: (a) Burgers relationship [44] and change of the lattice during transformation with values taken from the present study; (a) possible orientations of the {110} variants; (a) possible orientations of the hcp unit cell after transformation.

The $\{110\}_{bcc}$ plane has six possible variants in the bcc unit cell, which can be either aligned with the z-axis or hold a 45° angle with it, as shown in Figure 58 (b). According to this and BOR, there are only two possible orientations of the α-crystal in respect to the z-axis, illustrated in Figure 58 (c), which is known from previous EBSD studies on Ti–6Al–4V WAAM [86]. Even with a free rotation around z, some hcp planes can never

align with the required global orientation x- or y-direction. When measuring the normal strain, only the {1120} or the {1012} plane (depending on the $\{110\}_{bcc}$ variant respecting BOR) will align normal with the global z-direction (Figure 58 c), and a rotation around z does not change the relative orientation of either of the planes. Fortunately the {1013} has a small deviation to the {1012} plane and can be picked up by the detectors as well.

Inter-pass rolling is generally used to improve the mechanical properties in Ti–6Al–4V WAAM. The microstructural effect is the significant reduction in β-grain size from several millimetres to less than 100 µm, as well as the reduction of α colony and plate size [77], [86], which is the phase that is being used for strain measurement in the present work. More important however is the elimination of texture. A larger number of smaller α-grains with a random orientation, caused by inter-pass rolling, facilitates neutron diffraction measurement.

For a consistent residual stress evaluation of all specimens, only the stress calculation based on the single-peak-fitted {1011} plane were used, as Pawley refinement is only compatible with the rolled specimen that diffracts all peaks. Lattice strain for all detectable planes and residual stresses based on the {1013} plane in the three principal directions were calculated using eq. (31) and (32). ε_{ii} is the strain in the respective orientation, based on a specific crystallographic plane d_{hkl}. σ_{ii} is the calculated stress in the corresponding direction [136]; It was attempted to calculate the stress based on as many planes as possible using the individual elastic constants E_{hkl} and ν_{hkl}. Stapleton *et al*. [50] have measured the Young's moduli for six different α-planes and derived the single-crystal elastic constants $\boldsymbol{C_{ij}}$ from them, which allows the completion of the full stiffness matrix $\underline{C}$ and its inverse, the compliance matrix $\underline{S}$. However only the {1013} plane was suitable for stress calculation (E_{1013} = 105 GPa; ν = 0.342), which was only clear after the data analysis. The uncertainty for the strain and stress values were calculated with eq. (34) and (35), based on the partial differential eq. (33) for the propagation of uncertainty, using the uncertainty Δd_{hkl} of the single peak fit. The error bars therefore only account for the fitting errors of the Gaussian distribution with the detected peak of the {1013} plane and does not consider texture effects. Texture uncertainty can stem from the relatively large prior β grains in the as-deposited

condition, so that only a few of them populate the gauge volume. It is furthermore unlikely that the morphology of the d_0 specimen is the same as the measured specimen and could therefore consist of dissimilar β-grain size or even composition of the α-phase. Inter-granular strain and β-phase contributions had to be ignored as well. However, a good point-to-point consistency of the different scans, as well as comparison with independent residual stress measurement techniques, such as the contour method can increase confidence in neutron strain scanning.

$$\varepsilon(d_{hkl})_{ii} = \frac{d_{hkl} - d_{hkl,0}}{d_{hkl,0}} \tag{31}$$

$$\sigma_{ii} = \frac{\nu_{1013} E_{1013}}{(1+\nu_{1013})(1-2\nu_{1013})}\left(\varepsilon_{xx} + \varepsilon_{yy} + \varepsilon_{zz}\right) + \frac{E_{1013}}{1+\nu_{1013}}\varepsilon_{ii} \tag{32}$$

$$\Delta y = \sum_{i=1}^{n} \left| \frac{\partial f}{\partial x_i} * \Delta x_i \right| \tag{33}$$

$$\Delta\varepsilon = \left(\frac{1}{d_0}\right) * \Delta d + \left(-\frac{d}{{d_0}^2}\right) * \Delta d_0 \tag{34}$$

$$\Delta\sigma_{ii} = \frac{\upsilon E}{(1+\upsilon)(1-2\upsilon)}\left(\Delta\varepsilon_{\mathrm{xx}} + \Delta\varepsilon_{\mathrm{yy}} + \Delta\varepsilon_{\mathrm{zz}}\right) + \frac{E}{1+\upsilon}\Delta\varepsilon_{\mathrm{ii}} \tag{35}$$

3.2.3 Contour Method

After the non-destructive neutron experiments the contour method (section 1.7.2) was performed for residual stress analysis. A Fanuc Robocut α-C600i EDM machine was used to cut the specimen in a deionised water bath, while the specimen remained clamped on the 36-mm-thick backing bar. 250-µm-diameter brass wire was used to perform the contour cut, oriented parallel to the y-axis and located in the symmetry plane of the intersection, as indicated with the dashed line in Figure 56. The cut was performed in the negative z-direction from the top to the bottom of the specimen, thereby cutting through the location of the neutron gauge volume locations to give a direct comparison. As soon as the contour cut was completed and the wire entered the backing bar, the cut was stopped and both halves of the specimen were removed from the backing bar. This is unconventional procedure and does not satisfy the zero-net-stress assumption. It was

chosen with the attempt to measure the as-deposited stress before unclamping and consequent distortion (to be comparable with the neutron diffraction result). After ultrasonic cleaning, the surface displacement of both cut halves were measured in a temperature-controlled room on a Zeiss Contura g2 coordinate measuring machine (CMM) with 3-mm-diameter ruby touch probe with a step size of 0.5 mm. The topographical data cloud from both cut surfaces of the samples was processed with Matlab analysis routines for data aligning, cleaning, flattening and smoothing [222]. For smoothing, a cubic spline with a knot spacing of 5.5 mm in both directions was used. For the finite element (FE) analysis one cut half of the sample was modelled in Abaqus software using an 8-node brick element and a uniform mesh with 1 mm distance between the adjacent FE nodes. The stress calculation was based on the linear elastic properties E = 114 GPa and ν = 0.342.

3.2.4 Microstructure

Optical microstructural analysis was performed on the surface of the contour cut at the location of the neutron gauge on the as-deposited and the inter-pass-rolled specimens (dashed line in Figure 56). Conventional sample preparation including grinding, polishing and etching with hydrofluoric acid exposed the microstructure, which was then analysed using an optical microscope with 50x magnification.

3.3 Results

3.3.1 Microstructure

Figure 59 (a) and (b) compare the cross-sectional Ti–6Al–4V microstructures in the additively manufactured intersections of the as-deposited and the inter-pass-rolled specimen. The location and size of the first and last ND gauge volumes are shown in their actual location and size.

Large columnar prior-β grains are visible in the as-deposited specimen (Figure 59 a) and only a few are incorporated by the neutron gauge volume. The high magnification image is located on a prior-β grain boundary, showing the α-plate organised in the typical basket-weave fashion. Alignment constraints of the hcp α-crystal in respect to the orientation of the plate and prior-β grain boundary was discussed by Mathisen *et al*.

[65]. Inter-pass rolling produced the expected fine and equiaxed prior-β microstructure (Figure 59 b), of which approximately 5000 populate the neutron gauge volume and each of those contain a large number of α-plate. The high magnification shows a 100-µm-diameter grain, which developed α-plate that are smaller compared to the as-deposited microstructure. The random orientation and large number of prior β-grains however imparts its texture-free morphology to the incorporated α-phase. The identical pattern of the heat-affected zones in both specimen (HAZ) highlights the similarity of the thermal history, showing that the smaller α-plate are not due to a faster cooling rate.

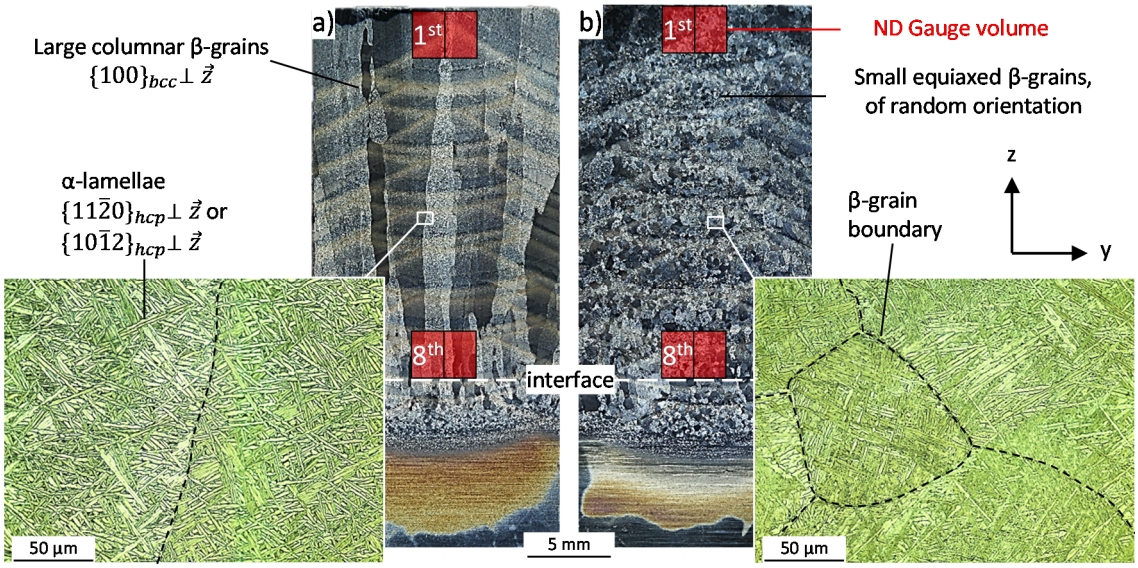

Figure 59: Microstructure in the neutron diffraction gauge volume located on the contour cut surface (YZ) of (a) the as-deposited sample with large columnar prior-β grains containing hcp α-plate; the hcp cell is oriented according to Figure 58 and [65]**; (b) the inter-pass rolled sample with very small, round and equiaxed prior-β grains containing smaller hcp α-plate. The identical horizontal bowed lines are the layer bands (or HAZ).**

3.3.2 Neutron Diffraction

Figure 60 shows typical spectra in the longitudinal and the normal configuration of the as-deposited and the inter-pass-rolled intersection. The inter-pass rolled specimen did not show significant texture, whereas the diffraction pattern of the as-deposited specimen showed a highly orientation-dependent behaviour. The {1120} and the {1012} planes did not show a peak in the longitudinal direction of the as-deposited sample, but they were the strongest peaks in the normal direction. In turn, the basal {0002} plane and the prismatic {1010} plane were relatively strong in the longitudinal direction, but c vanished in the normal direction. Table 6 compares the measured plane spacings with

the expected detectability of α-planes according to the typical texture and BOR, as explained in the methodology section.

Table 6: Theoretical and experimental detection of hcp-planes in Ti–6Al–4V WAAM with the typical texture

		$\{20\bar{2}1\}$	$\{11\bar{2}2\}$	$\{10\bar{1}3\}$	$\{11\bar{2}0\}$	$\{10\bar{1}2\}$	$\{10\bar{1}1\}$	$\{0002\}$	$\{10\bar{1}0\}$
Longitudinal direction (x & y)	90° hcp orient.	good		good			good	good	good
	45° hcp orient.	good		good			good		
	Experimental	moderate	moderate	good			very good	good	good
Normal direction (z)	90° hcp orient.			moderate	very good		moderate		
	45° hcp orient.					very good			
	Experimental			good	very good	very good	good		

Also detected were the $\{110\}_{bcc}$ plane in the longitudinal direction and the $\{200\}_{bcc}$ plane in the normal direction, confirming the prior-β orientation. All stress-free lattice parameters d_0 were found to be isotropic and independent from their location in the wall or whether the wall was inter-pass rolled or not.

Table 7: Stress free d-spacings of the hcp α-phase

		$\{20\bar{2}1\}$	$\{11\bar{2}2\}$	$\{10\bar{1}3\}$	$\{11\bar{2}0\}$	$\{10\bar{1}2\}$	$\{10\bar{1}1\}$	$\{0002\}$	$\{10\bar{1}0\}$
As-deposited	d_north [Å]	1.22075	1.23781	1.32506	1.46095	1.71492	2.22392	2.33436	2.52858
	error [10^{-4} Å]	2.6	1.9	1.8	2.2	2.2	1.1	2.4	4.3
	d_south [Å]	1.22010	1.23746	1.32463	1.46090	1.71484	2.22352	2.33385	2.52817
	error [10^{-4} Å]	2.3	1.8	2.1	1.9	2.2	1.1	2.2	3.9
Stress relieved	d_north [Å]	1.22063	1.23784	1.32480	1.46060	1.71464	2.22375	2.33349	2.52846
	error [10^{-4} Å]	2.2	1.8	1.5	1.3	1.4	0.8	2.1	3.4
	d_south [Å]	1.22003	1.23740	1.32449	1.46043	1.71444	2.22336	2.33343	2.52827
	error [10^{-4} Å]	1.7	1.5	1.5	1.5	1.6	0.8	1.6	3.2

Table 7 shows the determined stress-free d_0 of all detected planes of both detectors. Throughout all conditions the {1011} was fitted with the smallest error. Thermal stress relieving slightly decreased the plane spacings by 2.3×10^{-4} Å on average.

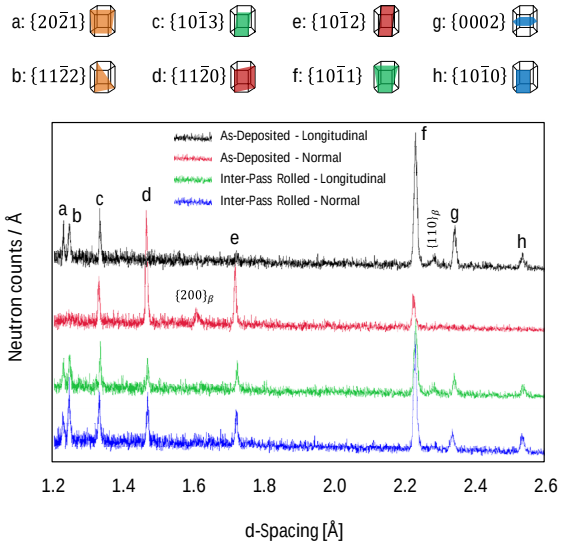

Figure 60: Exemplary spectra of longitudinal and normal directions of as-deposited and inter-pass rolled samples.

Throughout all measurements, the north detector measured a d-spacing of approximately 4×10^{-4} Å more than the one measured by the south detector. Therefore each strain was calculated by comparing the strained d-values against the d_0 measured by the same detector to take detector errors into account. The diagrams in Figure 61 show the strain profiles in the three orthogonal directions for the as-deposited and inter-pass-rolled specimens from those planes that gave a diffraction pattern, as well as the strain of the lattice parameters a_{hcp} and c_{hcp} using the Pawley refinement for comparison.

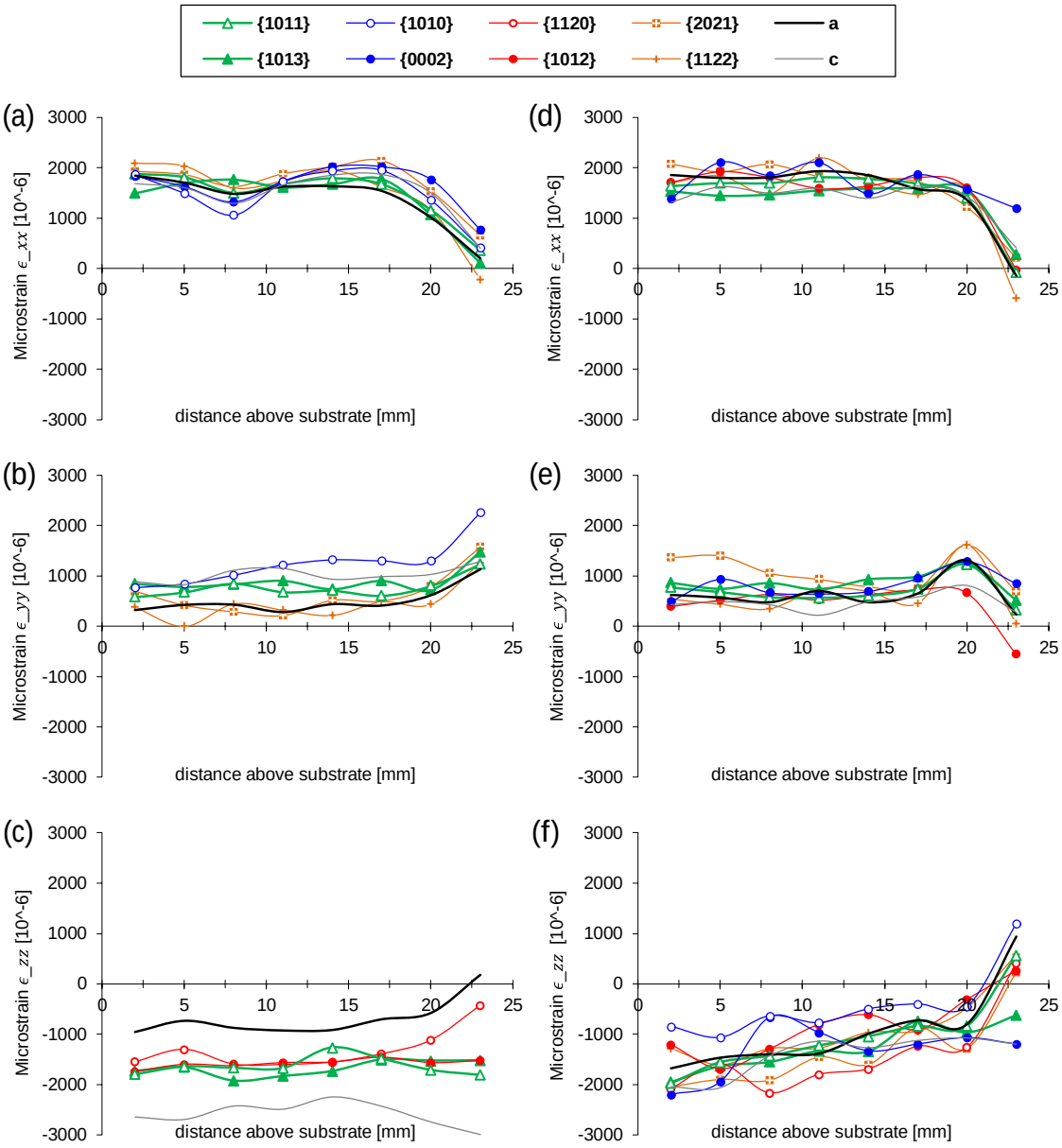

Figure 61: Residual strain profile along the symmetry line in all three principle directions of the as-deposited sample in (a) x, (b) y and (c) z direction; and of the and inter-pass rolled sample in (d) x, (e) y and (f) z direction.

The profiles from the different planes are comparable. The {1120}, {1012}, {0002} and {1010} planes sometimes diverge from the other profiles. In particular, the *a* and *c* strain values in the normal direction of the as-deposited specimen diverge dramatically from the other planes and each other (Figure 61 c). Finally only the {1013} plane was used for stress calculation. Error bars are not displayed intentionally to preserve clarity. The {1011} and {1013} planes for example were fitted with an average error of 101 and 269 microstrain respectively.

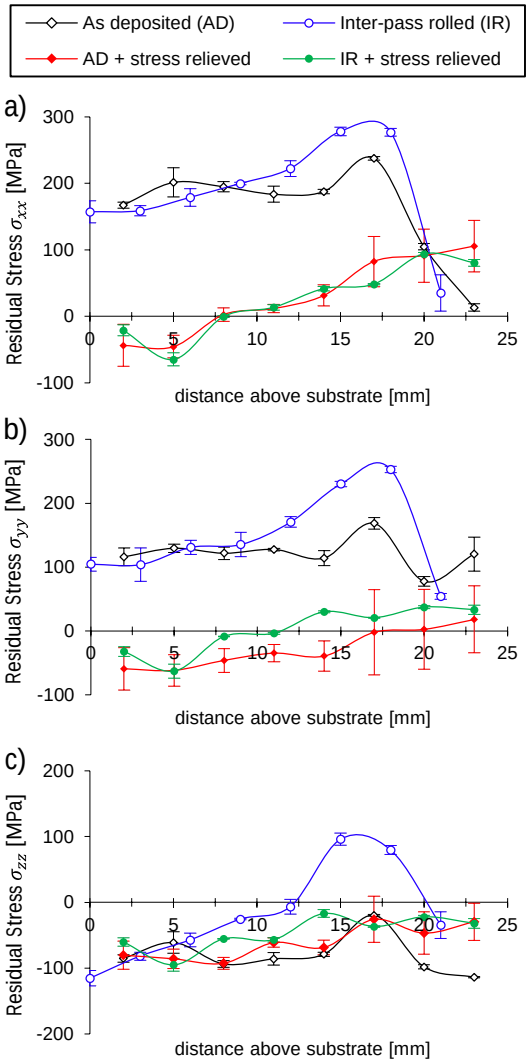

Figure 62: Calculated residual stresses using neutron diffraction with the {1013} plane in the symmetry axis in (a) the longitudinal direction of the continuous deposit (σ_{xx}), (b) it's transverse direction, which is the discontinuous deposit (σ_{yy}) and (c) the normal direction (σ_{zz}), as per Figure 57.

Figure 62 (a-c) shows the residual stresses based on the {1013} plane in (a) the longitudinal x, in (b) the transverse y and (c) the normal z-directions. The longitudinal

residual stress profile in the x-direction of the as-deposited specimen is constant along the height at approximately 200 MPa and drops to almost zero towards the top of the specimen. In the transverse y-direction the stress is constant along the height at approximately 100 MPa, but without the drop at the top. The inter-pass-rolled specimen has similar profiles, with slightly larger values in both directions.

The only difference is the drop in tensile stress in the top region of the transverse direction, caused by the last rolling step. The stress-relieved specimens did not contain significant residual stresses in any direction. The longitudinal stresses are slightly tensile, while the normal stresses are slightly compressive. Noteworthy is the tensile region in the upper half of the inter-pass rolled specimen in the normal direction while the as-deposited one is effectively stress-free or slightly compressive.

3.3.3 Contour Method

Figure 63 shows the residual stress maps in the y-z plane for all four specimens. Both the non-heat-treated specimens (as-deposited (a) and inter-pass rolled (b)) have virtually identical residual stress maps. At the top centre both have a small region of very large compressive stress, reaching -356 MPa and -313 MPa respectively. Large tensile stresses can be seen below the interface, where they are the largest just under the intersections at 338 MPa and 325 MPa. Further balancing compressive regions are located at the wide edges and the bottom of the substrate. The through-thickness stress in the lateral deposit (on the left and the right side of the longitudinal deposit) is practically zero.

The only noteworthy difference of the as-deposited and the inter-pass rolled stress map is the slightly increased compressive region under the rolled length in the inter-pass rolled specimen, revealing little impact of the cold work on the residual stresses in general. Both stress-relieved specimens (Figure 63 c and d) are virtually stress-free, as they range between -32 MPa and 20 MPa. Only the strong compressive field at the top of the intersection and the balancing tensile field just below were not relieved entirely.

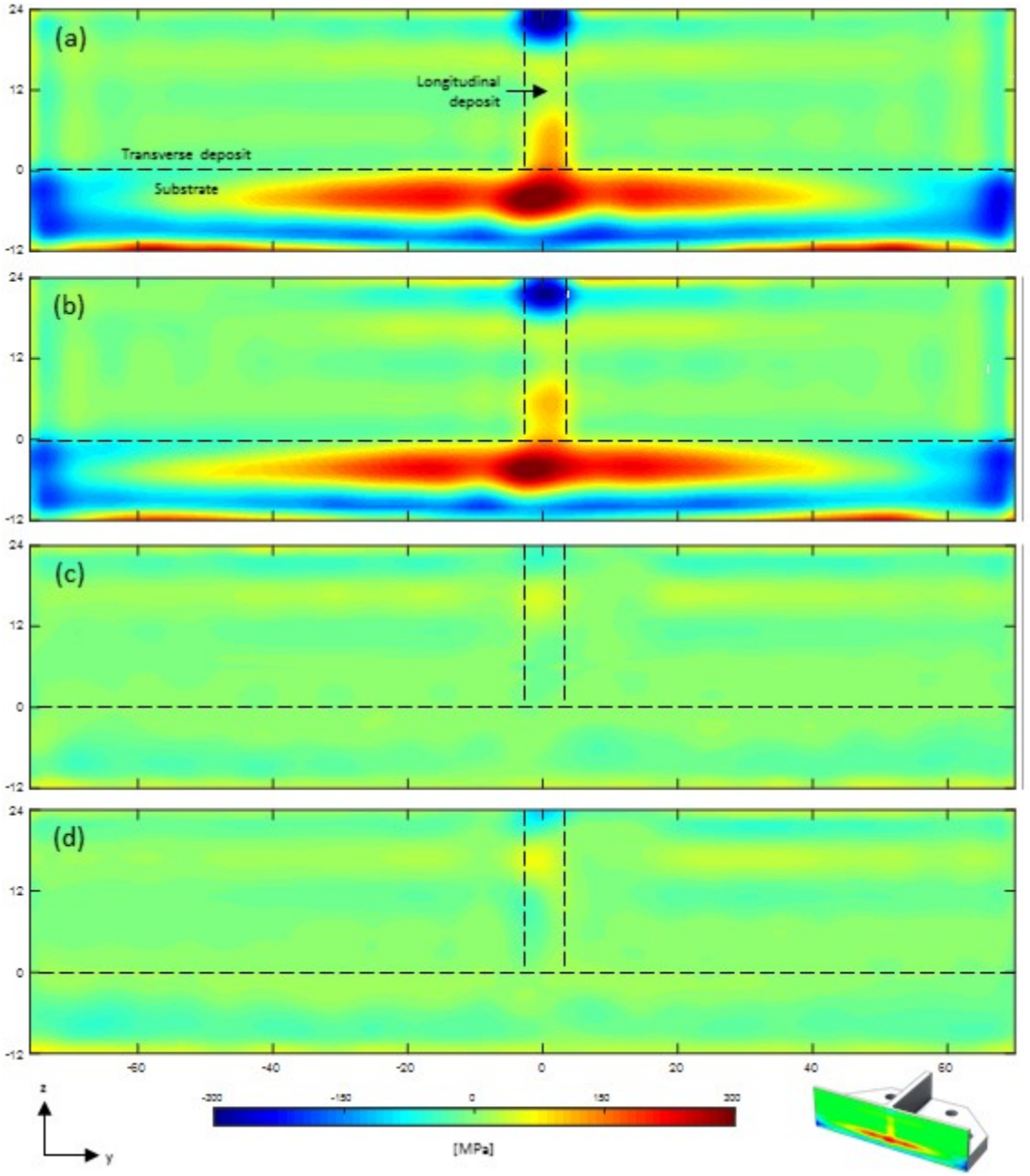

Figure 63: Full residual stress maps produced by the contour method on the y-z plane of all four specimens: (a) as deposited and (b) inter-pass rolled and both after stress-relieving (c, d); units in [mm]; horizontal and vertical dashed lines indicate the interface with the substrate and the wall contour respectively.

3.4 Discussion

3.4.1 Neutron Diffraction

Ti–6Al–4V is an α+β alloy. The low-temperature hcp α-phase completes the transformation into full body-centred cubic (bcc) β-phase at approximately 995 °C [44]. The moderate-to-fast cooling rates resulted in the formation of a fully lamellar

microstructure, in which the α-plate start growing from the parent β grain boundary, as shown in Figure 59 (a). These plate are separated by a small residual β phases and can form a colonies within the parent β grain [43], [47]. At room temperature Ti–6Al–4V typically contains between 3% and 9% of the high-temperature β-phase [45], [54] and non-instantaneous cooling allows partitioning, which in this case is the diffusion of Al and V into the respective phase that they stabilise. This influences the lattice parameters of both hcp and bcc unit cells [55], [235], [236]. Elmer *et al*. [59] reported no diffusion or change in lattice size up to 550 °C. However, above a stress relieving temperature of 600 °C the lattice size can change, but this was observed in a non-lamellar, equiaxed-like and oversaturated Ti–6Al–4V microstructure with 12.1 % β-phase prior to stress relieving. This may have allowed diffusion and lattice change at a lower temperature, while no significant lattice size change was observed in the present study. Furthermore the rapid cooling rate used by Elmer *et al*. [59] retained homogenised elements in the matrix and did not allow partitioning after heat treatment, while the slow furnace cooling during the stress relief of the intersections could have reset the initial lattice size.

Inter-pass rolling changes the microstructure significantly, as shown in Figure 59 (b). The stress-free lattice parameter however did not change within the resolution of ENGIN-X, suggesting a comparable composition in the α-phase, regardless of the reduced α-plate size and reorientation. Hence rolling did not influence the composition (i.e. partitioning) at identical thermal histories. The argument is supported by the similar appearance of the HAZ (Figure 59 (a, b), which is evidence for a similar thermal cycle.

Furthermore, rolling did not make any significant difference to the final residual stress state. Hence the thermal history must have been dominant. However rolling had a positive impact on the material texture, reducing the preferred orientation and allowing the detection of all hcp planes during the neutron measurements, so exploiting the potential of the white beam at ENGIN-X.

3.4.2 Stress Development in intersections

In comparison to previous work, where the longitudinal residual stress in a single free-standing Ti–6Al–4V WAAM wall reached 500 MPa [114]–[116], [141], the residual stress

in the intersection was, at 200 MPa, significantly lower. Two reasons could be that the total longitudinal (and transverse) length of the wall was 150 mm, which is shorter than the samples reported in the literature or finish machining might have released tensile residual stresses. A third reason could be the oscillating path strategy, which has a comparably high energy input per unit length, resulting in a higher component temperature and smaller temperature gradient. A final explanation could be the self-stress-relieving nature of intersections, determined by the path strategy and sequence of passes. Figure 64 illustrates the residual stress development during the deposition of a single intersection layer, generated by three subsequent intersecting passes.

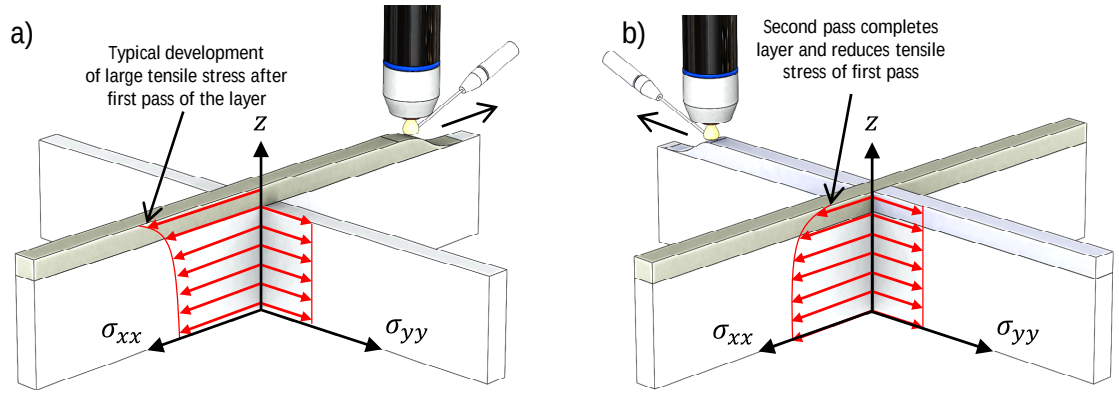

Figure 64: Longitudinal tensile residual stress development in additively manufactured intersections showing (a) the tensile stress build up in a deposit and its relieve (b), once the lateral pass is deposited.

The first pass of the continuous intersection layer presumably generates typical longitudinal tensile residual stresses (Figure 64 a). The following laterally-deposited pass completes the layer (Figure 64 b). Thermal shrinkage also results in the development of tensile residual stress in the longitudinal direction, but it also affects the previous deposition, as the through-thickness shrinkage of the second pass is constrained by the intersection. The through-thickness shrinkage of the second pass compresses the first pass longitudinally and therefore counteracts the previously developed tensile stress. The established residual stress profile along the additively manufactured intersection is therefore tensile in both directions and constant along the height, larger in the direction of the continuous wall, but still lower than in a free-standing wall. The steep drop in stress at the top in x-direction is therefore caused by the second pass in y-direction. A similar observation was made in simulations of intersections [39]. The stress profile in the normal direction is close to zero or slightly compressive, which averts development

of possible hydrostatic tensile stresses. The second and third gauge volume from the top of the inter-pass rolled specimen however do show low but potentially problematic hydrostatic tensile stress with a minimum of 100 MPa. This is an effect that was also observed in rolling of free-standing single pass walls [111]. The residual stress profile as-deposited, which is strongly tensile in two directions and near zero or slightly compressive in the third direction can be thermally stress-relieved. The achieved residual stress of a little less than 100 MPa was still larger than expected [185] using the stress relieving temperature of 650 °C, hence little residual distortion after unclamping was observed. A higher stress relieving temperature would further reduce the stresses [185] but could involve a microstructural modification at and above 700 °C.

3.4.3 Contour Method

The contour method is normally performed on a free-standing specimen without superimposed external clamping loads. When post-processing the topography of a contour surface, the net-stress on that cross section is assumed to be zero. However, in the present study the substrate remained clamped onto the backing bar, maintaining significant clamping loads in the specimen, so the cross-sectional residual stress was not self-balanced. The zero-stress assumption for the contour method is therefore no longer valid. Figure 65 shows the comparison of the neutron diffraction results with the equivalent profile taken from the contour stress map. The difference originates from the contour cut traversing through the unbalanced stress field: neutron diffraction measurement show large tensile stresses along the height of the specimen (Figure 62 (a, b)), as is also known for the clamped condition in single pass walls [119], [141]. The relatively large area on both sides from that location is expected to contain very little stress normal to the cut surface, as this stress represents the through-thickness stress of the lateral deposits. The backing bar in turn must contain balancing compressive stresses. As the contour cut propagates in a negative z-direction through the specimen, tensile stressed material is removed continuously, which in turn reduces the balancing compressive stresses in the substrate. Once the contour cut has passed through the entire cross section of the specimen, the tensile stresses on the y-z plane are removed and the backing bar will no longer carry a balancing compressive stress.

Based on the incomplete cut through one component of the assembly two explanations for the deviation from the CM to ND are possible, as follows.

The balancing stresses in the backing bar are responsible for the discrepancy between the neutron and contour results, as they offset the contour cut surface from the net-zero assumption. This offset decreases continuously as the contour cut propagates until it reaches the interface between specimen and backing bar. Comparing the stresses obtained by the two methods from the as-deposited and the inter-pass rolled specimen in Figure 65 (a, b) shows the continuously decreasing mismatch from the top of the specimen to the interface.

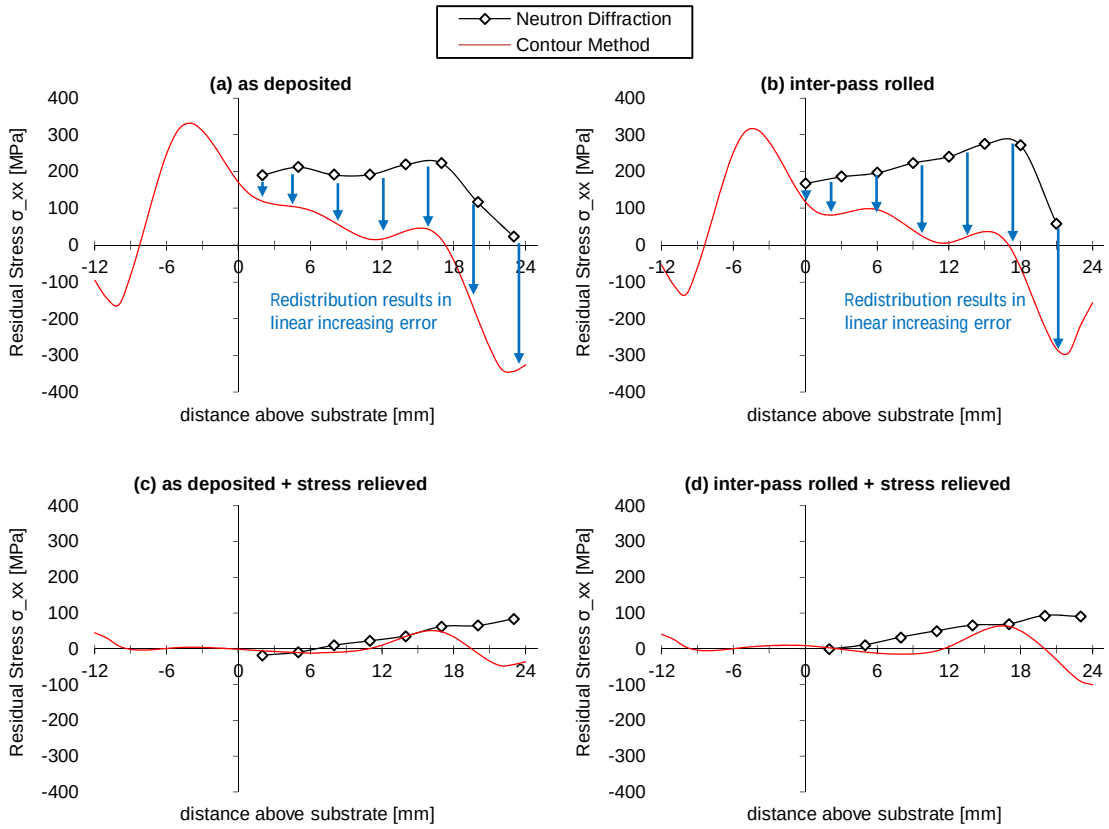

Figure 65: Comparison of the neutron diffraction experiment of the as-deposited (a) and inter-pass rolled specimen (b) and both after stress relieving (c, d).

Figuratively, performing the contour cut on the clamped specimen is effectively continuously unclamping it and therefore suggests a stress-profile that appears like the profile of an unclamped wall compared to a clamped wall (Chapter 2.1). Furthermore the zero stress assumption is not valid in any case and requires post-processing for a better understanding. The difference in the stress-relieved specimen between CM and

ND Figure 65 (c, d) is smaller, because the EDM cutting error would be reduced by stress relieving. The slight waviness in the stress plots taken from the contour method can be attributed to the spline fit, as half the wavelength is equivalent to the knot spacing in the spline fit. Plasticity has been reported to play a role when the stresses are either above or close to the material yield strength, however with a typical longitudinal yield strength of 850 MPa [139] plasticity is not expected to be an issue. Nevertheless, comparing the as-deposited and inter-pass rolled contour maps (Figure 63 (a, b)) shows that rolling did not influence the residual stresses and the location of most critical stress can be identified with confidence at the root of the deposit, and especially at the intersection. Finally the stress-relieved contour maps suggest a successful stress relief without any stress gradients (Q.E.D) and agrees with the neutron diffraction results.

3.5 Conclusions

In this study the effect of vertical inter-pass rolling and thermal stress relieving on Ti–6Al–4V intersections produced by Wire + Arc Additive Manufacturing has been investigated. We have demonstrated that:

1. The as-deposited material shows a strong crystallographic texture, which is eliminated by inter-pass rolling. As deposited, only the {1011} and {1013} planes diffract consistently neutrons in all three assumed principal directions in Ti–6Al–4V WAAM. As a consequence Pawley refinement is unsuitable for stress calculation. It only becomes suitable when the texture is eliminated and the prior-β grains are significantly refined.
2. Biaxial residual stresses were found in the centre of the intersections instead of a triaxial stress state, hence thermal stress-relieving significantly reduced the residual stress. The inter-pass rolled intersection contained low hydrostatic stress below the plastically deformed region of the last rolling step, but it did not limit the thermal stress relieving at this location.
3. The residual stress in the intersections is tensile in the longitudinal directions of both walls and constant along the height. The stress in the continuously deposited wall is higher than in the discontinuous one. After the first and

continuous deposition of the intersection, the subsequent transverse deposit, which completes the layer, diminishes the residual stress of the previous deposit. Normal stresses are relatively constant along the wall height as well, but compressive.

4. The zero-stress assumption for the contour method is not valid in this unbalanced stress field and requires post-processing. Nevertheless the contour method results reveal qualitatively the regions of large stresses and gradients in as-deposited intersections and furthermore suggest that thermal stress relieving can eliminate residual stresses in AM intersections entirely.

Since the thermal cycle and consequent development of tensile stresses can exceed the effective depth of the stress manipulation by rolling, different strategies, other than vertical inter-pass rolling must be investigated. The following chapter 4 will discuss the effect of side rolling. Chapter 5 will proof the effectiveness of machine hammer peening (MHP) to control residual stresses and the microstructure in Ti–6Al–4V WAA

Chapter 4 Residual Stress and Distortion Control by Side-Rolling

Parts of the content of this chapter was published in the conference proceedings of the 10th International Conference on Residual Stresses in Sydney 2016 [141].

4.1 Introduction

The literature showed the limitations of vertical inter-pass rolling to control RS & D (section 1.6.2.1), which is due to the lack of lateral restraint [111]. Intersections are their own inherent lateral restraint, but inter-pass rolling was virtually without any effect in the previous chapter on the residual stress. This chapter addresses therefore the limitations of vertical. Colegrove et al. [111] prevented undesired lateral deformation by the use of a "slotted roller". There was a greater improvement on the distortion compared to other roller geometries that did not restrain the deposit laterally. However, the use of the slotted roller is very cumbersome, time consuming and limited. It only works with a constant wall width, it is prone to jamming, cannot be applied to curved or inclined walls.

The concept of the pinch-rolling involves rolling the wall from both sides and it will avoid some of the limitations of the slotted roller. This would be a similar approach to the one already applied by Xie et al. [191]. Pinch rolling would prevent the lateral deformation and keep the rolling forces within the tool instead of the entire frame and manipulator. Before developing such a tool, the existing vertical rolling equipment will be used to roll on one side of the wall as a preliminary study. The effect of side rolling a Ti–6Al–4V single-path WAAM part on the RS & D will be presented in this chapter and compared to literature on vertical rolling.

4.2 Methodology

4.2.1 Sample production

Nine specimen walls were built using the setup in Figure 66 (a) of which eight were side rolled after the entire wall was built using different parameters. The ninth specimen was the control, which was measured in two variants, before and after unclamping. An EWM

plasma power supply was used to deposit the 1.2 mm Ti–6Al–4V wire on a clamped 7 mm thick substrate. Twenty layers of approximately 1.1 mm height and 5.8 mm width were built with 150 A and 10 l/min and 1 l/min plasma and shielding gas flow rates. The current for the first five layers was increased by 10 % to compensate for the heat sink effect of the substrate. Travel speed and work piece distance were kept constant at 7 mm/s and 8 mm respectively. The actual width and height of each layer was measured using a height gauge and a calliper. After the final layer, the wall remained clamped on the aluminium backing bar and cooled to room temperature for cold side-rolling.

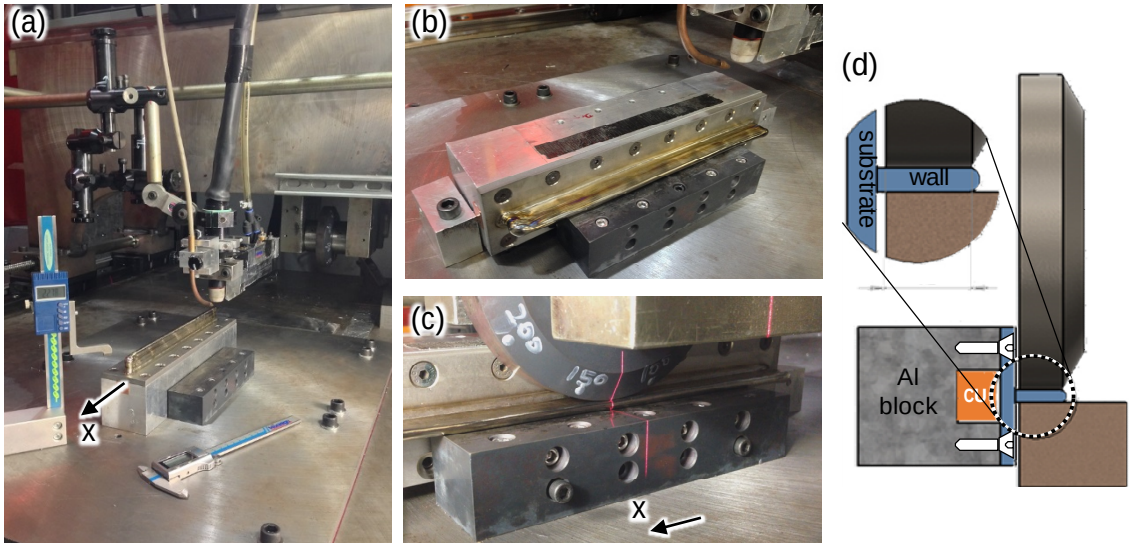

Figure 66: (a) setup during the deposition; (b) clamped specimen turned by 90° and beared with one side on a tool steel block; (c) a laser line indicates roller axis and contact point with the wall; (d) schematic front view

The specimens were turned by 90°, so that one side of the deposit evenly rested on a tool steel block, as shown in Figure 66 (b). A hydraulic cylinder was used to roll both sides of four specimens along the centre 200 mm length with loads of 100 kN, 130 kN, 160 kN and 190 kN using a 150 mm diameter roller (Figure 66 (c)). The roller width of 20 mm was in contact with the entire wall height (Figure 66 (d)). The same procedure was repeated with the four remaining samples using a 200 mm diameter roller. After unclamping, the height gauge was used again to measure the out-of-plane distortion D of the substrate of the unclamped sample in the xz-plane, as shown in Figure 67.

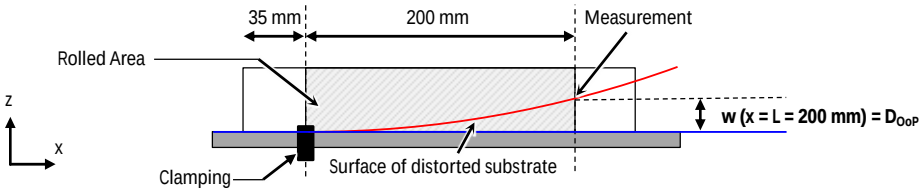

Figure 67: Schematic of the measurement of the out-of-plane distortion D.

4.2.2 Neutron Diffraction

Neutron Diffraction strain analysis was carried out at the ENGIN_X instrument at ISIS Rutherford Appleton Laboratory in Didcot/UK. Ten gauge volumes along the vertical centreline (Figure 68 (a) and (b)) of 2 x 2 x 2 mm each were exposed to the monochromatic beam for 40 µA counting time. The diffraction pattern appeared with the same anisotropy as the unrolled intersection from the previous chapter 3, due to comparable texture and methodology. Therefore only the $\{1013\}_\alpha$ and $\{1011\}_\alpha$ planes yielded diffraction patterns in all three directions, which were finally fitted individually to determine their d-spacing. The strain was calculated using eq. (31) with the stress-free d_0, which was determined separately for this study. Residual stresses were calculated using Hooks law (eq. (32)) with the following measured stress-free lattice spacings: $d_{0,103}$ = 1.3253 Å and $d_{0,101}$ = 2.2238 Å. The longitudinal residual stresses calculated from both planes agreed well with each other and were averaged to find the final stress.

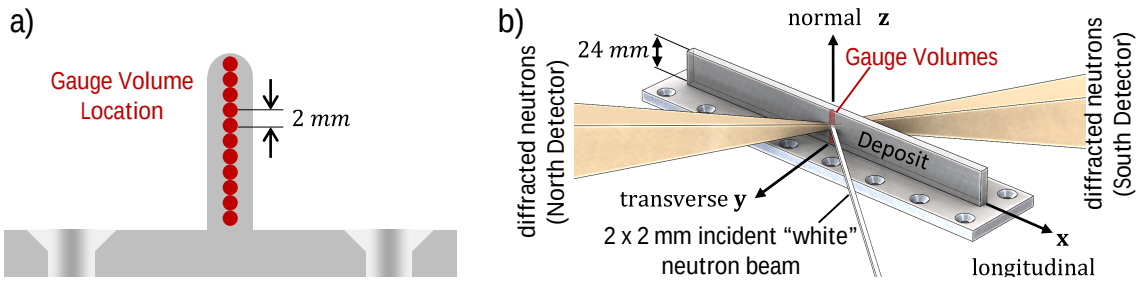

Figure 68: (a) location of gauge volumes and hardness plot line (b) setup of ND experiment on ENGIN-X

4.2.3 Contour Method

Afterwards, the contour method was employed on the same specimens at the University of Manchester to generate a stress map on the longitudinal yz-plane in the centre of the sample. The post-processing and the methodology was produced by Roy [237].

The specimens were cut by EDM, with a 250 µm diameter hard brass wire, on an Agie-Charmilles FI440CCS CNC Wire EDM machine using slightly modified 'E2' finish cut parameters for titanium. With these cutting parameters, constant cutting power was employed whilst the machine controlled the speed to maintain this cutting power. The EDM wire encountered the 'top' or the topmost bead first, and passed through baseplate of the specimen last where the mounting holes are located. The wire either sped up or slowed down when navigating the different cut widths; the cut proceeded relatively fast through the deposit compared to the baseplate. Note that the fixture restrained the component rigidly in all directions and accommodated distortion in all directions. Once the cut had been completed, the specimen was scanned with a Nanofocus µScan laser profilometer, with a resolution of 30 by 30 µm. The principal direction of scanning was from top to the baseplate, which is the y-direction in the subsequent images. The two unregistered point clouds (Figure 69 (a) and (b)) were aligned and averaged to remove non symmetric errors and shear effects (Figure 69 (c)). Figure 69 (d) shows an example of the averaged height of the symmetry line.

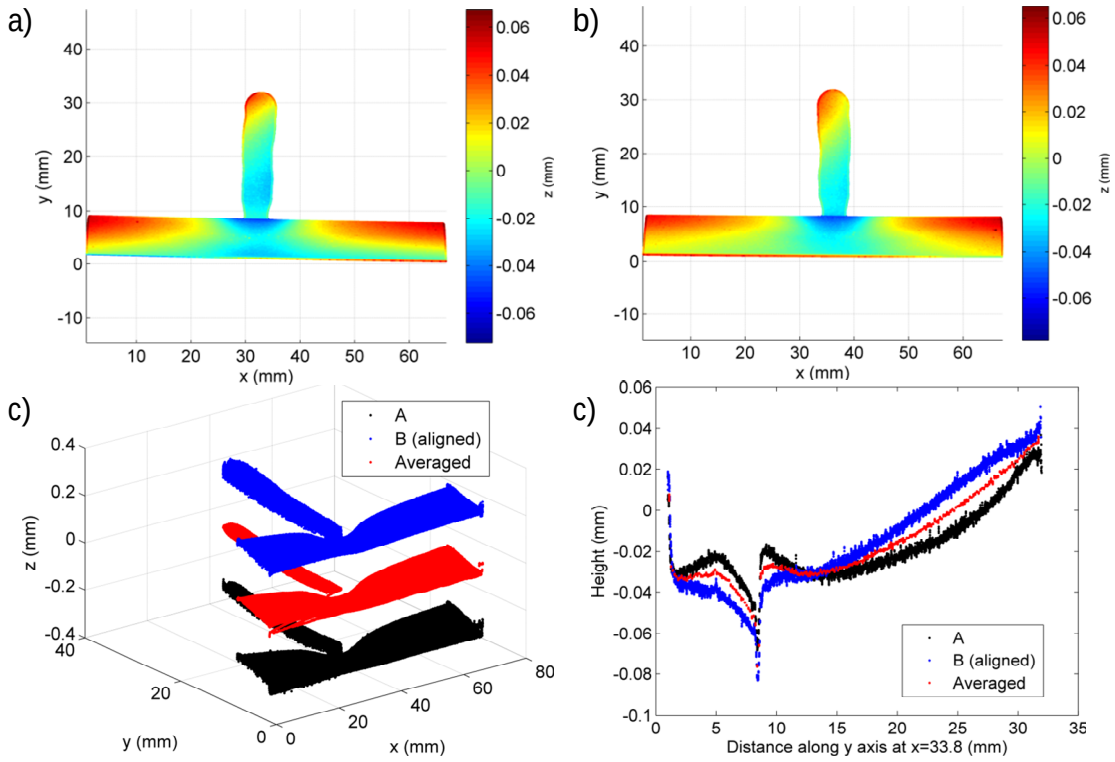

Figure 69: (a, b) Laser scans for each side of the control specimen. (c) Surface and (d) symmetry line displacements after averaging

Spline fitting was then applied to the averaged surface. Preliminary results were generated by a Fast-Fourier algorithm which sought to optimize knot spacing according to the 'noise' found in the surface. The fitting statistics/error are as follows: a standard deviation of 1.89 µm, a range of 51.90 µm and a root mean square error equivalent to the standard deviation. Note that this corresponds to mean knot spacing of approximately 1.5 mm, and was imposed to avoid some of the plastically affected region at the tail end of cut.

After compressive stresses were found with this algorithm, a revised/recently developed algorithm that permits fixed knot spacing was implemented. Figure 70 (b-f) shows the five different spline fits for different knot spacings chosen, which affect the residual stress calculation. A small knot spacing will converge precisely to the measured surface including all artefacts. A large knot spacing will smooth the residual stress result and smear artefacts out. Once the spline was defined, the outline was seeded with 300 nodes equidistant along the perimeter of the component. This was accomplished by solving for the path integral around the periphery, and respacing line segments equally along the perimeter.

The result was then output as a drawing exchange format file, which was then imported into Abaqus. A 3D mesh was extruded from the 2D profile, 50 mm along the z-direction, with 20 seeds geometrically distributed, with the spacing of the first seed equal to the mean line segment contained in the imported drawing exchange format file. Figure 70 (a) shows the finite element mesh of the cross section with substrate and deposit and the location of the averaged data and spline fits. This rendered a mesh with 148,242 nodes defining 33,500 C3D20 elements. Displacement boundary conditions on the front face of the mesh were imposed directly as defined by the fitted spline as well as to prevent rigid body movement. These rigid body boundary conditions were applied which restricted all movement in the 2nd degree of freedom (y-direction) on one corner of the baseplate, and restricted all movement in the 1st and 2nd degrees of freedom (x- and y-directions). This characteristic mesh was employed for all components and spline combinations. Elastic material properties imposed throughout were a modulus of elasticity of 113.8 GPa and Poisson's ratio of 0.342.

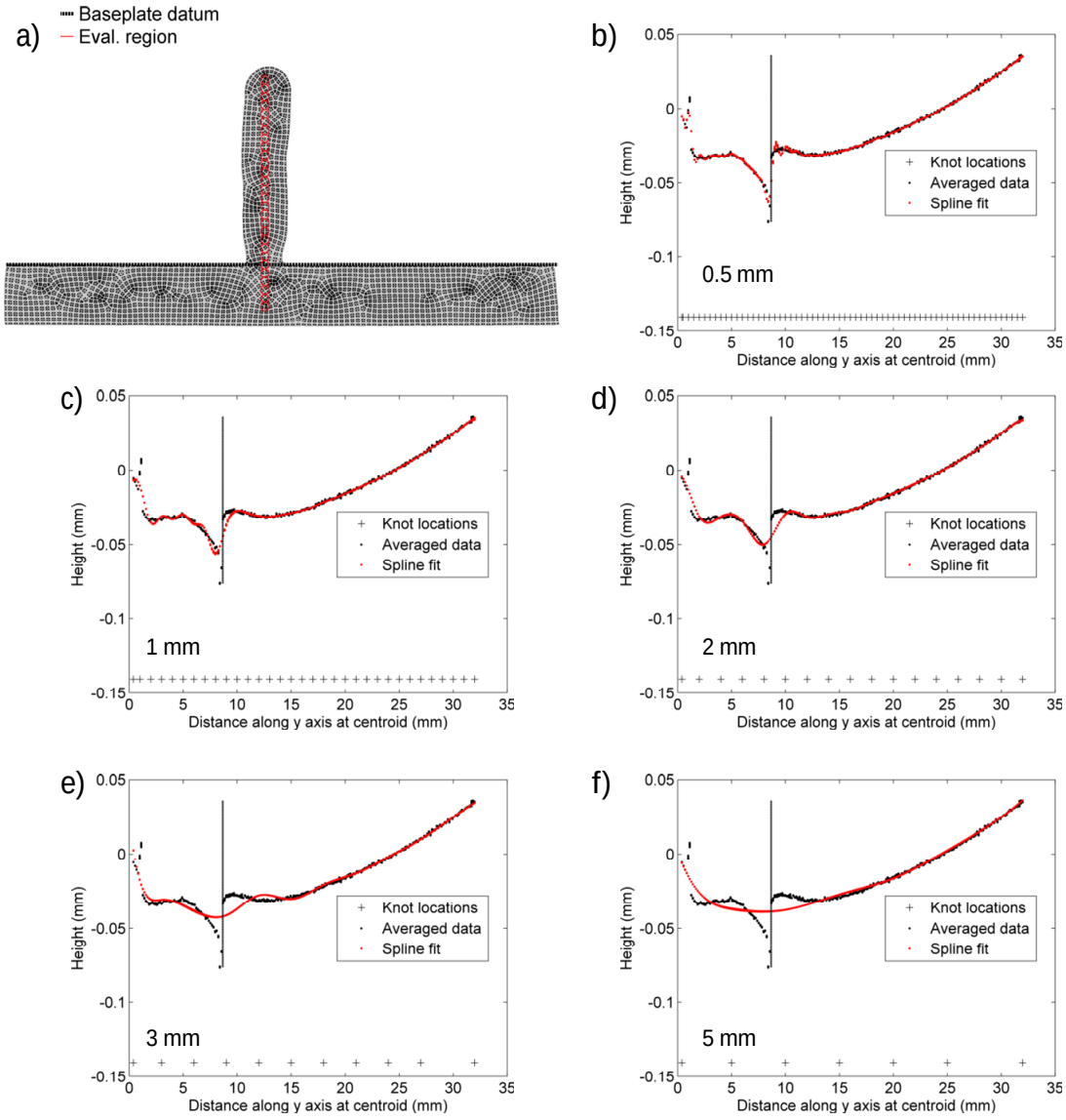

Figure 70: (a) FE mesh and plot location of spline fits of the averaged data using (b) 0.5 mm, (c) 1 mm, (d) 2 mm, (e) 3 mm and (f) 5 mm knot spacing

4.2.4 Microstructure

Optical microstructural analysis was performed on the surface of the contour cut at the location of the neutron gauge on the as-deposited and the inter-pass-rolled specimens. Conventional sample preparation including grinding, polishing and etching with hydrofluoric acid exposed the microstructure, which was then analysed using an optical microscope with 50 x magnification.

4.3 Results

4.3.1 Layer dimensions

The measured layer width for each specimen is shown in Figure 71, which are the widths of each layer just after their deposition. The legend shows the load used for rolling this particular wall. The bottom four layers were less wide due to the heat sink effect, despite the applied current compensation.

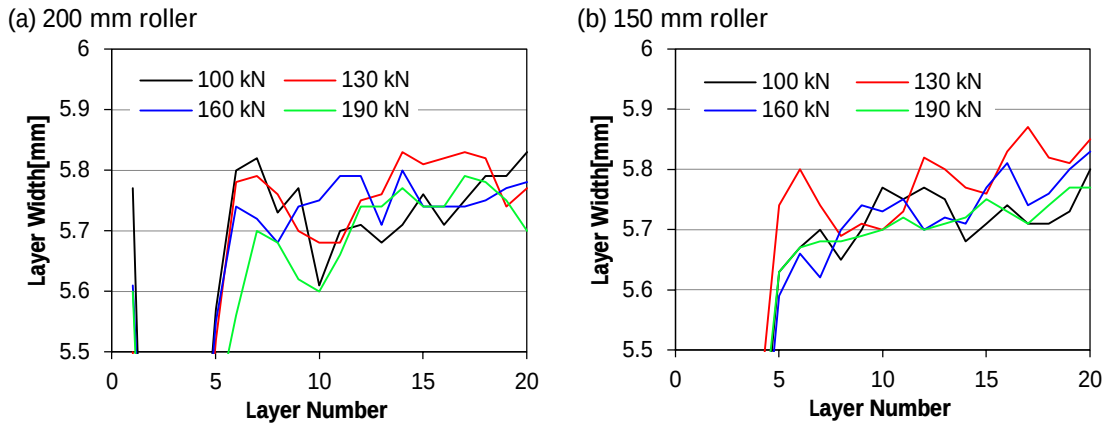

Figure 71: Layer widths of the specimen used for rolling with (a) the 200 mm roller and (b) the 150 mm roller

Starting from layer 5, the layer width ranged roughly between 5.6 mm and 5.8 mm. The average layer width and height was taken from layer 5 to 20 and is shown in Figure 72, where the standard deviation, which was never more than 66 µm, is indicated in form of the error bars.

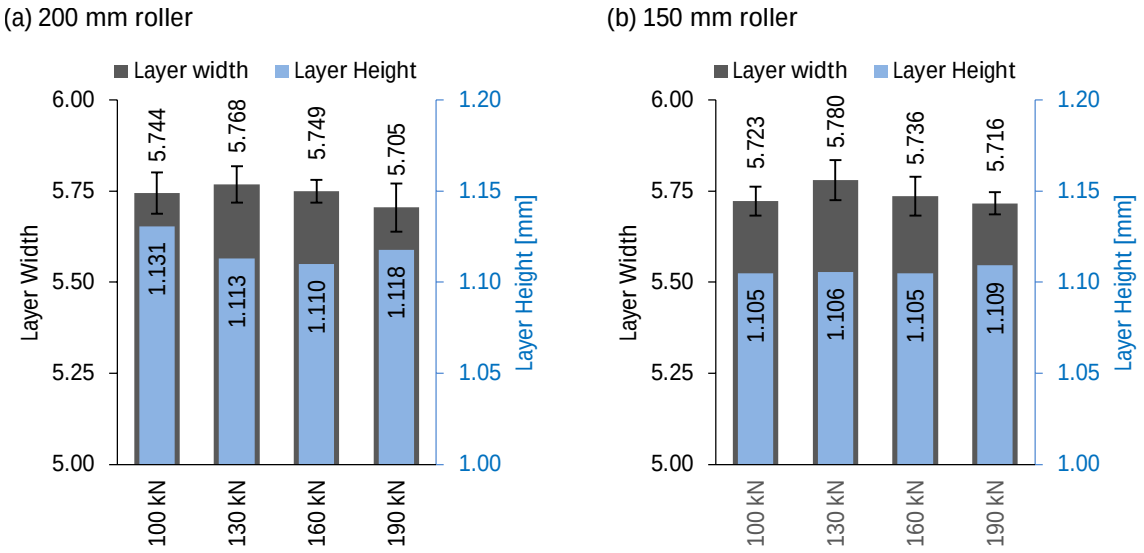

Figure 72: Average layer width and height during the deposition of the specimen used for rolling with (a) the 200 mm roller and (b) the 150 mm roller

The average layer height was the total height divided by the layer number and does therefore have no standard deviation.

4.3.2 Distortion

The out-of-Plane distortion of the substrate of the unclamped control sample was 6.8 mm, which is comparable to what has been found before [115]. The reduction after side rolling is plotted in Figure 73.

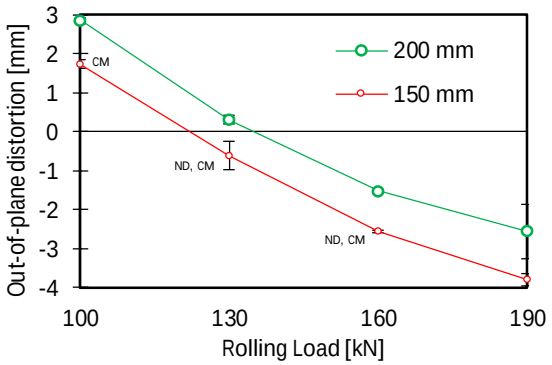

Figure 73: Out-of-Plane Distortion of the substrate after rolling with a small and a big roller with different loads; the residual stress of the indicated specimen were measured using neutron diffraction (ND) and the contour method (CM).

Side rolling shows a greater reduction in distortion with increasing rolling loads and decreasing roller diameter. For both rollers, the distortion closest to zero has been achieved using 130 kN load. The result suggests that ~85%...90% of the rolling load applied by the bigger roller achieves comparable results when using the smaller roller. Forces higher than 130 kN even resulted in negative distortion.

4.3.3 Residual Stress

4.3.3.1 Contour Method

Figure 74 shows the residual stress maps of the control specimen in the unclamped and distorted condition using knot spacings from 0.5 mm to 5 mm (a-e). The stress profile was taken from the centre line of the corresponding stress map. With a knot spacing of 0.5 mm a suspicious compressive region can be found just above the interface between wall and substrate. This compression artefact diminishes and traverses upwards with increasing knot spacing until it disappears with the 5 mm knot spacing. The stress profiles above 10 mm are not affected by variations.

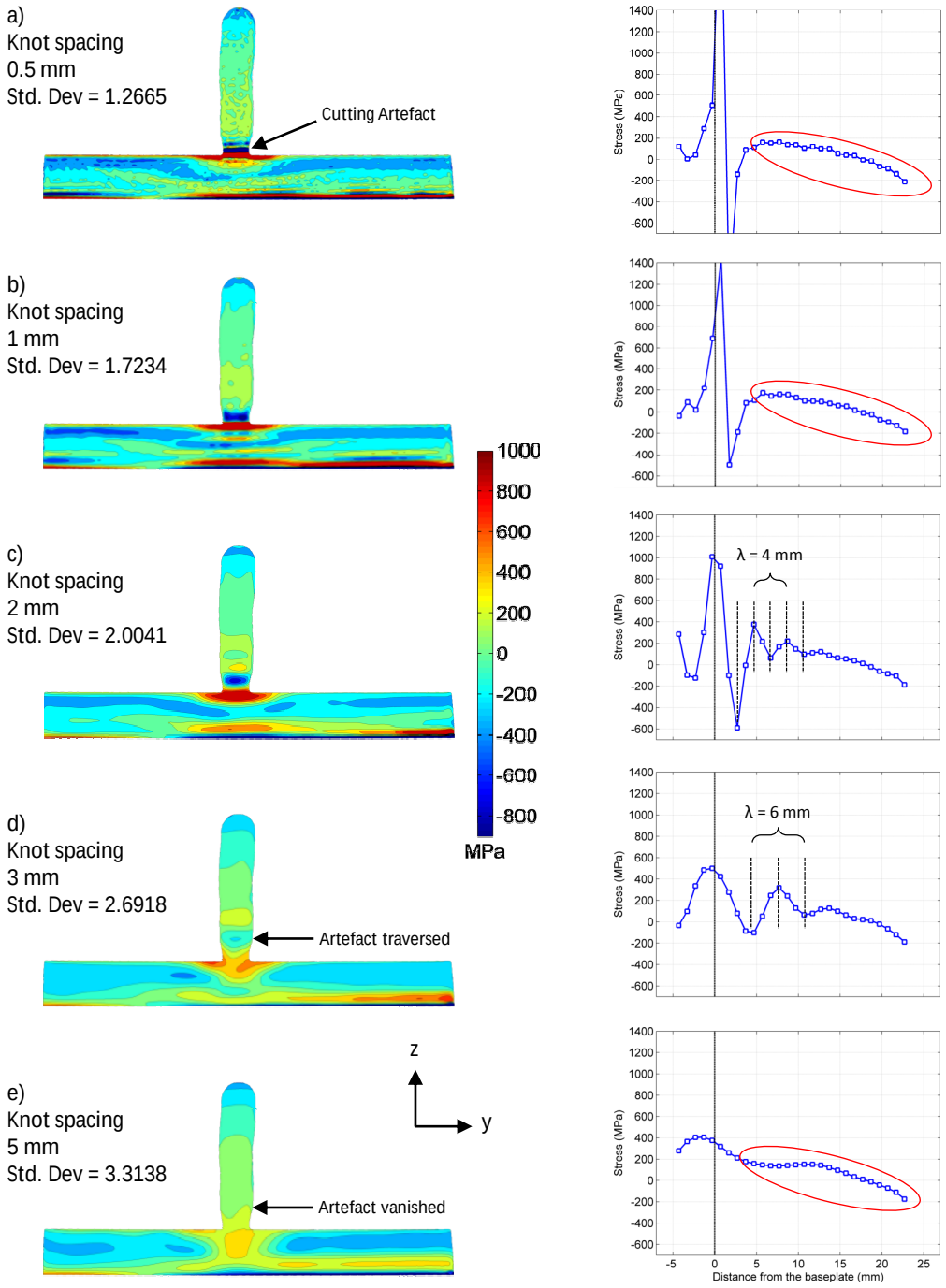

Figure 74: Longitudinal residual stress maps (σ_{xx}) and profiles along the centreline for (a) 0.5 mm, (b) 1 mm, (c) 2 mm, (d) 3 mm and (e) 5 mm knot spacing.

Figure 75 (a) shows the control sample stress map with 2 mm knot spacing. Stress gradients are eminent in z-direction, but less in the traverse y-direction. Figure 75 (b-d) show the same adjustment (2 mm) for the side-rolled specimen using the 150 mm roller at 100 kN, 130 kN and 160 kN respectively. The stress gradients appear less in z-direction, but y-gradients do appear in the wall. All four maps show evidence of the

cutting artefact near the interface. It should be noted, that the control sample was the one with 7 mm out-of-plane distortion of the substrate, while the other three specimens had significantly reduced distortion (Figure 73).

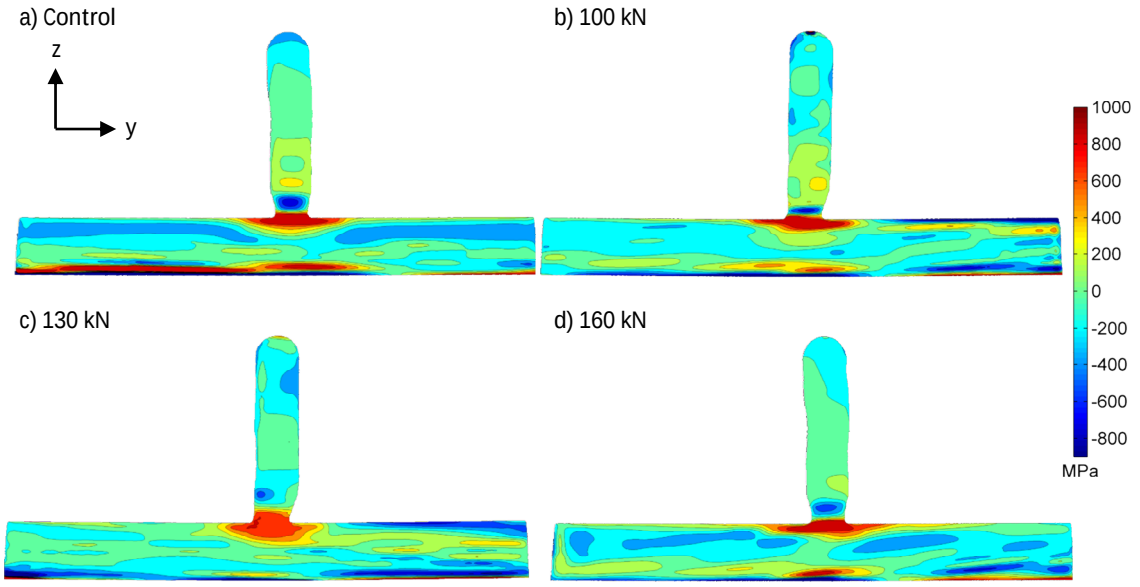

Figure 75: Longitudinal residual stress maps (σ_{xx}) using 2 mm knot spacing of (a) the unclamped control sample and the rolled samples using the 150 mm roller at (b) 100 kN, (c) 130 kN and (d) 160 kN.

4.3.3.2 Neutron Diffraction

Figure 76 compares the neutron diffraction results with the contour method results of 2 mm knot spacing. The interface region contains artefacts and are hence not shown. Figure 76 a) shows the longitudinal residual stress profiles above the substrate while the specimen remained clamped. While still clamped, the residual stress of the unrolled control sample along the centre line is fairly constant at around 550 MPa, which is significantly lower than the yield strength (~850 MPa). This constant tensile stress has only been previously reported with a numerical simulation in mild steel WAAM walls [119]. After unclamping, the profile shows a constant drop of residual stress with increasing distance to the substrate and is slightly compressive in the top four layers. This trend is also supported by the numerical simulation [119] and measurements from other investigators [111], [115], [116]. The residual stress of 550 MPa is equivalent to 4780 µm/m, which requires a longitudinal plastic stretch of 0.97 mm for mismatch elimination with the substrate. Figure 76 b) and c) shows the plots using 130 kN and 160 kN respectively. Side Rolling affected the specimen from approximately 4.5 mm

above the substrate to the top of the wall. In this region, tensile residual stresses were reduced significantly, due to the imposed plastic deformation and longitudinal stretch. The peak stress in both dropped from 550 MPa to between -200 to +200 MPa. This ultimately was the reason for the successful reduction of distortion. Prior to rolling, the contact surface of the wall was uneven, varying by ± 0.05 mm over the nominal width of 5.7 mm. Therefore, the roller imposed non-uniform strain across the wall height. In particular, near the surface where the wall was wider, higher compressive stress can be observed. In all three plots, the neutron diffraction measurements agree well with those obtained from the contour method.

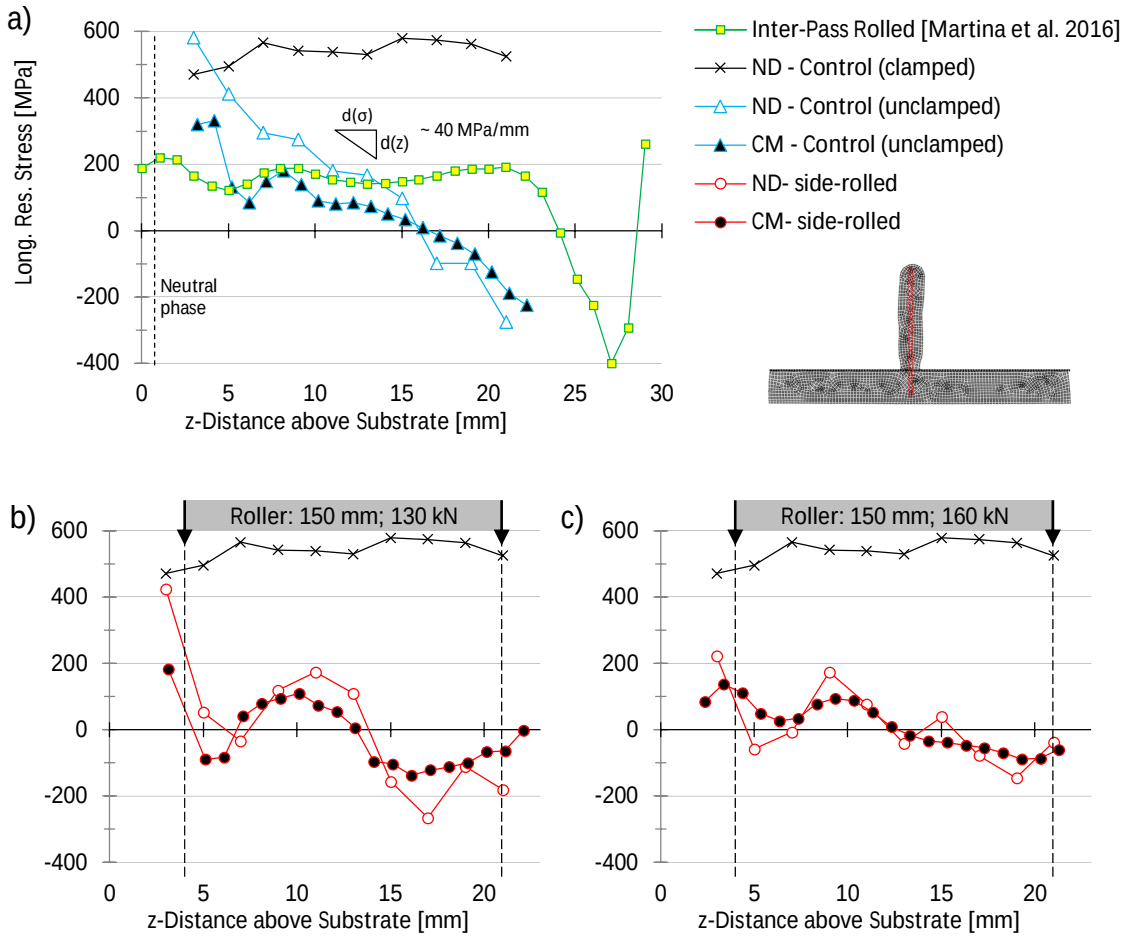

Figure 76: Comparison of longitudinal residual stress measurements using neutron diffraction (ND) and the contour method (CM) clamped and unclamped control: (a) as deposited stress redistribution compared to vertical inter-pass rolling from [115] and residual stress after side rolling using the 150 mm roller with (b) 130 kN and (c) 160 kN load (The dashed lines indicate the roller location).

4.3.4 Wall geometry

Figure 77 shows the wall geometries with the microstructure of the cross section taken from the specimen rolled with the 150 mm roller after the contour cut. The cross section of the control sample shows that even though each layer had a constant geometry, the entire wall was slightly curved due to inaccurate positioning of the torch during deposition. The specimens after rolling appear straighter, but that was also the case before the cold work. The microstructure in all four cross sections are virtually identical. Cold rolling after deposition did not result in grain refinement, since there was no subsequent heat treatment.

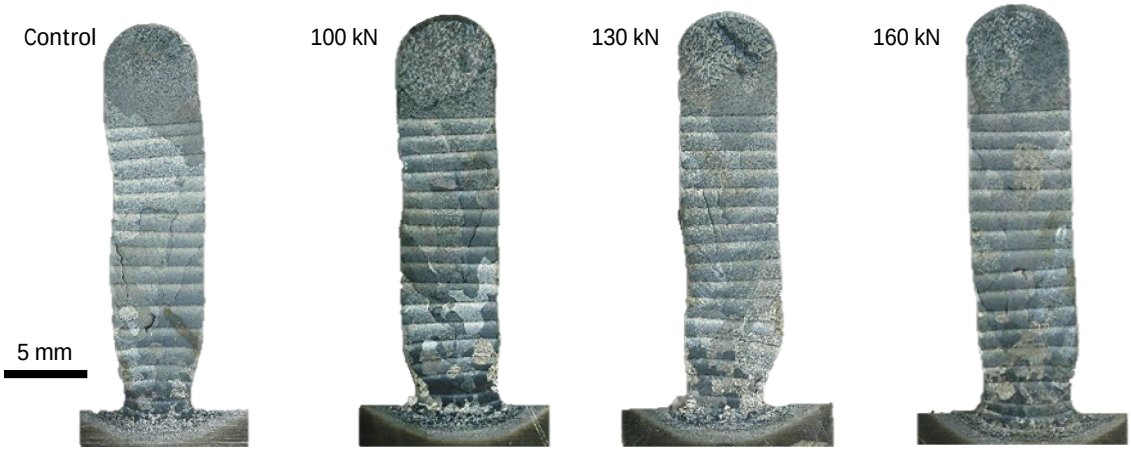

Figure 77: Cross section and microstructure on the contour surface of the samples rolled with 150 mm diameter.

4.4 Discussion

Before discussing the residual stresses results, the accuracy of both measurement techniques, neutron diffraction and the contour method, need to be evaluated.

4.4.1 Measurement Accuracy

4.4.1.1 Contour Method

Instant changes in cutting length of EDM wire through specimen at otherwise constant parameters produces cutting artefacts. When the cutting length increases at constant discharge energy per unit length there will be less removal of material, which results in narrower cutting width. A cutting artefact is irreversible and difficult to account for during post-processing and must therefore be avoided. The use of sacrificial material is one way to avoid artefacts caused by instant changes in cutting length [224]. However, its use also increases significantly the amount of work required to make the

measurement. In this chapter this issue was addressed by accommodating the travel speed when the cutting length changed at the transition from the deposit to the substrate. A classic cutting artefact on such a T-section would remove less material in the longer cutting length and therefore appear as if compressive stresses were relaxed, which is the opposite to what can be observed in this work. Figure 69 (a) and (b) show a clear discontinuity on the laser-scanned surfaces at the interface between deposit and substrate. It appears as if the cutting speed adjustment overcompensated the error so the slower travel speed has allowed the removal of more material and hence produced a deeper cut.

To an extent, this artefact can be removed with careful selection of the knot spacing of the spline fitting algorithm. The spline fitting did not eliminate the artefact as shown in Figure 74 (c) and (d). Instead, the resulting peak residual stress is reduced and it is shifted or diluted away from the interface with a half wavelength equal to the knot spacing. Very large knot spacings as were used in Figure 74 (e) and smear the artefacts out at the expense of the desired resolution. Very low knot spacings show the artefacts clearly at their actual location and do not falsify the surrounding stresses, which allows a more honest discussion of the results. This is a matter of taste, as contour maps are typically produced with a relatively high degree of smoothing. Due to the violent artefact in the interface and the high resolution required in the present study it would have been advisable to use a knot spacing of 1 mm. Figure 74 shows that knot spacings of 0.5 mm, 1 mm and 5 mm show a comparable stress profile in the rolled section of the deposit, while the knot spacings 2 mm and 3 mm drifted the artefacts into the rolled region. However, the high degree of smoothing of the 5 mm knot spacing eliminates the resolution, as no actual features can be resolved in the 5.8 mm wide wall.

The abrupt changes in cutting length are typical for additively deposited features on a substrate and adjusting the cutting parameters through the transition of cutting length did not eliminate cutting artefacts. Sacrificial material can resolve this problem, but there is a significant increase in the time and effort to make the measurements.

4.4.1.2 Neutron Diffraction

The microstructure of the control and the rolled specimen shows large columnar grains (Figure 77 (a-d)). The β grains are typically aligned with the {100} plane parallel normal to the build direction z, as discussed in the theory Chapter 2.3, reported in the literature [86] and shown in the previous measurements in Chapter 3. The present study showed the same anisotropic behaviour of peak intensity due to the similar β grain orientation. The residual stresses calculated from both, the {1011} and {1013} plane resulted in comparable stresses using their individual elastic constants. In all measurements of the residual stresses in longitudinal direction, both independent techniques agree in the calculated residual stresses, giving confidence in both.

4.4.2 As-Deposited RS & D

Figure 78 shows the comparison of the neutron diffraction results and the contour method plot with the prediction from the analytical model from chapter 2.1. The as deposited stress resulted in the predicted constant tensile residual stress profile along the wall height. The neutral axis of the T-section is 1 mm above the interface of the deposit with the substrate, which is just below the location of the lowest neutron diffraction gauge volume. The near-interface (-2 mm to 4 mm) artefact of the contour method are excluded from the results, hence the gap.

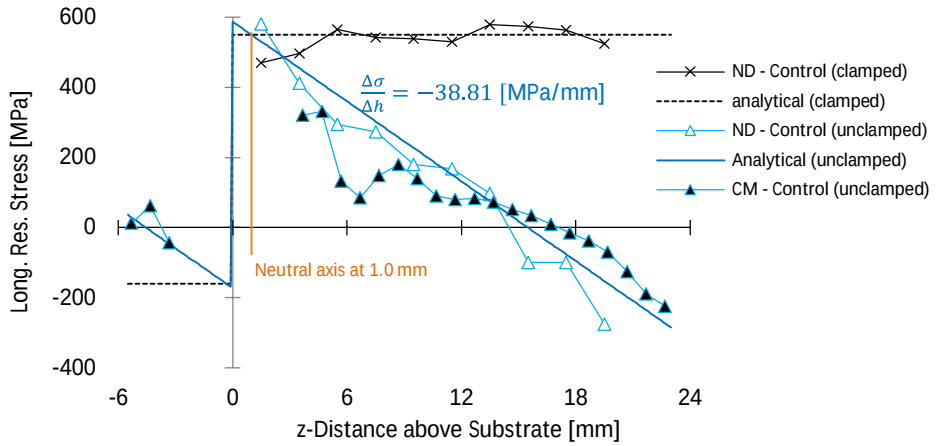

Figure 78: Comparison of longitudinal residual stresses using neutron diffraction (ND) and contour method (CM) with the analytical approach (AN) in the clamped and unclamped control.

The contour map of the unclamped control specimen does not show through thickness residual stress gradients (Figure 75 (a)). It is unlikely that there were any gradients

before unclamping. Unclamping resulted in distortion of 6.8 mm with a stress gradient of approximately -40 MPa/mm. The analytical model predicted 6.75 mm distortion and -38.81 MPa/mm stress gradient, which is in good agreement with both the measurements. The results not only agree with each other, but also match previous investigations using a TIG power source to produce the same geometry [113].

4.4.3 Effectiveness of Side Rolling

The singular side rolling was significantly more effective in eliminating RS & D compared to vertical inter-pass rolling. The dominant plastic strain of vertical rolling is known to be lost in the transverse direction of the wall due to the absence of lateral restraint. By rolling from the side, the plastic stretch was partially induced in the normal and longitudinal direction of the wall, of which the latter is responsible for the successful reduction in distortion. The contour maps of the rolled specimen show that no severe, but visible through thickness gradients of the longitudinal residual stresses were induced with side rolling (Figure 75 (b-d)). The reason is the large contact radius on the comparably thin wall width does not allow the development of a Hertz' pressure profile in the deposit under the contact line. Increased rolling loads resulted in more evenly distributed stresses through thickness, which stretched the wall more homogeneously. Using a 130 kN rolling load with the 150 mm diameter and 20 mm wide roller resulted in a virtually distortion-free specimen. The almost non-existent distortion of -0.61 mm upon unclamping supposedly redistributed the residual stresses by only +3.53 MPa/mm. However the contour method and neutron diffraction measurements reveal non-linear stress gradients along the wall height induced by rolling. The slight variations in wall widths along the height resulted in an unevenly distributed contact between the roller and the wall. This waviness is not due to the knot spacing, as the neutron diffraction measurements show this as well. More compressive strain was induced in the wider region of the wall (130 kN in Figure 71 (b)), where the roller touched the wall first between 5 mm and 7 mm and above 13 mm of the substrate (Figure 76 (b)). The 160 kN load using the same roller resulted in the maximum inverted distortion of -2.56 mm. This results in more compressive stress while clamped. Unclamping resulted in the balanced stress profile in Figure 76 (c) after an estimated redistribution of +14.75 MPa/mm. The

Figure 71 (b) shows that the width of the 160 kN wall was less wavy compared to the 130 kN wall before rolling, resulting in a slightly smoother stress profile (Figure 76 (c) compared to (b)). The residual stress in the other specimens were not measured, but the distortion measurements shown in Figure 73 show a consistent trend in all eight measured specimens. Increasing the load allowed the roller to penetrate the wall deeper (not measured), which resulted in more plastic longitudinal stretch and hence greater distortion reduction. The 150 mm diameter roller reduced the distortion by approximately 1 mm more than the 200 mm diameter roller for all four forces, due to higher contact pressure allowing more penetration and plastic stretch. In fact, comparing both plots of the distortion shows that approximately 85 % to 90 % of the load used with the larger diameter was required to achieve the same distortion using the smaller diameter. This agrees with the theory from chapter 2.2 that the required force ratio F_1/F_2 equals to the square root of the diameter ratio $(D_1/D_2)^{1/2}$, which is 86.6 % for the present combination.

Diameters smaller than 150 mm cannot be tested with this setup, as the bearing of the roller would collide with the specimen. However, a smaller roller diameter is probably even more effective. Not only is it easier to manipulate a smaller roller but it also has better accessibility closer to intersecting features or curvature, it also requires less contact force to achieve comparable reduction in distortion. The manipulation force was already concluded to be regardless the roller diameter and cannot be decreased (Appendix A) the certain stress reduction is required. Further reducing the diameter to 25 mm for example would in theory require “only” 51 kN side rolling load to eliminate distortion. However, side rolling is limited at reducing stresses close to the interface with the substrate, as it is difficult for the roller to reach that region and bottom layers are intended to be deposited wider than the actual wall. It should also be assessed whether very small roller diameters would induce through thickness stress gradients. It is also possible to decrease the roller width, which has a linear effect on the required force to induce the same longitudinal stretch. This would also overcome issues with varying wall width along the height. There is no evidence that suggest why a pinch rolling tool shouldn’t have the same effect as side rolling using identical forces and geometries.

4.5 Conclusions

The results from the study presented in this chapter show that:

1. Side rolling has the potential to eliminate longitudinal residual stresses and distortion in straight AM parts entirely after one rolling pass only. It is more effective than vertical rolling, which also has to be applied after each layer.
2. A smaller roller diameter is more effective at reducing distortion with the same rolling load. The effect can also be estimated analytically.
3. The longitudinal plastic stretch induced by a flat roller from the side on a WAAM wall is very sensitive the unevenness of the rolled surfaces' profile. Initial wall profile variation of only ±0.05 mm before side rolling can cause residual stress variations of approximately ±200 MPa.
4. The longitudinal tensile residual stress in the clamped condition proved to be constant along the height of the wall. This had only previously been shown using numerical simulations. The value of the constant stress was significantly lower than the material's yield value in a single path Ti–6Al–4V WAAM wall.
5. The contour method analysis of the T-shaped single WAAM wall is likely to be sensitive to EDM-cut artefacts caused by steep cutting length changes and plasticity effects. The only effective way of avoiding this artefact is using sacrificial material.

Even though side-rolling or pinch rolling can eliminate RS & D, the wall geometry used in this chapter was relatively small for WAAM features, which can reach wall widths up to 100 mm. Especially side rolling, but also pinch rolling would also be limited in the number of possible features to be treated, as the technique requires straight walls and accessible features. Machine hammer peening (MHP) tools can be manipulated with much more freedom compared to side or pinch rollers and could be used to treat less accessible regions in the component. Their effectiveness to manipulate RS & D will be investigated in chapter 5 and 6

Chapter 5 Assessment of Machine Hammer Peening as Alternative to Rolling

5.1 Introduction

One effect of inter-pass rolling on additively manufactured Ti–6Al–4V is the improvement of the microstructure in terms of grain refinement and thereby the elimination of anisotropy and increase in the material's strength. Another effect is reduction of the large residual stresses, caused by the process. However, rigid frames and tools are required to apply the large rolling loads, which significantly limit the degree of freedom of the otherwise open-frame WAAM process. Machine Hammer Peening (MHP) constitutes a potential alternative to rolling, since the tools are advertised as recoilless. The relatively light tools can easily be manipulated to any location of the deposit between each layer. The sole proof of concept was adduced on Ti–6Al–4V WAAM already [167], [168], but without any description of the tool characteristics or peening parameters. The present chapter addresses these gaps in three steps shown in the experimental flow chart in Figure 79.

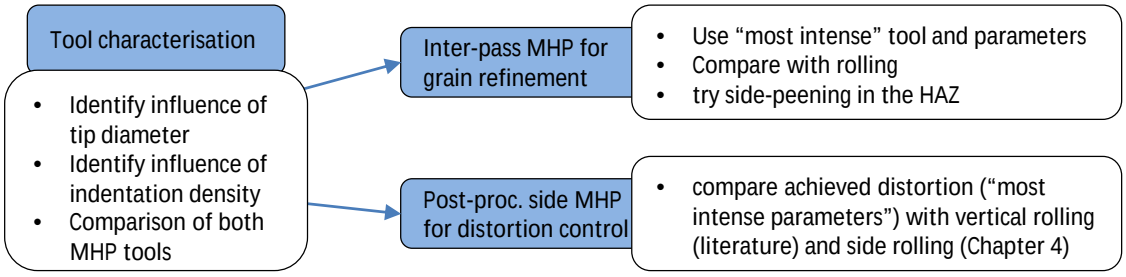

Figure 79: Experimental flow chart

First two different MHP tools are quantified and compared to assess the influence of peening parameters on the plastic deformation response of the surface of Ti–6Al–4V WAAM material. Then one of the tools was used in the typical inter-pass fashion to investigate the effectiveness of inter-pass MHP on the grain refinement. Here the conventional vertical inter-pass strategy was used, as well as inter-pass side MHP to exploit this capability. Finally MHP is used as a post-process, similar to side rolling from chapter 4 and on the same geometry for comparison, to show the effect on RS & D reduction. The typical generalised peening pattern variables are introduced in Figure 80:

The tool oscillates with a frequency *f* in z-direction and creates with the traverse speed *v* impacts at a distance *t* in the peening direction x with the impact energy *E*. The step distance *s* in y-direction completes the alternating peening pattern. Both tools used in this chapter can be described with this parameters. These tools are the pneumatic MHP prototype ForgeFix XP and the electromagnetic tool Accurapuls, introduced in the literature review.

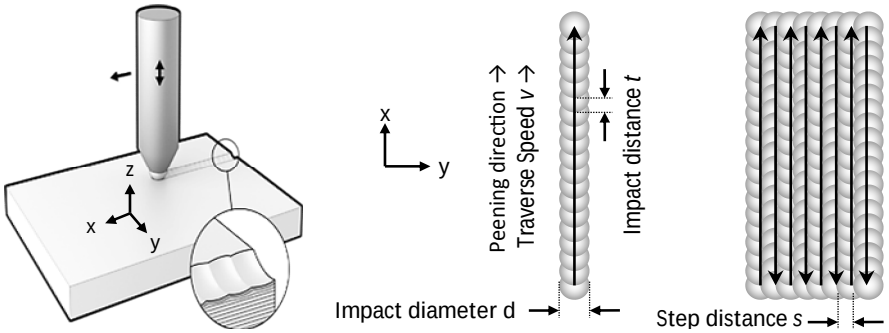

Figure 80: Peening path and pattern

5.2 Methodology

5.2.1 MHP Tool Characterisation

5.2.1.1 Production of WAAM material

For the production of bulk WAAM material, an EWM T552 Tetrix Plasma power supply was used to deposit Ti−6Al−4V wire on a 12 mm thick Ti−6Al−4V substrate.

Table 8: Welding Parameters

Current [A]	180
Wire Feed Speed [mm/s]	40
Travel Speed [mm/s]	6
Wire Diameter [mm]	1.2
Work Piece Distance [mm]	8
Plasma Gas Flow [l/min]	0.8
Shielding Gas Flow [l/min]	8

For each layer, four side by side parallel passes were deposited 4 mm apart using the parameters in Table 8, which resulted in 1.5 mm high and 20 mm wide layers at a deposition rate and heat input of 0.75 kg/h and 615 J/mm respectively. The plasma gas, shielding gas and the working environment in the tent chamber were all pure-shield argon (BOC). The latter was kept at a residual oxygen content between 200 and 600 ppm to prevent oxidisation [52]. After deposition, the wall typically contained large tensile

residual stresses [141], but removing the wall from the substrate relieved most of them. Final stress relieving for 4h at 650 °C in inert argon atmosphere provided stress free material. Nine blocks were then machined from the wall, numbered in ascending order, of which the end parts (#1 and #9) were disregarded to avoid end effects. The location of the 55 x 80 x 15 mm large specimens in the wall are shown in Figure 81. The ForgeFix XP was tested on specimen #6 and the Accurapuls on specimen #8. The other specimens were used in chapter 6 and for preliminary trials.

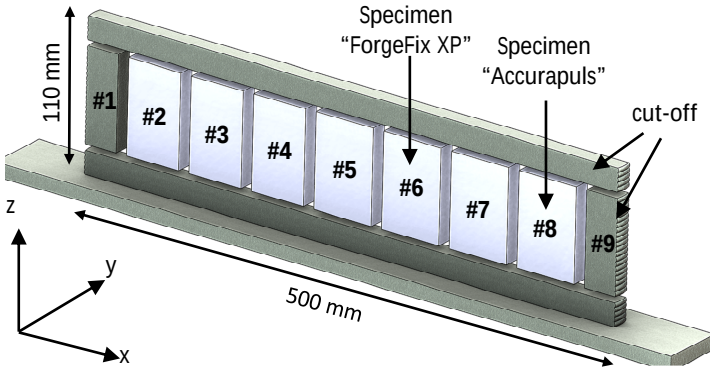

Figure 81: Position and extraction of the specimen from the 500 mm long and 110 mm high Ti–6Al–4V wall.

5.2.1.2 Machine Hammer Peening

Both specimens were peened on-site and by the MHP tool supplier. As shown in Figure 82 (a) the ForgeFix was mounted to the spindle of a Hermle CNC machine with internal air supply of 6 bar, allowing the full integration into the CNC program.

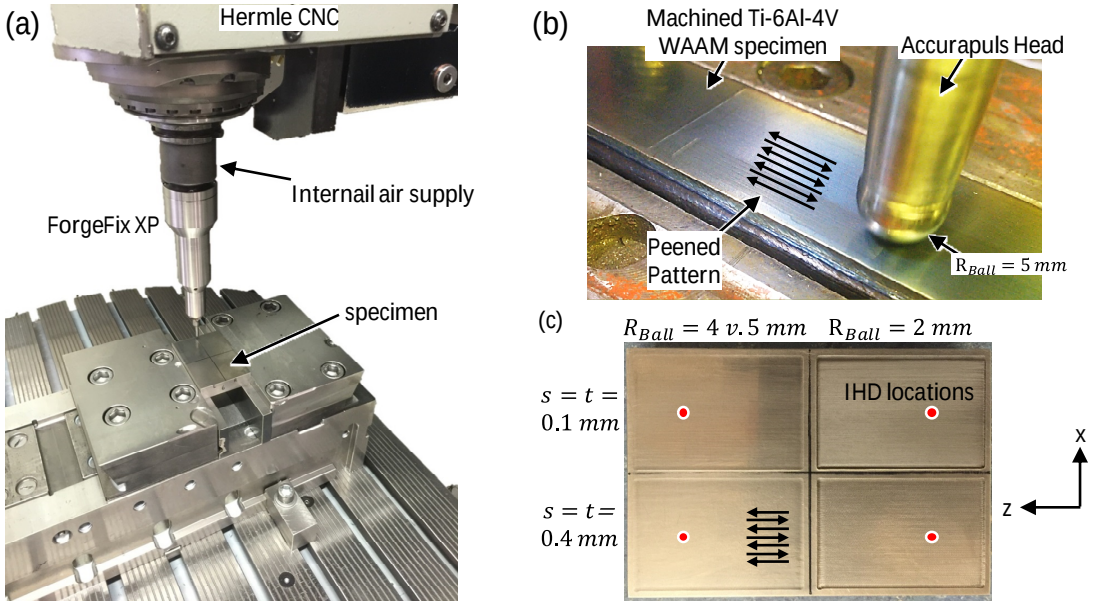

Figure 82: Setup the (a) ForgeFix and (b) Accurapuls MHP experiment; (c) MHP pattern, coordinate system in respect to the global ona and MHP parameters.

A large Mecof CNC machine was used to manipulate the Accurapuls (Figure 82 (b)), which was operated with an external controller unit that synchronised the tool and manipulator. Both tools were equipped with a spherical indenter of 2 mm radius, which were core-hardened tool steel and coated with tungsten carbide in the case of the Accurapuls. The ForgeFix also came with a 4 mm radius ball and the Accurapuls with a 5 mm radius ball. MHP produced rectangular areas (20 x 35 mm) with square impact pattern of 0.1 mm or 0.4 mm side length, controlled with step distance and travel speed. The locations of the four peening fields per specimen are shown with the peening direction in Figure 82 (c). The impact energies of both tools are unknown, but probably between 100 mJ and 200 mJ at a rough estimate.

5.2.1.3 Residual Stress Measurement

Residual stresses were measured with incremental hole drilling (HD) and the contour method (CM). HD involves the application of a strain gauge rosette on a surface and subsequent incremental drilling in the centre of the rosette (ASTM Standard E837). The strain caused by stress relaxation due to removed material is then measured with the strain gauges, which can be post-processed to the calculate the residual stresses prior to drilling. For the hole-drilling method EA-01-125RE-120 residual stress strain gauge rosettes were mounted on each pattern with the centre on the IHD location indicated

in Figure 82 (c). A 2.3 mm drill was used in eccentric mode to produce a 3.8 mm diameter and 2.8 mm deep drill holes with 8 µm increments to calculate the plane stress profile up to 2 mm deep.

The contour method was only applied on the ForgeFix Specimen #6 after the HD experiment. The sample was cut by EDM following the cutting path (red lines) shown in Figure 83 (a). Four self-restraint holes with a diameter of 3mm were manufactured through the centre of the features created by Hole Drill Method. Cutting sequence and direction are also labelled in Figure 83 (a). Once the cut had been completed, the surface was scanned and the data was averaged, as in the previous experiment in chapter 4. Figure 83 (b) shows the averaged displacement. The area around the holes was disregarded, as indicated by the dashed lines. The centre region was 5 mm away from the edge of the hole. Though this is not a precise method, it is believed that the residual stress distribution generated by the shot peening process should be uniform along the X direction and the residual stress near the surface is balanced by the stress downwards, rather than horizontally. Removing the data outside of the two holes is much easier to implement than re-meshing the refined averaged surface of the cutting surfaces (Figure 83 (c)). Spline fitting was applied to define the average surface, with the fitting error of 0.7095 µm, represented by the standard deviation. After surface spline fitting, the outline was seeded with 200 equal-spaced nodes along the perimeter. The spline surface was then meshed and extruded 28mm (Figure 83 (d)). Displacement boundary conditions on the meshed surface were set at the two bottom corners. The left bottom corner was locked in X and Y direction and right bottom corner was restrained in the Y direction. If the averaged surface was not cropped, significant displacement would be found at the two bottom corners, which would induce a large error when the boundary condition was applied there. Elastic material properties were imposed throughout with a modulus of elasticity of 113.8 GPa and Poisson's ratio of 0.342.

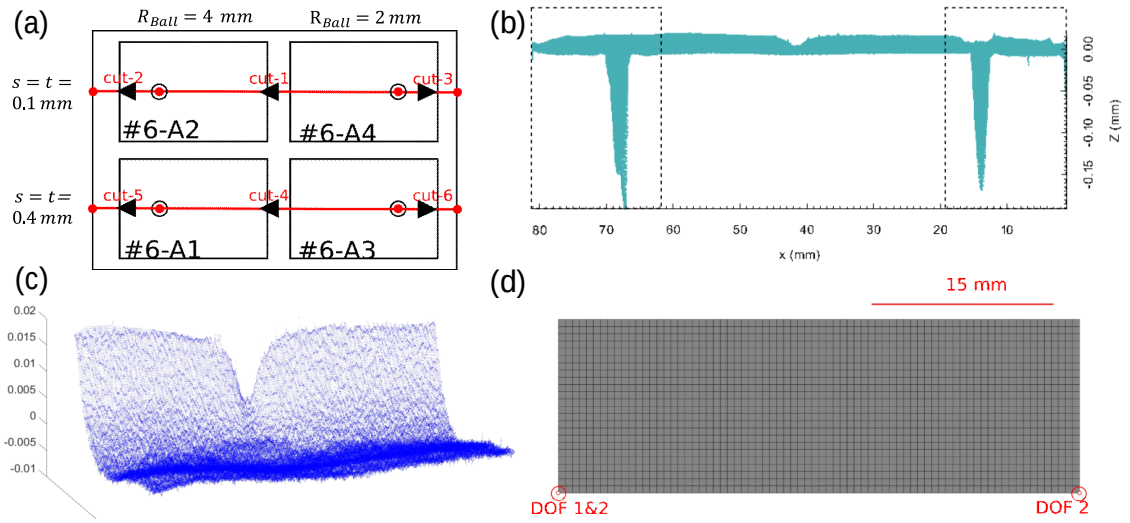

Figure 83: (a) Contour cut sequence and path, path is shown by red line and cutting direction is shown by the arrow; (b) removed region after averaging (dashed box), which was disregarded during spline fitting; (c) refined averaged surface; (d) location of rigid body boundary conditions, applied in the FEA.

5.2.1.4 Plastic Deformation Measurement

The ForgeFix XP was chosen with the smaller 2 mm radius pin for further investigation. A single peening pass and an indent distance *t* of 0.1 mm was implemented on a spare piece of identical material to investigate the plastic deformation behaviour of a single pass. Figure 84 shows the schematic of the 3 x 3 x 3 mm cube on which the topography was measured using an Olympus Lext confocal microscope. A 2.56 x 1.92 mm area was scanned in depth using the 5x magnification lens. The specimen was then mounted in conductive raisin and the y-z cross-section was ground and polished for SEM using standard sample preparation procedure. Aztec acquisition software was used to process the EBSD data to generate the strain maps, which were scanned at a step distance of 2 µm. Appendix C contains the detailed description of the EBSD-based reconstruction and strain mapping technique.

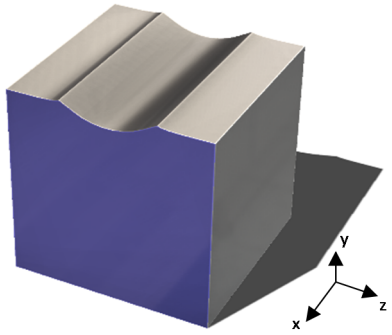

Figure 84: Schematic of the plastic deformation specimen.

5.2.2 Inter-Pass MHP for Grain Refinement

Inter-pass peening for grain refinement using the ForgeFix XP tool took place on a similar setup (Figure 85) to the one used in chapter 3, using identical deposition parameters to produce comparable wall dimensions, as in chapter 3 and elsewhere [77], [141]: An EWM plasma power supply was used to deposit the 1.2 mm Ti–6Al–4V wire on a clamped 7 mm thick substrate. Prior to peening, ten 300 mm long layers were built with 150 A at 10 l/min and 1 l/min plasma and shielding gas flow rate.

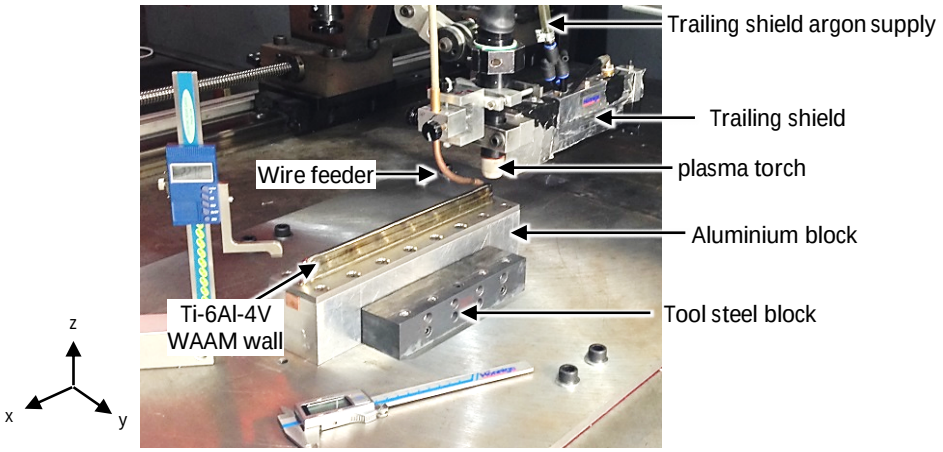

Figure 85: Setup of the sample production for the side-peening trials

Travel speed and work piece distance were kept constant at 7 mm/s and 8 mm respectively. These parameters produced 1.1 mm thick layers with a width of 5.8 mm. The setup for vertical and side inter-pass peening is shown in Figure 86 a) and b) respectively. The tool position for vertical peening was central to the top of the wall. For side peening the tool was manipulated normal to the side surface of the wall and located in the HAZ of the subsequent deposit close the fusion boundary. For both cases, inter-pass peening produced 10 indents per mm and was applied four times between each of the subsequent 4 layers (after the ten initial layers without peening). Each peening step on the cold wall took 10 sec.

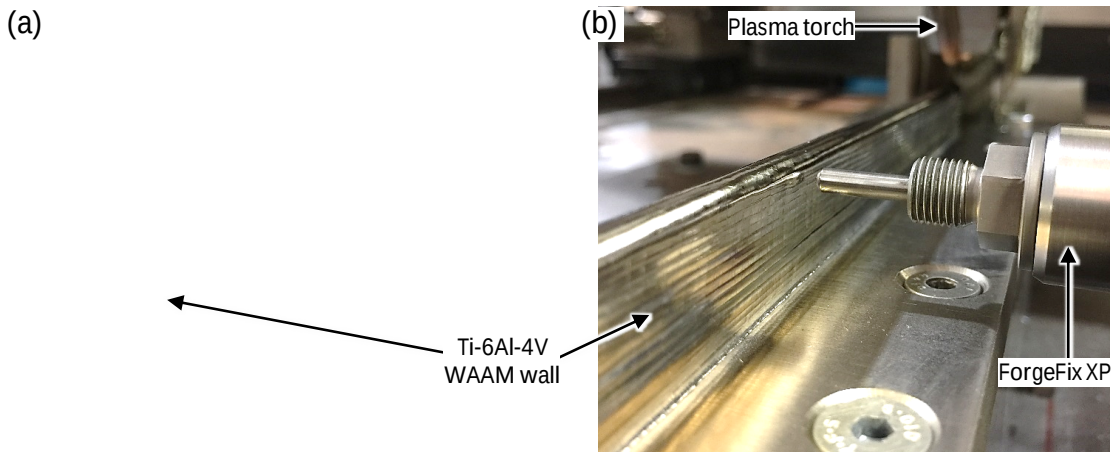

Figure 86: Setups for (a) inter-pass-top MHP and (b) inter-pass-side MHP

Four Cross-sectional specimens were taken in total: one control sample of vertical and horizontal peening was produced, which consisted of the ten initial layers plus the first subsequent peening pass. Four more layers were deposited with a peening step between each layer for both strategies, vertical and side peening, from which the other two cross-sections are taken. The four cross-sections were mounted, ground, polished and etched with hydrofluoric acid to reveal the prior-β grains, which were finally observed with an optical microscope.

5.2.3 Post-Process MHP for Distortion Control

Like for the grain refinement application, the ForgeFix XP was finally used to investigate the effectiveness on RS & D control, which is the other key target. In this experiment a finished and otherwise untreated Ti–6Al–4V WAAM wall was side peened. Side peening was chosen instead of vertical inter-pass peening, as side rolling has proven to be more effective than vertical inter-pass rolling for reducing distortion [141]. A 20 mm high wall was built using identical parameters to the previous section. The clamped wall was machined to 5.5 mm thickness to produce a flat plane. This was chosen to prevent the tool performance being impacted by the surface roughness, as the impact energy may differ with different pin-tip to work-piece distances. Peening took place on both sides using the ForgeFix XP with 6 bar pressure (Figure 87 (a)). A KUKA robot manipulated the tool, as shown in the simulation in Figure 87 (b) controlled by the in-house developed path planning software WAAMSoft. The out-of-plane distortion was measured in the same way mentioned in chapter 4 and compared against an un-peened specimen.

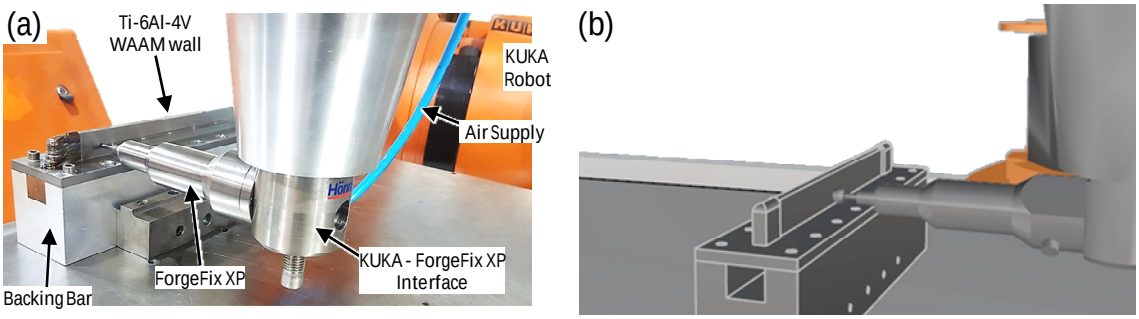

Figure 87: MHP as Distortion Control: (a) Setup of the side-peening experiment using the ForgeFix XP on a KUKA robot and (b) the path planning simulation of the experiment using the in-house developed software "WAAMSoft".

5.3 Results

5.3.1 MHP Tool Characterisation

5.3.1.1 Topography and Plastic Strain of a single Pass

Figure 88 shows the results of the confocal microscope. The average width of the peened line between the bulged edges is 1.23 ± 0.03 mm, the error representing the standard deviation of the twelve measurements taken. The residual depth of the peened groove is 68.5 ± 12.7 µm against the surrounding surface, which results in a residual radius of the groove of 2.8 mm. The elastic contact between the 2 mm radius tip and the surface caused spring back of the groove, resulting in a larger residual radius. At this point, the surface experienced great plastic deformation, but it also contains elastic strain that recovered, when the pin retracted. The material of this displaced cross-sectional area flowed from the centre towards the edges, generating a protrusion along the top surface.

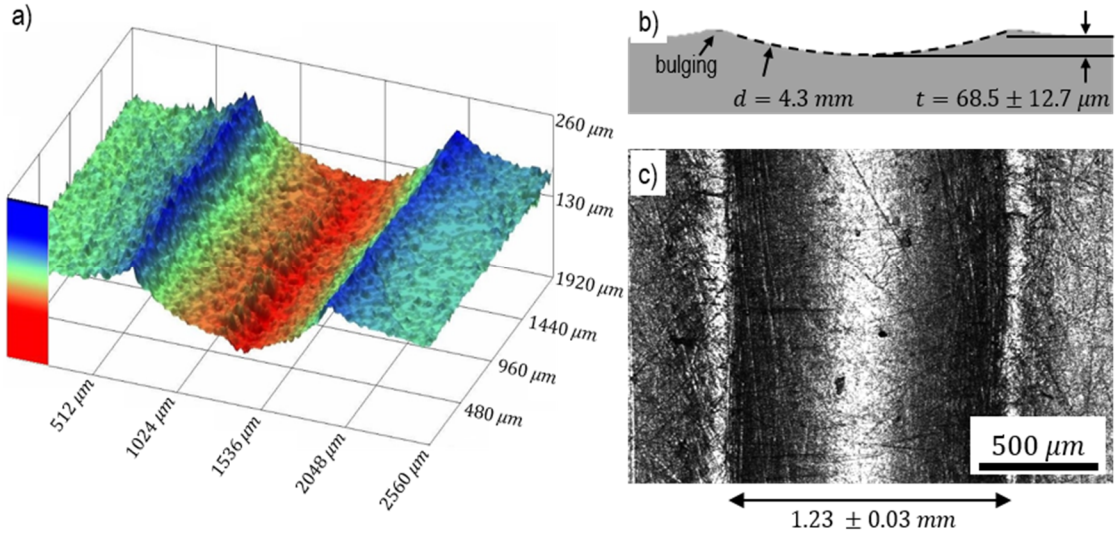

Figure 88: Images of the peening line groove, using the confocal microscopy data: (a) 3D image, (b) the cross-sectional groove geometry and (c) the original confocal microscope image.

The actual plastic deformation inside the material can be observed in the EBSD maps. Figure 89 a) is the reference SE image and (b) the band contrast (BC) map. The EBSD plastic strain map is shown in Figure 89 c). Very large plastic deformation below the peened groove resulted in this region not being indexed. In the BC map prior-β grain boundaries can be identified, which contain only grain boundary α_{GB} at room temperature and therefore appear bright against the background. Inside the large prior-β grains the microstructure is composed of the typical α plate. The EBSD strain map in Figure 89 c) shows the deviation (from 0° to 3°) of the crystals from fulfilling the ideal BOR during phase transformation. In the region that could not be indexed in the BC, no plastic strain could be calculated due to extremely large plastic deformation. It should be noted that the actual plastic strain cannot be derived from the EBSD map, which only provides a qualitative indication of plastic strain.

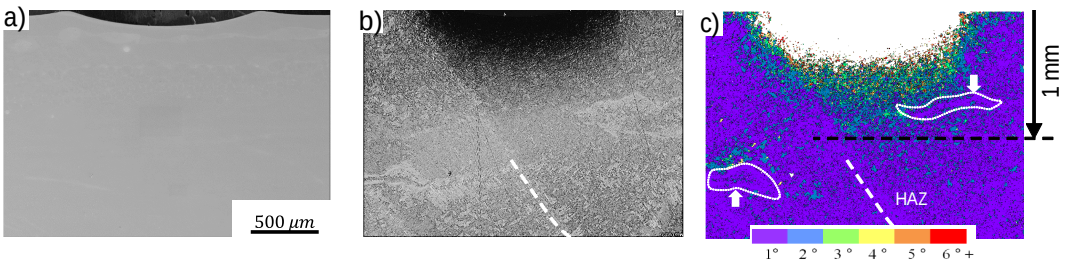

Figure 89: EBSD maps of the cross-sectional peening line groove: (a) reference SE (b) contrast map and (c) plastic strain map.

Further into the material, at distances greater than 0.3 mm, the strain map shows a deviation due to plastic deformation up to 3°. The maximum depth of the plastically deformed material of a single peening path is 1 mm. Even though the strain is very small at this depth, it should be noted that the threshold of engineering plastic strain being picked up by EBSD strain mapping is not established and might be relatively large. The results from Martina et al. and Donoghue et al. [77], [86] suggest at least 5 % or more. The grain boundary α_{GB} in the prior-β grain boundaries in that region appear without any plastic deformation and is indicated with the white arrows in Figure 89 (c).

5.3.1.2 Residual Stress of Peening Patterns

Figure 90 (a-d) show the four hole-drill stress profiles produced with the ForgeFix XP and they all appear similar. The compressive stresses transverse to the peening direction are larger than the longitudinal ones with a peak stress over -1300 MPa at 200 µm depth below the surface. The peak compressive stress in the longitudinal x-direction reaches a plateau of -750 MPa until it meets the transverse profile between 500 µm and 700 µm depth, from where both decrease to zero stress at approximately 1.2 mm depth.

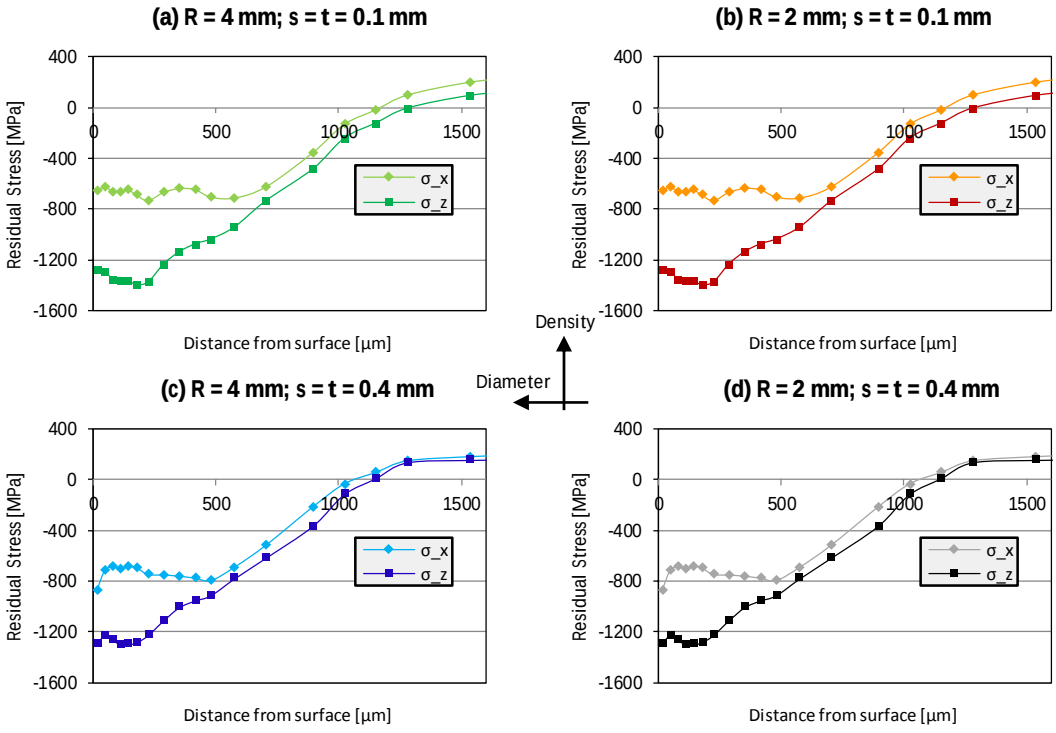

Figure 90: ForgeFix XP - compressive stress profiles using different MHP parameters with σ_x being longitudinal and σ_z transverse to the peening direction

The radius did not show any effect on the residual stress profiles, but increasing the peening density produced peak compressive stresses up to -1400 MPa and pushed the zero-crossing point from 1.1 mm to 1.3 mm.

The residual stress profiles of the Accurapuls are shown in Figure 91 (a-d). The smaller diameter profiles (b) and (d) match the ForgeFix XP profiles (Figure 90 (b) and (d)), which were produced using identical MHP parameters. The oddly low magnitude compressive stress below 100 µm in Figure 91 (b) is likely to be a measurement error.

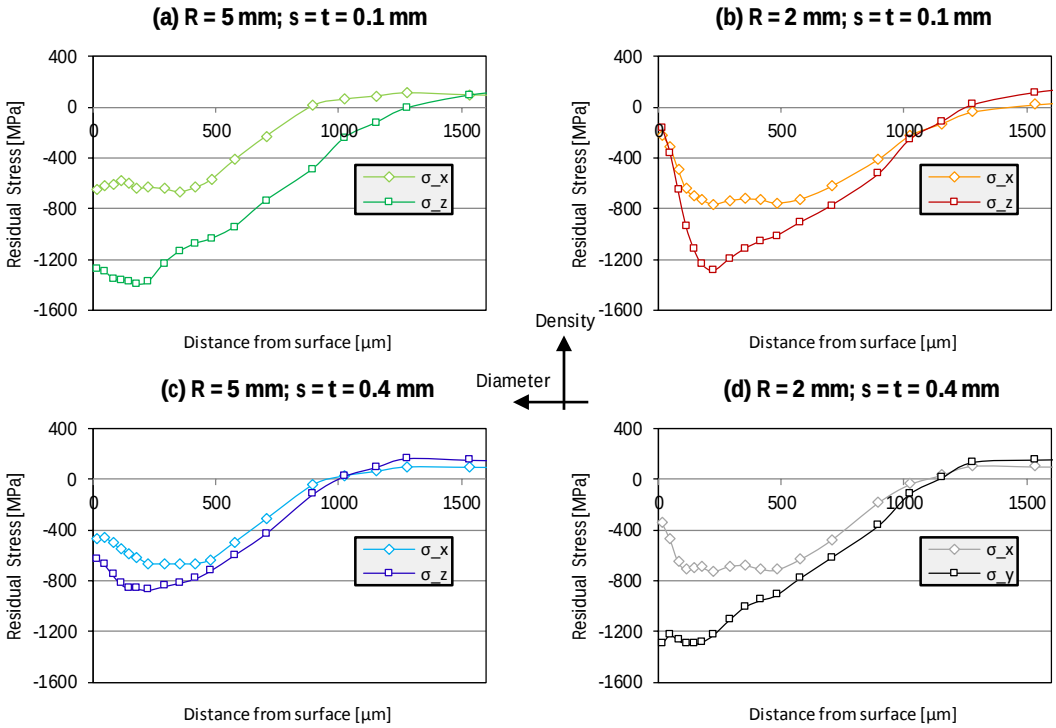

Figure 91: Accurapuls - compressive stress profiles using different MHP parameters with σ_x being longitudinal and σ_z transverse to the peening direction

The large Accurapuls radius resulted in less compressive stress and the zero-crossing point was less deep (Figure 91 (c) compared to (d)). However, increasing the peening pattern density mitigated this effect (Figure 91 (a)) and resulted in a profile more similar to the one with the smaller diameter (Figure 91 (b)). The contour method was only performed on the ForgeFix specimen #6 in the direction transverse to the peening direction, which is the direction with larger stresses. The contour stress maps in Figure 92 (a) show that the overall specimen is virtually stress free below the four peening fields. Peening on the surface induced a very homogeneous compressive stress field the

peening direction x. The stress plots through the sample thickness are shown in Figure 92 (b) (a comparison of the near surface stresses with the HD method follows in the discussion section in Figure 96). They all show the zero-crossing at roughly 1.2 mm. The peak compressive stress of the low peening density with t = s = 0.4 mm reach -2000 MPa, while the other two only reach -750 MPa. A detailed description and comparison of these results with hole drilling is covered in the discussion section.

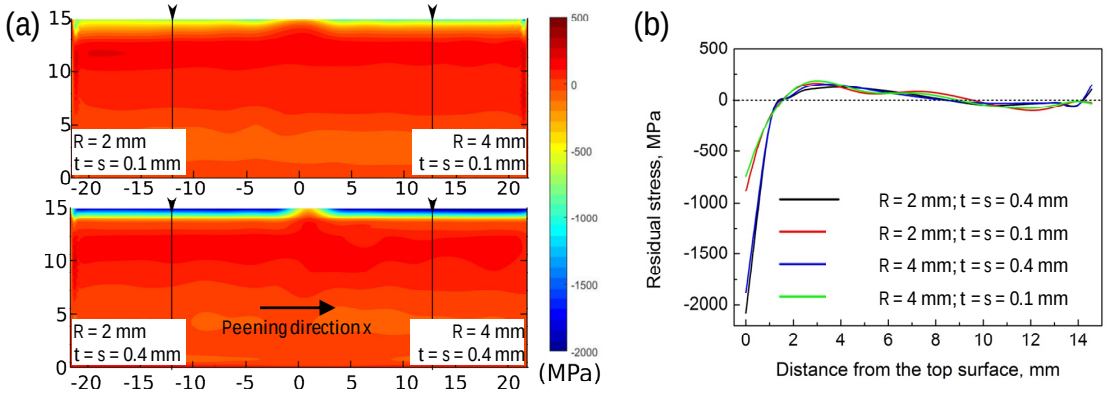

Figure 92: Contour Method results: (a) full stress map and (b) stress profiles along the respective indicated lines.

5.3.2 Post-Process MHP for Distortion Control

Figure 93 shows the effect of MHP on distortion reduction and the comparison to vertical inter-pass rolling. Without any cold mechanical treatment, the out-of-plane distortion was 7 mm. Side-peening mitigated the residual distortion to 4.1 mm, which is better than 50 kN inter-pass rolling and almost as good as inter-pass rolling with 75 kN rolling load [115].

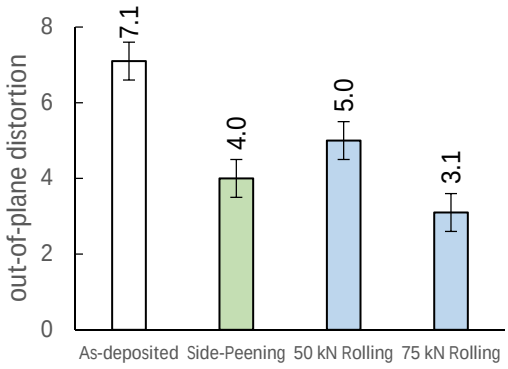

Figure 93: Effect of the side-peening surface finish on the out-of-plane distortion in comparison to vertical inter-pass rolling from Martina et al. [115].

During the MHP treatment on the side of the wall, low amplitude vibrations were felt, but were not visible with the bare eye. Therefore it is believed that most of the peening energy was consumed by plastic deformation, rather than elastic movement of the wall.

5.3.3 Inter-Pass MHP for Grain Refinement

The microstructure images of the inter-pass peening study observed with the optical microscope are shown in Figure 94. Figure 94 a) shows the top of the wall of the first control sample, which consists of ten layers, after the first peening pass has been applied. The two dark lines with the bright shadow below are the layer bands (border of HAZs) of the last two deposits. The distance between the bands is equal to the layer height of one deposit, which reflects the difference in the heat affected regions as each layer is deposited. Above this line the temperature was sufficiently high to trigger grain refinement, if it has been plastically deformed previously [86]. The dimensions of the peening line groove at the top centre of the wall are similar to the one in the tool characterisation study in section 5.3.1. The microstructure in Figure 94 b) consists of four more layer bands, caused by the subsequent layers, which were peened prior to each deposition. The top region of the cross-section shows that inter-pass peening achieved the desired grain refinement in the centre of the wall. The diameter of the refined prior-β grains is around or less than 1 mm.

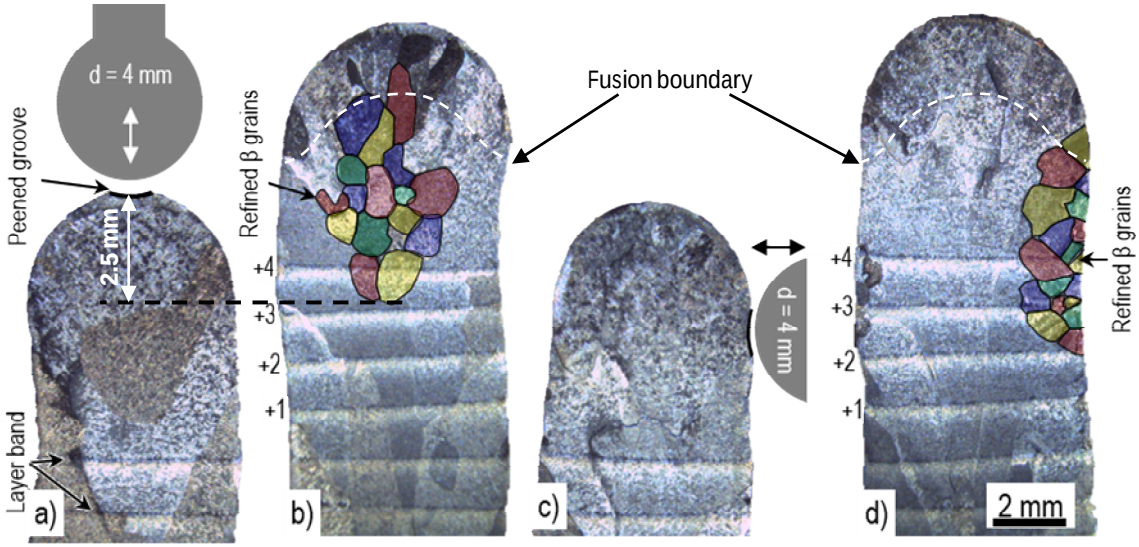

Figure 94: Microstructure before and after four inter-pass peening steps: (a) as-deposited microstructure after applying MHP once without subsequent heat treatment; (b) four repetitions of inter-pass peening, with heat treatment as the last process step; (c) like (a) with side peening; (d) like (c) with side peening.

Figure 94 (c) shows the control microstructure of the inter-pass side peened specimen. The groove of the peening line is located below the side edge of the fusion line of the next deposit, so that no remelting could spoil the refinement by liquidising the plastically deformed metal. After 4 repetitions of inter-pass side peening, the grain refinement occurs on the side of the wall, as shown in Figure 94 d). The refined grain size is relatively constant along the centreline, but it only reaches up to approximately 2 mm below the surface, which is slightly more than the plastic deformation or residual stress measured during the tool characterisation.

5.4 Discussion

5.4.1 MHP Tool Characterisation

A comparison between different MHP tools is generally not trivial. Tool suppliers claim that their tools generate a certain reaction force during a single impact that is transmitted to the manipulator. This impact force is typically less than 5 kN on the surface and virtually non-existing on the manipulator, as the acceleration of tool consumes almost the entire reaction force. The latter is easy to measure, however the measurement of the force on the surface is more difficult. The impact force furthermore changes during the very short non-linear impact.

Impact energy allows a better comparison between tools, but the measurement is even more complex during this highly dynamic process, where the measurement of the speed of the tip plus inertia, elasticity and the driving force (e.g. air or Lorentz force) is required, as well as the tool speed after the elastic impact. The impact energies of the manufacturers' instructions are often design estimations above the practical value. One approach is therefore not to directly measure the impact energy of a MHP tool, but to calibrate the produced plastic indent geometry with an indent produced by a drop ball with identical tip diameter and known potential energy.

For the comparison of MHP tool performance, identical pin tip radii (if available) and peening indent distances s and t were used. Both the ForgeFix XP and the Accurapuls produced almost identical stress profiles using the same peening density of 100 hits/mm^2 and a pin radius of 2 mm, as shown in the red and black curves in Figure 95 (a)

and (b), where the lower case letters (a-d) refer to the results from Figure 90 and Figure 91 respectively.

This suggests that the impact energy of both tools at their individual frequency is comparable. The compressive stress profile of the ForgeFix using a larger pin radius of 4 mm (mass of the pin is the same) was virtually the same. The large Accurapuls radius was slightly larger (5 mm), which might be the cause for a reduced compressive stress profile, as the larger diameter resulted in more contact area and therefore less contact pressure. The radii of both tool tips are ground on a green part, which is why different pins of are identical in mass. The effect on the stress induction is therefore only due to geometrical features.

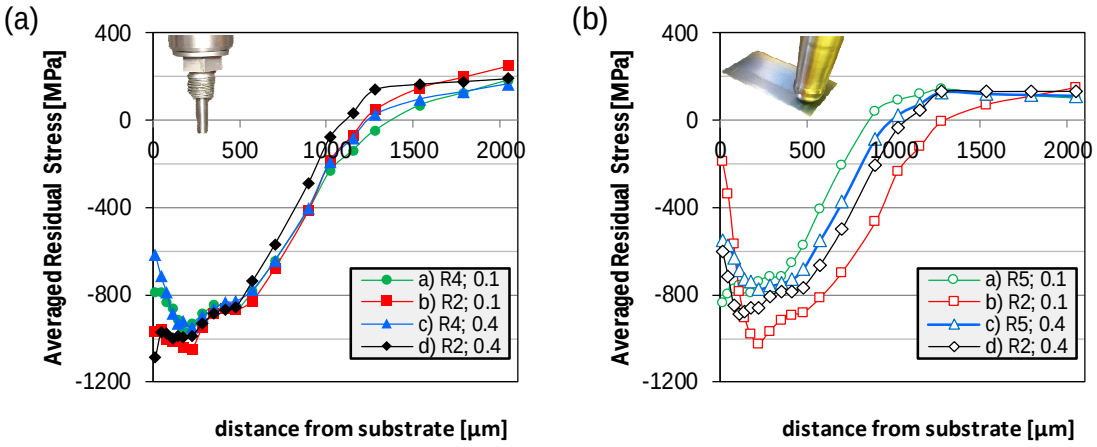

Figure 95: Summary and Comparison: Averaged Residual Stresses of both directions using (A) the pneumatic ForgeFix XP (values taken from Figure 90 (a-d)) and (b) the electromagnetic Accurapuls (values taken from Figure 91 (a-d)).[4]

5.4.2 Inter-Pass MHP for Grain Refinement

In vertical inter-pass MHP, the two lowest refined prior-β grains (Figure 94 (b)) formed after depositing on the top-peened wall (Figure 94 (a)). Grain refinement was only possible, because peening induced plastic deformation must have exceeded the remelting depth of the deposition. The bottom edge of the refined grains represent the maximum plastic deformation of the first peening line from Figure 94 (a). This depth

[4] Parameter Set (a) and (b) are identical for both tools. The ball radius in (c) and (d) was 4 mm for the ForgeFix XP and 5 mm for the Accurapuls respectively.

however is approximately 2.5 mm deeper from the peened surface than the plastic penetration measured using the EBSD strain map in Figure 89 (c). Either the EBSD strain map did not resolve low plastic strain that was still able to achieve grain refinement, or the large residual stresses in this deposit (chapter 4) facilitated plastic straining of the MHP step and allowed a deeper penetration. The residual stress profile in Figure 90 (b) suggest a zero-crossing point at 1.2 mm depth, where no plastic strain is shown in Figure 89 (c) whatsoever. However, the compressive stress induced by peening can only occur if plastic strain was induced. Chapter 6 contains an example with large residual stresses, where no plastic strain was measured using EBSD anywhere. Nevertheless, since the compressive stress profile was only half as deep (1.2 mm) as the effect of the grain refinement (2.5 mm), there must be a different explanation, which the results from the present chapter do not allow to answer. In the final chapter 7 is evidence that these grains did in fact not refine where they are, but instead probably refined within the bespoke top 1 mm and then grew deeper into the wall: After refinement in the top 1 mm, they first grew in in size, as the approaching molten pool raised the temperature far above the β-transus [238]. After that they grew downwards below the depth of the plastic deformation, where the molten pool then increased the temperature significantly above the β-transus as well. At this stage, the molten pool has remelted the complete region of plastic deformation and the nucleation site for refinement from where the growth has started.

Measurements of the fusion boundary in Ti–6Al–4V WAAM are not available, but it is believed that the shape is probably represented by the dashed line in Figure 94 [90]. The isothermal lines become more horizontal below the fusion boundary and are completely flat at the first layer band [90]. The depth of the molten pool in the centreline is not known and neither is the depth of remelting. However, if the remelting was deeper than the plastic deformation of MHP then no grain refinement would have been possible, as all the dislocations would have been melted, allowing fully epitaxial growth after solidification. This indicates that the remelting cannot have exceeded 0.5 mm depth. Donoghue et al [167], who used a UIT tool with comparable penetration depth [239] achieved a similar grain refinement, suggesting the same low amount of re-melting and

similar plastic deformation (Chapter 7 will focus on the thermal history and discuss remelting in more detail). The actual MHP tool used by Byun et al. [168] was not mentioned in the publication, but the achieved β-grain size of less than 460 µm in their WAAM (TIG) deposits was slightly smaller compared to the present results. The decrease in α-plate width was even comparable to the one achieved by inter-pass rolling [77].

Side Inter-pass MHP also resulted in grain refinement. Since the peening location was kept constant, relative to the top of the wall (Figure 94 (c)), the refined region travelled together with the growth of the wall. The groove width of one peening line was 1.23 mm (Figure 88 (c)), which was slightly wider than the layer height of 1.1 mm, which resulted in overlapping refinement regions on the side of the wall that travelled with each deposition in the build direction. The maximum penetration depth of approximately 2 mm into the material also exceeded the suggested plastic penetration of the EBSD strain map (Figure 89 (c)) or the residual stress profile (Figure 90 (b)) from the tool characterisation study in section 5.3.1. No re-melting effects or vertical thermal profiles spoil the characterisation, when MHP was applied on the side with a strain gradient through thickness. Hence the highly strained region near the surface was not remelted and can be used entirely to refine the microstructure. It should be noted that the location of side-peening was still close to the molten pool, where very high temperatures close to the melting point are present, which caused β-grain growth after refinement [238]. MHP could have been applied up to 2.5 mm further away from the top just above or at the HAZ, where the refinement could be different. Evidence for this explanation cannot be found with the present results, but only from those in chapter 7, as already mentioned.

In summary it was demonstrated that vertical, as well as side inter-pass peening can achieve grain refinement, as has been demonstrated for inter-pass rolling. Both techniques resulted in refinement at approximately the same distance above the last layer band up to a penetration depth below the contact surface. The achieved grain size of the inter-pass peened microstructure however is still large compared to the ones observed using inter-pass rolling. The reason is that plastic strain was not produced,

where it is needed, which is deeper into the material and further away from the fusion boundary.

The limiting factor for the application of inter-pass MHP is the large deposited volume per layer of the WAAM process and the high deposition rate resulting in a large HAZ. This means that the penetration depth of MHP is not sufficiently deep for many applications that involve a high deposition rate. Nevertheless it was a successful proof of concept that showed that inter-pass MHP applied on Ti–6Al–4V WAAM is effective for grain refinement.

5.4.3 Post-Process MHP for Distortion Control

The stress induction of MHP on an as-deposited and clamped wall was not measured, but the depth of the grain refinement suggests that MHP affected the wall that contained tensile stresses deeper than the stress-relieved material. The stress induction potential of the ForgeFix XP was tested for the effectiveness of distortion reduction in WAAM. The result showed a reduction in residual distortion, but not the desired elimination. The penetration depth of the measured stress profiles (Figure 90) was not sufficient to treat the 5.5 mm thick wall through thickness from both sides, which means that MHP is only suitable for thinner walls found in other AM processes or heavier tools are required for distortion reduction in WAAM. Flexibility issues were not observed during the MHP treatment, but tall and slender walls can potentially suffer from side-peening stimulated vibration that impedes the stress reduction or plastic strain induction. Both MHP tools produce generally respectable stress profiles compared to other peening techniques [152], [162], but even greater stress induction is required to successfully control RS & D in WAAM.

5.4.4 Ideal Stress Measurement Technique

The contour method is not limited to a practical penetration depth, which is not the case for hole drilling. The typical measurement depth is 1000 µm, but can be increased to 2000 µm by using a special strain gauge. It was concluded that heavier MHP tools are required, which also demands the measurement of stress deeper than 2 mm and therefore other measurement techniques. Figure 96 shows the partial agreement of both techniques. Both techniques agree very well with the zero-crossing of the stress at

roughly 1.2 mm. The extrapolation of the CM can be seen in the blue (d) and black (b) curves, as they deviate from the hole drill results from 0.5 mm depth (2x wire diameter) to the surface. The red (a) and green (c) curves agree well in the zero-crossing but don't match at all in the compressive region for no apparent reason. In any case both techniques are suitable to characterise MHP tools in respect to their potential for penetration depth or residual stresses, because the zero-crossing seems to be the limit for plastic strain induction as well. Of the two techniques, hole drilling appears to provide the more accurate measurements of residual stresses induced by peening.

However, the contour method not only provides the required resolution and penetration depth, it also does not have the constraint of the hole-drilling method of requiring a flat surface with a constant stress profile below the strain gauge measurement grids and drill hole.

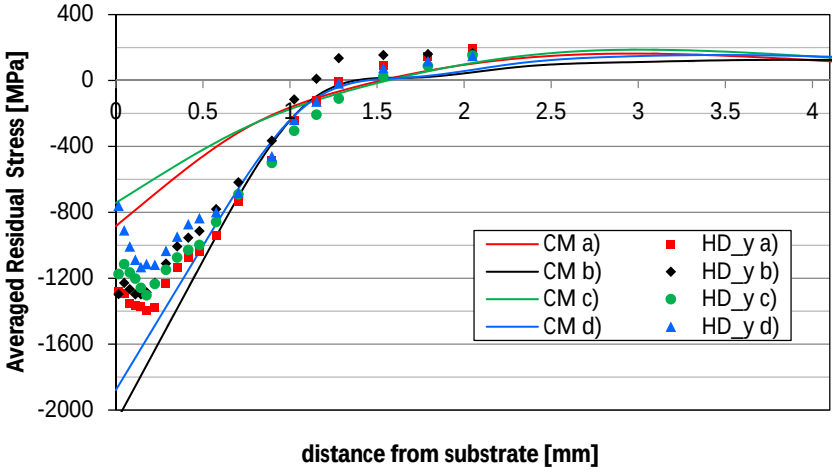

Figure 96: Comparison of ForgeFix XP residual stress measurement using the contour results from Figure 90 and Figure 92 (b)

However it is still relatively laborious and comes with individual constraints [224]. Near surface residual stresses cannot be properly resolved without sample preparation, such as the use of sacrificial material. Therefore cutting artefacts are induced at the wire entrance and exit, which causes uncertainty up to double the depth of the EDM wire diameter, which was 250 µm in the present study. Furthermore spline fitting does not work satisfactorily at the surface, as no measurement points exist above the surface that

can be interpolated, so the surface values need to be extrapolated in the region where the highest resolution is required.

5.4.5 Ideal Plastic Strain Induction and Measurement

MHP seems to produce more plastic strain compared to rolling, but it reaches less deep into the surface [86] using a certain set of parameters, as shown in the comparison of EBSD strain maps in Figure 97 from the present study (a) with an equivalent strain map of a rolling pass (b) (Appendix C). The latter was produced with a 150 mm diameter roller and a 3 mm profile radius at 90 kN load. Near the surface the peened groove produced an un-indexable microstructure due to overstraining the material, but the penetration depth of the roller was much deeper. The rolled groove shows instead very little plastic deformation near the surface, which is due to friction during the rolling process [240], which is not the case for peening. A strain distribution induced by rolling is therefore favoured for grain refinement, because the subsequent deposition would re-melt mostly unstrained material. The large near-surface deformation induced by MHP is re-melted by the next layer and therefore wasted.

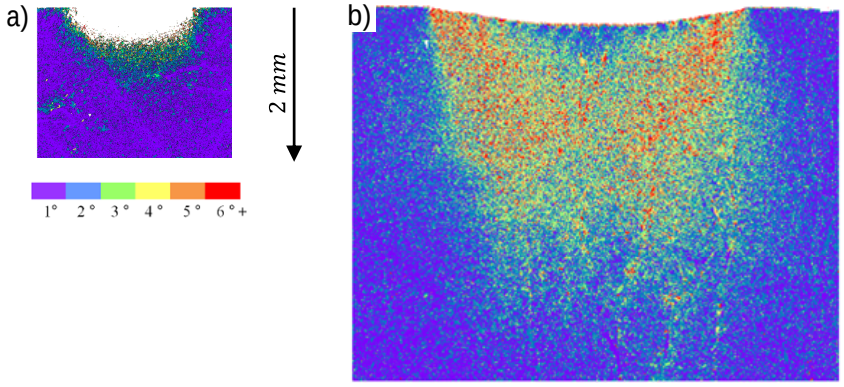

Figure 97: EBSD plastic strain maps – comparison of typical strain profiles produced with the (a) MHP tool "ForgeFix XP" and (b) profiled rolling.

It is neither well understood how much strain actually needs to be provided to achieve refinement, nor how much strain the EBSD strain map can indicate and what EBSD strain colour represents which amount of plastic strain. According to previous studies, the EBSD strain map can approximately resolve plastic strain above a few % [86] and the minimum required strain to yield grain refinement was suggested to be above 7 % [77], which must be induced by compressive deformation [72].

5.4.6 Practical Summary

The sole potential of both tools, the pneumatic ForgeFix XP and the electromagnetic Accurapuls, showed to be absolutely identical in performance, because they produced the same stress profile, when used with identical peening parameters (Figure 95) and the same impact frequency. It can be concluded that both tools deliver a similar impact energy, whatever exactly it is. The choice between both is therefore regarding ease of integration into the manufacturing chain and working environment, maintenance, robustness and price.

Whatever tool is chosen, the handy and light construction of MHP tools in general allow an easy integration into the WAAM process. The ease of tool manipulation is advantageous compared to rolling and allows robotic application precisely where it is needed. It would be worth investigating heavier MHP tools with higher impact energies that produce plastic deformation up to ideally 5 mm [165], [194]–[196] or more into the material for a refinement comparable to inter-pass rolling.

5.5 Conclusion

In this chapter it was shown that:

1. ForgeFix XP and Accurapuls showed virtually identical tool performance.
2. Inter-pass MHP is a suitable technique to achieve grain refinement in Ti–6Al–4V WAAM. It is likely that it also works as good or probably better in combination with other AM processes with a small feature size and therefore smaller HAZs. WAAM would benefit from MHP tools that deliver higher impact energies than the ones used.
3. EBSD strain maps can be used to identify plastically deformed material under a cold worked region to predict the size of the refinement zone. It can be deployed when easier techniques, such as hardness measurements are not compatible with a specific alloy, such as Ti–6Al–4V.

The investigation in the present chapter was a proof of concept for MHP to be theoretically suitable to perform inter-pass cold work in AM for stress mitigation and

grain refinement purposes. The following chapter 6 investigates the influence of the different MHP parameters and profiled rolling parameters on the precise residual stress and plastic strain induction. It will therefore allow more detailed conclusions for practical applications. During the research a third MHP tool prototype was presented, which according to the manufacturer has an impact energy of 700 mJ [241], as opposed to the 100 mJ to 200 mJ tools in this chapter. The investigation of the performance of MHP was put further with this new and heavier tool

Chapter 6 Plastic Deformation Characteristics of Rolling and Machine Hammer Peening

6.1 Introduction

Cold rolling and MHP can both be used to mitigate and control RS & D in WAAM. When applied inter pass, the induced plastic strain results in grain refinement and increase in mechanical properties. However, it is not well understood how different cold work parameters, such as tool geometry or rolling load or MHP impact energy influence the process' effectiveness.

Development of residual stresses and rolling as a full-scale mitigation strategy were investigated in chapter 3 to 4 and elsewhere [115]. The effect of inter-pass rolling on the final microstructure was also shown in chapter 3 and various literature [77], [86], [111], [137], [139], which is beneficial for the mechanical properties. In addition peening can be used to control residual stress and to achieve grain refinement as shown in the previous chapter 5 and elsewhere [167], [168]. However, no information is available that shows the effect of a single cold working pass and therefore the ideal parameters for either purpose, stress control or grain refinement. Grain refinement in Ti–6Al–4V WAAM was mostly described in thin single pass walls only, with a semi-circular cross section on the top, as shown in Figure 98 (a). The small contact area that a flat roller forms, generates very large pressure and plastic deformation during rolling.

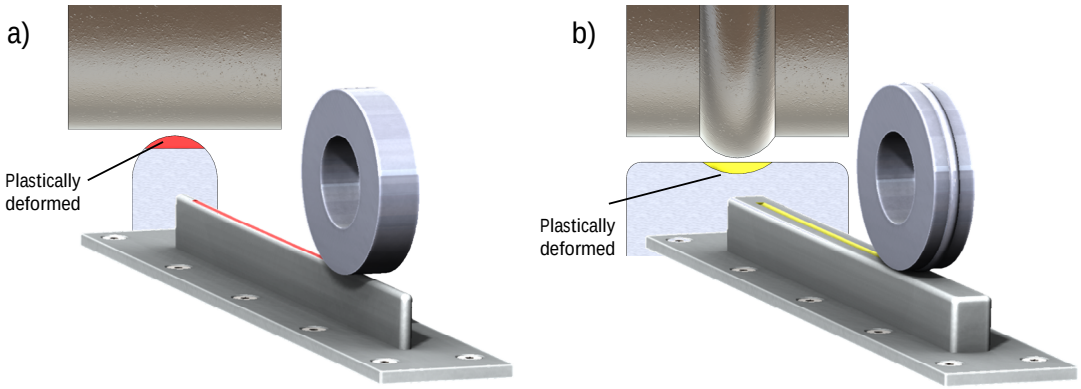

Figure 98: Plastic deformation of a WAAM wall: (a) rolling a thin wall using a flat roller and (b) rolling a wide and flat wall using a profiled roller.

However, actual WAAM applications often have much larger features. A flat roller would supposedly not induce sufficient strain on a wide wall, which is why a convex profiled roller can be used for rolling them (Figure 98 (b)) [242]. At present it is understood that more plastic strain yields greater α and β grain refinement [77], but the actual strain required in combination with a certain thermal history has not yet been quantified. The latter is determined by the deposition parameters, which primarily account for the layer geometry. The cold working tool geometry and the applied load determine the location and magnitude of plastic deformation. The present chapter characterises the influence of both parameters and the nature of both cold working techniques in terms of residual stress manipulation and plastic strain induction, using the Contour Method (CM), hardness and plastic strain mapping, as well as the comparison with numerical simulations. The final heat treatment reveals the microstructure and locates the area of grain refinement, which can be compared against the strain and stress measurements. The structure of this chapter is shown in the flow chart in Figure 99.

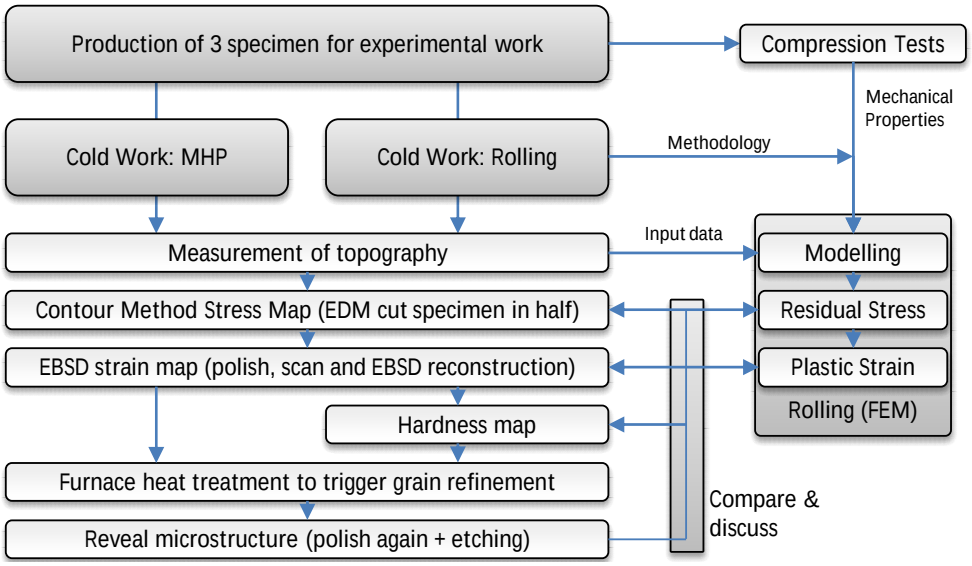

Figure 99: Plastic deformation of a WAAM wall: (a) rolling a thin wall using a flat roller and (b) rolling a wide and flat wall using a profiled roller.

Both MHP tools characterised in the previous chapter were found to be not sufficiently powerful for controlling residual stress and refining the microstructure in Ti–6Al–4V WAAM. ECOROLL, a third tool manufacturer who is experienced in deep rolling of Ti–6Al–4V [192], recently introduced a mechanically driven MHP tool [166]. Compressive stresses can be induced up to 4 mm deep in Inconel [241], which suggests

that this tool is much more powerful than the ones used in the previous chapter. The plastic impact energy of the shaft driven prototype (HAM-C) was up to 700 mJ. Therefore this heavy MHP tool was used in the present investigation, instead of the ones used in the previous chapter.

6.2 Methodology

The same wall from the previous chapter was used to produce the specimens for the present chapter. The location of the stress relieved 55 x 80 x 15 mm large specimen in the wall is shown in Figure 81. Specimen #6 and #8 from this wall were used in the previous chapter. Specimens #2 and #5 were used for the MHP and rolling experiments respectively, while specimen #7 was used for performing compression tests to obtain the material parameters for the numerical simulation [243], for which the results are shown in the appendix D.

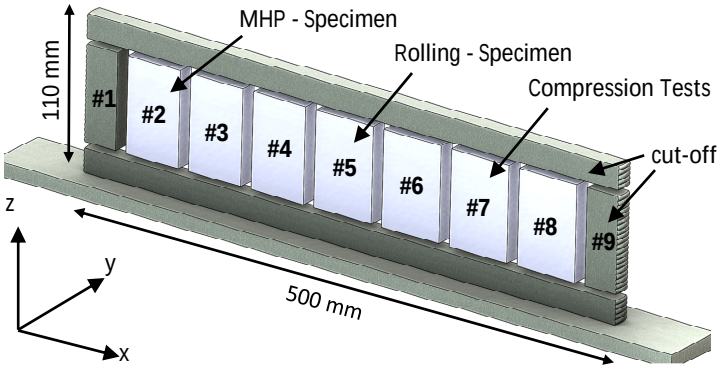

Figure 100: Position and extraction of the specimen from the 500 mm long and 110 mm high Ti–6Al–4V wall.

The two peening tools used in this study were the HAM-A (250 mJ) and HAM-C (700 mJ) supplied by the ECOROLL AG in Germany and are shown in Figure 101. The specimen and the spindle driven tool were mounted on a 3-axis CNC machine for MHP.

Figure 101: Both MHP HAM-A and HAM-C [241].

The tool steel indenter material was coated with 88% WC and 0.12% Co (similar to K30 according to ISO 513) and hit the surface with 330 Hz and 250 Hz, using the HAM-A and the HAM-C respectively. The travel speed was set to 165 mm/s and 22.5 mm/s, which resulted in an impact distance of 0.5 mm for the HAM-A on area #2.1 and 0.1 mm for the HAM-C on area #2.5. The step advance in x-direction was set accordingly to produce square pattern, which resulted in 4 impacts/mm^2 for the HAM-A and 100 impacts/mm^2 for the HAM-C. Rolling trials were traditionally performed on the in-house built rolling rig [135]. Three roller geometries were used with a total diameter of 150 mm and three convex radii of 1.5 mm, 3 mm and 6 mm. The roller material was core hardened H13 tool steel, nitrided to 72 HRC. Peening took place on the large surface of the cuboid specimen #2 and rolling on specimen #5, as shown in Figure 102 (a) and (b).

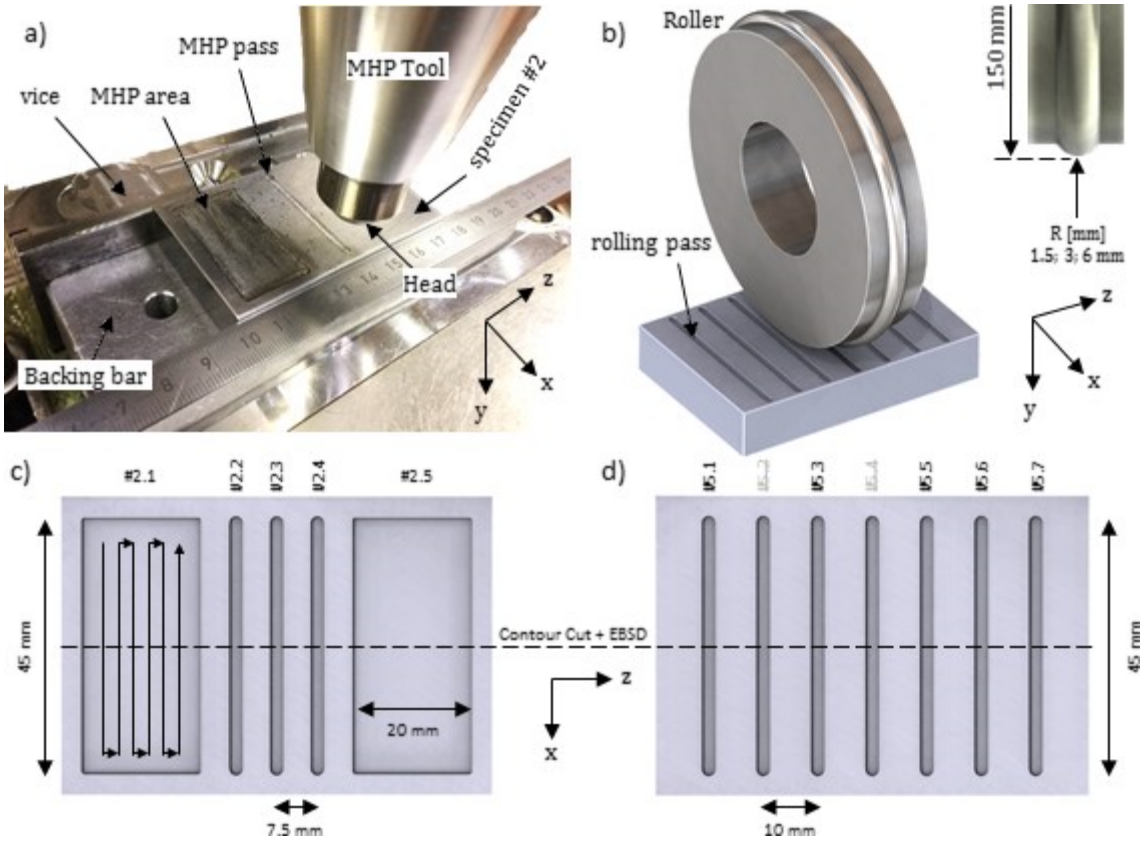

Figure 102: Experimental layout and names on the MHP specimen #2 (a) and the rolling specimen #5 (b)

The peening and rolling parameters used in both layouts (Figure 102 (c) and (d)) and the respective labelling are shown in Table 9.

Table 9: Cold work parameters of MHP and rolling

MHP (specimen #2)				Rolling (specimen #5)		
Specimen #	Tool	R_{MHP} [mm]	E_{Imp} [mJ]	Specimen #	R_{prof} [mm]	Load [kN]
2.1	HAM-A	6	250	5.1	3	20
2.2	HAM-C	16	700	5.3	1.5	45
2.3	HAM-A	6	250	5.5	6	45
2.4	HAM-C	25	700	5.6	3	45
2.5	HAM-C	25	700	5.7	3	70

6.2.1 Topography Measurement

The peened and rolled grooves were measured using a tactile Dektak and the Olympus confocal microscope Lext SurFace respectively. The groove depth of rolling exceeded the range of the Dektak and the peened grooves were not deep enough for the resolution of the Olympus.

6.2.2 Residual Stress Measurement

The contour method was performed by StressMap at the Open University in Milton Keynes and was used to map the resudual stresses in the plastically deformed cross

section. An Agie Charmilles Cut 1000 EDM machine was used to perform a cut in the y-z symmetry plane (Figure 102 c-d) using a 50 µm diameter brass wire. Prior to the cut, a layer of sacrificial material was attached to the top and bottom surfaces using electrically conductive glue to mitigate the effect of wire entry and exit cutting artefacts [224]. The sample was firmly clamped to the EDM stage, which was then filled with deionised water and left to reach thermal equilibrium before the cut was performed. The cut surfaces were cleaned using acetone, isopropanol, and a soft brush and placed in the metrology lab to reach thermal equilibrium with the ambient air. A Zeiss Eclipse coordinate measuring machine (CMM), fitted with a Micro-Epsilon laser probe and a 2 mm diameter ruby-tipped Renishaw PH10M touch trigger probe was used for the measurements. The surface profile was measured using the laser probe, which has a fixed out-of-plane resolution of 0.15 µm, while for this particular measurement, an in-plane resolution of 25 µm was adopted. In addition, the perimeters of the two cut parts were measured with the touch-probe and later used for precisely aligning the measurements of the two cut parts before averaging the profiles and for creating an accurate FE model geometry.

The data sets for opposing cut surfaces were aligned using the measured perimeters and then interpolated onto a common grid before averaging to remove errors due to shear stress and possible anti-symmetric cutting artefacts, resulting in a displacement profile. Due to the uncertainty in CMM measurements and the roughness of the EDM cut surfaces, noise in the displacement profile is unavoidable and it would be further amplified in the stress calculation. Therefore, the profile was smoothed using a robust local polynomial fit (StressMap's proprietary algorithm). The smoothing level was modulated by varying the 'mask size' between 1.5 and 4 mm in steps of 0.25 mm and the optimum smoothing level within this range was given by a 3.75 mm mask size, since larger mask sizes started to reduce the peak stress in the regions of interest. For this mask size, the fitting error, estimated using the approach from Prime et al. [223], was less than 4 MPa. To calculate the stresses, an FE model was created in Abaqus 6.13 by extruding the measured perimeters to a depth of 27.5 mm; thus creating the geometry of one cut half. The model was meshed using linear hexahedral elements with reduced

integration (C3D8R). The mesh at the cut surface was biased from 0.2 mm near the treated surface up to 1.5 mm away from the surface of interest, while in the extruded direction (away from the cut plane), the mesh was biased from 0.2 to 3 mm going away from the cut surface. The model with the mesh are shown in Figure 103.

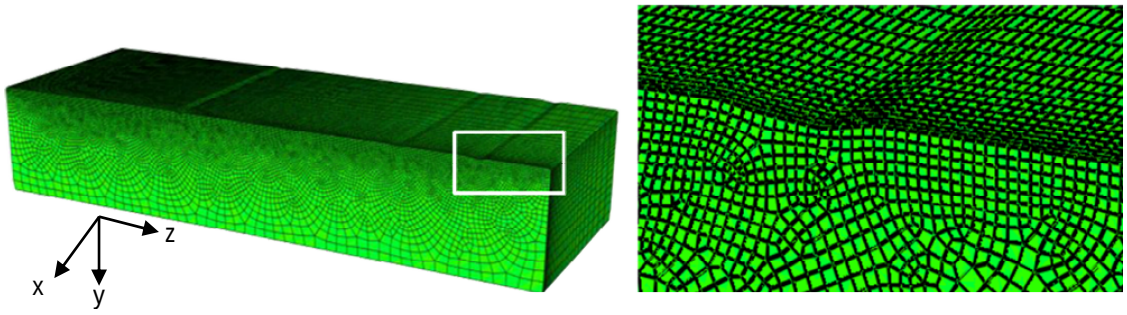

Figure 103: Illustration of the extruded geometry and mesh used for the CM residual stress determination.

The model was assigned uniform isotropic elastic properties, with a Young's modulus of 113.4 and Poisson's ratio of 0.342 [192]. The smoothed displacement profile, with a reverse sign, was applied as boundary condition on the surface nodes of the simulated cut parts. The initial residual stresses acting normal to the cut plane of the samples is given by the resulting stress component acting in the same direction at the simulated cut surface.

To gain confidence in the contour method results (σ_{xx} stress map), hole drilling was performed on a separate identically produced and peened specimen. The peening pattern using the 700 mJ tool and the 25 mm radius tip was repeated on a spare specimen (#3). An EA-01-125RE-120 residual stress strain gauge rosette was mounted according to the application procedure recommended by Vishay with one of the grids in x-direction. The 19.2 x 19.2 mm large rosette was located in the centre of the peened area. The three grids were connected using a three-wire configuration to the terminal and represent one of four resistances in the Wheatstone bridge inside the terminal. After soldering the wires, clamping the specimen carefully without adding extra stress and waiting for constant temperature, the strain gauge was adjusted to zero. A 2.3 mm drill was used in eccentric mode to produce a 3.8 mm diameter and 2.8 mm deep drill hole at 8 µm increments. The setup during the drilling phase is shown in Figure 104. The

strain data was post-processed using an excel-spread sheet provided by the tool supplier to calculate the residual stresses up to a depth of 2 mm.

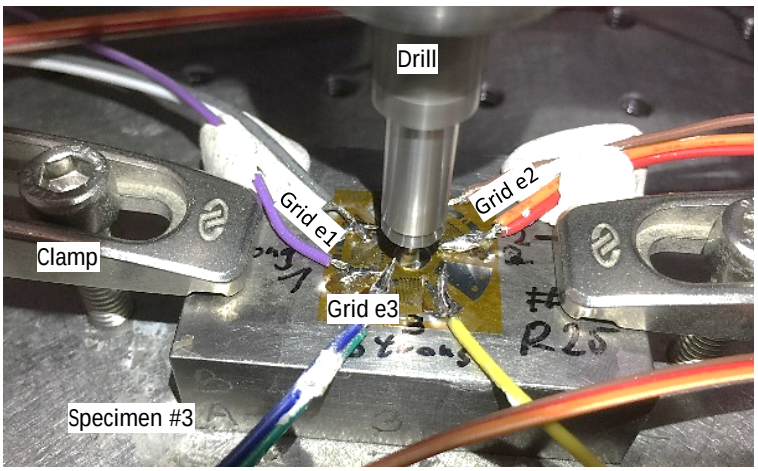

Figure 104: Hole drill setup for plane stress measurement

6.2.3 EBSD Plastic Strain Mapping

After the topographical measurement of the contour surface, it was further post-processed for plastic strain mapping using the bespoke EBSD-based technique, as in the previous chapter. The specimens were mounted in conductive raisin, followed by standard sample preparation, which included five grinding steps using 120, 250, 1200, 2500 and 4000 grid paper and polishing for 1h with oxalic acid and colloidal silica. Maxim FEG SEM by CamScam and the Aztec acquisition software was used to process the data with a step distance of 2 µm from the Oxford instruments EBSD system. The EBSD data was post-processed by the School of Materials at the University of Manchester using the bespoke titanium β-reconstruction technique developed by the University of Sheffield [234], [244] and explained in more detail in Appendix C. Strain maps were produced by plotting minimum misorientations of neighbouring α plates to fulfil the ideal BOR, taken from partially reconstructed β-IPF. This technique has already been used successfully for strain mapping in Ti–6Al–4V WAAM material [86], [167].

6.2.4 Hardness Mapping

After strain mapping, the samples were etched for 20 s using cotton wool soaked with diluted hydrofluoric acid, after which Vickers hardness maps were produced under the groove. The 1 kg load of the diamond indenter was applied for 15 s on each measurement point. The grids with a step size of 200 µm were located under the rolled

groove up to 4 mm under the surface. The width of each grid was adapted for each sample so that it exceeded the groove width by 1.2 mm.

6.2.5 Numerical Rolling Simulation

The numerical simulations were performed at the Helmholtz-Zentrum in Geesthacht, as well as the compression tests required for the material properties. The methodology of the rolling trials were used for the load steps in the numerical simulations, for which the topography measurements were used to calibrate the displacement controlled simulation. An implicit analysis using direct integration in ABAQUS/Standard software was used for the simulation of the rolling process. As in the experiment, a stress-free block of 80×55×15 mm^3 volume with Ti–6Al–4V WAAM elastic-plastic mechanical properties (taken from [92]) was modelled. These tensile properties were used, because the compression tests (on specimen #7) have not been completed at the time of the simulations. Due to the symmetric nature of the rolling process and to reduce the computational costs, only one half of the deformation actually modelled, shown in Figure 105 (a). The finite element model was discretized by 8-node linear hexahedral elements with reduced integration (C3D8R). The discretisation was done in a way that there was a very fine mesh in and near the deformation zone. In order to decrease the simulation time, a biased mesh was used leading to a coarse mesh in the area far from the deformation zone. Figure 105 (b) shows the discretized finite element model with an indication of the element sizes used in each coordinate direction. The same roller geometries, used for the experiments were modelled to produce similar groove geometries. The roller was assumed to be rigid body, because a test simulation with an elastic deformable roller led to equivalent results as for the rigid roller. The rollers were discretized by 4-node 3-D bilinear rigid quadrilateral elements and the average element size was 250 um. The longitudinal residual stress S11 (x-direction) and equivalent plastic strain PEEQ, equivalent to the contour method stress maps and the EBSD strain maps were plotted. They were mesh-independent. The MHP trials were not simulated.

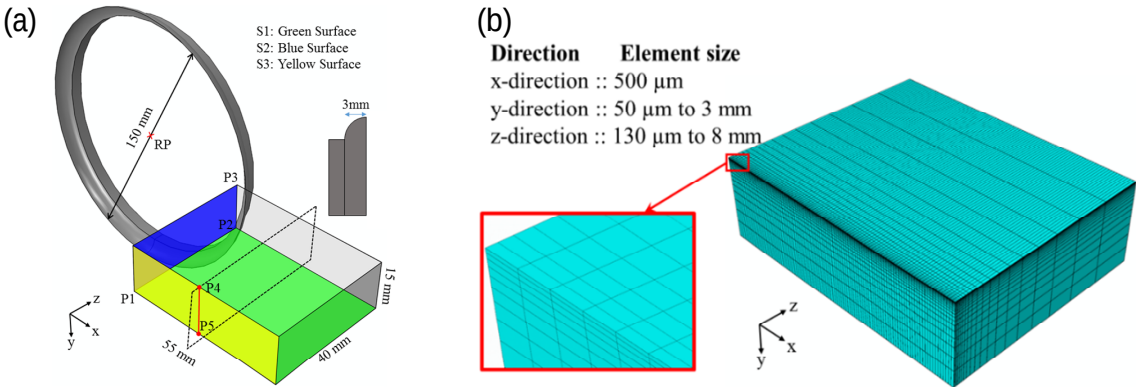

Figure 105: (a) ABAQUS model and (b) specified meshing parameters for rolling.

6.2.6 Heat Treatment and Microstructure Analysis

After all measurements were completed on the cold worked material, the specimens were finally heat treated to produce grain refinement of the plastically deformed region. The specimens were laid with the observation face down onto a 2 mm thick stainless steel plate, which prevented exposure to environmental oxygen. An 8 kg mild steel block served as a thermal mass inside the furnace, which was kept at a temperature of 1080 °C. The stainless steel plate with the specimen on top was put onto the steel block, so that the heat conduction resulted in a relatively fast increase in temperature. A K-type thermocouple was spot welded onto the stainless steel plate at the edge of the specimen to capture the temperature at the interface. The thermocouple reader started to record, once the temperature reached 500 °C, resulting in the thermal history during the heat treatment in Figure 106 (a). It took the specimen 73 s to pass through the β-transformation range between 700 °C and 1000 °C. To ensure full β-transformation, the specimens were kept for another 93 s in the furnace, while they reached 1073 °C maximum temperature, after which the furnace was opened. The environmental atmosphere caused oxidisation of the surface [52]. Oxygen did not diffuse deeper into the surface than 50 µm to form α case, as shown in Figure 106 (b). The specimen was taken out of the furnace and air cooled with a cooling rate of 12 °C/s through the β-transformation range, which is similar to the typical cooling rates in Ti–6Al–4V WAAM [77]. After heat treatment, a lamellar microstructure was established, similar to how it was before the treatment [87]. The β→α phase transformation temperature at the peak cooling rate of -15 °C/s drops to approximately 930 °C and the resulting microstructure at these cooling rates should contain traces of martensite [51].

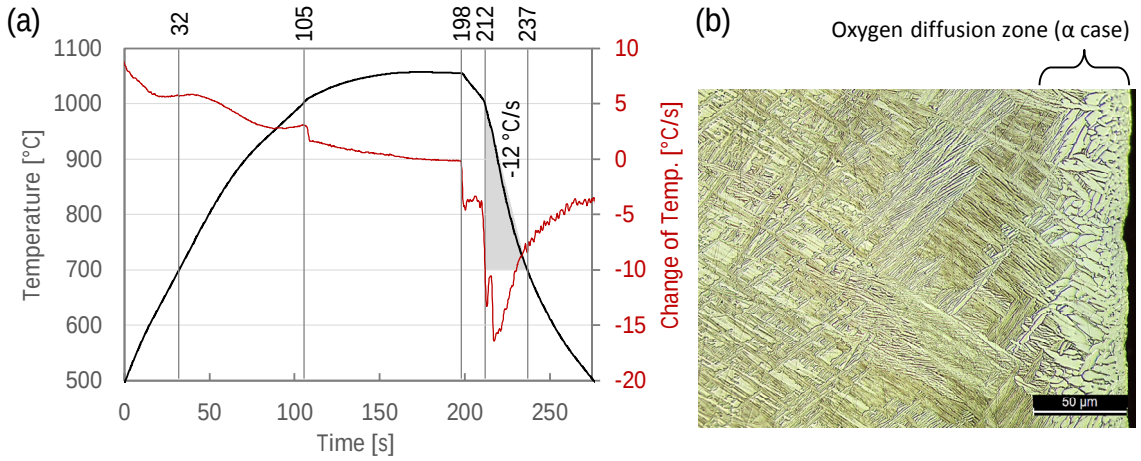

Figure 106: (a) Thermal history and the corresponding heat/cooling rates during Ti–6Al–4V β-refinement heat treatment; (b) surface microstructure showing the influential depth of oxygen.

Diffusion kinetics of AL and V can delay the α → β transform, or require superheat above the β transus to complete the transformation. Fast heating rates for example require a few seconds and a superheat of 160 °C according to Elmer at al. [235]. The present temperature time history exceeded this requirement and therefore guaranteed to produce grain refinement everywhere, where the strain was sufficient [86]. However, the time/temperature history was also sufficient for subsequent β-grain growth after the refinement [238], but the primary target in this study was to identify the border of the refined region, rather than the β-grain size at this stage. Finally optical microstructural analysis was performed on the surface of the contour cut. Conventional sample preparation, as in the EBSD measurement above, plus etching with hydrofluoric acid exposed the microstructure, which was then analysed using an optical microscope with 5x magnification.

6.3 Results Section A: Rolling Experiments

For clarity, the results for rolling and MHP are presented separately. The scale in the results from Figure 109 to Figure 114 are similar, but not identical.

6.3.1 Topography

Figure 107 (a) shows an exemplary 3D topography produced by the confocal microscope of the rolled groove using the R3 roller profile at 45 kN load. These results were used to extract the values for the groove width and depth in Figure 107 (b).

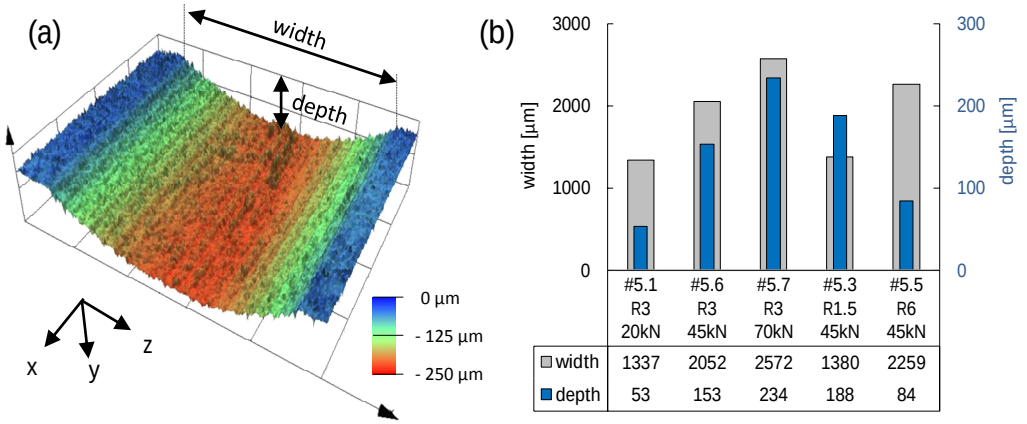

Figure 107: (a) Exemplary result of the confocal microscope of the groove using the 3 mm profile and 45 kN load and (b) the complete results.

Both the groove width and depth increased with increasing rolling load using the R3 mm convex profiled roller. Increasing the profile radius from 1.5 mm to 6 mm at a constant rolling load of 45 kN increased the groove width, but decreased the penetration depth.

6.3.2 Residual Stress Maps

The residual stress map in Figure 108 shows the results from the contour method of the rolled specimen #5 with a colour bar indicating stress σ_{xx} between -500 MPa and 250 MPa. The two "X" cover two disregarded experiments. Each rolling trial produced a circular area of compressive stress, which is balanced by a tensile region below. The balancing tensile regions of neighbouring passes overlap slightly. The high magnification contour maps of residual stress beneath each pass is shown in Figure 109, where the colour bar indicates stresses between -450 MPa and +450 MPa. Increasing the load from 20 kN to 45 kN and 70 kN using the 3 mm profiled radius increased the peak compressive stress and moves it together with the zero-crossing point deeper below the surface. Increasing the profiled radius from 1.5 mm to 3 mm and 6 mm but keeping the load constant at 45 kN has a comparable, but much less pronounced effect. As it produced a wider groove however, the region of plastic deformation becomes larger as well.

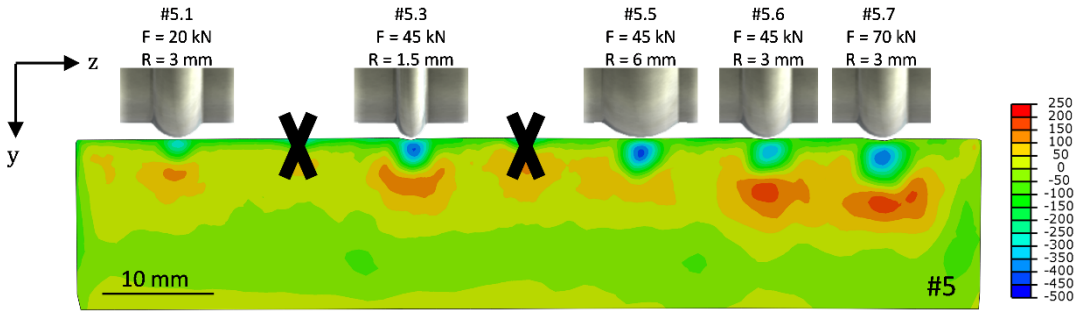

Figure 108: Residual stress map (σ_{xx}) of the rolled specimen #5.

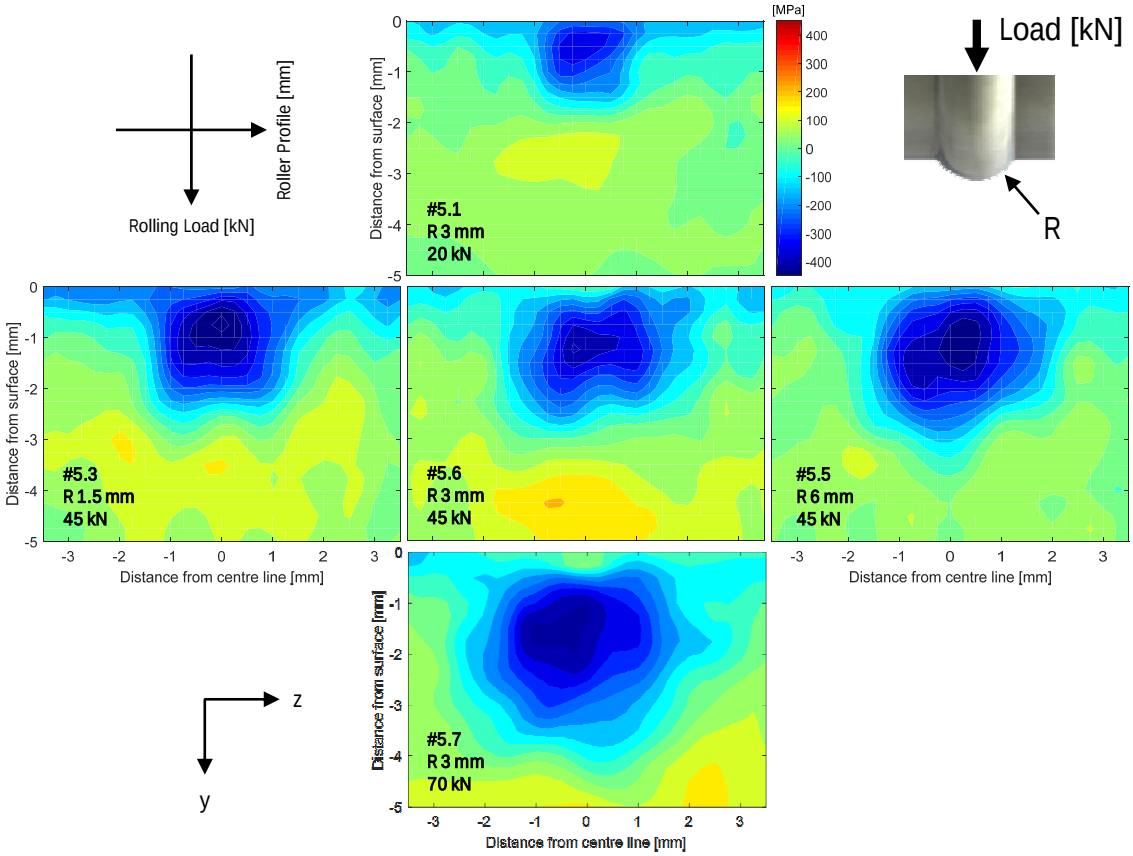

Figure 109: High magnification contour stress maps (σ_{xx}) of the rolling experiments

6.3.3 EBSD Strain Maps

The EBSD strain maps were produced at the same location as the residual stress maps above and are shown in Figure 110. The colour bar ranges from 1° to 6° lattice misorientation, which indicates no or low plastic deformation and strong plastic deformation respectively. White regions could not be indexed by the EBSD detector, because severe plastic deformation made the material unrecognisable. Keeping the load constant, but changing the roller radius did not change the penetration depth

significantly. The amount of plastic strain however increased dramatically with a smaller roller profile.

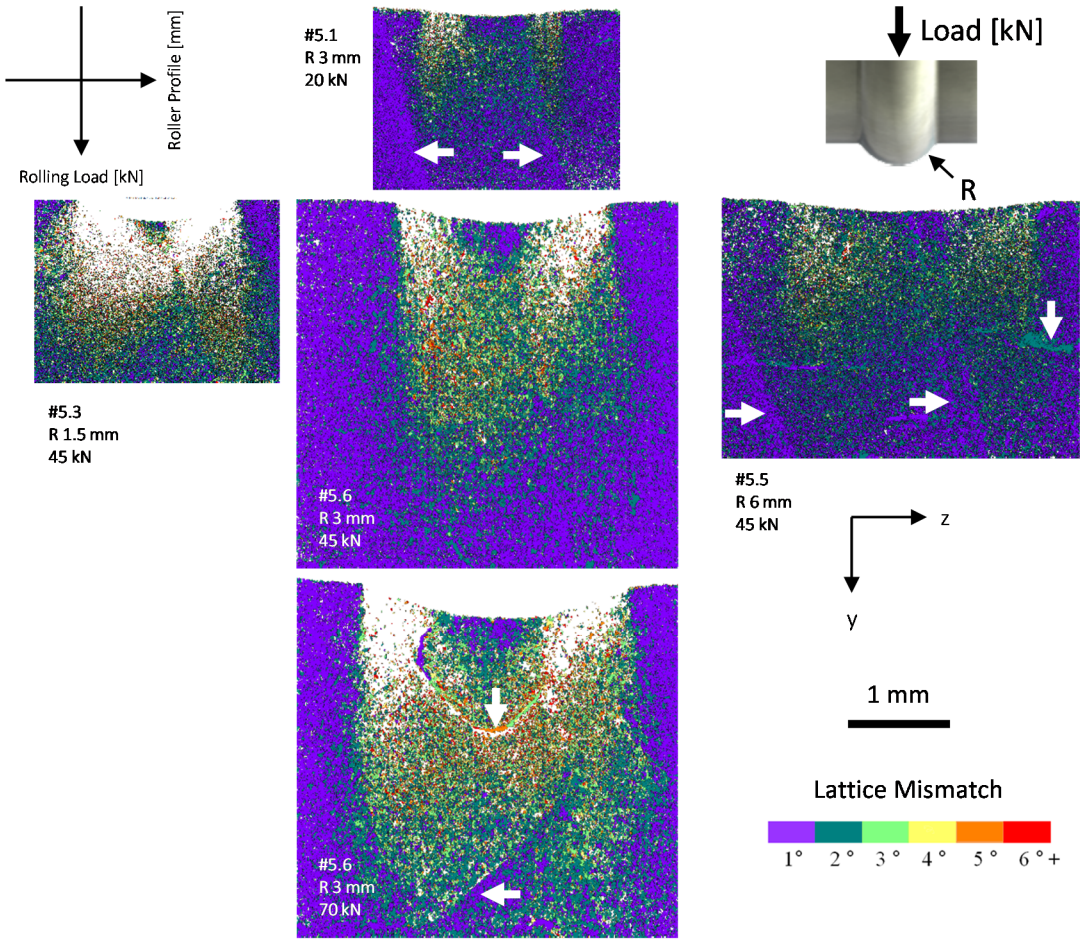

Figure 110: EBSD plastic strain maps of the rolling experiments

Increasing the roller load from 20 kN over 45 kN to 70 kN, while keeping the profile constant at 3 mm radius increased both the penetration depth and the amount of plastic deformation. All strain maps show that the largest amount of strain can be found below the edges of the roller contact, while the region just below the surface is virtually strain free. The white arrows indicate where layer bands or β-grain boundaries either affected the plastic deformation behaviour or the reconstruction procedure for strain mapping.

6.3.4 Hardness Maps

The hardness maps in Figure 111 are also located at the positions of the residual stress and EBSD strain map from above. The average stress of bulk material was 361 HV with a standard deviation of 7.3 HV. The colour bar was therefore set from 360 HV to 400 HV to highlight the area with increased hardness caused by work hardening. The plots are

symmetrical, because both values on either side of the symmetry line were averaged to mitigate microstructural features. Hardness indents that were located on a particular microstructural feature, such as a grain boundary, were disregarded, as they sometimes showed unnaturally low or high values that exceeded the influence of the cold work.

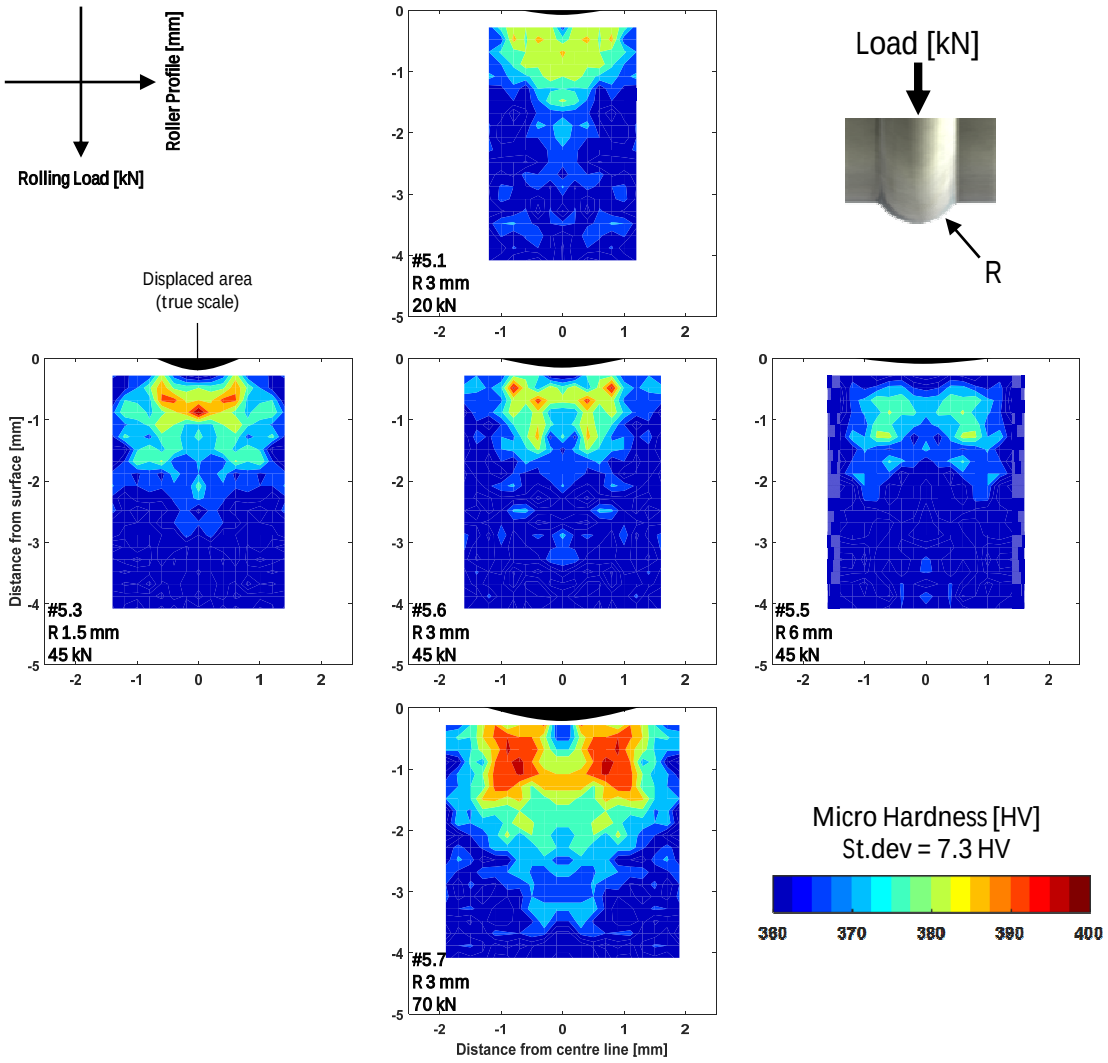

Figure 111: Vickers micro hardness maps of the rolling experiments

Generally the same observations made in the EBSD strain maps can also be made on the hardness maps. Decreasing the roller profile radius increases the hardness, but doesn't change the penetration depth significantly. Increasing the load however increased both, the hardness and the penetration depth. Looking at the hardness map using the small 1.5 mm radius with 45 kN load does not seem to produce significantly more hardness compared to the 3 mm radius. All five hardness maps show a greater amount of work

hardening below the edges of the groove and almost no hardening in the centre of the contact interface, like the EBSD strain map.

6.3.5 Numerical Simulation

The S11 residual stress and the PEEQ plastic strain are the equivalent numerical predictions to the contour stress map and the EBSD plastic strain map respectively. The two strain maps are only comparable qualitatively, as the EBSD map shows strain in form of lattice misorientation, while the simulation calculates actual strain. Also the hardness map should be comparable to the plastic strain.

6.3.5.1 Residual Stress Maps

The stress maps in Figure 112 show the results within a range between -850 MPa and +850 MPa, which is a larger range than the map of the contour method (Figure 109).

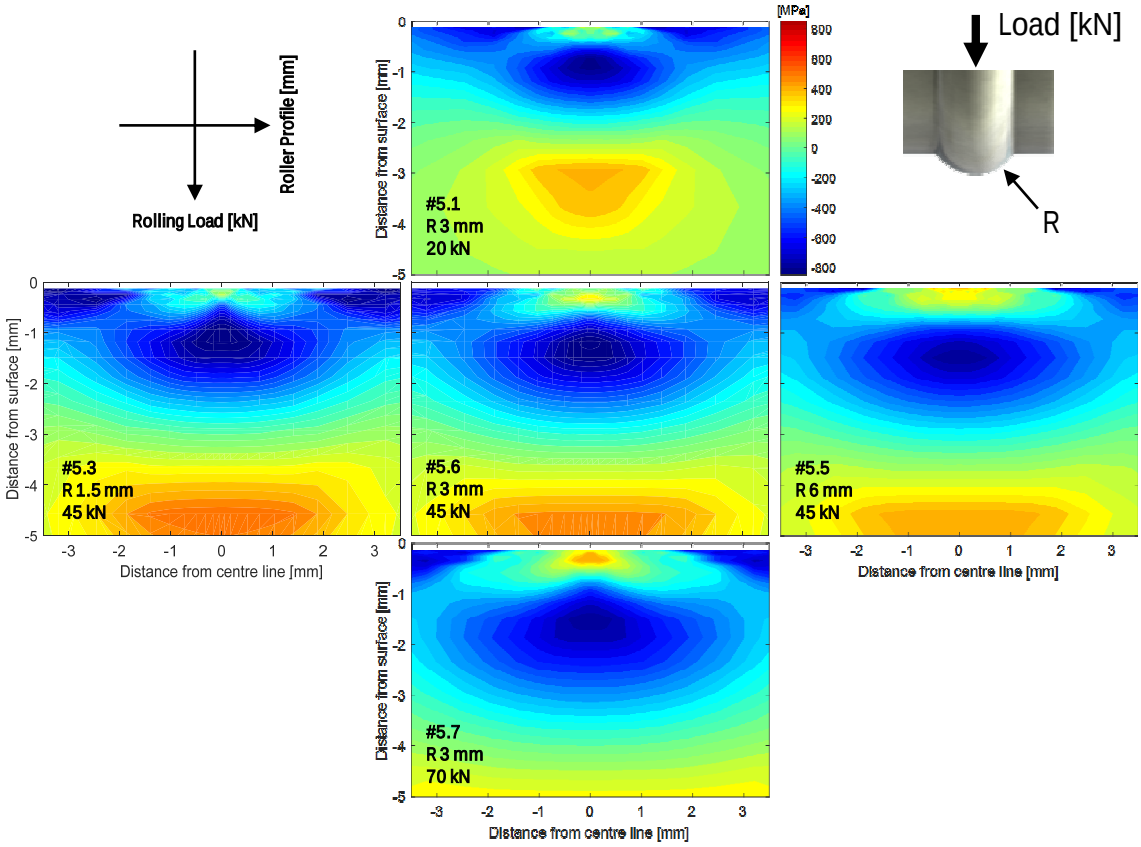

Figure 112: Simulated residual stress maps (S_{11} corresponds to σ_{xx} in Figure 109) of the rolling experiments.

This was necessary, because the calculated peak compressive stresses significantly exceeded the ones measured. However, the zero-crossing point and the influence of different rolling parameters allow the same observations to be made in the contour stress map. Increasing the load yields a greater penetration of both, peak compressive stress and zero-crossing, while the influence of the roller profile is negligible.

6.3.5.2 Plastic Strain Maps

The simulated plastic strain map (PEEQ) is shown in Figure 113. The observations made match the ones made in the EBSD strain map (Figure 110) and the hardness map (Figure 111). Increasing the load, also increases the maximum plastic strain and the penetration depth. The roller profile has virtually no effect on the penetration depth, but the smaller the profile was, the larger was the plastic strain.

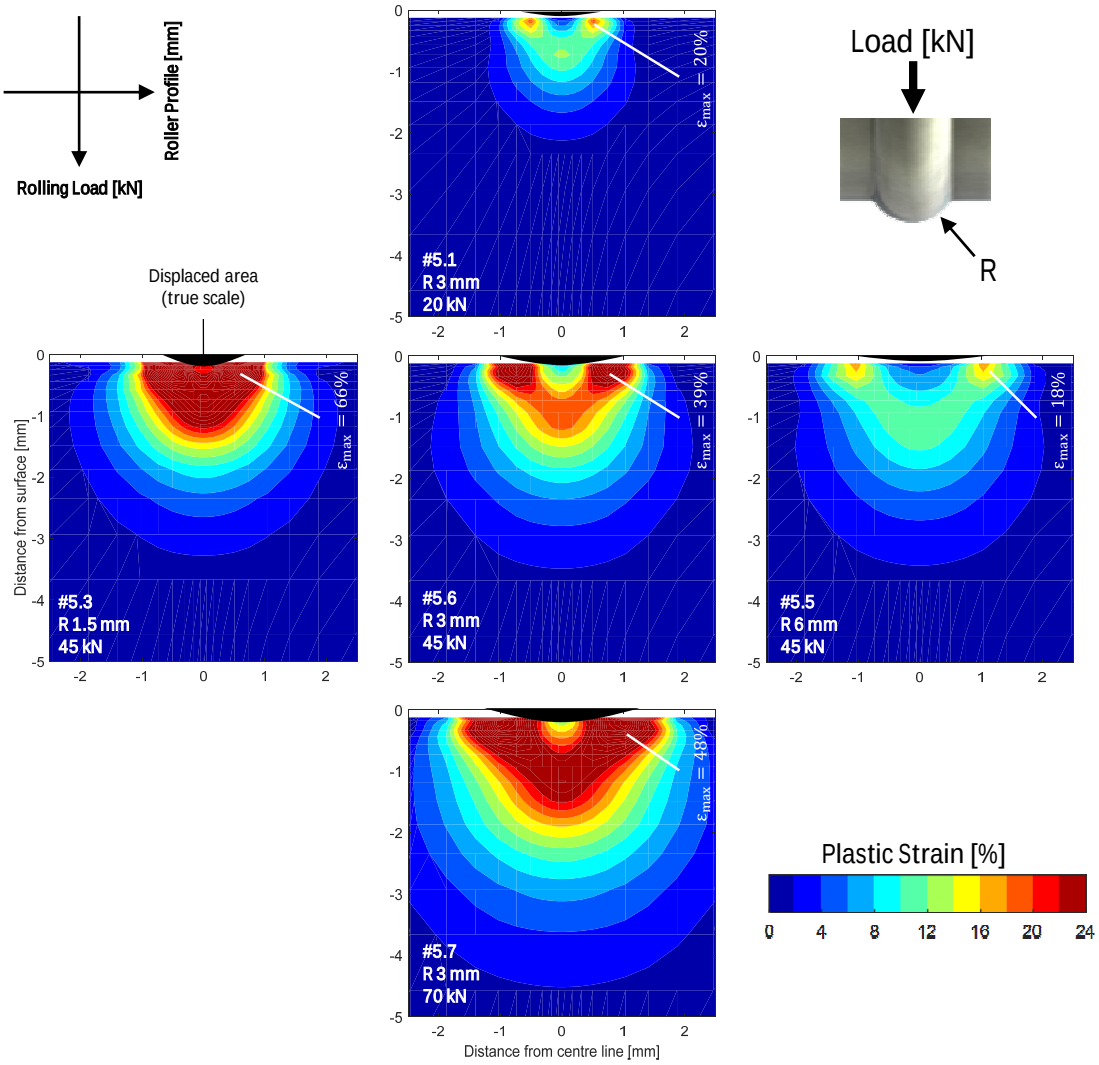

Figure 113: Simulated plastic equivalent strain (PEEQ) maps of the rolling experiments.

6.3.6 Grain Refinement after Heat Treatment

Finally Figure 114 shows the refined microstructure after β-heat treatment, in which the temperature history was quasi homogeneously distributed, unlike in WAAM, where the time that the material remains above the β-transus is much shorter and has a steep thermal gradient [77]. The individual refined β-grains are highlighted in random colours.

In specimens #5.1 (R = 3 mm; F = 20 kN) and #5.5 (R = 6 mm; F = 45) the degree of refinement was minimal and produced just a few grains in total, each between 1 mm and 3 mm in size. Increasing the load from 20 kN with the 3 mm profile increased the degree of refinement and the width and the depth of the refined region. The roller profile did not affect the maximum penetration depth significantly, but a smaller profile yielded much finer grains. The smallest grains achieved in specimen #5.3 (R = 1.5 mm; F = 45 kN) were approximately 200 µm to 250 µm in diameter.

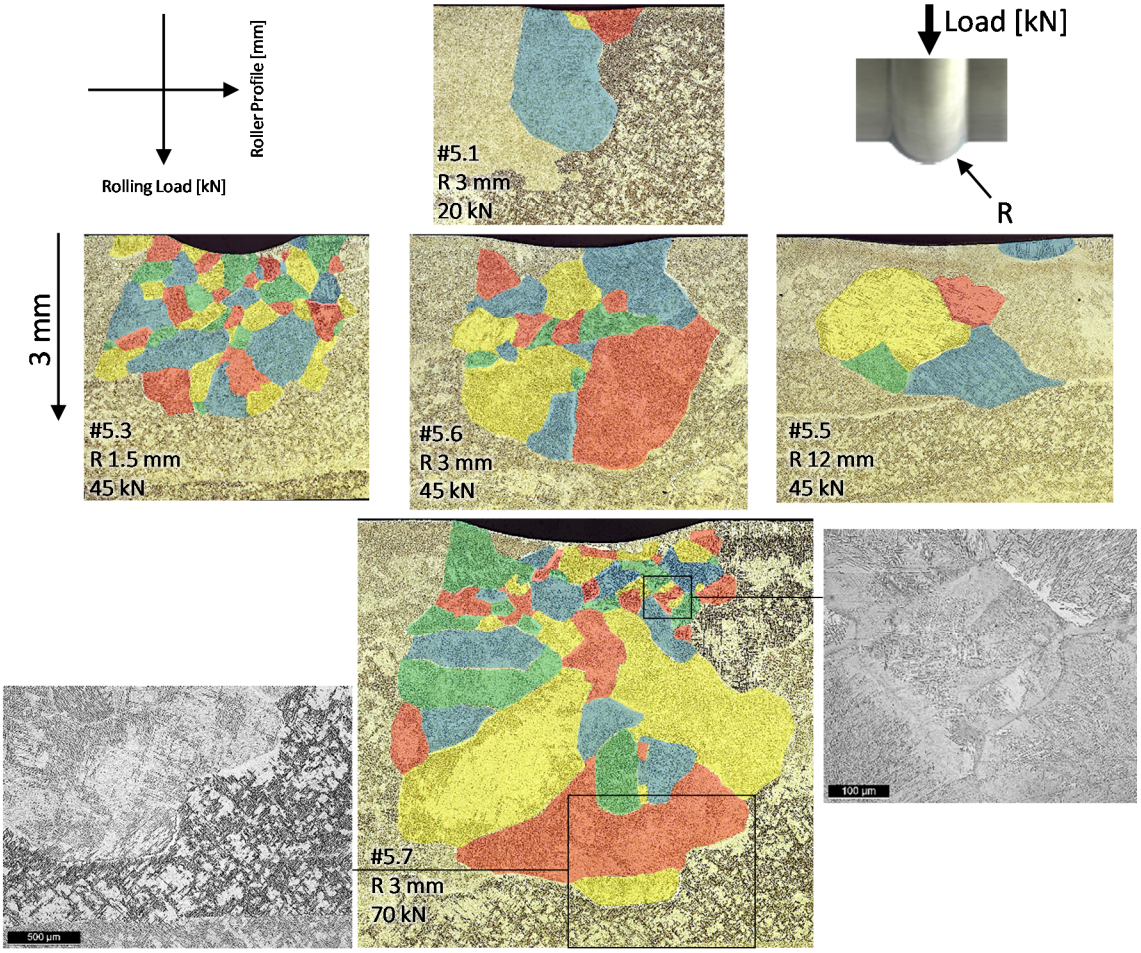

Figure 114: Refined microstructure after cold rolling and subsequent β-heat treatment (90 s @ above β transus; 1070 °C peak temperature) with a cooling rate of 12 °C/s through the transformation field.

6.4 Results Section B: MHP Experiments

Three different MHP parameters were tested in total. After the topography was taken, residual stress and EBSD plastic strain maps were measured. Finally the refinement was

observed using optical microscopy after heat treatment. MHP was not simulated and hardness measurements were not produced either.

6.4.1 Topography

The MHP groove profiles are shown in Figure 115 (a), from which the width and depth values in Figure 115 (b) were extracted. It shows that the larger radii produced wider grooves, but much less deep ones, despite the higher impact energy. The small tip radius of 6 mm did not only produce a much deeper groove, it also generated bulging at the edges of the groove, which was not the case for the larger geometries. Comparing specimen #2.3 (R = 6 mm; 250 mJ) and #5.5 (R = 6; 45 kN) shows that MHP and Rolling with 45 kN load can produce very similar groove geometries ($w_{\#2.3}$ = 2.17 mm; $w_{\#5.5}$ = 2.26 mm; $d_{\#2.3}$ = 46 µm; $d_{\#5.5}$ = 84 µm). The MHP tool and the Roller in this case both had a 6 mm profiled cross-sectional radius. However, the large circumferential diameter of the roller needs to be taken into account as well in this comparison.

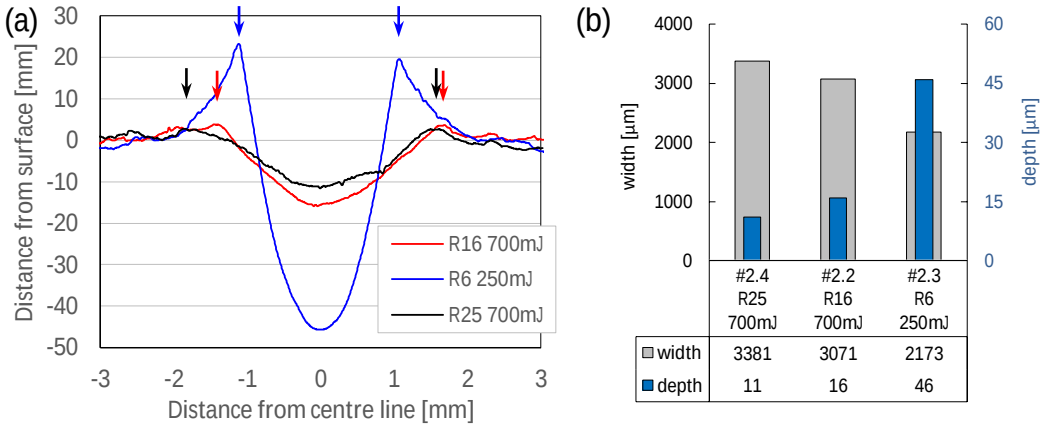

Figure 115: (a) surface profile of the MHP grooves and (b) the extracted results.

6.4.2 Residual Stress Maps

The full residual stress map in Figure 116 is the contour method results of the MHP specimen #2 and is equivalent to the rolling result in Figure 108 with an identical scale bar. The peened areas #2.1 (R = 6 mm; E = 250 mJ) and #2.5 (R = 25 mm; E = 700 mJ) show a typical peening stress profile, being compressive at the surface with a peak compression below the surface and balancing tensile stresses in the bulk material near to the compressive region. The measurement plane is normal to the peening direction, so the stresses in step direction z are expected to be larger in magnitude, but similar in

penetration. Interestingly, the compressive stress seems to increase slightly in the step direction. The area treated with the smaller ball radius of 6 mm generated larger compressive stress, even though the impact energy with 250 mJ was lower than the 700 mJ tool using a 25 mm radius and the peening density was with 4 impacts/mm^2 also much smaller compared to 100 impacts/mm^2.

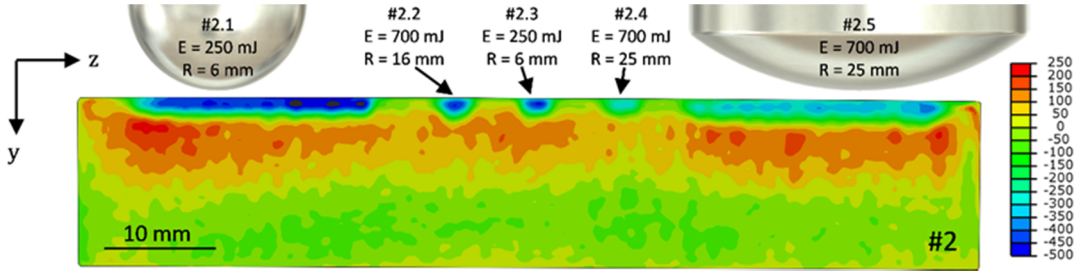

Figure 116: Residual stress map (σ_{xx}) of the peened specimen #5.

The three peened lines are shown with higher magnification in Figure 117 (a-c) and compares them directly with the EBSD plastic strain maps (d-f) and the refined microstructure (g-i). The 250 mJ tool with 6 mm radius (a) produced a virtually identical stress map to the one produced by the 700 mJ tool with 16 mm radius (b). Using the high energy tool with an even larger diameter impeded the effectiveness and decreased both, the peak compressive stress and the penetration depth (c).

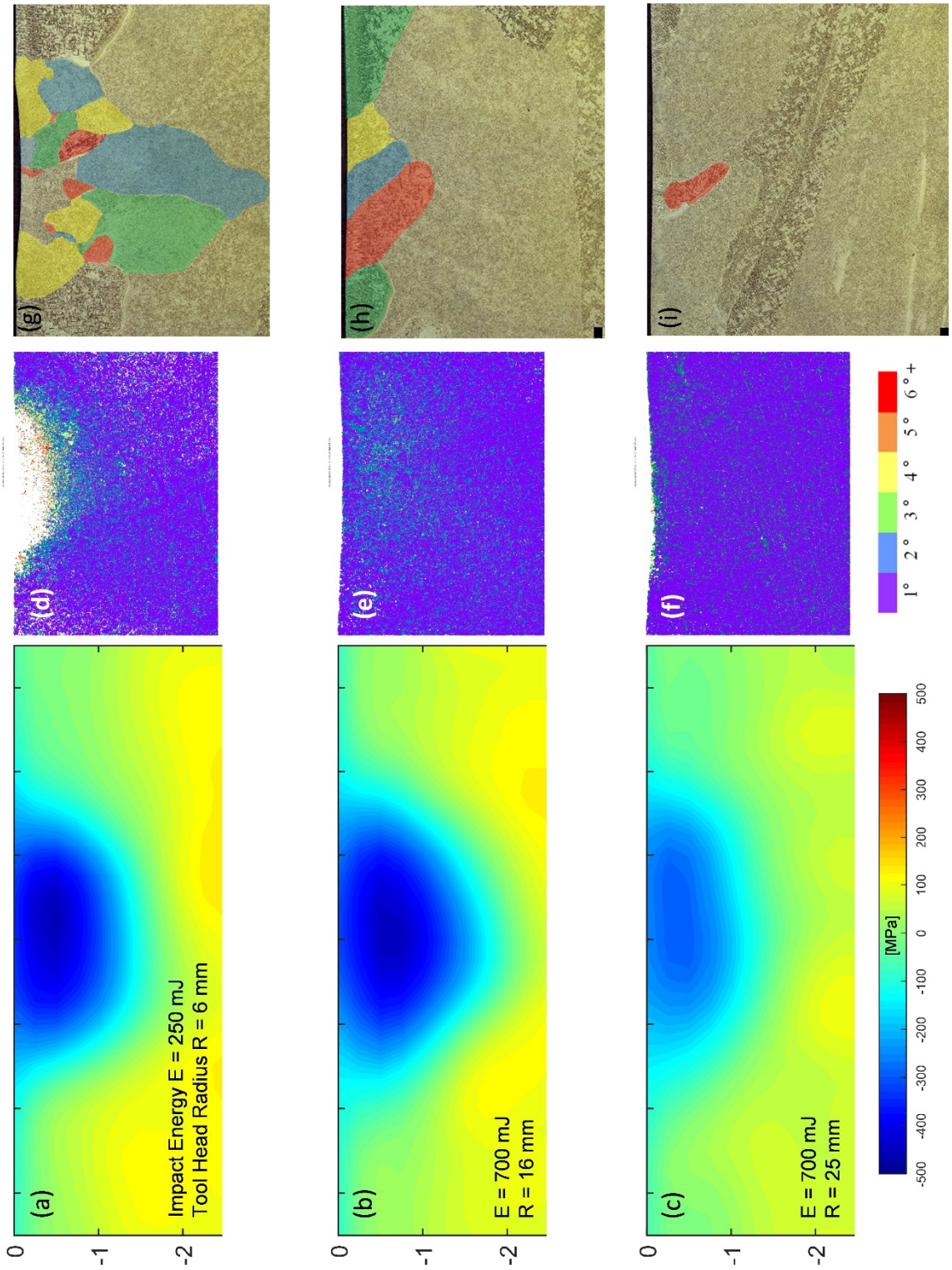

Figure 117: (a-c) Contour Method residual stress map (σ_{xx}) of the three MHP single lines; (d-f) respective EBSD plastic strain maps and (g-i) microstructure after heat treatment. All figures with identical scale.

6.4.3 EBSD Strain Maps

Even though the compressive stress fields of (a) and (b) are very similar, the equivalent plastic strain maps (d) and (e) with these parameters show significant differences. The small radius induced plastic deformation to an extent that the EBSD system could not even index the material anymore, producing the plane white area (d), which is surrounded by material that shows hcp deviation of between 4° and 6°. This strain field produced is nearly identical to the one produced by the ForgeFix XP in the previous chapter. 2° and 3° deviation can be observed up to approximately 1.2 mm below the surface. The plastic strain from the high energy tool using the 16 mm radius (e) produced hardly any strain that can be resolved using the EBSD strain mapping technique. Only 2° or maybe 3° deviations can be found, which are evenly distributed up to approximately 1.2 mm below the surface. Finally EBSD mapping could not identify any strain induced lattice misorientation using the largest radius of 25 mm (f), even though residual stress was induced (c).

6.4.4 Grain Refinement after Heat Treatment

No grain or at most a single grain was refined (i) after heat treating the material that was peened with the 25 mm radius ball. The 16 mm radius provided slightly more deformation that yielded slightly more refinement (h). However, the refinement of both is ultimately still not noteworthy. MHP with the small 6 mm radius allowed more significant grain refinement, as shown in Figure 117 (g), even though the impact energy was less than the other two. The smallest grains achieved were approximately 400 µm in diameter and are located near the surface, while the refined grains deeper inside the material are approximately 1.5 mm and are much larger. The distribution of grain refinement is therefore much more inhomogeneous compared to the refinement achieved by rolling (Figure 114).

6.5 Discussion

6.5.1 Accuracy and Comparison of Characterisation Techniques

6.5.1.1 Contour Method

The contour method (CM) produces residual stress maps with high resolution and measurement depth, but the limits of this relatively young technique are debatable

[189], [222], [224]–[226], as discussed in chapter 1.7. The present results were tested with different smoothing and knot spacings and they appear to be independent. The maximum compressive stress measured in this chapter using the contour method was 500 MPa (Figure 108) and is significantly lower than the material's yield value [92] [Appendix D] and lower than the compressive stresses expected and numerically predicted (Figure 112).

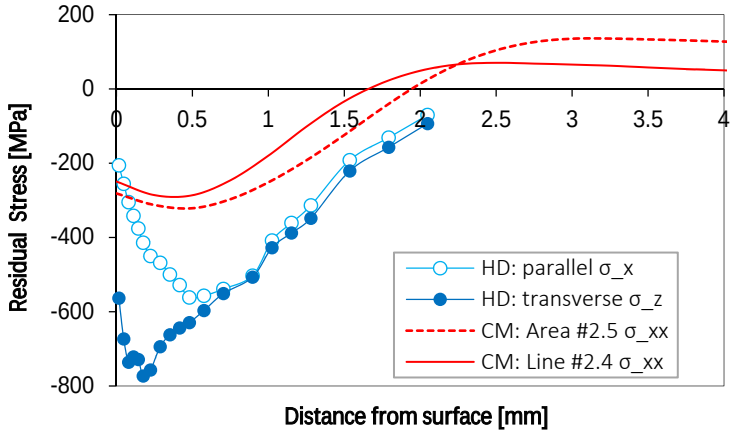

Figure 118: Comparison of MHP residual stress measurement (700 mJ, 25 mm ball radius): CM vs. HD.

A common issue of the CM is plasticity, which occurs during the wire-EDM cut, when the residual stresses are close to the material's tensile yield value and causes plastic strain at the edge of the EDM wire [226], [245]. Cutting through compressive stresses can cause a different problem. When compressive stresses are relieved, the cut surface expands. This gap can close and pinch behind the EDM wire, resulting in underestimated compressive stresses [245]. This effect is especially problematic with thin EDM wires and cuts, could be a reason for the "relatively small" compressive stresses measured. The CM is often compared against other more established residual stress measurement techniques, such as XRD or incremental hole drilling (HD) [104]. Like the CM, HD is a stress relaxation techniques that measures strain during material removal. HD in this chapter was only performed to validate the contour results, as it cannot be performed to measure the stress under the peened grooves, nor can it yield the required spatial resolution.

In this chapter one comparative HD measurement was performed with the only purpose to discuss the measurement accuracy of the CM. Figure 118 shows the comparison of

the HD method in the directions parallel and transverse to the peening directions with the contour method of the 700 mJ tool and 25 mm ball radius. The transverse direction shows larger compressive stress than the longitudinal direction, but they converge deeper into the material, which is typical for peening induced stresses [152]. The contour stress is significantly lower than the corresponding parallel stress measured with hole drilling. Both measurements calculate a surface residual stress of -250 MPa, which increases to a maximum at 0.6 mm deep. The maximum in the hole drilling profile is -570 MPa, while the contour method only calculates -300 MPa. The zero-crossing point of the peened area measured with the contour method is nearly 2 mm from the surface, which is the maximum depth measured with HD, which seems to result a mariginably deeper zero-crossing point. Even though both techniqes agree in the depth of the compressive maxima and the zero-crossing point, the magnitude calculated by the contour method is doubtfull, suggesting issues during the EDM cut for the contour method. This could be due to gap closing, plasticity or other effects.

Even though the comparative HD revealed some discrepances with CM, typical landmarks, such as location of peak compressive stress and zero-crossing match. This can also be assessed in the stress maps of the rolling trials, when comparing the contour method (Figure 109) with the numerical simulation (Figure 112). In this comparison, the simulation predicts higher peak compressive stresses than the CM, but the locations of peak compressive stress and zero-crossing match as well. This suggest the same underprediction of residual stress measured using the CM, which was also suggested by the comparison with the HD.

6.5.1.2 EBSD Strain Map

The exemplary plastic strain map in the appendix D in Figure 151 was produced using 90 kN rolling load and the 3 mm radius profile. A large plastically deformed region can be identified, which is indicated in red colour. Instead the results in the present chapter showed a not-indexed white region, which was expected to be orange or red, indicating 5° or 6° lattice misorientation respectively. This lattice misorientation was too high for the EBSD detector used in this study to index or identify the lattice at all.

One reason can be careless sample preparation. But this can be excluded, because the overall indexability during the scan in this study was above 85 %, which is comparable to the one achieved in the appendix. Another reason could be the relatively old EBSD detector used compared to the reference. Finally, longer scanning time per point also could have helped to identify the local lattice orientation at the expense of scanning time. Nevertheless, the plastic strain map might appear less appealing, but it does not lack of significance, as the region of very large plastic deformation appears white instead of red.

6.5.1.3 Hardness

The hardness of bulk Ti–6Al–4V WAAM material that was not plastically deformed was 361 HV with a standard deviation of 7.3 HV. The maximum hardness due to cold work measured was in very rare cases around 400 HV. The standard deviation is therefore relatively large compared to the work hardening effect that is supposed to be revealed. This is more due to the poor work hardening characteristics of Ti–6Al–4V, rather than a high standard deviation. However, large errors of hardness measurements can occur when the indent coincides with landmarks, such as different α plates sizes or grain boundaries, as shown in Figure 119 (a).

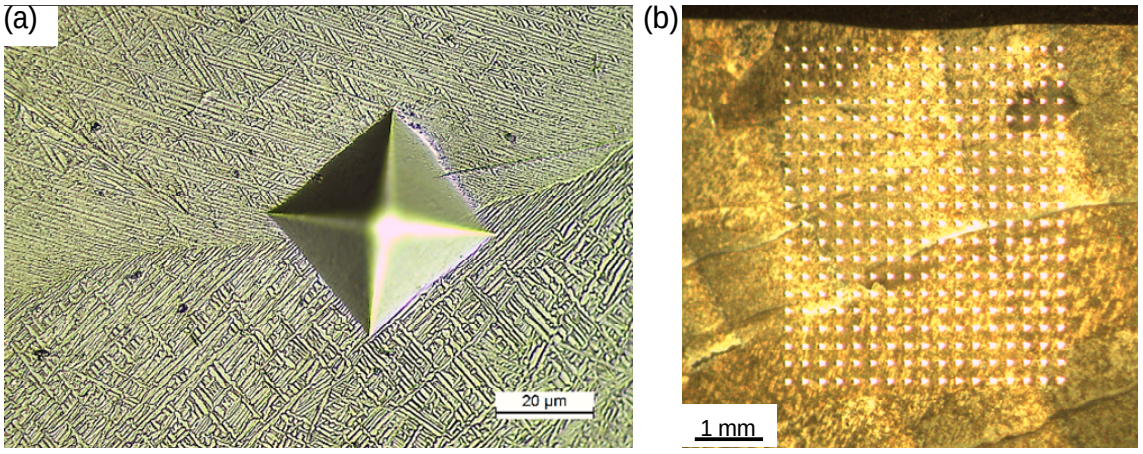

Figure 119: (a) A hardness indent coincides with a grain boundary and results a wrong hardness value; (b) indentation location of the #5.5 hardness map.

Unexpected deviation from certain values should be excluded, if (and only then) this deviation is due to an unfortunate location of a hardness indent. It should be noted that the α-plates of this Widmanstätten microstructure are probably identical in size, but

appear different, due to their orientation, as suggested in appendix B in Figure 147. If they were different in size, then dissimilar values of hardness should have been observed on either side of the prior β grain boundary [131], which was not the case. A second source of error can be that the measurement location within layer bands, as this also influences the hardness, since the α-plate size changes within the bands [77] and smaller plate, constitute harder material [23]. Also residual stresses can influence hardness measurements, which are relieved normal to the surface, but can still be present in-plane. Compressive stresses can hinder the diamond indentation, and tensile stresses can facilitate it, finally suggesting too high or too low hardness values, respectively [246]. A large number of measurement points is therefore required for significance, but the highest possible indentation density does not allow more measurements per point that can be averaged, as shown in Figure 119 (b). Averaging both symmetrical points on either side of the centreline mitigated the effect of inhomogeneously hard raw material and other features.

6.5.1.4 Simulation

A weakness of this simulation are the limited material properties. Only tensile properties [92] were available at the time of the simulation, as the compression tests in the appendix D were not completed before the end of the project. The relatively high discrepancy between the simulation of the residual stresses (Figure 112) and the contour method stress measurement (Figure 109) certainly impedes the confidence in at least one of the characterisation techniques. Future work will involve including compressive properties and material failure.

6.5.2 Influence of Rolling Parameters

6.5.2.1 The Effect on Stress Induction

The plots in Figure 120 (a) and (b) are taken from the stress maps in Figure 108 and Figure 112 and highlight the effect of the rolling load and the profile radius. Both plots show the results of both, the contour map (dashed lines) and the simulation (solid lines). Regardless of the accuracy of the measurement, both techniques agree with the location of maximum compressive stress and zero-crossing point. Increasing the load shifts the compressive stress profile deeper below the surface (Figure 120 (a)). More interestingly,

the roller profile has a marginable effect on the compressive stress profile. Larger radii produce a profile with the peak compressive stress and the zero-crossing point deeper. It is anticipated that further increasing the radius will reduce the contact pressure to an extent that impedes plastic deformation.

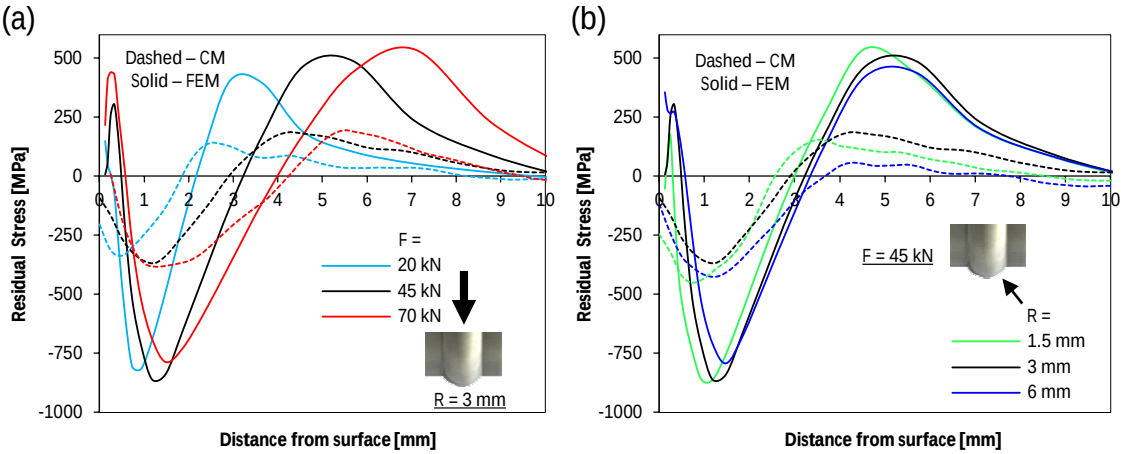

Figure 120: Influence of (a) the rolling load and (b) the roller profile radius and the residual stress induction. The solid lines show the numerically predicted stress using ABAQUS (Figure 112) and the dashed lines show the contour method results (Figure 109).

Cold rolling appears unsuitable for the purpose of near-surface compressive stress induction, as all parameters produced a tensile residual stress, before the compressive region developed, which facilitates crack initiation [192], [193]. The EBSD plastic strain, the simulated plastic strain and the hardness maps show that the material near the central contact point was virtually undeformed. This is due to friction at the contact interface, which prevents plastic stretch transverse to the rolling direction [240].

6.5.2.2 The Effect on Strain Induction

The effect of the same parameters on the plastic deformation behaviour is of interest, because it determines the size of the refinement area and the degree of refinement within this area. Figure 113 and Figure 114 suggest the minimum plastic strain required to achieve refinement. The border of the refined microstructure in Figure 113 coincides approximately with plastic strain in Figure 114, where 6 % to 8 % of plastic strain was induced, which is a similar to the values predicted by Martina et al [77]. Higher values above 12 % however are much more effective to produce smaller grains, leading to an assumption that the large refined grains actually grew from the refined grains and did

not refine themselves. The final chapter 7 contains evidence that support this assumption.

The strain profiles in Figure 121 are shown for values up to 24 %, however plastic strain above approximately 18 % resulted in a decrease in hardness values. The hardness indent is effectively plastic deformation on prestrained material. Prestraining by MHP above 18 % presumably led to work softening [247] and therefore facilitated the hardness indentation. An ideal plastic strain with the purpose of grain refinement can therefore be concluded to be between 12 % and 15 %. It should be noted that iterative rolling and re-heating the same region can further refine a refined β-grain size [86]. Also the long holding time above the β-transus during the heat treatment in this study could have allowed β-grain growth after refinement [238]. This effect was also observed in a preliminary study (appendix E). Furthermore deforming bulk material is more difficult compared to a slender WAAM wall without lateral restraint. The obtained β-grain sizes can therefore not be compared against an inter-pass rolled Ti–6Al–4V WAAM wall microstructure [77], [86].

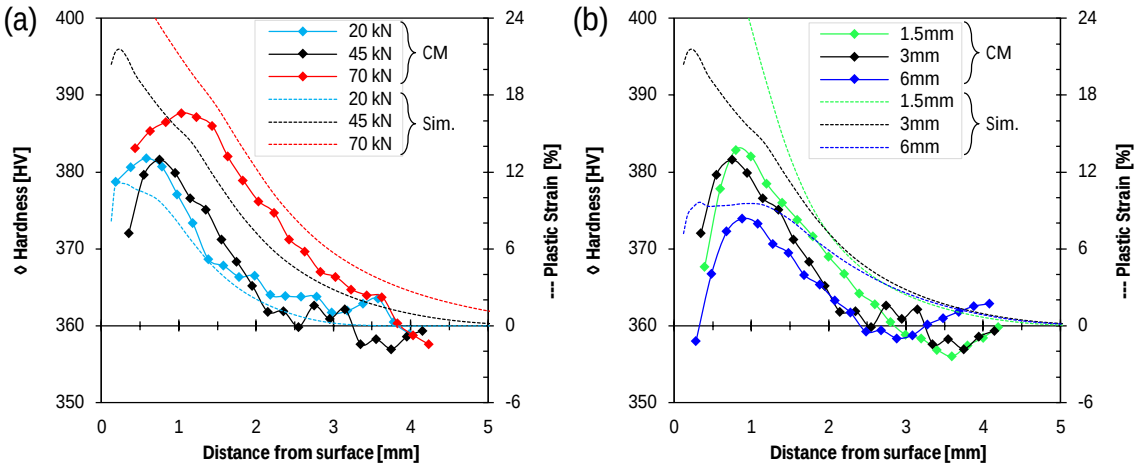

Figure 121: Effect of (a) rolling load and (b) roller profile on cold work penetration. The diamond marker indicate hardness measurements and the dashed lines the plastic strain. The values are the average of all measurements taken below and within the rolled groove. Zero plastic strain was referenced to 360 HV, which is the bulk material hardness.

The effect of the parameters, load and geometry, on the work hardening behaviour is similar to stress induction. Figure 121 (a) shows that increasing the load shifts the hardness and plastic strain profiles deeper into the material, but they have similar

slopes. The roller geometry again does not influence the penetration depth, as all three simulated profiles converge at and below 2 mm depth. Closer to the surface smaller radii produce a larger strain gradient. This effect is attributed to very large contact pressure of a small radius near the surface that distributes inside the material.

6.5.3 Influence of MHP Parameters

6.5.3.1 The Effect on Stress Induction

The MHP tools HAM-A and HAM-C with 250 mJ and 700 mJ impact energy respectively achieve stress profiles that exceed the ones produced by the ForgeFix XP and the Accurapuls in the previous chapter. Figure 122 shows the stress profiles taken from the contour map in Figure 116 through the entire thickness. 250 mJ impact energy using a 6 mm profile radius produced a compressive profile up to 1.75 mm distance from the surface with a peak compressive stress of -450 MPa at 0.5 mm. Similar to the findings from Figure 120, it can be suspected that the contour method results underpredict the real stresses. The locations of peak compressive stress and zero-crossing however are trustworthy. Unlike in the rolling experiments, no tensile stresses were induced at the surface, because the MHP does not prevent near-surface plastic flow by friction between both surfaces in the contact zone.

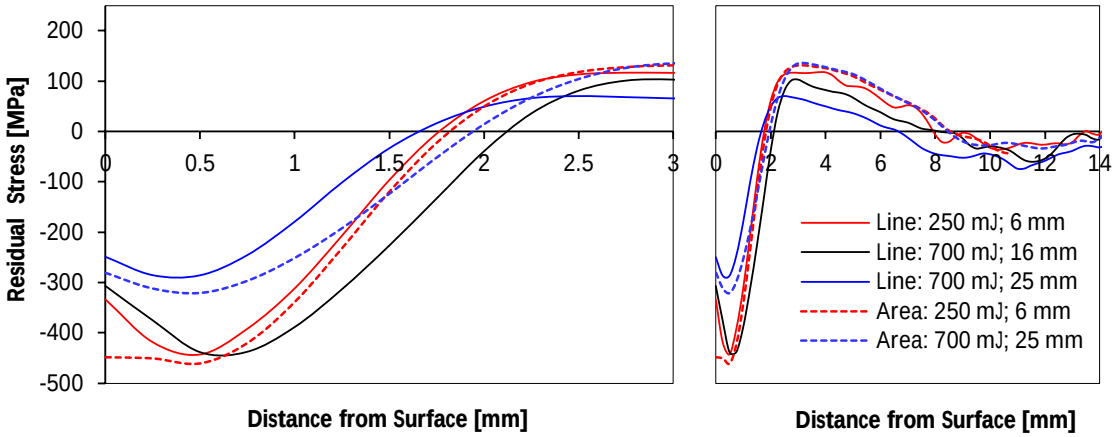

Figure 122: Stress profiles extracted from the five peening experiments in Figure 116.

The high impact energy of 700 mJ using a 16 mm radius produced compressive stresses up to 2.1 mm distance from the surface and the profile of the peened line reaches the maximum of -450 MPa at 0.7 mm depth. These are respectable penetrations, compared to other peening techniques [162], [197]. However, the zero-crossing was expected to

be closer to 4 mm distance from the surface, which would have been equivalent to the stress profile produced by the same tool on tough Inconel [241]. Further increasing the radius to 25 mm reduced the peak compressive stress to approximately -300 MPa at 0.5 mm distance from the surface. This means that the contact area became so large that not much plastic strain was induced. Using the R16 pin is therefore more suitable for a deep compressive stress induction.

A direct comparison with the 250 mJ tool and the 700 mJ tool is difficult, because the experiments were performed with different tip radii and impact density. However, theoretical contact mechanics (appendix A) supports these results. According to Hertzian pressure the impact energy would have to be 250 mJ * $2^{2.5}$ = 1415 mJ to double the penetration depth.

6.5.3.2 The Effect on Strain Induction

The results in Figure 117 show that hardly any plastic strain was induced with the larger diameter peening tool. Only the 250 mJ tool induced more severe plastic deformation, which resulted in moderate grain refinement, thanks to the small contact tip. Even though the heavy 700 mJ tool produced larger stress profiles, the strain induced was actually less and insufficient for refinement purpose. The reason for this is the typical application of MHP tools: They were initially designed for surface smoothing applications and near-surface hardness to improve wear resistance [155], [157], [158]. This involves a large ball diameter for a typical impact energy that other tools provide [199]. Compressive residual stress near the surface to prevent crack initiation for improving the fatigue life [161] requires a smaller contact for the same impact energy to deform more material plastically.

Figure 117 shows that more plastic deformation is required to produce grain refinement, compared to compressive stress induction. Indeed the amount of plastic strain required for the present purpose is detrimental to all other MHP application, which is why small tip diameters are not available and need to be custom built. A tip radius for the 700 mJ MHP tool "HAM-C" would benefit from a slightly smaller tip around 10 mm. However, the accomplished penetration depth of 2 mm maximum is insufficient and should be increased for Ti–6Al–4V WAAM applications to be competitive to rolling.

This is only possible with even higher impact energies of a few joule or more, for which the ideal tip radius needs to be established as well. Such an application makes high demands on the material of the pin, which has to have a hard surface with high strength to prevent plastic deformation of the tool, but at the same time needs a tough and ductile core to prevent brittle failure.

6.5.4 Practicality

6.5.4.1 How to achieve grain refinement

In order to achieve grain refinement, plastically deformed Ti−6Al−4V material needs to be taken above the α-dissolution temperature [77], but the degree of strain in combination with a certain temperature and time is unknown. Martina et al. [77] found that the strain is the dominant factor, rather than the temperature, which is already the partial answer. However, the effect is described as a common recrystallisation processes based on stored energy, even though the actual strain is surprisingly low for the observed effect [86]. The concurrent understanding of the refinement process is therefore the following [72]: Compression induced twinning of the residual β-phase is less favourable in Ti−6Al−4V [71], but can occur at relatively low critical resolved shear stresses, when the dimension of the phase is below a critical, but unknown value [73], [248]. After rolling, the α-plates and surrounding twinned β-cells are not aligned according to BOR anymore. Therefore, when the twinned β-phase start to grow due to heating (at the Ti−6Al−4V α-dissolution temperature of 748 °C [88]), it ingests the neighbouring α-phase. Once a sufficient amount of α-plates are incorporated by the growing β-phase, then it loses the memory of its initial orientation and follows the new twinned β-orientation according to BOR. This is the case for the respective degree of strain if sufficient temperature is given in combination with enough time, because Ti−6Al−4V diffusion kinetics apply [235]. Refinement can be achieved more than once on the same section in an repetitive process [86] and does not require full β-transformation or even temperature, as previously suggested [29].

The present study sought to focus on the dominant effect first, the plastic strain, which is why a homogeneous heat treatment above the β-transus was chosen. This should have allowed refinement for the minimum plastic strain, conceding eventual β-grain

growth in the same step [238]. The effect of the temperature distribution on the degree of refinement at homogeneously distributed strain is the subject of the last chapter 7.

Figure 123 compares directly the degree of refinement (a) with spatially resolved hardness maps (b), EBSD strain maps, which precisely shows where plastic strain occurred (c) and the numerically predicted plastic strain. The four images show the results of 70 kN rolling load using the 3 mm roller profile radius.

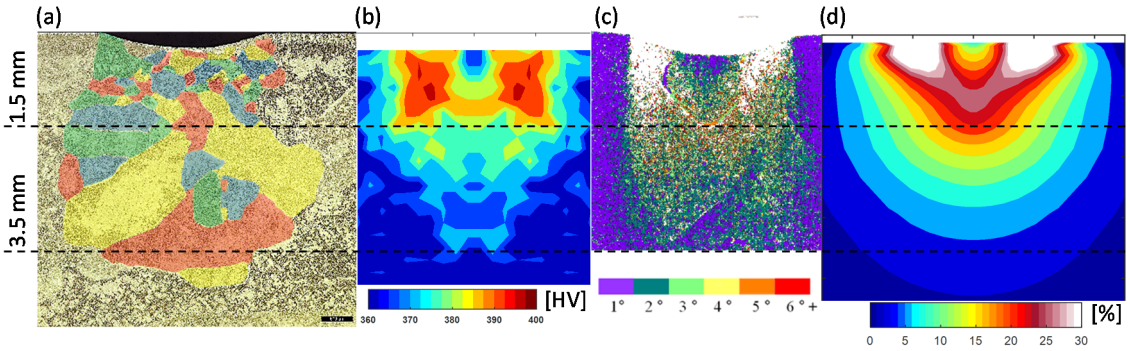

Figure 123: Effect of cold work on grain refinement using 70 kN rolling load with a profiled radius of 3 mm: (a) refinement after heat treatment; (b) Vickers hardness map; (c) EBSD plastic strain map; (d) modelled plastic strain.

Two significant regions can be assigned to all four of them: Region I is located between the surface and 1.5 mm distance from the surface. Very small grains can be found, which are caused by the large plastic deformation (c, d) prior to heat treatment. The region with the most plastic strain (> 20 % and > 4 ° respectively) below both edges of the rolled groove also exhibit the highest hardness of up to 400 HV. Further increasing the plastic strain caused the hardness to reduce again, and did not result in smaller refined grains This becomes evident, when comparing #5.3 (R = 1.5 mm; 45 kN) with #5.7 (R = 3 mm; 70 kN) in Figure 111, Figure 113 and Figure 114. Region II is located between 1.5 mm and 3.5 mm distance from the surface. Interestingly, this is near the zero-crossing point of the residual stress (Figure 120). The induced strain is lower, the hardness values hardly exceed 380 HV and the EBSD strain map shows between 2° and 3° lattice misorientation. This allowed basic refinement, but not to very much. It is believed that rolling and heating again can produce significantly smaller grains in both regions [86], which is what preliminary tests show more clearly (appendix E). The depth of both

regions is almost entirely driven by the rolling load, while the roller profile determines the amount of plastic strain in region I, but hardly the penetration depth of either region (Figure 121).

70 kN rolling load with a 3 mm radius profile resulted in the ideal amount of plastic strain in region 1, suggesting that the material has been deformed to the end of the stress/strain curve [92]. Higher loads would move both regions deeper inside the material, but it would also produce more plastic strain in region I, which is of no further benefit. For higher loads, up to 100 kN, a larger profile could be chosen to distribute the required plastic strain over a larger area and to produce wider rolling grooves, which allows to cover the same area with less passes. To assign the required rolling load, the deposition parameters determine the required depth of plastic strain: Grain refinement can occur within the HAZ, if the material was deformed prior to deposition. In other words, the material can be strained up to the depth, where the HAZ of the subsequent layer is expected. Plastic strain that exceeds this depth does not yield refinement triggered by process heat, but it could be useful to mitigate the residual stresses.

Figure 124 calibrates the measurement techniques against each other, which appear to have a relatively linear relationship. Little refinement occurs when material is heated, which is indicated between 2° and 3° lattice misorientation in the EBSD strain map.

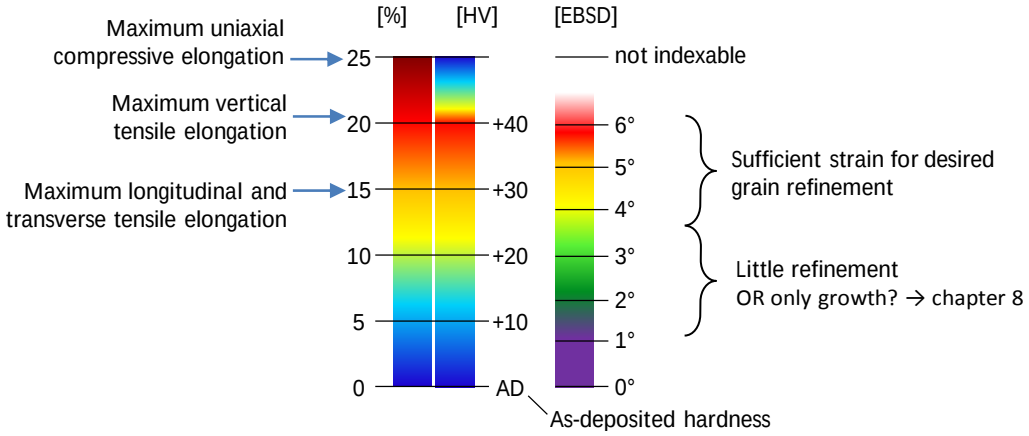

Figure 124: Proposed correlation between plastic strain measurements and grain refinement

This is supposedly reached at approximately 5 to 10 % plastic strain, which can be measured with Vickers hardness values around 10 HV to 20 HV above the as-deposited hardness. Great refinement can be achieved at EBSD lattice misorientation of more than

4°. This refers to more than 12 % plastic strain and can be measured with hardness values that are between 25 HV to 40 HV above the as-deposited hardness. The peening strain maps are less well distributed, if they induced measurable plastic strain at all (Figure 117 (d)). Extreme plastic strain (region I) is localised at the very top and resulted in good refinement, while region II contains hardly any plastic strain and only produced minimum refinement Figure 117 (g)). Region I is approximately 0.75 mm deep. Using MHP with these parameters for inter-pass grain refinement would not plastically deform all the material, as the typical layer height usually exceeds 1 mm [77], [92], [141] and this does not even consider remelting. However, since the β-grains that form during solidification grow epitaxially on the existing grains [83], it is beneficial if these are smaller already and not textured, as opposed to the established microstructure. In other words, if the remelting does not exceed the depth of large plastic strain regions, produced by MHP, a reasonably refined microstructure can still be established through the entire wall height. But for maximum grain refinement, region I of MHP should be at least as deep as the layer height plus the remelting depth. The latter is not well understood either, as optical inspection of the deposit does not allow the view inside the molten pool and the bottom of it. Also the fusion boundary cannot easily be revealed in Ti–6Al–4V in etched microstructures [77], [86], [90]. The depth of the remelting is therefore also the subject of the last chapter 7.

6.5.4.2 The ideal cold work application

Inter-pass rolling of single pass walls wall concentrates the refinement in the centre of the wall, while the near-surface grains remain larger [77], [86]. The lack of lateral restraint of the wall allowed large plastic strain [111] and therefore great refinement in the centre. MHP evidently concentrates the refinement at the surface region under the peened area. Since it can be applied on the side, MHP can be used to surface finish the sides and subsequent laser or furnace heat treatment can achieve the refinement, where rolling could not. Deforming bulk material, for example in wide walls using multi-pass or oscillating pass strategy [92], is therefore more difficult, as the surrounding material of the deformed zones, prevents large strain [143], [144]. Those wide features are typically near net-shape and will be machined [27], which is why refinement would

not make sense here. Inter-pass cold work must therefore be applied vertically. One advantage of MHP is the much greater manipulation speed of the tool over the part compared to rolling. The results in Figure 117 were achieved with travel speeds of 200 mm/s (impact frequency was 400 Hz) as opposed to the 7 mm/s of rolling. A second advantage is that the walls do not have to be vertical and straight anymore for cold work treatment by MHP. Furthermore, the manipulator only has to manipulate the payload (<20 kg) of the MHP tool and does not have to bear the reaction forces of the impacts [241]. The stiff gantry required that bears the reaction forces in rolling (up to 100 kN) also constrains the working envelope significantly [27], [143], [144]. However, for taking advantage of the benefits of MHP, the tools need to provide higher impact energies in order to compete with rolling. An example would be the RRH06P riveting hammer, which has an impact energy of 6000 mJ (at 36 Hz impact frequency) and can be manipulated by a robot to induce compressive stresses between 5 mm to 10 mm deep into steel [195], [196], [249].

6.6 Conclusion

1) Higher loads achieve higher penetration depth regarding residual stress induction and plastic deformation, of which the latter yields a greater depth of grain refinement. Reducing the profile radius increases the degree of plastic strain, but the penetration depth doesn't seem to be influenced dramatically.

2) 6 % to 8 % of plastic strain reorient β-grains and reduces their size. However, they probably developed during growth of other refined grains. Plastic strain above 12 % or even more induced by compressive deformation is required to achieve the smallest possible grain size.

3) Identical compressive stress induction can be caused by completely different plastic straining. In fact, it is even possible to induce compressive stress without deforming the material to the resolution of EBSD strain mapping.

4) Profiled rolling and MHP produce characteristic plastic deformation profiles. Rolling produces the greatest amount of plastic deformation at the edges of the

treated groove, while MHP deforms the material concentrated in the centre. Plastic deformation never exceeded the width of the groove laterally.

5) None of the three MHP tools used in this thesis supplied sufficient impact energy for plastically deforming the material sufficiently in the required depth. MHP tools should provide at least 5000 mJ impact energy to be considered as complementary or substitutional cold working technique.

The next and final chapter 7 investigates the thermal history in the HAZ during the WAAM deposition. In combination with the results from the present chapter this allows conclusions about the required amount and the ideal location of plastic deformation.

Chapter 7 Thermal History and the Impact on the Microstructure with and without Plastic Deformation

7.1 Introduction

The static and dynamic mechanical properties in Ti−6Al−4V depend mostly on the morphology of the α-plates, caused by the thermal history, which was established in chapter 1.2.3. More precisely it is the cooling rate through the phase transformation field between 1000 °C and 750 °C that matters the most [43], [44], [47], [88], which also determines the strength of the additively manufactured [65], [82], [87], [92], [93], [95], [98]–[101], [137], [139]. Inter-pass rolling refines the microstructure and improves mechanical properties, as shown in chapter 1.5.2 and chapter 3. In the previous chapter 6 is was identified how different rolling conditions provide the certain amount of plastic strain that yields refinement when the material is subsequently heated above the β-transus. This final chapter investigates the influence of the thermal cycle in combination with a certain amount of strain to identify the required combination of both for achieving refined and equiaxed grains.

7.1.1 Microstructure

Microstructural images of Ti−6Al−4V don't feature the fusion boundary very well, but only the HAZ, which in AM appear as horizontal lines [77]. Figure 125 (a) is a schematic of a typical Ti−6Al−4V WAAM microstructure of a single pass wall, in which the following typical landmarks can be found: The fusion boundary typically appears in an convex shape [90], unlike the concave shape typical for welding [56], [235]. But the exact shape can be influenced by the deposition parameters [126]. The high-temperature β-grains solidify epitaxially and can grow several centimetres through the entire component [87]. They are aligned with the $\{100\}_{bcc}$ fibre in z-direction towards the heat source [167]. The heat affected zones (HAZ) appear as horizontal and isothermal lines, are called "layer bands" in AM and are understood to represent the α-dissolution temperature [77], which is 748 °C for Ti−6Al−4V [88]. The static β-transus of 995 °C [90], [250] must be between the layer band and fusion boundary. Below the top layer band, the established microstructure constitutes repetitive layer bands of previous layers, which are

equidistant and equal to the layer height [87]. The size of the α-plates are ultimately responsible for the mechanical properties and their thickness varies between the layer bands [77], as shown in Figure 125. Their preferred orientation depends on the parent β-orientation and Burgers orientation relationship (BOR) variants [48], which results in the alignment of the $\{1120\}_{hcp}$ fibre or the $\{1012\}_{hcp}$ fibre with the z-direction in Ti–6Al–4V AM [86]. The relevant thermal history that established this typical microstructure is located between the fusion boundary and the last layer band.

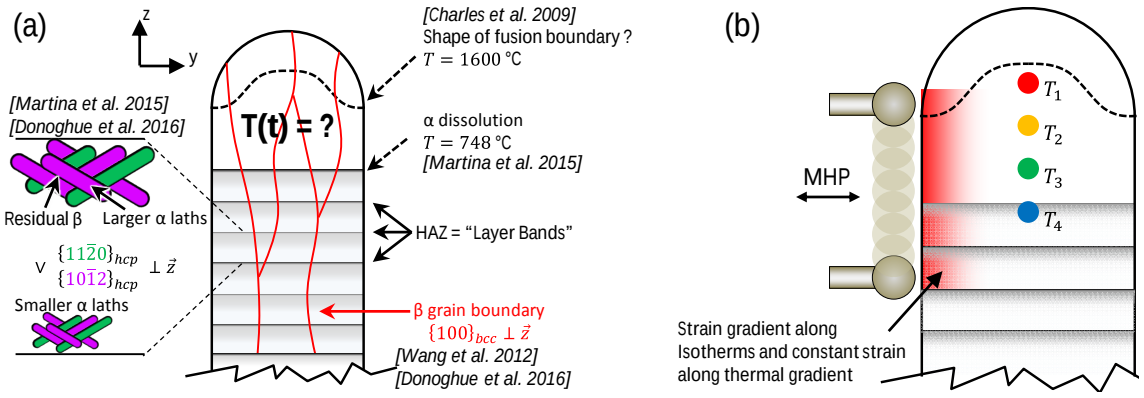

Figure 125: (a) Schematic of a typical cross-sectional Ti–6Al–4V microstructure in single-bead deposition; (b) visual summary of the methodology in this chapter.

7.1.2 Challenges to measuring the relevant temperatures

However the simulation of the thermal history [90], [91] and especially the heating and cooling rates have not been confirmed by measurements yet. Cooling rates above 2 °C/s produce the typical lamellar microstructure, which can be accompanied by martensitic traces above 20 °C/s [51], [79]. Martina et al. [77] measured the temperature/time history at the layer band and derived the cooling rate (-7.4 °C/s). However, it is the thermal history between this location and the fusion boundary that matters for the microstructure and mechanical properties.

Temperature measurement in this region is very difficult. A thermal gradient of approximately few hundred °C/mm make the precise positioning difficult. Positioning spot-weldable thermocouples closer to the molten pool would directly expose them to the zone of influence of the WAAM welding torch, which could falsify the measurement or destroy the thermocouple. This can be mitigated by placing them in drill holes [77]. Finally standard K-type thermocouples were found to be incompatible with the

Ti−6Al−4V alloy at higher temperatures, which requires the use of costly R-types in the location of interest. A different approach would be the use of thermal imaging to capture the thermal history on WAAM with a high resolution [251], [252]. However, this would measure the surface temperature only. To have an insight into the material, a simulation is still required to investigate the thermal history inside the material. Secondly, the thermal data is mostly used to predict the stresses [119], [120], [125], rather than to use the data to predict the microstructure. Thermal imaging furthermore is troublesome with liquid and glowing metals, as the emissivity changes non-linearly [253], [254]. This is especially troublesome with Ti−6Al−4V [255], as it can furthermore suffer from oxidisation [52], which additionally modifies the emissivity.

7.1.3 Refinement by inter-pass cold work

Inter-pass rolling refines the β-microstructure, which requires re-heating of plastically deformed material, delivered by the process heat of the subsequent layer. Martina et al. [77] furthermore found that inter-pass rolling, also reduces the α-plate thickness between the layer bands. This is indeed the reason for the increase in mechanical properties [27], [137], [139]. However the reasons why the refined β-grains also contain refined α-plates were only proposed, but not confirmed [77]. The degree of the required plastic strain was briefly investigated by Donoghue et al. [86] and in more detail in the previous chapter 6. However, the temperature/time history that refines in combination with a certain amount of strain is unknown for the same reasons described above.

The present chapter addresses this in two steps: In a fundamental study the precise thermal history is investigated at different locations in the relevant section between the expected fusion boundary and the last layer band using thermocouples according to Figure 125 (b). The degree in which the determined thermal history modifies a homogeneous control microstructure allows conclusions about the phase-history. In a second experiment, homogeneous plastic strain will be induced into the side of the wall using machine hammer peening (MHP) to reveal the influence of only the thermal history on the refinement process, also shown in Figure 125 (b).

7.2 Methodology

7.2.1 Temperature History in the HAZ

To investigate the microstructural changes of the thermal history, a Ti−6Al−4V dummy wall was machined from substrate material. This dummy had the same dimensions a typical WAAM wall would have, using the set of parameters used in chapter 4. It was 6 mm wide with a semi-circle on the top, 15 mm high and 250 mm long. Two series of four equidistant (14 mm apart) holes up to different depths (1.5 mm apart) were drilled from the bottom of the dummy into the expected HAZ (Figure 125 (b)). The R-type thermocouples were spot-welded to the tip of the hole. The side-section of the specimen in Figure 126 shows the locations.

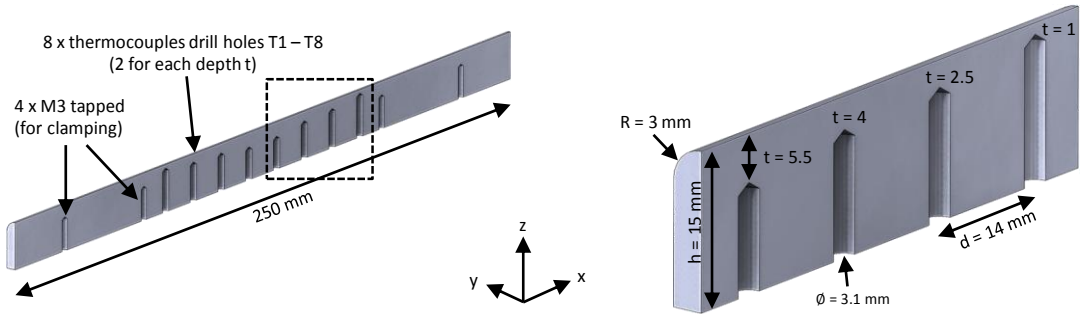

Figure 126: The substrate: dimensions and thermocouple locations in the side-section view

The diameter of the holes accommodated the 3 mm diameter thermocouple wire insulation. The dummy was mounted with M3 bolts to an aluminium plate, which had the substrate dimensions from chapter 4 (300 x 60 x 7 mm), shown in Figure 127 (a).

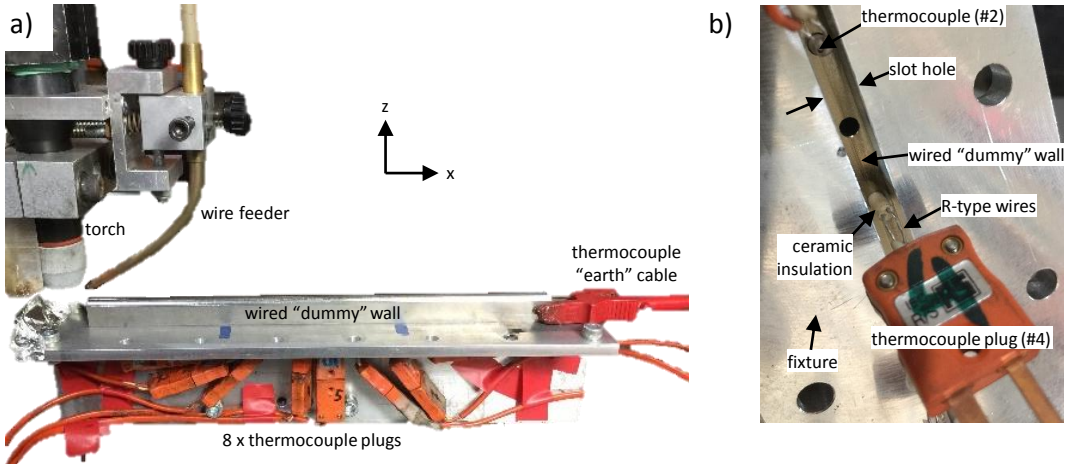

Figure 127: Setup of experiment (a) and bottom view of the thermocouple connection (b).

A long slot hole in the centre of the fixture allowed the thermocouple connection from the bottom (b). This setup was in turn mounted to a large aluminium backing bar. An earth cable was attached to the dummy to prevent interference of the thermocouple logger with the welding equipment. Ti–6Al–4V wire was deposited on the round edge, as if it was the next layer of a wall. The EWM-T352 Tetrix plasma power supply was used again with the deposition parameters from Table 10. The produced layer was 1.2 mm and slightly higher than the expected 1.11 mm. This experiment was repeated three times with three different dummies, which produced eight readings, two for each location. Dummy three was then heat treated three more times, by running the torch three further times, but without adding more wire. The purpose was to quantify the thermocouple measurement error, as the thermocouples remained at the same location. Side sections and cross section cuts were performed on the thermocouple locations of dummy 1 and 2 to investigate how the thermal history affected the raw material microstructure. The specimens were hot mounted in conductive resin, ground and polished. Scanning electron microscopy (SEM) was performed with 3500x magnification and 20 kV using the Back Scatter Detector (BSD). The SEM locations were located at the four thermocouple locations, in the molten pool and in the layer band. The microstructure was compared against the control of the as-received substrate material in Figure 128.

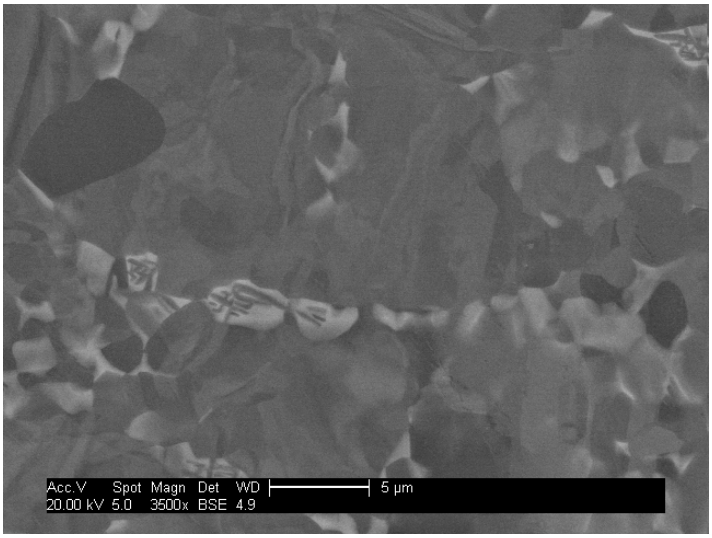

Figure 128: SEM image of the initial microstructure of the Ti–6Al–4V substrate (343 HV)

Table 10: Welding Parameters

Current [A]	145	Work Piece Distance [mm]	8
Wire Feed Speed [mm/s]	40	Plasma Gas Flow [l/min]	1
Travel Speed [mm/s]	7	Shielding Gas Flow [l/min]	10
Wire Diameter [mm]	1.2	Trailing Gas Flow [l/min]	25

7.2.2 Machine Hammer Peening and Grain Refinement

The temperature measurement setup was then replaced by an actual (300 x 60 x 7 mm) Ti–6Al–4V substrate. The parameters from Table 10 were used again to deposit a 250 mm long wall, which resulted in a 5.8 mm wide wall. After the completion of 15 layers, the wall was believed to contain an established microstructure with large columnar prior β-grains [137]. The Machine Hammer Peening (MHP) tool used in this chapter was the ForgeFix XP (chapter 5) using the 2 mm tip radius. MHP was performed extensively on one side of the wall along its entire length and between the estimated location of the fusion boundary and the third top most layer band. This is shown in the schematic in Figure 125 (b) and in the image of the setup in Figure 129.

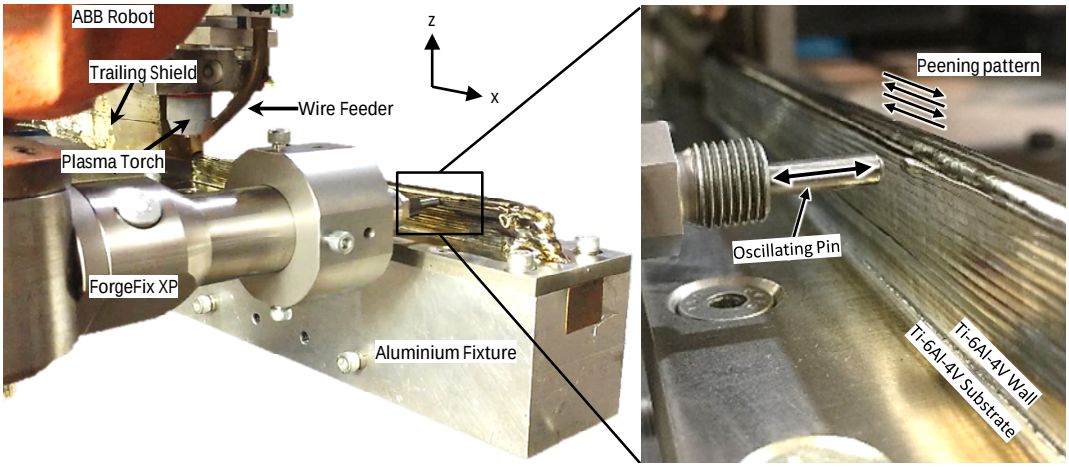

Figure 129: Side peening using the MHP tool ForgeFix XP.

The MHP travel speed was 36 mm/s in x-direction at a tool frequency of 180 Hz, producing one impact every 0.2 mm. Each of the nine following passes of the MHP tool were performed in alternating direction at a step distance of 0.5 mm. A homogeneous strain distribution in z-direction was anticipated with a plastically deformed region from the fusion boundary to below the last layer band. Finally the plasma power supply was used again with the same deposition parameters, but this time without adding wire into the molten pool. The purpose was to performing the WAAM typical heat cycle in the

HAZ. The geometry of the wall did not change during this step. Two cross sections were taken in total, of which one was in the as-peened condition before the heat treatment and the other one after. Conventional EBSD sample preparation was performed, including mounting in conductive resin, grinding and polishing. EBSD scans were performed on both specimens in the top part of the wall. The EBSD data was then post-processed at the University of Manchester using an in-house build software [234], [244] to reconstruct the parent β-grain orientation and to investigate the plastic deformation according to the principle described in appendix E. Finally, the polished samples were etched with hydrofluoric acid to reveal the microstructure.

7.3 Results

7.3.1 Thermal History

Table 11: Peak temperatures of the thermocouples [°C]Table 11 shows the peak temperatures of all thermocouple readings. Five of the 24 thermocouples failed during the experiment. The ones that did not fail were mostly in good agreement. The T1 thermocouples of dummy 2 and 3 completed the reading and showed 1285 °C and 1280 °C peak temperature respectively.

Table 11: Peak temperatures of the thermocouples [°C]

Thermocouple	T1	/ T8	T2	/ T7	T3	/ T6	T4	/ T5
Distance t from top	1 mm		2.5 mm		4 mm		5.5 mm	
Dummy 1	X	/ (1375)	1050	/ 1020	X	/ 860	X	/ 700
Dummy 2	1285	/ (1350)	1060	/ 1040	860	/ X	715	/ 725
Dummy 3	1280	/ (1460)	X	/ 1100	820	/ 800	725	/ 720
Dummy 3 (2nd run)	1275	/ (1450)	X	/ 1070	840	/ 815	720	/ 715
Dummy 3 (3rd run)	(1400)	/ (1440)	X	/ 1050	850	/ 800	725	/ 720
Dummy 3 (4th run)	(1420)	/ (1440)	X	/ 1050	860	/ 810	730	/ 725
Averade ± StDev.	1280 ± 4 °C (1380 ± 68 °C)		1054 ± 19 °C		832 ± 24 °C		720 ± 8 °C	

Interestingly, all T8 readings were completed as well, but show higher peak temperatures, even though their distance to the initial top prior to deposition was with 1 mm identical to the T1 thermocouples. The readings of all T8 thermocouples also showed a disproportional amount of noise. A measurement error due to interference with the welding current, when the torch was close to the thermocouple T8 and the "earth"-cable is suspected. The measurements where this was observed are therefore

presented in brackets and excluded from consideration. Figure 130 (a) shows the thermal history within the HAZ of the thermocouples T1 to T4 in dummy 2. The thermocouples were 14 mm apart and with a the travel speed of 7 mm/s resulted in an offset of 2 s for each profile. The plots account for this offset and present the curves as if the measurements were at the same location in travel direction.

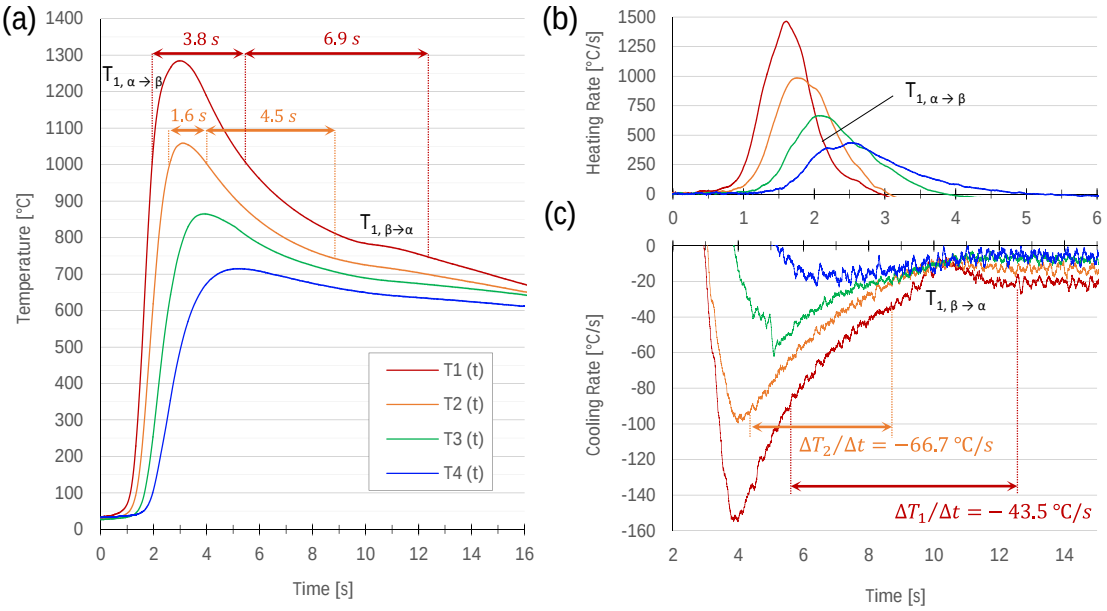

Figure 130: (a) Thermocouple reading of T1 – T4 in dummy 2 and the derived (b) heating rates and (c) cooling rates

Also indicated is the time that each thermocouple was above the β-transus and how long it took to cool back down below the α-dissolution temperature. The actual time depended on heating and cooling rates derived from the thermocouple readings which are plotted in Figure 130 (b) and (c) respectively. All T1 thermocouple readings also showed a unique feature. It is difficult to identify due to the extremely high heating rates, but at about 1200 °C, the heating curve seemed to bend slightly, which can also be identified within the heating rate profile (b). T1 thermocouples of other specimen shows this bend slightly more pronounced. Upon cooling the temperature profile had a short plateau and the cooling rates at this location drops from −20 °C/s to −10 °C/s, after which it increased again to −20 °C/s. Harder to identify the reading from T2 also seemed to shows a miniscule plateau during cooling.

The average gradient of the peak temperature between T1 and T4 respecting their depth below the top of the wall is 125 °C/mm. The bottom of the molten pool is estimated to be roughly 0.7 mm above the thermocouple T1, which both highlights the sensitivity of this measurement to the position. The side section of the thermocouple locations of the readings T1 to T4 and the micro-hardness locations are shown in Figure 131.

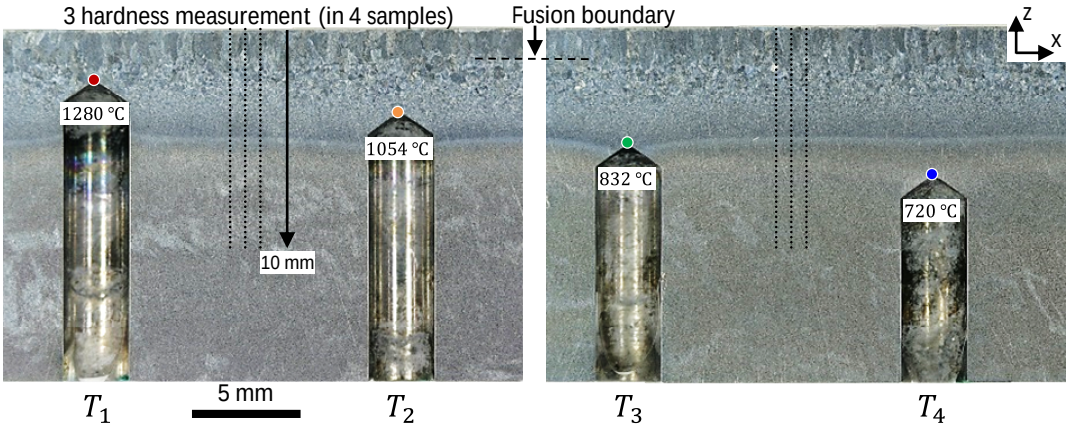

Figure 131: Side section of the microstructure at the thermocouple locations T1 – T4 and hardness profile locations

The stationary heat input produced relatively constant grain morphology in the travel direction. At the location of the thermocouples however, the microstructure "dips" down slightly, due to the lack of material (i.e. lack of heat sink). Three hardness profiles were taken from four different specimens that were located in the stationary region between the two thermocouple drill holes, as shown in Figure 131. This resulted in 12 measurements for each location. 22 outliers occurred due to deficient indents were removed from a total of 588 measurements. The averaged profiles with local standard deviation errors are shown in Figure 132. The hardness in the unaffected substrate material was 332.9 ± 2.9 HV. The error in the heat affected material for each measurement point was between 4 HV and 8 HV. During the thermocouple measurements, three errors can influence the measurement.

The first is the systematic error of the temperature measurement, indicated by the vertical error bars. The second one is another systematic error, in which the thermocouple drill hole increases the temperature at the measurement location. This would result in the measurement of a higher temperature or the temperature at a location closer to the heat source and is therefore represented by the left-hand side

horizontal error bar. The right-hand side error bar shows potential inaccuracy of the thermocouple location, which could have been applied not in the tip of the cone and therefore further away from the heat source. The location of the melting point (1600 °C) was estimated from the step in hardness and the visible transition of epitaxially grown columnar β grains to the equiaxed ones. Finally a logarithmic trend line of the 5 temperature points was provided, which also predicted the melting temperature at this location and it had has a coefficient of determination of $R^2 = 0.9998$.

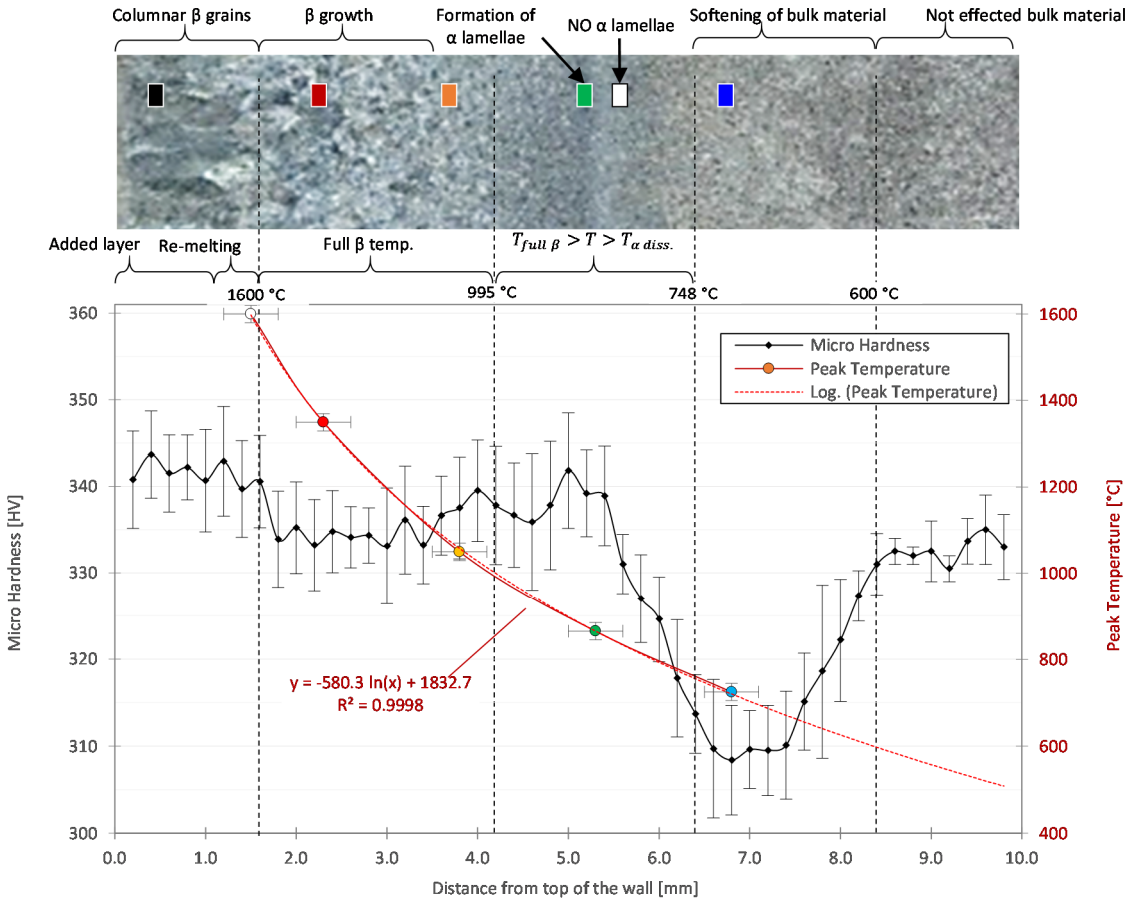

Figure 132: Microstructure and peak temperature and the corresponding microstructure

The hardness values can be compared against the microstructural features and the peak temperatures. Solidification of molten material, which is the 1.2 mm added material plus approximately 0.3 mm remelting resulted in the highest hardness. The equiaxed β-grains are slightly softer, but the hardness increases insignificantly to the thin white line. Below this line the hardness decreases dramatically in the material that reached between 600 °C and 850 °C peak temperature. The microstructure in this wide band

appeared slightly illuminated. At distances greater than 8.5 mm from the top of the wall, where the temperature did not reach 600 °C, neither the hardness, nor the microstructure shows any change.

The SEM images, of which the locations are indicated in Figure 132 are shown in Figure 133 together with the respective hardness values and peak temperatures.

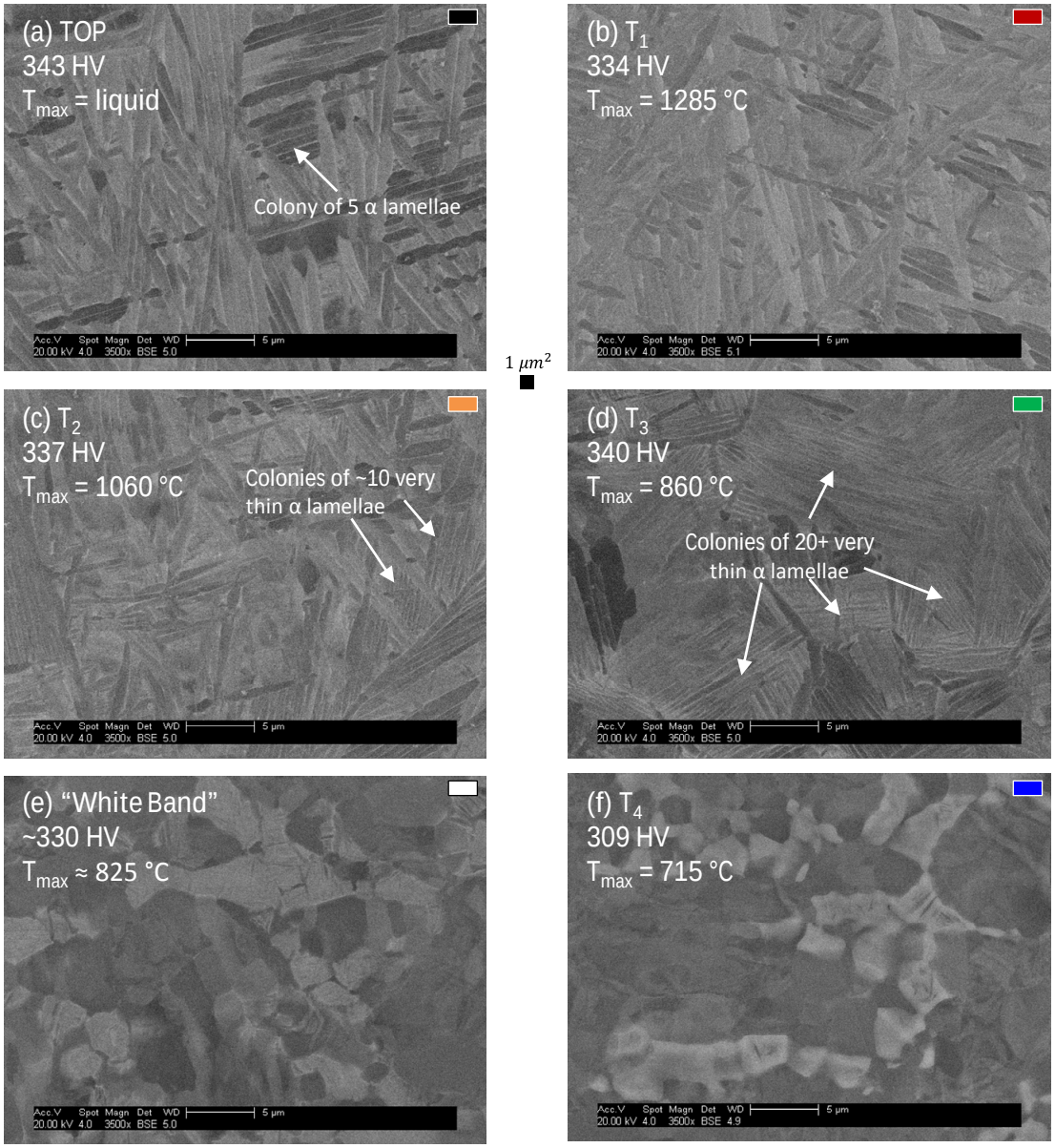

Figure 133: SEM Images from different locations. (a) molten pool; (b) T_2; (c) T_2; (d) T_3; (e) white band and (f) T_4.

In the solidified molten pool Widmanstätten α-plates of approximately 1 µm thickness were formed, of which some gather in small colonies up to five α-plates (a). Virtually no difference can be identified in the microstructure at the location of thermocouple T1

(b). The microstructure at location T2 (c) is similar, apart from a few colonies that consist of 5 to 10 very thin α-plates that are roughly 0.3 µm thick. The same thin α-plates can be found at thermocouple location T3 (d) as well, but here they form relatively large colonies of 20 α-plates and more. Only 0.5 mm further away from the molten pool (e), at the location of the steep hardness gradient, no α plates can be found whatsoever. The estimated peak temperature 825 °C at this point was significantly larger than the α-dissolution temperature. The same microstructure can be observed at the thermocouple location T4 (f). Indeed the microstructures of both, Figure 133 (e) and (f), do not show any difference compared to the control microstructure of the substrate material in Figure 128, despite the difference in peak temperature and hardness.

7.3.2 Machine Hammer Peening and Grain Refinement

Figure 134 (a) shows the microstructure in the as-deposited Ti–6Al–4V WAAM wall after machine hammer peening was performed on the left side of the wall. The dark dashed line represents the previous top of the wall, which was reproduced by offsetting the actual top of the wall downwards by the layer band distance observed in the bottom part of the image.

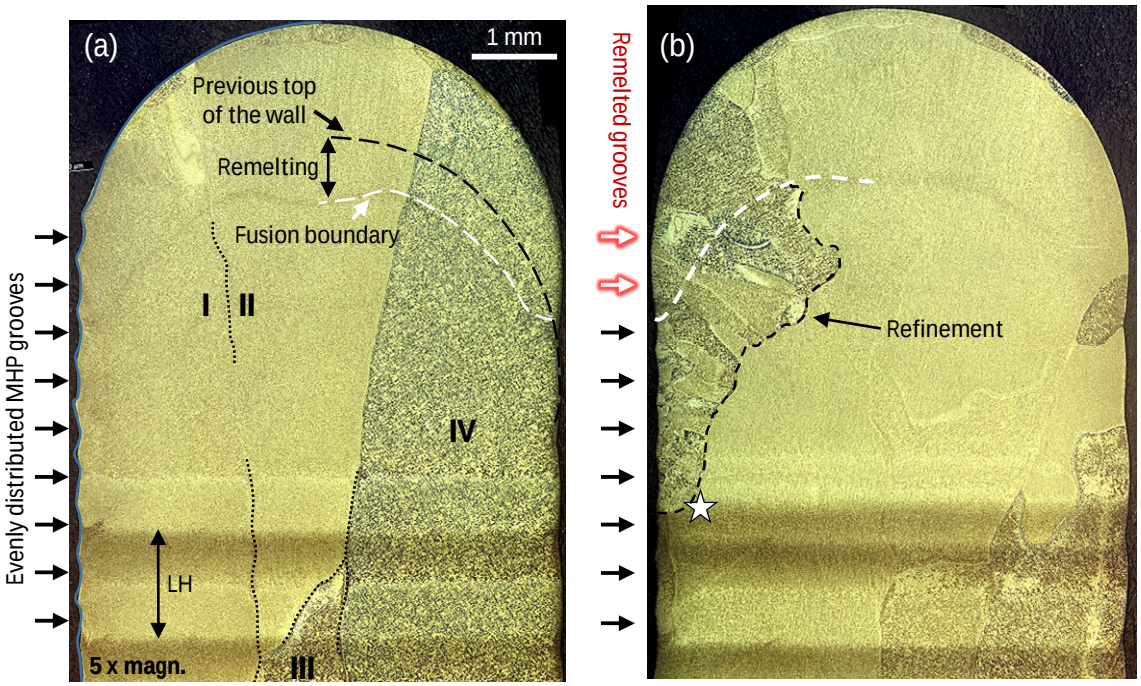

Figure 134: Microstructure of the as deposited and as-peened

A faint outline of the fusion boundary can be observed due to slight darker shading below the previous top of the wall, indicated by the bright dashed line. The area in between is therefore the remelted material. Four individual large columnar β-grains were identified and are labelled with Roman numerals I – IV. They grew epitaxially through several layers. The equidistant indentations on the left side are the MHP passes, which deformed the left side of the wall between top left corner and the second last layer band. The refined microstructure after the subsequent heat treatment with the torch is shown in Figure 134 (b). Refinement occurred, where MHP took place before. The MHP indents are still visible apart from the top two passes, which were completely remelted. No refinement was observed below the top most layer band, indicated with the star. The depth of the refinement at this location is nearly 1 mm deep, while close to the fusion boundary it reaches almost to the centre of the wall. The α-phase inverse-pole-figure (IPF-z) maps in respect to the z-fibre of both specimen are shown in Figure 135 (a) and (b). The dominant alignment of the hexagonal-close-packed (hcp) unit cell is with the magenta-coloured $\{1012\}_{hcp}$ plane normal to the build direction z.

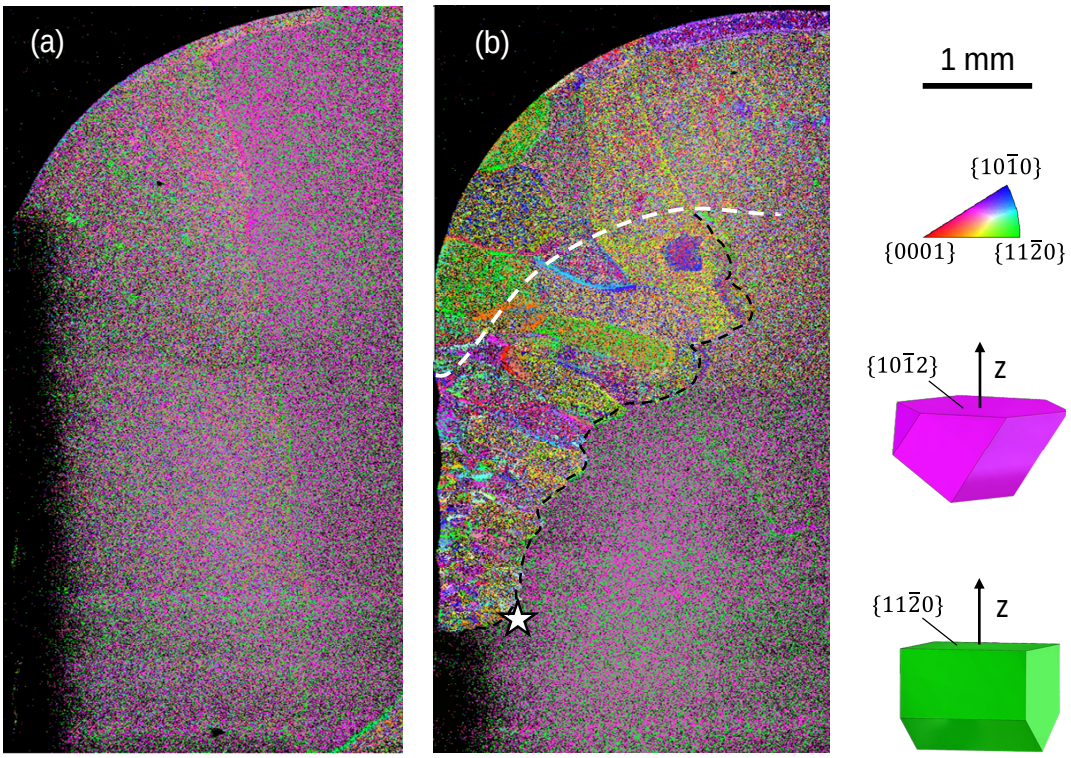

Figure 135: The α-phase IPF-z map of the top left corner of the wall (a) after MHP and (b) after heat treatment.

The second most common alignment with this fibre is the green-coloured $\{1120\}_{hcp}$ plane. No other orientation could be identified in the as-deposited and peened specimen in Figure 135 (a). As discussed in appendix B, only these two options can occur according to BOR. However, the variant selection is not only statistical, but also depends on the cooling rate [45] and the β-grain growth [256]. The dark region on the left, where MHP was performed could not be indexed. After the heat treatment various α-orientation can be identified within the region of refined β-grains, shown in Figure 135 (b). Each refined β-grain however seemed to contain two dominant α-orientations. The dark region on the left surface could be recovered and indexed by EBSD up to the layer band, of which the location is indicated by the star.

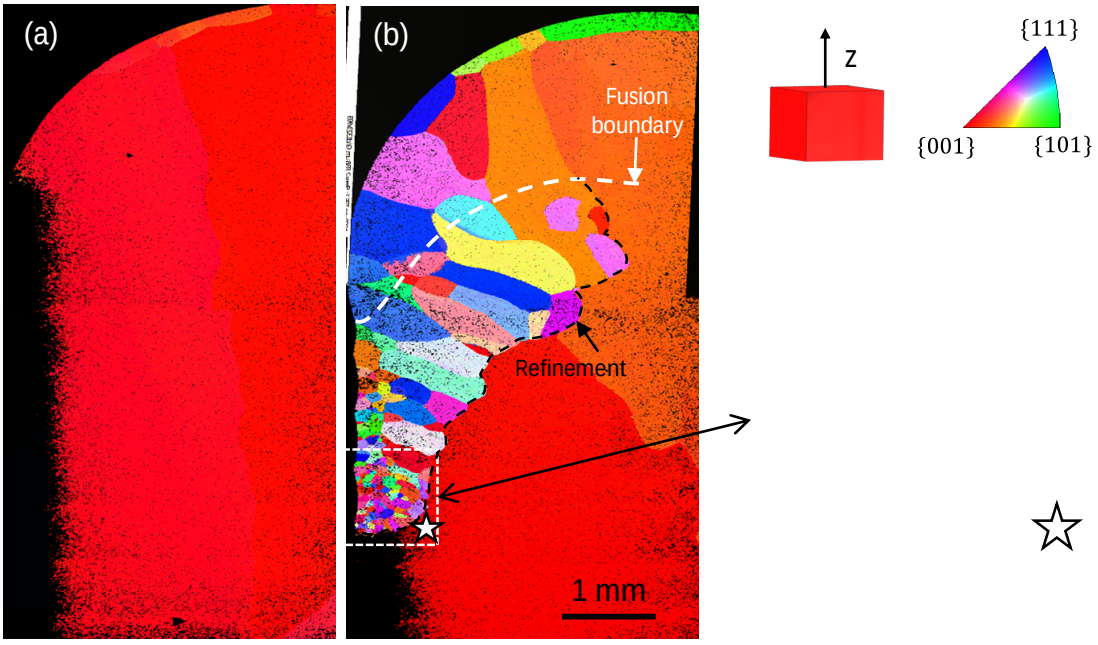

Figure 136: The reconstructed β-phase IPF-z map of the top left corner of the wall (a) after MHP and (b) after heat treatment with higher magnification showing the refined grain size.

The reconstructed β-phase IPF-z maps of both specimens are shown in Figure 136 (a) and (b). The as-deposited and peened specimen showed a complete alignment of all β-grains with the $\{001\}_{bcc}$ fibre in z-direction. Not only the β-grain grain size, but also the orientation was influenced dramatically by the heat treatment, shown in Figure 136 (b). Within the refinement boundary a wide range of β-orientations could be identified without any of them being dominant. The β-grain size close to the layer band appeared

very small, while closer to the fusion boundary, the grains became larger, columnar and aligned perpendicular with the fusion boundary.

The EBSD strain maps in Figure 137 show qualitatively the amount of plastic strain represented by α-lattice misorientation. Both specimens did not contain much lattice imperfections caused by plastic deformation in most of the material, represented by purple coloured α-lattice with a deviation of 1° or less. After MHP strong plastic deformation could be observed between 500 µm and 800 µm depth on the left side of the peened specimen in Figure 137 (a), where the 3° and 4° α-lattice misorientation is indicated with green and yellow. Within 500 µm of the surface the plastic deformation was so severe, that the material could not be indexed, due to extreme plastic deformation. The location of the edge of the wall is therefore represented by the dashed line in Figure 137 (a). The heat treatment recovered the material, which allowed indexing again of the lattices within the refined region. In the high magnification image in Figure 137 (b), at the refinement region at the layer band, an abrupt transition from plastically deformed to recovered and refined material can be observed. The complete recovery also allowed identification of the locations of the MHP passes on the left surface.

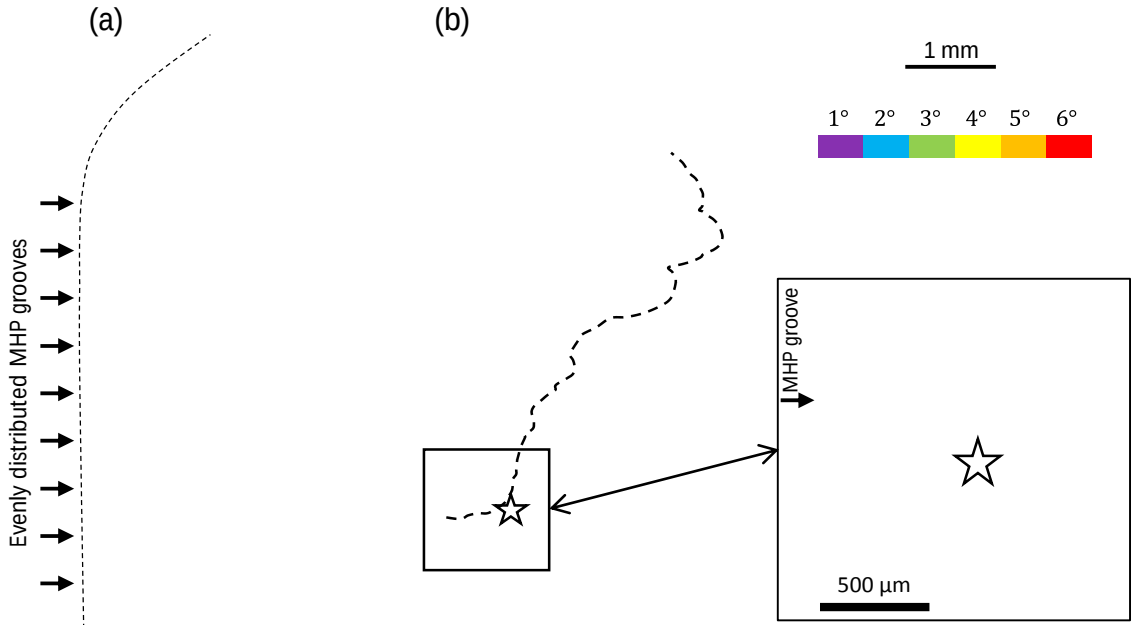

Figure 137: The EBSD strain map of the top left corner of the wall (a) after MHP and (b) after heat treatment with higher magnification showing border and depth of plastic deformation and recovery.

7.4 Discussion

7.4.1 Temperature/time history and resulting microstructure

Any transformation related key temperatures in this discussion are referred to Ti−6Al−4V according to literature [51], [57], [76]. Oxygen is a strong α-stabaliser in small quantities [43] and can influence these temperatures, but the actual content has not been measured in this study. Local shielding during the deposition was performed carefully and no discolouration could be observed, suggesting insignificant addition of environmental oxygen into the deposit. Thermocouple T4 was with a peak temperature of 720 °C and comparable cooling rates (Figure 130) close to the findings of Martina et al. [77], which was the target of this experiment. The proposed 748 °C (α-dissolution temperature in Ti−6Al−4V [88]) were located at the top-most layer band during the WAAM (TIG) deposition. In the present study, the T3 measurements, which recorded 860 °C was located just 0.5 mm above a distinct white band. With the help of the logarithmic interpolation in Figure 132, the white band reached approximately 825 °C peak temperature. Elmer et al. [55] reported that heating rates of +30 °C/s required 50 °C overheating of Ti−6Al−4V so observe equivalent amount of transformed β-phase compared to equilibrium thermodynamics. The heating rates at T3 were in fact higher than +500 °C/s. This could have caused the material to require approximately 110 °C overheat over the α-dissolution temperature to establish α-plates. The hardness values in the region that reached between 600 °C and 825 °C dropped, even though no microstructural changes can be observed compared to the base material using the back-scatter detector of the SEM (Figure 133 (e) and (f)). This is because diffusion and α→β transformation becomes kinetically active at approximately 550 °C [59]. This allowed softening of the as-received microstructure of the base-material to less than 310 HV, but the time was too short to allow visible transformation using SEM. Martina et al. [77], who suggested the layer band represents the α-dissolution temperature of 748 °C, while the present work suggests 825 °C. They may have recorded a lower peak temperature, because they used a TIG process, with a lower travel speed compared to the plasma process in the present experiment. The longer exposure time could have allowed more diffusion and transformation at similar temperatures, because

microstructural features, such as bespoke layer bands or any other transformed morphology, represent a degree of diffusion or phase transformation. They are the result of temperature and time history, and not evidence of the peak temperature only.

Just above the white line in contrast, where the material reached 860 °C and stayed for approximately 2.5 s above the α-dissolution temperature, microstructural change could be observed using the SEM. Figure 133 (d) shows the formation of α-colonies of many and very thin α-plates (~ 0.3 µm). The morphology of these α-colonies appeared to be somewhat related in size and shape to the grain morphology in the base material (Figure 128), which did not have a lamellar microstructure prior to heating. Here the temperature/time history was sufficient to allow diffusion-based partitioning of the aluminium and vanadium to segregate in the respective phase they stabilise [55]. The result are established α-plates surrounded by β-shells organised in colonies. The relation of the colony morphology to the parent microstructure suggests that the α-plates arose by diffusion and growth during heating and not during rapid cooling of β-grains. In fact, this location was never taken above 860 °C, which is still 140 °C less than the β-transus.

T2 has reached 1060 °C peak temperature and remained for 1.6 s above the β-transus. Widmanstätten microstructure can be identified at this location in the SEM image in Figure 133 (c). The α-plates here have typical dimensions of WAAM material of approximately 1 µm thickness and 10 µm length [77]. A few thinner α-plates that were as small as those at the T3 location persisted, indicated with the white arrows. This allows the conclusion that the lamellar microstructure at the T2 location developed during heating as well and not cooling. It also shows that the material did not fully transform into the high temperature β-phase. The extreme heating rates [55] and the short time of 1.6 s and only 65 °C overheat above β-transus did not allow a complete α→β transformation [235].

The temperature profile of T1, shown in Figure 130 (a), featured two abnormalities. The increase in temperature seems to decrease disproportionally at about 2.3 s, when the material heated between 1200 °C and the peak temperature of 1260 °C. This is more evident in the heating rate chart in Figure 130 (b). The heat provided be the welding torch at this point was not used to increase the temperature, but to perform the

α→β phase transformation. During heating from room temperature, the specific heat capacity of Ti−6Al−4V increases slowly from 0.6 J/kg/K to 0.8 J/kg/K. At the β-transus it shows an almost instantaneous increase to 1.15 J/kg/K [257], after which it drops again to 0.8 J/kg/K after the transformation [258]. This delays the temperature increase while heating through the β-transus. The observations are also in agreement with Elmer et al. [235], who found that it required approximately 4 s of time and between 120 °C and 200 °C superheat above the β-transus to complete the full transformation, regardless of the welding parameters. In a subsequent study [56] they found that diffusion kinetics can drastically delay the α→β transformation to higher temperatures at more extreme heating rates closer to the weld pool. In fact, the α→β transformation with the highest heating rate (360 °C/s at 1000 °C) occurred at aproximately 1500 °C. Slower heating rates are therefore required for the material to complete the transformation at lower temperatures [56]. The Widmanstätten morphology of the lamellar microstructure at the T1 location suggests a completed α→β transformation, because (and unlike the T2 location) it does not seem to be related to the base material morphology.

After reaching the peak temperature at T1, the material cooled with approximately −90 °C/s through the β-transus. The temperature then shows a short plateau-like profile at 780 °C between 10 s and 11 s and the cooling rate at this point decreased from −20 °C/s to −10 °C/s, after which it increased again to −20 °C/s, as shown in Figure 130 (c). This is the thermal record of the β→α phase transformation in the HAZ, as the released heat during the transformation prevents faster cooling. This is linked to the phase transformation modes during weld cooling, which affects the resulting microstructure in a similar way [56]: Cooling in the HAZ initiates at the β-transus and terminates below the M_S temperature of 650 °C and results in a substantial amount of α'-martensite in the otherwise lamellar microstructure. Cooling in the fusion zone with cooling rates of −100 °C/s in the relevant range begins at or below the M_S temperature and finally results in nearly complete α''-martensite. More recent work suggests that 850 °C is the actual M_S temperature and 680 °C the M_F temperature instead [51]. Either way, the thermal profile at the T1 location suggest a transformation at approximately 780 °C, and therefore considerably lower than the β-transus of 995 °C. The thermal

profile therefore does not suggest full α''-martensite, but certainly a share of α' in the lamellar microstructure. The martensitic α''-phase has an orthorhombic unit cell and can therefore be identified using XRD, as it results a different diffraction pattern [58]. The present martensitic α'-phase in the lamellar microstructure however has like the normal α-phase an hcp unit cell, which does not allow differentiating by the diffraction pattern. Phase compositions in the hcp unit cell in the diffusion-less transformed α'-phase by determining the d-spacings of the planes must be performed to conclude a volume fraction of martensitic α'-phase and the α-phase.

Finally, when observing the cooling of the T2 temperature profile more attentive, a slight drop in cooling rate can be seen at roughly the same time as well, but much less pronounced. This suggest that only a very small volume fraction of the material had previously transformed into the high-temperature β-phase, which could then transform back to α. The 1.6 s of time were not enough for the superheat to allow α→β transformation [235]. The thermal history therefore confirms, what the SEM images suggested in the first place.

7.4.2 Machine Hammer Peening and grain refinement

The geometry of the specimen used to identify the thermal history was identical to the deposited WAAM wall, on which inter-pass MHP was applied. This allows the transfer of the thermal profile to the refinement experiment to some extent. The purpose of this MHP experiment was to identify the relationship between plastic strain and thermal history, which results in a certain degree of β-grain refinement.

It was found that the region above last layer band is the location with the lowest temperature that allows refinement, shown in Figure 134 (b). The peak temperature at this point was supposedly 825 °C and the material was kept above 748 °C approximately for 3 s. The β-grain size in this region, as shown in Figure 136 (b), is homogeneously distributed and the smallest in the refined field with grains between 20 µm and 150 mm in size. Within 1 mm distance from the fusion boundary at the surface of the peening contact, the β grains become larger. As MHP produced the same plastic deformation on the entire side surface. It can be concluded that the temperature exceeded the β-transus to an extent that allowed full α→β transformation and immediate subsequent β-grain

growth. β-grain growth can already be observed a few seconds after the material was brought to temperatures of just 15 °C above the static β-transus, depending on the initial β-grain size [238]. Repeated α→β transformation on the other hand is not understood to lead to grain growth, if the initial grain size is already coarse [45]. The location of the plastic strain (and not the magnitude) and therefore the thermal history probably play a bigger role than previously expected [77], where β-grain growth was not considered after refinement. The microstructure achieved by inter-pass rolling can produce a grain size so small, that it can facilitate subsequent growth within the thermal cycle that refined it in the first place. This would also explain why the β-grains refined by inter-pass MHP close to the layer band and with severe plastic deformation did not produce a finer β-grain size compared to inter-pass rolling [137]. It is believed that the achieved β-grain size in the literature and the present study is therefore the bottom threshold, limited by the thermal history. The reason for smaller β-grain sizes by increasing the rolling load can also be attributed to strain that was induced further away from the heat source, which impedes subsequent growth, rather than more strain than producing smaller grains.

A second finding is the suspicious depth of the refinement region near the fusion boundary in the present work (Figure 134 and Figure 136), which reaches 3 mm from the peened surface into the material. The EBSD strain map after peening in Figure 137 (a) does not suggest that plastic strain was induced deeper than 1 mm. The region with the large columnar grains can therefore not be evidence of refinement. Instead these grains started to grow from the surface at the top-most peening pass, where refinement and reorientation started. The appearance of the β-grains strongly suggest that they grew from the side edge of the wall to the centre before the region where they nucleated was completely remelted. The molten pool then solidified on these medium sized columnar β-grains with new orientation and established itself epitaxially grown grains.

7.4.3 The effect of repeated heat cycles in WAAM and α-plate size in refined β grains

The α-plates morphology and therefore the mechanical properties depend on the cooling rates through the phase-transformation field [51], which in this case was between −20 °C/s and −90 °C/s. This should yield a strong α'-martensitic lamellar microstructure with high strength [44], [47], [74], [75], [259]. However, previous work has shown that walls manufactured using the WAAM (TIG) process shows slightly lower strength [87], [137], compared to what the cooling rate would suggest. Also the thickness measured of the α-plates in these WAAM walls would promise higher strength [44], [47], [75].

One factor is the isotropy and strong texture of the α-plates in respect to the build direction z, as shown in Figure 135. Because the orientation of the hcp unit cells within the α-plates is constrained [43], [65], [78], so are the preferred slip systems $\{10\bar{1}0\}$ $\langle 11\bar{2}0\rangle$ and $\{0002\}$ $\langle 11\bar{2}0\rangle$ [50], [61]–[63]. This not only transfers the anisotropic characteristics of the unit cell to the structure, but also it weakens the material in the normal directions. However, this cannot be the only explanation, because the strength in the longitudinal direction does not reach values that, cooling rates and α-plate size suggest.

The actual reason for this cannot be identified with the present results, but another explanation is that repeated heat cycles of the same material can contribute to subsequent weakening. After the development of the Widmanstätten microstructure during cooling from the full-β microstructure, diffusion and partitioning of Al and V, when subsequent depositions reheat the material, weakens it. This is only valid if the material did not complete the full β→α transformation again. The present deposition parameters for example produced layer heights of 1.2 mm. The peak temperature profile in Figure 132 suggests that the material at the T1 location will be heated to approximately 1100 °C and 900 °C in the two subsequent heat cycles respectively. This will lead to diffusion, potential further growth of the α-plates and ultimately decreases the strength. The softening between 6 mm and 8 mm from the top needs to be investigated further. It cannot be concluded if any Ti−6Al−4V material including the

WAAM microstructure would soften due to this thermal cycle or if this is an effect that only applies to the differently processed substrate material, which has different strengthening mechanisms [47] that weakens as soon as diffusion starts.

The refined β-grains when using inter-pass rolling also contain smaller α-plates [77], which is the actual reason for the improved properties [47], [128], but is has not been confirmed why the α-plates is reduced at all [77]: One possible explanation was that the increased number of β-grains and grain boundaries provide a much larger number of nucleation sites for the α-plates. Their competitive growth stops during collision and limits the final size [43]. A second explanation proposed that plastically deformed martensite has a different transformation behaviour and provides more nucleation sites, resulting in a larger number of competitively growing α-plates, which collide sooner [47]. Both explanations were critically discussed [77] and some contradictions prevented the authors to propose a most-probable cause. Recently it was found elsewhere that waiting for 40 s between each layer instead of continuous deposition can increase the strength in Ti−6Al−4V AM from 815 MPa to 930 MPa, as the lower starting temperature increases cooling rate and decreases α-plate size [128]. The time required to perform rolling therefore might actually allow the wall to cool, rather than anything else, which might cause the main improvement. However, since 75 kN actually produces smaller α-plates compared to 50 kN [77] and a higher strength [137] −assuming the time required for both is the same− allows the conclusion that rolling does have an additional effect. Chapter 3, where inter-pass rolling did not influence the inter-layer dwell time, but produced smaller α-plates, also confirms the observation.

The findings in this chapter and in-situ EBSD measurements of Ti−6Al−4V during heating to β-transformation [72] offers another explanation: It was observed that the α-plate size depends on the cooling rate through the transformation temperature range (Figure 133 (a) and (b)). However, it was also observed that material that has never completed the α→β transformation can still feature α-plates, as shown in Figure 133 (d). The unit cells of the α-plates and of the surrounding retained β-shells are aligned according to BOR. Subsequent heat cycles on the same material, as they occur in WAAM, can cause further α-plate growth, without being hindered by the growth of the retained

β-phase. Rolling however twins the β-unit cell [72] and thereby would reset the orientation memory effect [256], when the β-grains regrow. Heating of twinned β-grains promotes the growth in a different orientation, which imposes the new β-orientation on the α-phase [72]. The α-grains are figuratively being "consumed" by the growing twinned β-grains, lose their texture memory and start to grow from scratch in a new orientation. The resulting α-plate's thickness is therefore as small, as if the material has only seen one thermal cycle and no re-heating.

7.5 Conclusion

1. The thermal history in the HAZ in WAAM was resolved in detail for one set of parameters. The peak temperatures, heating rates and cooling rates are the first measurement of its kind and allow detailed discussion about the resulting microstructure
2. 60 °C of overheat above the β-transus and 1.6 s was not enough for α→β transformation (T2). It required approximately 200 °C overheat and 3.8 s due to the high heating rate of over 1000 °C/s for full transformation (T1). The cooling rates between −90 °C/s at the β-transus and −20 °C/s at 780 °C delayed the β→α transformation to the latter temperature.
3. Lamellar microstructure can grow during heating above 860 °C of non-lamellar microstructure, without cooling from the β-phase field. It is likely that the lamellar microstructure can also form at lower temperatures, if the heating and cooling rates were slower.
4. Peak temperatures between 550 °C and 748 °C are located below the last layer band, regardless the diffusion kinetics, but they can soften the material.
5. Microstructural features are caused by temperature/time history and cannot be labelled as a certain peak temperature achieved, as the diffusion kinetics limit transformation.
6. Grain refinement can be achieved just above the last layer band, which is where the smallest grains occur as well. Plastic deformation should therefore be

induced to the location that will become a layer band during the subsequent deposition.

7. Increasing the plastic strain, decreases the β-grain size after refinement. But once a certain amount of strain is induced, then the thermal profile becomes the limiting factor for the smallest β-grain size that can be achieved, as very small grains can grow directly after they were refined within the same thermal cycle. Grain refinement closer to the fusion zone can result in subsequent β-grain growth within the same thermal cycle
8. Multiple heat cycles that allow diffusion within Widmanstätten microstructure without completing α→β transformation probably allow α-plate growth and thereby softening of the material, if inter-pass rolling is not applied. The application of inter-pass cold work instead "resets" the orientation memory and provokes a new α-establishment, rather than growth of the existing ones. This could be the actual reason why inter-pass cold work causes material strengthening.

Chapter 8 Conclusions and Future Research

The two aims of this research were to investigate rolling and other cold working techniques for the purpose of a) residual stress control and b) microstructure control in Ti–6Al–4V WAAM. After concluding the research findings for each aim individually, the practical application will be concluded, as well as the consequent future research.

8.1 Residual Stress Control in WAAM

Before addressing the mitigation and control of residual stresses, their development in representative features was investigated and understood in a fundamental study.

Stress Development in WAAM – The key finding was that longitudinal tensile residual stresses can reach yield stress in WAAM and are constant along the wall height during the deposition. Depending on thermomechanical properties some metals are more prone to develop large stresses (relative to their as-deposited yield value) than others. Relevant is the relationship of the flow strength vs. temperature $\sigma_{0.2}$ (T) and the thermal development of stress $\Delta\sigma/\Delta T$ during constrained contraction during cooling. Aluminium (article submitted to journal) and steel (literature) deposits are likely to develop stresses near the yield value. Titanium alloys can develop stresses near yield in extreme conditions, but are generally less critical and typically generate residual stresses between 30 % and 70 % of yield stress (chapter 3 & 4). However, the very high absolute values of this strong alloy produces very large forces, which requires adequate and rigid clamping during the deposition. Different to expected, the residual stresses in intersections appear to produce lower residual stresses compared to a free-standing wall. The explanation lies in a complicated self-stress-relieving mechanism due to the crossing path strategy (chapter 3).

Distortion upon part unclamping results in redistribution of the residual stresses. The redistributed profile pivots around the neutral axis with a slope $\Delta\sigma/\Delta z$ compared to the constant stress profile. Clamping distortion and redistributed stress can be predicted efficiently using the analytical model (chapter 2). Nevertheless, the residual stresses should be minimised before unclamping to avoid distortion in the first place.

Residual Stress Controlling in WAAM – One key finding for stress control is the great effectiveness of side rolling to eliminate longitudinal tensile residual stresses in additively manufactured material and thereby distortion (chapter 4). The fundamental reason is that lateral rolling constrains the wall to deform in the desired longitudinal direction, while vertical rolling produces strain mainly into the transverse direction, making it far more effective than vertical rolling. In fact, applying vertical-inter-pass rolling on Ti–6Al–4V WAAM intersections with more practical feature dimensions (chapter 3) appeared to be completely ineffective. On the other hand, due to the great ductility of aluminium WAAM deposits, it was possible to eliminate RS & D using vertical inter-pass rolling (paper submitted to journal).

A practical use of the side-rolling findings (chapter 4) would be the design of a pinch rolling tool, however this could face some practical limitations, such as the treatment of complex deposits, curved sections or the intersections. Nevertheless, pinch-rolling would be the only cold-work treatment that actually could on-line manipulate the stress in Ti–6Al–4V WAAM effectively.

The second important finding for stress control was the proof that thermal stress relieving of the near-net-shape part in the furnace can eliminate the residual stresses in Ti-6Al-4V WAAM entirely without influencing the microstructure (chapter 3). Since it is furthermore not practical (or often impossible) to monitor the stress reduction of cold-work using NDT on-line, thermal stress relief becomes a requirement to ensure complete stress relaxation. However, if the initial part distortion is significant, thermal stress relieving must be performed, while the part remains clamped on a backing bar to prevent distortion. The material of the clamping mechanism must withstand the temperatures used for stress relief.

8.2 Microstructure Control in Ti–6Al–4V WAAM

To understand the thermo-mechanical process that controls the microstructure, the strain induction mechanism of cold work and the subsequent thermal history, were both investigated.

Plastic Deformation Behaviour – Contact mechanics was used to understand the associated strain induction behaviour of cold working techniques (chapter 6). Higher loads for instance improve the penetration and smaller contact profiles increase the strain, but don't influence the penetration very much. The greatest plastic deformation during profiled rolling occurs at the edges below a rolling path, but the effectiveness is limited to the width of the rolled groove. Friction during the roller-surface contact prevented near-surface plastic strain and instead deformed the material deeper inside, which is desired. This does not entirely apply for the MHP contact mechanics, which deforms the material dominantly near the contact surface, due to the absence of friction during the impact. The plastic deformation characteristics of profiled rolling is therefore the preferred one.

Plastic Deformation Measurement – Plastic deformation quantification can be difficult, unpractical and unsuitable for the purpose of this investigation. The best qualitative indication of plastic strain offers the EBSD strain map, for which the unit [° α-lattice misorientation] will have to be calibrated to plastic strain for better use of the technique. The present results suggest that at least 3° to 4° of α-lattice misorientation is required to allow refinement, which can indirectly be measured by an increase of approximately 20 HV caused by strain hardening. A numerical simulation was verified using residual measurements and calculation. The model predicts approximately 12 % of plastic strain or more in the region that finally produced grain refinement after β-heat treatment of the specimen.

Thermal history – The other key finding regarding β-grain refinement is the identified region in which plastic strain must be induced. This region is the material that initiates the α→β transformation during the subsequent deposition (chapter 7), but does not complete it to avoid instant β-growth after refinement. Due to diffusion kinetics, these regions cannot be quantified by temperatures only, but only by temperature/time relations. However, one boundary of the region can be identified with the help of the microstructure. The layer band of the subsequent deposition is the threshold of the HAZ that provided enough temperature/time that allows refinement, if at least 12 % of plastic compressive strain (chapter 6) was induced before. This depth of this varies with

the various deposition parameters, strategies and feature geometries. It can reach between 3 mm (for relatively fast and low-heat-input depositions) to 10 mm or more (for slow depositions with a high heat input) from the top into the surface.

8.3 Practical Advice

The only effective and practical use of cold work to control RS & D is pinch-rolling of long, high and slender walls (chapter 4). Practical near-net-shape WAAM features however are usually between 15 mm and 100 mm thick and not very high, which probably exceeds the capability of side or pinch rolling. Residual stress must therefore be addressed using a different technique, such as thermal or vibratory stress relief or acoustic softening.

Even though it is probably not worth addressing residual stress and distortion with cold work, inter-pass cold work significantly improves microstructure and mechanical properties. Due to realistic penetration depth of rolling and MHP, and due to wide walls being a common feature of most parts, the only practical method of application is the vertical-inter-pass strategy. This makes the degree of freedom, which is one of the key advantages of MHP over rolling, almost irrelevant. Remaining advantages of MHP are the much higher operating speed of up to 200 mm/s and the fact that the tools do not require a stiff gantry. Instead a manipulator would only have to carry the payload of the MHP tool, which allows the use of cheap and flexible articulated robots, instead of stiff, slow and expensive CNC gantries, which also limit the build envelope. The advantages justify the development of tools that deliver more impact energy. A MHP tool with 5000 mJ impact energy or more can challenge the penetration depth of rolling and would constitute an easier, faster, more flexible and more economical way to perform inter-pass cold work.

The value of inter-pass work in Ti–6Al–4V WAAM is the increase of the strength by 10 % to 20 % and the elimination of texture and isotropy. This is the unique selling proposition over other HDR AM processes or other market competitors, such as casting and forging. However, if the same improvement could be achieved by an optimised composition of the titanium alloy, this would be preferable, because it would eliminate the complexity

of the additional processing step. Some early work on using boron as a grain refiner has shown some promising results, but more work needs to be done in this area.

8.4 Future Research

Further research to control RS &D, as well as the microstructure and mechanical properties in Ti–6Al–4V WAAM could include the following:

1. **Alternative Stress Control** – On-line stress control is vital for the success of WAAM. Entire stress elimination by cold work however is often not possible and it is challenging for practical WAAM components, making it not fit for industrial application. The only concurrent reliable technique is thermal stress relief, which can only be applied as a post-process.

   Instead vibratory stress relief could be applied on a rigid test bed of WAAM to eliminate residual stresses in-situ or as a post process. Fundamental experiments should be relatively easy to perform and allows conclusions about the feasibility to integrate this technique into WAAM. Alternatively, acoustic softening could be investigated, but the science behind it is far from being understood. However, there are currently some research activities, which have shown that it can reduce stresses in Ti-6Al-4V. If the application to additively manufactured components is feasible, then acoustic softening could be a break through.

2. **Plastic Deformation under realistic conditions** – Plastic deformation behaviour for grain refinement purpose was investigated with a standardised specimen without residual stress at room temperature. The behaviour under realistic conditions should be investigated, such as on material with residual stresses and/or at elevated temperatures. It must be identified whether or not or to what extent the plastic deformation characteristics of cold work techniques are influenced under those conditions. This information must also be provided for a complete validation of a process model using a numerical simulations.

3. **Alternative contact mechanics** – Other than the presented semi-circular cold working profiles, other profiles might distribute the plastic strain better or induce it to a greater depth, such as high-angled V-shaped profiles.

4. **Machine Hammer Peening** – Heavier MHP tools > 5000 mJ should be investigated to challenge rolling as a realistic cold-work alternative. This would set very high requirements on the properties of the tool material.
5. **Calibrate EBSD strain map** – Precise plastic deformation was not resolved accurately. A compression test on standardised material, which can be analysed numerically and using the EBSD strain mapping technique, would precisely calibrate the latter to engineering strain. Controlled dilatometer heat cycles can help calibrating the process map for grain refinement
6. **Titanium alloy development** – The use of an alternative titanium alloy designed for WAAM could be a game changer. The main requirement are the development of small equiaxed grains in the as-deposited condition. A secondary requirement is a generally high strength in the as-deposited condition. The latter could be fixed by post-deposition near-β annealing, followed by quenching, which would make inter-pass cold work redundant and simultaneously eliminate the residual stresses.

Bibliography

[1] M. Agarwala, D. Bourell, J. Beaman, H. Marcus, and J. Barlow, "Direct selective laser sintering of metals," *Rapid Prototyp. J.*, vol. 1, no. 1, pp. 26–36, 1995.

[2] W. Meiners, K. Wissenbach, and A. Gasser, "Shaped body especially prototype or replacement part production," DE 19649865 C1, 1996.

[3] A. International, "Additive Manufacturing Overview," 2009. [Online]. Available: https://www.astm.org/industry/additive-manufacturing-overview.html. [Accessed: 13-Nov-2017].

[4] I. Gibson, D. W. Rosen, and B. Stucker, *Additive Manufacturing Technologies*, vol. 76, no. 12. 2010.

[5] O. Yilmaz and A. A. Ugla, "Shaped metal deposition technique in additive manufacturing : A review," *Proc IMechE Part B J Eng. Manuf.*, vol. 230, no. 10, pp. 1–18, 2016.

[6] M. Tomlin and J. Meyer, "Topology Optimization of an Additive Layer Manufactured (ALM) Aerospace Part," in *The 7th Altair CAE Technology Conference*, 2011, pp. 1–9.

[7] S. N. Reddy K., I. Fergus, M. Frecker, and T. W. Simpson, "Topology optimization software for additive manufacturing: a review of current capabilities and a real-world example," in *ASME DETC*, 2016.

[8] J. Allen, "An Investigation into the Comparative Costs of Additive Manufacture vs. Machine from Solid for Aero Engine Parts," Neuilly-sur-Seine, France, 2006.

[9] "GE Additive." [Online]. Available: https://www.ge.com/additive/press-releases/ge-agrees-purchase-controlling-shares-arcam-ab. [Accessed: 04-Dec-2017].

[10] "CONCEPT LASER - a GE Additive Company." [Online]. Available: https://www.concept-laser.de/home.html. [Accessed: 04-Dec-2017].

[11] "Ti6Al4V ELI Titanium Alloy," *Arcam EBM System*. [Online]. Available: http://www.arcam.com/wp-content/uploads/Arcam-Ti6Al4V-ELI-Titanium-Alloy.pdf. [Accessed: 12-Nov-2017].

[12] "SLM Solutions." [Online]. Available: https://slm-solutions.de. [Accessed: 04-Dec-2017].

[13] "EOS AB." [Online]. Available: https://www.eos.info/en. [Accessed: 04-Dec-2017].

[14] "RENISHAW - Additive Manufacturing Systems." [Online]. Available: http://www.renishaw.com/en/additive-manufacturing-systems--15239. [Accessed: 07-Apr-2013].

[15] "TRUMPF - Additive Manufacturing." [Online]. Available: https://www.trumpf.com/en_CN/999/additive-fertigung/. [Accessed: 07-Apr-2018].

[16] "AP&C - a GE Additive Company." [Online]. Available: http://advancedpowders.com. [Accessed: 04-Dec-2017].

[17] T. Wang, Y. Y. Zhu, S. Q. Zhang, H. B. Tang, and H. M. Wang, "Grain morphology evolution behavior of titanium alloy components during laser melting deposition additive manufacturing," *J. Alloys Compd.*, vol. 632, pp. 505–513, 2015.

[18] S. H. Nikam and N. K. Jain, "Three-dimensional thermal analysis of multi-layer metallic deposition by micro-plasma transferred arc process using finite element simulation," *J. Mater. Process. Tech.*, 2017.

[19] H. Gong, K. Ra, H. Gu, G. D. J. Ram, T. Starr, and B. Stucker, "Influence of defects on mechanical properties of Ti–6Al–4V components produced by selective laser melting and electron beam melting," *Mater. Des.*, vol. 86, pp. 545–554, 2015.

[20] D. Agius, K. Kourousis, and C. Wallbrink, "A Review of the As-Built SLM Ti-6Al-4V Mechanical Resistant Designs," *Metals (Basel).*, vol. 8, no. 75, pp. 1–25, 2018.

[21] R. M. Miranda, G. Lopes, L. Quintino, J. P. Rodrigues, and S. Williams, "Rapid prototyping with high power fiber lasers," *Mater. Des.*, vol. 29, no. 10, pp. 2072–2075, 2008.

[22] D. Ding, Z. Pan, D. Cuiuri, and H. Li, "Wire-feed additive manufacturing of metal components: technologies, developments and future interests," *Int. J. Adv. Manuf. Technol.*, vol. 81, no. 1–4, pp. 465–481, 2015.

[23] B. Baufeld, E. Brandl, and O. Van Der Biest, "Wire based additive layer manufacturing: Comparison of microstructure and mechanical properties of Ti-6Al-4V components fabricated by laser-beam deposition and

shaped metal deposition," *J. Mater. Process. Technol.*, vol. 211, pp. 1146–1158, 2011.

[24] "SCIAKY INC." [Online]. Available: http://www.sciaky.com/additive-manufacturing/metal-additive-manufacturing-systems. [Accessed: 25-Jun-2015].

[25] F. Ribeiro, "Automated off-line programming for rapid prototyping using gas metal arc welding," Cranfield University, 1995.

[26] P. M. Sequeira Almeida and S. Williams, "Innovative process model of Ti–6Al–4V additive layer manufacturing using cold metal transfer (CMT)," 2010.

[27] S. W. Williams, F. Martina, a. C. Addison, J. Ding, G. Pardal, and P. Colegrove, "Wire+Arc Additive Manufacturing," *Mater. Sci. Technol.*, vol. 32, no. 7, pp. 641–647, 2015.

[28] P. Kazanas, P. Deherkar, P. Almeida, H. Lockett, and S. Williams, "Fabrication of geometrical features using wire and arc additive manufacture," *Proc. Inst. Mech. Eng. Part B J. Eng. Manuf.*, vol. 226, pp. 1042–1051, 2012.

[29] F. Martina, J. Mehnen, S. W. Williams, P. Colegrove, and F. Wang, "Investigation of the benefits of plasma deposition for the additive layer manufacture of Ti-6Al-4V," *J. Mater. Process. Technol.*, vol. 212, pp. 1377–1386, 2012.

[30] B. Baufeld, O. Van Der Biest, and R. Gault, "Additive manufacturing of Ti-6Al-4V components by shaped metal deposition: Microstructure and mechanical properties," *Mater. Des.*, vol. 31, pp. 106–111, 2010.

[31] C. M. A. Silva, I. M. F. Braganca, A. Cabrita, L. Quintino, and P. A. F. Martins, "Formability of a wire arc deposited aluminium alloy," *Brazilian Soc. Mech. Sci. Eng.*, vol. 39, pp. 4059–4068, 2017.

[32] J. Ding, F. Martina, and S. W. Williams, "Production of large metallic components by additive manufacture – issues and achievements," in *1st "Metallic Materials and processes: industrial challenges*, 2015.

[33] "IK4 Lortek." [Online]. Available: http://www.lortek.es. [Accessed: 03-Dec-2017].

[34] Y. Ma, D. Cuiuri, N. Hoye, H. Li, and Z. Pan, "The effect of location on the microstructure and mechanical properties of titanium aluminides produced by additive layer manufacturing using in-situ alloying and gas tungsten arc welding," *Mater. Sci. Eng. A*, vol. 631, pp. 230–240, 2015.

[35] G. Venturini, F. Montevecchi, A. Scippa, and G. Campatelli, "Optimization of WAAM Deposition Patterns for T-crossing Features," *Procedia CIRP*, vol. 55, pp. 95–100, 2016.

[36] "Norsk Titanium AS." [Online]. Available: http://www.norsktitanium.com. [Accessed: 03-Nov-2017].

[37] "Gefertec." [Online]. Available: http://www.gefertec.de. [Accessed: 03-Dec-2017].

[38] "The titanium revolution is here!" [Online]. Available: https://www.aero-mag.com/norsk-titanium-aerospace-grade-additive-manufactured-structural-components-boeing-787-dreamliner/. [Accessed: 03-Dec-2017].

[39] J. Mehnen, J. Ding, H. Lockett, and P. Kazanas, "Design study for wire and arc additive manufacture Jörn Mehnen * and Jialuo Ding Panos Kazanas," *Int. J. Prod. Dev.*, vol. 19, no. 1–3, pp. 2–20, 2014.

[40] Z. Ye, Z. Zhang, X. Jin, M.-Z. Xiao, and J. Su, "Study of hybrid additive manufacturing based on pulse laser wire depositing and milling," *Int. J. Adv. Manuf. Technol.*, 2016.

[41] "Laser Zentrum Nord (LZN)." [Online]. Available: http://www.lzn-hamburg.de. [Accessed: 03-Dec-2017].

[42] "LASIMM - about." [Online]. Available: http://www.lasimm.eu/about.html. [Accessed: 03-Dec-2017].

[43] G. Lutjering and J. C. Williams, "Titanium - 2nd Edition," *Engineering*, p. 442, 2007.

[44] M. Peters and C. Leyens, *Titanium and Titanium Alloys, Fundamentals and Applications*. 2003.

[45] G. A. Sargent, K. T. Kinsel, A. L. Pilchak, A. A. Salem, and S. L. Semiatin, "Variant Selection During Cooling after Beta Annealing of Ti-6Al-4V Ingot Material," *Metall. Mater. Trans. A*, vol. 43A, pp. 3570–3585, 2012.

[46] M. Humbert and N. Gey, "The calculation of a parent grain orientation from inherited variants for approximate (b.c.c. - h.c.p.) orientation relations research papers," *J. Appl. Crystallogr.*, pp. 401–405, 2002.

[47] G. Lütjering, "Influence of processing on microstructure and mechanical properties of (α+β) titanium alloys," *Mater. Sci. Eng. A*, vol. 243, pp. 32–45, 1998.

[48] W. G. Burgers, "Cubic-Body-Centered Modification Into The Hexagonal-Close-Packed Modification Of

Zirconium," *Phys. I.*, pp. 561–586, 1933.

[49] J. W. Flowers, K. C. O'Brien, and P. C. McEleney, "Elastic constants of alpha-titanium single crystals at 25°C," *J. Less Common Met.*, vol. 7, no. 5, pp. 393–395, 1964.

[50] A. M. Stapleton, S. L. Raghunathan, I. Bantounas, H. J. Stone, T. C. Lindley, and D. Dye, "Evolution of lattice strain in Ti-6Al-4V during tensile loading at room temperature," *Acta Mater.*, vol. 56, no. 20, pp. 6186–6196, 2008.

[51] J. Sieniawski, W. Ziaja, K. Kubiak, and M. Motyka, "Titanium Alloys - Advances in Properties Control," in *Titanium Alloys - Advances in Properties Control*, 2013, pp. 70–80.

[52] A. Caballero, "Discolouration of Titanium in Wire and Arc Additive Manufacturing," Cranfield University, 2015.

[53] a I. Kahveci and G. E. Welsch, "Pergamon Journals Ltd . All rights reserved N ON THE HARDNESS AND ALPHA / BETA PHASE Copyright (c) 1986 Pergamon Journals Ltd .," *Scr. Metall.*, vol. 20, no. c, pp. 1287–1290, 1986.

[54] J. J. Lin, Y. H. Lv, Y. X. Liu, B. S. Xu, Z. Sun, Z. G. Li, and Y. X. Wu, "Microstructural evolution and mechanical properties of Ti-6Al-4V wall deposited by pulsed plasma arc additive manufacturing," *Mater. Des.*, vol. 102, no. 102, pp. 30–40, 2016.

[55] J. W. Elmer, T. A. Palmer, S. S. Babu, and E. D. Specht, "In situ observations of lattice expansion and transformation rates of ?? and ?? phases in Ti-6Al-4V*," Mater. Sci. Eng. A*, vol. 391, no. 1–2, pp. 104–113, 2005.

[56] J. W. Elmer, T. A. Palmer, S. S. Babu, W. Zhang, and T. DebRoy, "Phase transformation dynamics during welding of Ti-6Al-4V," *J. Appl. Phys.*, vol. 95, no. 12, pp. 8327–8339, 2004.

[57] N. Kherrouba, M. Bouabdallah, R. Badji, and D. Carron, "Beta to alpha transformation kinetics and microstructure of Ti-6Al-4V alloy during continuous cooling," *Mater. Chem. Phys.*, vol. 181, pp. 462–469, 2016.

[58] G. Bruno and B. D. Dunn, "The precise measurement of Ti6Al4V microscopic elastic constants by means of neutron diffraction," *Meas. Sci. Technol.*, vol. 8, no. 11, p. 1244, 1997.

[59] J. W. Elmer, T. A. Palmer, S. S. Babu, and E. D. Specht, "Low temperature relaxation of residual stress in Ti-6Al-4V," *Scr. Mater.*, vol. 52, no. 10, pp. 1051–1056, 2005.

[60] R. F. Zhang, J. Wang, I. J. Beyerlein, T. C. Germann, J. Wang, I. J. Beyerlein, and T. C. G. Twinning, "Twinning in bcc metals under shock loading : a challenge to empirical potentials*,"* vol. 839*,* no. November*,* 2017.

[61] S. Xu, L. S. Toth, C. Schuman, and M. R. Barnett, "Dislocation mediated variant selection for secondary twinning in compression of pure titanium," *ACta Mater.*, vol. 124, pp. 59–70, 2017.

[62] L. Bao, J. S. Lecomte, C. Schuman, M. J. Philippe, X. Zhao, and C. Esling, "Study of plastic deformation in hexagonal metals by interrupted in-situ EBSD measurement," *Adv. Eng. Mater.*, vol. 12, no. 10, pp. 1053–1059, 2010.

[63] T. B. Britton, F. P. E. Dunne, and A. J. Wilkinson, "On the mechanistic basis of deformation at the microscale in hexagonal close-packed metals Subject Areas :*,"* in *Proc. R. Soc. A*, 2015, p. 471.

[64] C. J. McHargue and J. P. Hammondt, "Deformation Mechanism in Titanium at elevated Temperatures," *Acta Metall.*, vol. 1, pp. 700–705, 1953.

[65] M. Borlaug Mathisen, L. Eriksen, Y. Yu, O. Jensrud, and J. Hjelen, "Characterization of microstructure and strain response in Ti-6Al-4V plasma welding deposited material by combined EBSD and in-situ tensile test," *Trans. Nonferrous Met. Soc. China (English Ed.*, vol. 24, no. 12, pp. 3929–3943, 2014.

[66] A. T. Santhanam and R. E. Reed-Hill, "The Influence of Strain Rate Dependent Work Hardening on the Necking Strain in a-Titanium at Elevated Temperatures," *Metall. Trans.*, vol. 2, pp. 2619–2622, 1971.

[67] Y. B. Chun, S. H. Yu, S. L. Semiatin, and S. K. Hwang, "Effect of deformation twinning on microstructure and texture evolution during cold rolling of CP-titanium," vol. 398, pp. 209–219, 2005.

[68] Y. Ma, Q. Xue, H. Wang, S. Huang, J. Qiu, X. Feng, and J. Lei, "Materials Characterization Deformation twinning in fatigue crack tip plastic zone of Ti-6Al-4V alloy with Widmanstatten microstructure," *Mater. Charact.*, vol. 132, no. August, pp. 338–347, 2017.

[69] E. Bertrand, T. Gloriant, P. Castany, and I. Pe, "Twinning system selection in a metastable b-titanium alloy by

Schmid factor analysis," *Scr. Mater.*, vol. 64, pp. 1110–1113, 2011.

[70] Y. Yang, G. P. Li, G. M. Cheng, H. Wang, M. Zhang, F. Xu, and K. Yang, "Stress-introduced a'' martensite and twinning in a multifunctional titanium alloy," *Scr. Mater.*, vol. 58, pp. 9–12, 2008.

[71] S. Hanada and O. Izumi, "Transmission Electron Microscopic Observations of Mechanical Twinning in Metastable Beta Titanium Alloys," vol. 17, no. August, 1986.

[72] J. M. Donoghue, "Hybrid Additive Manufacture and Deformation Processing for Large Scale Near-Net Shape Manufacture of Titanium Aerospace Components," University of Manchester, 2016.

[73] Y. T. Zhu, X. Z. Liao, X. L. Wu, and J. Narayan, "Grain size effect on deformation twinning and detwinning," *Mater. Sci.*, vol. 48, pp. 4467–4475, 2013.

[74] R. Filip, K. Kubiak, J. Sieniawski, and W. Ziaja, "The effect of microstructure on the mechanical properties of two-phase titanium alloys," *Mater. Des.*, vol. 18, pp. 361–363, 2003.

[75] F. J. Gil, M. P. Ginebra, J. M. Manero, and J. A. Planell, "F.J. Gil * , M.P. Ginebra, J.M. Manero, J.A. Planell ´ ´ ," vol. 329, pp. 142–152, 2001.

[76] T. Ahmed and H. J. Rack, "Phase transformations during cooling in α+β titanium alloys," *Mater. Sci. Eng. A*, vol. 243, pp. 206–211, 1998.

[77] F. Martina, P. A. Colegrove, S. W. Williams, and J. Meyer, "Microstructure of Interpass Rolled Wire + Arc Additive Manufacturing Ti-6Al-4V Components," *Metall. Mater. Trans. A Phys. Metall. Mater. Sci.*, vol. 46, no. 12, pp. 6103–6118, 2015.

[78] L. Eriksen, "Combined EBSD-investigations and in-situ tensile tests of a direct metal deposited Ti−6Al−4V-alloy," Trondheim: Norwegian University of Science and Technology, 2013.

[79] H. Galarraga, R. J. Warren, D. A. Lados, R. R. Deho, M. M. Kirka, and P. Nandwana, "Effects of heat treatments on microstructure and properties of Ti-6Al-4V ELI alloy fabricated by electron beam melting (EBM)," *Mater. Sci. Eng. A*, vol. 685, pp. 417–428, 2017.

[80] A. I. Kahveci and G. E. Welsch, "Hardness versus strength correlation for oxygen-strengthened Ti-6Al-4V alloy," *Scr. Metall. Mater.*, vol. 25, no. 8, pp. 1957–1962, 1991.

[81] M. Yan, W. Xu, M. S. Dargusch, H. P. Tang, M. Brandt, M. Qian, W. Xu, M. S. Dargusch, H. P. Tang, M. Brandt, M. Qian, M. Yan, W. Xu, M. S. Dargusch, H. P. Tang, M. Brandt, and M. Qian, "Review of effect of oxygen on room temperature ductility of titanium and titanium alloys Review of effect of oxygen on room temperature ductility of titanium and titanium alloys," *Powder Metall.*, vol. 57, no. 4, pp. 251–257, 2014.

[82] P. Åkerfeldt, M.-L. Antti, and R. Pederson, "Influence of microstructure on mechanical properties of laser metal wire-deposited Ti-6Al-4V," *Mater. Sci. Eng. A*, vol. 674, pp. 428–437, 2016.

[83] F. Wang, S. Williams, and M. Rush, "Morphology investigation on direct current pulsed gas tungsten arc welded additive layer manufactured Ti6Al4V alloy," *Int. J. Adv. Manuf. Technol.*, vol. 57, pp. 597–603, 2011.

[84] S. David and J. Vitek, "Correlation between solidification parameters and weld microstructures," *Int. Mater. Rev.*, vol. 34, 1989.

[85] G. Nolze and R. Hielscher, "IPF coloring of crystal orientation data," *J. Appl. Crystallogr.*, vol. 0, pp. 000–000, 2016.

[86] J. Donoghue, A. A. Antonysamy, F. Martina, P. A. Colegrove, S. W. Williams, and P. B. Prangnell, "The effectiveness of combining rolling deformation with Wire-Arc Additive Manufacture on β-grain refinement and texture modification in Ti-6Al-4V," *Mater. Charact.*, vol. 114, pp. 103–114, 2016.

[87] F. Wang, S. Williams, P. Colegrove, and A. A. Antonysamy, "Microstructure and mechanical properties of wire and arc additive manufactured Ti-6Al-4V," *Metall. Mater. Trans. A Phys. Metall. Mater. Sci.*, vol. 44, pp. 968–977, 2012.

[88] S. M. Kelly and S. L. Kampe, "Microstructural evolution in laser-deposited multilayer Ti-6Al-4V builds: Part II. Thermal modeling," *Metall. Mater. Trans. A*, vol. 35, no. 6, pp. 1861–1867, 2004.

[89] W. Rae, Z. Lomas, M. Jackson, and S. Rahimi, "Materials Characterization Measurements of residual stress and microstructural evolution in electron beam welded Ti-6Al-4V using multiple techniques," *Mater. Charact.*, vol. 132, pp. 10–19, 2017.

[90] C. Charles and N. Jarvstrat, "Modelling Ti-6Al-4V microstructure by evolution laws implemented as finite

element subroutines: Application to TIG metal deposition," *Proc. 8th Int. Conf. Trends Weld. Res.*, pp. 477–485, 2009.

[91] C. Charles Murgau, "Microstructure Model for Ti-6Al-4V used in Simulation of Additive Manufacturing," 2016.

[92] F. Martina, A. Caballero, and Z. Pinter, "Mechanical properties of Wire + Arc Additive Ti – 6Al – 4V deposits: deposition strategies and wire quality," 2016.

[93] J. Zhang, X. Zhang, X. Wang, J. Ding, Y. Traoré, S. Paddea, and S. Williams, "Crack path selection at the interface of wrought and wire+arc additive manufactured Ti–6Al–4V," *Mater. Des.*, vol. 104, pp. 365–375, 2016.

[94] J. Zhang, X. Wang, S. Paddea, and X. Zhang, "Fatigue crack propagation behaviour in wire + arc additive manufactured Ti - 6Al - 4V : Effects of microstructure and residual stress," *Mater. Des. Des.*, vol. 90, pp. 551–561, 2016.

[95] Y. Xie, M. Gao, F. Wang, C. Zhang, K. Hao, H. Wang, and X. Zeng, "Anisotropy of fatigue crack growth in wire arc additive manufactured Ti-6Al-4V," *Mater. Sci. Eng. A*, vol. 709, pp. 265–269, 2018.

[96] J. Gu, J. Ding, S. W. Williams, H. Gu, P. Ma, and Y. Zhai, "The effect of inter-layer cold working and post-deposition heat treatment on porosity in additively manufactured aluminum alloys," *J. Mater. Process. Technol.*, vol. 230, pp. 26–34, 2016.

[97] J. Yang, H. Yu, J. Yin, M. Gao, Z. Wang, and X. Zeng, "Formation and control of martensite in Ti-6Al-4V alloy produced by selective laser melting," *Mater. Des.*, vol. 108, pp. 308–318, 2016.

[98] G. M. Bilgin, Z. Esen, S. K. Akin, and A. F. Dericioglu, "Optimization of the mechanical properties of Ti-6Al-4V alloy fabricated by selective laser melting using thermohydrogen processes," *Mater. Sci. Eng. A*, vol. 700, no. May, pp. 574–582, 2017.

[99] N. Hrabe, T. Gnaupel-Herold, and T. Quinn, "Fatigue properties of a titanium alloy (Ti-6Al-4V) fabricated via electron beam melting (EBM): Effects of internal defects and residual stress," *Int. J. Fatigue*, vol. 94, pp. 202–210, 2017.

[100] L. E. Murr, "Metallurgy of additive manufacturing: Examples from electron beam melting," *Addit. Manuf.*, vol. 5, pp. 40–53, 2015.

[101] C. Qiu, G. a. Ravi, C. Dance, A. Ranson, S. Dilworth, and M. M. Attallah, "Fabrication of large Ti–6Al–4V structures by direct laser deposition," *J. Alloys Compd.*, vol. 629, pp. 351–361, 2015.

[102] P. Alvarez and L. Vazquez Martinez, "Influence of post deposition heat treatments on microstructures and mechanical properties of Ti-6Al-4V Parts manufactured by CMT-WAAM." 2nd Metallic MAterials and Processes, 2017.

[103] E. Brandl, B. Baufeld, C. Leyens, and R. Gault, "Additive manufactured Ti-6A1-4V using welding wire: Comparison of laser and arc beam deposition and evaluation with respect to aerospace material specifications," *Phys. Procedia*, vol. 5, pp. 595–606, 2010.

[104] N. S. Rossini, M. Dassisti, K. Y. Benyounis, and a. G. Olabi, "Methods of measuring residual stresses in components," *Mater. Des.*, vol. 35, pp. 572–588, 2012.

[105] K. Deplus, A. Simar, W. Van Haver, and B. De Meester, "Residual stresses in aluminium alloy friction stir welds," *Int. J. Adv. Manuf. Technol.*, vol. 56, no. 5–8, pp. 493–504, 2011.

[106] K. Masubuchi, "Models of Stresses and Deformation Due to Welding-A Review," *J. Met.*, pp. 19–23, 1981.

[107] R. H. Leggatt, D. J. Smith, S. D. Smith, and F. Faure, "DEVELOPMENT AND EXPERIMENTAL VALIDATION OF THE DEEP HOLE METHOD FOR RESIDUAL STRESS MEASUREMENT," *J. Strain Anal.*, vol. 31, no. 3, pp. 177–186, 1996.

[108] P. A. Colegrove, C. Ikeagu, A. Thistlethwaite, S. Williams, T. Nagy, W. Suder, A. Steuwer, and T. Pirling, "Welding process impact on residual stress and distortion," vol. 14, no. 8, pp. 717–725, 2009.

[109] C. Liu and X. Yi, "Residual stress measurement on AA6061-T6 aluminum alloy friction stir butt welds using contour method," *Mater. Des.*, vol. 46, pp. 366–371, 2013.

[110] M. Peel, a. Steuwer, M. Preuss, and P. J. Withers, "Microstructure, mechanical properties and residual stresses as a function of welding speed in aluminium AA5083 friction stir welds," *Acta Mater.*, vol. 51, no. 16, pp. 4791–4801, 2003.

[111] P. A. Colegrove, H. E. Coules, J. Fairman, F. Martina, T. Kashoob, H. Mamash, and L. D. Cozzolino, "Microstructure and residual stress improvement in wire and arc additively manufactured parts through high-pressure rolling," *J. Mater. Process. Technol.*, vol. 213, pp. 1782–1791, 2013.

[112] N. Hoye, H. Li, D. Cuiuri, and A. Paradowska, "Measurement of Residual Stresses in Titanium Aerospace Components Formed via Additive Manufacturing," *Mater. Sci. Forum*, vol. 777, pp. 124–129, 2014.

[113] F. Martina, M. Roy, P. Colegrove, and S. Williams, "Residual Stress Reduction in High Pressure Interpass Rolled Wire + Arc Additive Manufacturing Ti-6Al-4V components," in *25th International Solid Freeform Fabrication*, 2014, pp. 89–94.

[114] P. A. Colegrove, F. Martina, M. J. Roy, B. Szost, S. Terzi, S. W. Williams, P. J. Withers, and D. Jarvis, "High pressure interpass rolling of Wire + Arc Additively Manufactured titanium components," *Adv. Mater. Res.*, vol. 996, pp. 694–700, 2014.

[115] F. Martina, M. J. Roy, B. A. Szost, S. Terzi, P. A. Colegrove, S. W. Williams, P. J. Withers, J. Meyer, and M. Hofmann, "Residual stress of as-deposited and rolled wire+arc additive manufacturing Ti–6Al–4V components," *Mater. Sci. Technol.*, vol. 836, no. April, 2016.

[116] B. A. Szost, S. Terzi, F. Martina, D. Boisselier, A. Prytuliak, T. Pirling, M. Hofmann, and D. J. Jarvis, "A comparative study of additive manufacturing techniques: Residual stress and microstructural analysis of CLAD and WAAM printed Ti-6Al-4V components," *Mater. Des.*, vol. 89, pp. 559–567, 2016.

[117] T. Mukherjee, W. Zhang, and T. Debroy, "An improved prediction of residual stresses and distortion in additive manufacturing," *Comput. Mater. Sci.*, vol. 126, pp. 360–372, 2017.

[118] J. Ding, P. Colegrove, J. Mehnen, S. Williams, F. Wang, and P. S. Almeida, "A computationally efficient finite element model of wire and arc additive manufacture," *Int. J. Adv. Manuf. Technol.*, vol. 70, pp. 227–236, 2014.

[119] J. Ding, P. Colegrove, J. Mehnen, S. Ganguly, P. M. S. Almeida, F. Wang, and S. Williams, "Thermo-mechanical analysis of Wire and Arc Additive Layer Manufacturing process on large multi-layer parts," *Comput. Mater. Sci.*, vol. 50, no. 12, pp. 3315–3322, 2011.

[120] E. R. Denlinger, J. C. Heigel, P. Michaleris, and T. A. Palmer, "Effect of Inter-Layer Dwell Time on Distortion and ResidualStress in Additive Manufacturing of Titanium and Nickel Alloys," *J. Mater. Process. Technol.*, vol. 215, pp. 123–131, 2015.

[121] E. R. Denlinger and P. Michaleris, "Effect of stress relaxation on distortion in additive manufacturing process modeling," *Addit. Manuf.*, vol. 12, pp. 51–59, 2016.

[122] G. Vastola, G. Zhang, Q. X. Pei, and Y.-W. Zhang, "Controlling of residual stress in additive manufacturing of Ti6Al4V by finite element modeling," *Addit. Manuf.*, 2016.

[123] F. Montevecchi, G. Venturini, A. Scippa, and G. Campatelli, "Finite element modelling of Wire-Arc-Additive-Manufacturing process," *Procedia CIRP*, vol. 55, pp. 109–114, 2016.

[124] X. Wang and A. Wang, "Finite element analysis of clamping form in wire and arc additive manufacturing," pp. 1–5, 2017.

[125] L. Parry, I. A. Ashcroft, and R. D. Wildman, "Understanding the effect of laser scan strategy on residual stress in selective laser melting through thermo-mechanical simulation," *Addit. Manuf.*, vol. 12, pp. 1–15, 2016.

[126] S. Rios Contesse, "Hardware development and process control for plasma-based Wire + Arc Additive Manufacturing," Cranfield University, 2017.

[127] A. A. Antonysamy, J. Meyer, and P. B. Prangnell, "Effect of build geometry on the β -grain structure and texture in additive manufacture of Ti-6Al-4V by selective electron beam melting," vol. 84, pp. 153–168, 2013.

[128] B. K. Foster, A. M. Beese, J. S. Keist, E. T. Mchale, and T. A. Palmer, "Impact of Interlayer Dwell Time on Microstructure and Mechanical Properties of Nickel and Titanium Alloys," *Metall. Mater. Trans. A*, vol. 48, no. 9, pp. 4411–4422, 2017.

[129] R. C. Fayolle, "CRYOGENIC COOLING OF WIRE + ARC ADDITIVE MANUFACTURE," Cranfield University, 2016.

[130] A. R. Nassar and E. W. Reutzel, "Additive Manufacturing of Ti-6Al-4V Using a Pulsed Laser Beam," *Metall. Mater. Trans. A*, vol. 46 A, pp. 2781–2789, 2015.

[131] G. Longhitano, M. Aparecida, A. Jardini, C. de Carvalho, and M. Filippini, "Correlation between microstructures and mechanical properties under tensile and compression tests of heat-treated Ti-6Al – 4 V

ELI alloy produced by additive manufacturing for biomedical applications," *J. Mater. Process. Tech.*, vol. 252, no. November 2016, pp. 202–210, 2018.

[132] V. I. Kurkin, S. A., Anufriev, "Preventing distortion of welded thin-walled members of AMg6 and 1201 aluminum alloys by rolling the weld with a roller behind the welding arc," *Sverochnoe Proizv.*, vol. 31, no. 10, pp. 52–55, 1984.

[133] D. F. O. Braga, H. E. Coules, T. Pirling, V. Richter-Trummer, P. Colegrove, and P. M. S. T. De Castro, "Assessment of residual stress of welded structural steel plates with or without post weld rolling using the contour method and neutron diffraction," *J. Mater. Process. Technol.*, vol. 213, no. 12, pp. 2323–2328, 2013.

[134] H. E. Coules, P. Colegrove, L. D. Cozzolino, S. W. Wen, S. Ganguly, and T. Pirling, "Effect of high pressure rolling on weld-induced residual stresses," *Sci. Technol. Weld. Join.*, vol. 17, no. 5, pp. 394–401, 2012.

[135] H. E. Coules, L. D. Cozzolino, P. A. Colegrove, and S. Wen, "The effect of pre-weld rolling on distortion and residual stress in fusion welded steel plate," vol. 681, pp. 486–491, 2011.

[136] H. E. Coules, L. D. Cozzolino, P. Colegrove, S. Ganguly, S. W. Wen, and T. Pirling, "Neutron Diffraction Analysis of Complete Residual Stress Tensors in Conventional and Rolled Gas Metal Arc Welds," *Exp. Mech.*, vol. 53, pp. 195–204, 2013.

[137] F. Martina, S. W. Williams, and P. Colegrove, "Improved microstructure and increased mechanical properties of additive manufacture produced Ti-6Al-4V by interpass cold rolling," *SFF Symp.*, pp. 490–496, 2013.

[138] J. Gu, J. Ding, S. W. Williams, H. Gu, P. Ma, and Y. Zhai, "The strengthening effect of inter-layer cold working and post-deposition heat treatment on the additively manufactured Al–6.3Cu alloy," *Mater. Sci. Eng. A*, vol. 651, pp. 18–26, 2016.

[139] P. A. Colegrove, J. Donoghue, F. Martina, J. Gu, P. Prangnell, and J. Hönnige, "Application of bulk deformation methods for microstructural and material property improvement and residual stress and distortion control in additively manufactured components," *Scr. Mater.*, vol. 2, 2016.

[140] J. Donoghue, A. Gholinia, J. Quinta da Fonseca, and P. B. Prangnell, "In-situ High Temperature EBSD Analysis of the Effect of a Deformation Step on the Alpha to Beta Transition in Additive Manufactured Ti6Al4V," in *3th World Conference on Titanium*, 2015, pp. 1283–1288.

[141] J. R. Hönnige, S. Williams, M. J. Roy, P. Colegrove, and S. Ganguly, "Residual Stress Characterization and Control in the Additive Manufacture of Large Scale Metal Structures," in *10th International Conference on Residual Stresses*, 2016.

[142] J. Sule, S. Ganguly, H. Coules, and T. Pirling, "Application of local mechanical tensioning and laser processing to refine microstructure and modify residual stress state of a multi-pass 304L austenitic steels welds," *J. Manuf. Process.*, vol. 18, pp. 141–150, 2015.

[143] M. Alvarez, "ROLLING OF WAAM INTERSECTIONS," Cranfield University, 2016.

[144] J. Pratt, "Intersection Design - design of intersections to allow machining of large radii in wire + arc additive manufacture parts," 2017.

[145] E. Maawad, Y. Sano, L. Wagner, H.-G. Brokmeier, and C. Genzel, "Investigation of laser shock peening effects on residual stress state and fatigue performance of titanium alloys," *Mater. Sci. Eng. A*, vol. 536, pp. 82–91, 2012.

[146] M. Dorman, M. B. Toparli, N. Smyth, a. Cini, M. E. Fitzpatrick, and P. E. Irving, "Effect of laser shock peening on residual stress and fatigue life of clad 2024 aluminium sheet containing scribe defects," *Mater. Sci. Eng. A*, vol. 548, pp. 142–151, 2012.

[147] A. Chahardehi, F. P. Brennan, and A. Steuwer, "The effect of residual stresses arising from laser shock peening on fatigue crack growth," *Eng. Fract. Mech.*, vol. 77, no. 11, pp. 2033–2039, 2010.

[148] N. Hfaiedh, P. Peyre, H. Song, I. Popa, V. Ji, and V. Vignal, "Finite Element analysis of Laser Shock Peening of 2050-T8 aluminum alloy," *Int. J. Fatigue*, vol. 70, pp. 480–489, 2014.

[149] B. Al Mangour and J.-M. Yang, "Improving the surface quality and mechanical properties by shot-peening of 17-4 stainless steel fabricated by additive manufacturing," *Mater. Des.*, vol. 110, pp. 914–924, 2016.

[150] Y. F. Al-Obaid, "A Rudimentary Analysis of Improving Fatigue Life of Metals by Shot-Peening," *J. Appl. Mech. Trans. ASME*, vol. 57, no. 2, pp. 307–312, 1990.

[151] E. S. Statnikov, V. O. Muktepavel, a Blomqvist, and T. Company, "Comparison of Ultrasonic Impact Treatment

(UIT) and other Fatigue Life Improvement Methods," *Weld. World*, vol. 46, no. 3/4, pp. 20–32, 2002.

[152] F. Lienert, J. Hoffmeister, and V. Schulze, "Residual Stress Depth Distribution after Piezo Peening of Quenched and Tempered AISI 4140," *Mater. Sci. Forum*, vol. 768–769, pp. 526–533, 2014.

[153] M. Kranz, "FORGEfix (Air) - Pneumatisches Kaltschmiedesystem / pneumatic cold forming system," *Werkzeug & Formenbau*, pp. 30–32, Jun-2012.

[154] C. Löcker, "Accuradur - Inherent Compressive Stress." [Online]. Available: http://www.accurapuls.de/accuradur _englisch.html. [Accessed: 31-Jan-2016].

[155] M. Rodríguez Ripoll, F. Heindl, C. Lechner, C. Habersohn, M. Jech, and F. Bleicher, "Improving wear resistance of functional surfaces using the machine hammer peening technique," *Tribol. - Mater. Surfaces Interfaces*, vol. 8, no. 1, pp. 21–26, 2014.

[156] D. Trauth, A. Feuerhack, P. Mattfeld, and F. Klocke, "Analysis of the Velocity Distribution of an Elliptic Surface Structure Manufactured by Machine Hammer Peening," *Tribol. Lett.*, vol. 60, no. 1, pp. 1–13, 2015.

[157] B. Adjassoho, E. Kozeschnik, C. Lechner, C. Habersohn, F. Bleicher, S. Gössinger, C. Bauer, F. Heindl, and M. R. Ripoll, "Controlled surface treatment with machine hammer peening," in *METAL 2013*, 2013, pp. 13–18.

[158] F. Bleicher, C. Lechner, C. Habersohn, E. Kozeschnik, B. Adjassoho, and H. Kaminski, "Mechanism of surface modification using machine hammer peening technology," *CIRP Ann. - Manuf. Technol.*, vol. 61, no. 1, pp. 375–378, 2012.

[159] F. Bleicher, C. Lechner, C. Habersohn, M. Obermair, F. Heindl, and M. Rodriguez Ripoll, "Improving the tribological characteristics of tool and mould surfaces by machine hammer peening," *CIRP Ann. - Manuf. Technol.*, vol. 62, no. 1, pp. 239–242, 2013.

[160] M. Oechsner, J. Wied, and J. Stock, "Influence of machine hammer peening on the tribology of sheet forming," *Adv. Mater. Res.*, vol. 967, pp. 397–405, 2014.

[161] D. Trauth, F. K. D. Welling, and M. T. P. Mattfeld, "Investigation of the surface integrity and fatigue strength of Inconel718 after wire EDM and machine hammer peening," *Int. J. Mater. Form.*, vol. 9, pp. 635–651, 2016.

[162] M. K. Kulekci and U. Esme, "Critical analysis of processes and apparatus for industrial surface peening technologies," *Int. J. Adv. Manuf. Technol.*, pp. 1551–1565, 2014.

[163] W. Zhou, X. Ren, F. Liu, Y. Ren, and L. Li, "Nanocrystallization in the Duplex Ti-6Al-4V Alloy Processed by Multiple Laser Shock Peening," *Metals (Basel).*, vol. 6, no. 297, pp. 1–10, 2016.

[164] F. Bleicher, "6th Workshop MACHINE HAMMER PEENING, TU Wien," 2017. [Online]. Available: https://wmhp.tuwien.ac.at/home/. [Accessed: 12-Nov-2017].

[165] A. Ostertag and S. Zenk, "Festhammervorrichtung zum Beeinflussen von Werkstücken und zugehöriges Verfahren," DE 102015203487 A1, 2016.

[166] P. Groche, "5th Workshop on Machine Hammer Peening," Darmstadt, 2016.

[167] J. Donoghue, J. Sidhu, A. Wescott, and P. Prangnell, "Integration of deformation processing with additive manufacture of Ti-6Al-4V components for improved β grain structure and texture," *TMS Annu. Meet.*, vol. 2015–March, pp. 437–444, 2015.

[168] J.-G. Byun, H. Yi, and S.-M. Cho, "The Effect of Interpass Peening on Mechanical Properties in Additive Manufacturing of Ti-," *J. Weld. Join.*, vol. 35, no. 2, pp. 6–12, 2017.

[169] *ASTM-International, ASTM Standard F136-13: Standard Specification for Wrought Titanium-6Aluminum-4Vanadium ELI (Extra Low Interstitial) Alloy for Surgical Implant Applications*. 2003.

[170] C. Zopp, S. Blümer, F. Schubert, and L. Kroll, "Processing of a metastable titanium alloy (Ti-5553) by selective laser melting," *Ain Shams Eng. J.*, vol. 8, no. 3, pp. 475–479, 2017.

[171] F. Palm, R. Leuschner, T. Schubert, and B. Kieback, "Scalmalloy® = A unique high strength ALMgSc type material concept processed by innovative technologies for aerospace applications.," in *Proceedings of the World Powder Metallurgy Congress and Exhibition, World PM*, 2010, p. 4.

[172] J. H. Martin, B. D. Yahata, J. M. Hundley, J. A. Mayer, T. A. Schaedler, and T. M. Pollock, "3D printing of high-strength aluminium alloys," *Nature*, vol. 549, pp. 365–369, 2017.

[173] S. Tamirisakandala, R. B. Bhat, J. S. Tiley, and D. B. Miracle, "Grain refinement of cast titanium alloys via trace boron addition," *Scr. Mater.*, vol. 53, no. 12, pp. 1421–1426, 2005.

[174] Z. Mahbooba, H. West, O. L. A. Harrysson, A. Wojcieszynski, R. Dehoff, P. Nandwana, and T. Horn, "Effect of Hypoeutectic Boron Additions on the Grain Size and Mechanical Properties of Ti-6Al-4V Manufactured with Powder Bed Electron Beam Additive Manufacturing," *Miner. Met. Mater. Soc.*, vol. 69, no. 3, pp. 472–478, 2017.

[175] M. J. Bermingham, D. Kent, H. Zhan, D. H. StJohn, and M. S. Dargusch, "Controlling the microstructure and properties of wire arc additive manufactured Ti–6Al–4V with trace boron additions," *Acta Mater.*, vol. 91, pp. 289–303, 2015.

[176] F. Martina, "Investigation of methods to manipulate geometry , microstructure and mechanical properties in titanium large scale Wire + Arc Additive Manufacturing," Cranfield University, 2014.

[177] H. Choe, S. M. Abkowitz, S. Abkowitz, and D. C. Dunand, "Effect of tungsten additions on the mechanical properties of Ti-6Al-4V," *Mater. Sci. Eng. A*, vol. 396, pp. 99–106, 2005.

[178] H. E. Coules, "Contemporary approaches to reducing weld-induced residual stress," *Mater. Sci. Technol.*, vol. 29, no. 1, 2012.

[179] K. Weman and R. Kovacevic, *Welding Processes Handbook*, 2nd ed. Stockholm: Woodhead Publishing, 2012.

[180] S. H. Wang, M. D. Wei, and L. W. Tsay, "Tensile properties of LBW welds in Ti – 6Al – 4V alloy at evaluated temperatures below 450 oC," *Mater. Lett.*, vol. 57, pp. 1815–1823, 2003.

[181] Z. Guo, N. Saunders, A. P. Miodownik, and S. T. Centre, "MODELLING HIGH TEMPERATURE FLOW STRESS CURVES OF TITANIUM ALLOYS," in *MRS International MAterials Research Conference*, 2008.

[182] G. Chen, C. Ren, X. Qin, and J. Li, "Temperature dependent work hardening in Ti – 6Al – 4V alloy over large temperature and strain rate ranges : Experiments and constitutive modeling," *Mater. Des.*, vol. 83, pp. 598–610, 2015.

[183] P. Edwards and M. Ramulu, "Surface Residual Stresses in Ti-6Al-4V Friction Stir Welds : Pre- and Post-Thermal Stress Relief," *J. Mater. Eng. Perform.*, vol. 24, no. 9, pp. 3263–3270, 2015.

[184] "Der Werkstoff Titan – Wärmebehandlungsmöglichkeiten." [Online]. Available: http://www.sgersing.de/pdf/SFT051.pdf. [Accessed: 29-Aug-2016].

[185] Z. Wang, A. D. Stoica, D. Ma, and A. M. Beese, "Stress relaxation behavior and mechanisms in Ti-6Al-4V determined via in situ neutron diffraction: Application to additive manufacturing," *Mater. Sci. Eng. A*, vol. 707, pp. 585–592, 2017.

[186] J. Xiong, Y. Lei, and R. Li, "Finite element analysis and experimental validation of thermal behavior for thin-walled parts in GMAW-based additive manufacturing with various substrate preheating temperatures," *Appl. Therm. Eng.*, vol. 126, pp. 43–52, 2017.

[187] W. T. Han, F. R. Wan, G. Li, C. L. Dong, and J. H. Tong, "Effect of trailing heat sink on residual stresses and welding distortion in friction stir welding Al sheets," vol. 16, no. 5, pp. 453–458, 2011.

[188] L. Mordfin, *Mechanical Relaxation of Residual Stresses*. 1988.

[189] M. B. Prime, "Cross-Sectional Mapping of Residual Stresses by Measuring the Surface Contour After a Cut," *J. Eng. Mater. Technol.*, vol. 123, no. April 2001, p. 162, 2001.

[190] S. W. Wen, P. A. Colegrove, S. W. Williams, S. A. Morgan, A. Wescott, and M. Poad, "Rolling to control residual stress and distortion in friction stir welds," *Sci. Technol. Weld. Join.*, vol. 15, no. 6, pp. 440–447, 2010.

[191] Y. Xie, H. Zhang, and F. Zhou, "Improvement in geometrical accuracy and mechanical property for arc-based additive manufacturing using metamorphic rolling mechanism," *J. Manuf. Sci. Eng.*, vol. 138, no. November, pp. 1–8, 2015.

[192] A. Lim, S. Castagne, and C. C. Wong, "Quasi-static Process Modelling of Deep Cold Rolling on Ti-6Al-4V," vol. 2, pp. 7–12, 2016.

[193] A. Prithiviraj and W. Wei, "Residual Stress and Contact Force Study for Deep Cold Rolling of Aero-engine Material," vol. 2, pp. 247–252, 2016.

[194] J. Curtat, J. Lanteigne, H. Champliaud, Z. Liu, and J. Lévesque, "Influence of hammer peening on fatigue life of E309L steel used for 13 % Cr-4 % Ni blade runner repairs," *Int. J. Fatigue*, vol. 100, pp. 68–77, 2017.

[195] L. Hacini, N. Van Lê, and P. Bocher, "Evaluation of Residual Stresses Induced by Robotized Hammer Peening by the Contour Method," *Exp. Mech.*, no. 49, pp. 775–783, 2009.

[196] R. Simoneau, D. Thibault, and J. Fihey, "A Comparison of Resiodual Stress in Hammer-Peened, Multi-pass Steel Welds," *Weld. World*, vol. 53, pp. 124–134, 2009.

[197] X. Cheng, J. W. Fisher, H. J. Prask, T. Gnäupel-Herold, B. T. Yen, and S. Roy, "Residual stress modification by post-weld treatment and its beneficial effect on fatigue strength of welded structures," *Int. J. Fatigue*, vol. 25, pp. 1259–1269, 2003.

[198] H. Wohlfahrt, "Ein Modell zur Vorhersage kugelstrahlbedingter Eigenspannungszustände. Eigenspannungen: Enstehung- Messung-Bewertung," *DGM-Informationsgesellschaft*, Oberursel, pp. 301–319, 1983.

[199] P. Sticht, M. Steitz, and P. Groche, "Prediction and Experimental Validation of an Impact Energy Threshold for Mechanical Surface Smoothing," *Procedia CIRP*, vol. 45, pp. 159–162, 2016.

[200] R. A. Claxton, "Vibratory Stress Relieving – an Effective Alternative to Thermal Treatment for Component Stabilisation," *Heat Treat. Met.*, vol. 2, pp. 53–59, 2003.

[201] A. Jurcius, A. V. Valiulis, O. Cernasejus, K. J. Kurzydlowski, A. Jaskiewicz, and M. Lech-Grega, "Influence of vibratory stress relief on residual stresses in weldments and mechanical properties of structural steel joint.pdf," *J. Vibroengineering*, vol. 12, no. 1, pp. 133–141, 2010.

[202] V. Prieb, "Ultrasonic treatment of metallic workpieces and equipment parts," 2001.

[203] A. Siddiq and T. El Sayed, "Acoustic softening in metals during ultrasonic assisted deformation via CP-FEM," *Mater. Lett.*, vol. 65, no. 2, pp. 356–359, 2011.

[204] A. Krajewski, W. Włosiński, T. Chmielewski, and P. Kołodziejczak, "Ultrasonic-vibration assisted arc-welding of aluminum alloys," *Bull. Polish Acad. Sci. Tech. Sci.*, vol. 60, no. 4, pp. 841–852, 2012.

[205] G.-T. Zhou, H.-H. Huang, and H.-Y. Fang, "Controlling welding stress and distortion of aluminium alloy sheet by welding with trailing ultrasonic bibration method," *Chinese J. Noinferrous Met.*, vol. 24, no. 4, pp. 919–925, 2014.

[206] W. He, C. Xiao, F. Shi, H. Zhao, S. Li, and C. Yi, "Reduction of welding residual stress by in-situ ultrasonic impact treatment," *Hanjie Xuebao/Transactions China Weld. Inst.*, vol. 36, no. 8, pp. 84–87, 2015.

[207] V. Fartashvand, A. Abdullah, and S. A. S. Vanini, "Ultrasonics Sonochemistry Investigation of Ti-6Al-4V alloy acoustic softening," *Ultrason. - Sonochemistry*, vol. 38, pp. 744–749, 2017.

[208] J. Altenkirch, a. Steuwer, M. Peel, D. G. Richards, and P. J. Withers, "The effect of tensioning and sectioning on residual stresses in aluminium AA7749 friction stir welds," *Mater. Sci. Eng. A*, vol. 488, pp. 16–24, 2008.

[209] P. Staron, M. Koçak, S. Williams, and a Wescott, "Residual stress in friction stir-welded Al sheets," *Phys. B Condens. Matter*, vol. 350, no. 1–3, pp. E491–E493, 2004.

[210] D. A. Price, S. W. Williams, A. Wescott, C. J. C. Harrison, A. Rezai, A. Steuwer, M. Peel, P. Staron, and M. Koçak, "Distortion control in welding by mechanical tensioning," *Sci. Technol. Weld. Join.*, vol. 12, no. 7, pp. 620–633, 2007.

[211] V. Kostov, J. Gibmeier, K. Lichtenberg, and A. Wanner, "Effect of Preloading on Local Residual Stresses Induced by Laser Surface Hardening of Steel," vol. 996, pp. 562–567, 2014.

[212] P. J. Withers, M. Turski, L. Edwards, P. J. Bouchard, and D. J. Buttle, "Recent advances in residual stress measurement," *Int. J. Press. Vessel. Pip.*, vol. 85, no. 3, pp. 118–127, 2008.

[213] T. Proulx, *Engineering Applications of Residual Stress*, 8th ed. Springer, 2011.

[214] M. E. Fitzpatrick, A. T. Fry, P. Holdway, F. A. Kandil, J. Shackleton, and L. Suominen, "Determination of Residual Stresses by X-ray Diffraction - Issue 2," *A NATIONAL MEASUREMENT GOOD PRACTICE GUIDE - No52*, no. 52, 2005.

[215] M. T. Hutchings, P. J. Withers, T. M. Holden, and T. Lorentzen, *Introduction to the characterization of residual stress by neutron diffraction*. Boca Raton: CRC Press Taylor & Francis Group, 2005.

[216] W. Reimers, A. R. Pyzalla, A. Schreyer, and H. Clemens, *Neutrons and Synchrotron Radiation in Engineering Materials Science*. Weinheim: Wiley-VCH Verlag GmbH, 2008.

[217] P. Staron, A. Schreyer, H. Clemens, and S. Mayer, *Neutrons and Synchrotron Radiation in Engineering and Material Science*, Second. Weinheim: Wiley-VCH Verlag GmbH, 2017.

[218] J. R. Santisteban, M. R. Daymond, J. A. James, and L. Edwards, "ENGIN-X: A third-generation neutron strain scanner," *J. Appl. Crystallogr.*, vol. 39, no. 6, pp. 812–825, 2006.

[219] M. Hofmann, R. Schneider, G. A. Seidl, J. Rebelo-kornmeier, and R. C. Wimpory, “The new materials science diffractometer STRESS-SPEC at FRM-II,” in *Physica B*, 2006, vol. 386, pp. 1035–1037.

[220] T. Pirling, G. Bruno, and P. J. Withers, “SALSA-A new instrument for strain imaging in engineering materials and components,” *Mater. Sci. Eng. A*, vol. 437, pp. 139–144, 2006.

[221] N. Schell, A. King, F. Beckmann, H. U. Ruhnau, R. Kirchhof, R. Kiehn, M. M??ller, and A. Schreyer, “The High Energy Materials Science Beamline (HEMS) at PETRA III,” *AIP Conf. Proc.*, vol. 1234, pp. 391–394, 2010.

[222] G. Johnson, “Residual Stress Measurement Using Contour Method,” The University of Manchester, 2008.

[223] M. B. Prime, R. J. Sebring, J. M. Edwards, D. J. Hughes, and P. J. Webster, “Laser Surface-contouring and Spline Data-smoothing for Residual Stress Measurement,” vol. 44, no. 2, 2004.

[224] F. Hosseinzadeh, J. Kowal, and P. J. Bouchard, “Towards good practice guidelines for the contour method of residual stress measurement,” *Engineering*, 2014.

[225] B. Ahmad and M. E. Fitzpatrick, “Minimization and Mitigation of Wire EDM Cutting Errors in the Application of the Contour Method of Residual Stress Measurement,” *Metall. Mater. Trans. A*, vol. 47, no. 1, pp. 301–313, 2016.

[226] Y. L. Sun, M. J. Roy, A. N. Vasileiou, M. C. Smith, J. A. Francis, and F. Hosseinzadeh, “Evaluation of Errors Associated with Cutting-Induced Plasticity in Residual Stress Measurements Using the Contour Method,” *Exp. Mech.*, vol. 57, pp. 719–734, 2017.

[227] F. Montevecchi, G. Venturini, N. Grossi, A. Scippa, and G. Campatelli, “Finite Element mesh coarsening for effective distortion prediction in Wire Arc Additive Manufacturing,” *Addit. Manuf.*, vol. 18, pp. 145–155, 2017.

[228] G. R. Cowper, “The Shear Coefficient in Timoshenko â€™s Beam Theory,” vol. 6, no. 4, 2017.

[229] F. Romano, “Deflections of Timoshenko Beam with varying Cross-Section,” *Pergamon*, vol. 38, no. 84, pp. 1017–1035, 1996.

[230] A. J. M. Ferreira, *MATLAB Codes for Finite Element Analysis*. Springer, 2009.

[231] J. Ding, P. Colegrove, F. Martina, S. Williams, R. Wiktorowicz, and M. R. Palt, “Development of a laminar flow local shielding device for wire+arc additive manufacture,” *J. Mater. Process. Technol.*, vol. 226, pp. 99–105, 2015.

[232] T. M. Holden, Y. Traore, J. James, J. Kelleher, and P. J. Bouchard, “short communications Determination and mitigation of the uncertainty of neutron diffraction measurements of residual strain in large-grained polycrystalline material,” pp. 582–584, 2015.

[233] G. S. Pawley, “Unit-cell refinement from powder diffraction scans,” *J. Appl. Crystallogr.*, vol. 14, p. 357, 1981.

[234] P. Davies, W. Kockelmann, B. Wynne, R. Eccleston, B. Hutchinson, and W. M. Rainforth, “Validation of neutron texture data on GEM at ISIS using electron backscattered diffraction,” *Meas. Sci. Technol.*, vol. 19, pp. 1–4, 2008.

[235] J. W. Elmer, T. A. Palmer, and J. Wong, “In situ observations of phase transitions in Ti-6Al-4V alloy welds using spatially resolved x-ray diffraction,” *J. Appl. Phys.*, vol. 93, no. 4, pp. 1941–1947, 2003.

[236] A. K. Swarnakar, O. Van Der Biest, and B. Baufeld, “Thermal expansion and lattice parameters of shaped metal deposited Ti-6Al-4V,” *J. Alloys Compd.*, vol. 509, no. 6, pp. 2723–2728, 2011.

[237] M. Roy, “Pinch-rolled WAAM Ti samples contour method process overview,” Manchester, 2016.

[238] A. L. Pilchak, G. A. Sargent, and S. L. Semiatin, “Early Stages of Microstructure and Texture Evolution during Beta Annealing of Ti-6Al-4V,” *Metall. Mater. Trans. A*, 2017.

[239] Y. Kudryavtsev and J. Kleiman, “Fatigue Life Improvement of Welded Elements by Ultrasonic Peening,” 2010.

[240] L. D. Cozzolino, H. E. Coules, P. A. Colegrove, and S. Wen, “Investigation of post-weld rolling methods to reduce residual stress and distortion,” *J. Mater. Process. Technol.*, vol. 247, pp. 243–256, 2017.

[241] A. Ostertag, “Machine Hammer Peening mit mechanisch angetriebenen Werkzeugen,” in *6thWorkshop MACHINE HAMMER PEENING*, 2017, p. 5.

[242] P. A. Colegrove, A. McAndrew, M. Rosales, J. R. Hönnige, and A. Ho, “Interpass Rolling of Ti-6Al-4V Wire + Arc Additively Manufactured Features for Microstructural Refinement,” *Addit. Manuf.*, 2018.

[243] J. G. Williams and C. Gamonpilas, "Using the simple compression test to determine Young ' s modulus , Poisson's ratio and the Coulomb friction coefficient," *Int. J. Solids Struct.*, vol. 45, pp. 4448–4459, 2008.

[244] P. S. Davies, B. P. Wynne, W. M. Rainforth, M. J. Thomas, and P. L. Threadgill, "Development of Microstructure and Crystallographic Texture during Stationary Shoulder Friction Stir Welding of Ti-6Al-4V," *Metall. Mater. Trans. A*, vol. 42A, pp. 2278–2289, 2011.

[245] M. W. Czabaj, W. R. Tubbs, A. T. Zehnder, and B. D. Davidson, "Experimental and Applied Mechanics," in *Experimental and Applied Mechanics*, vol. 6, 2011, pp. 393–398.

[246] X. Wang and K. Chou, "A Method to Estimate Residual Stress in Metal Parts Made by Selective Laser Melting," in *ASME 2015 International Mechanical Engineering Congress and Exposition*, 2015, p. V02AT02A002.

[247] W. P. Longo and R. E. Reed-Hill, "Work Softening in Polycrystalline metals," *Scr. Metall.*, vol. 4, pp. 765–770, 1970.

[248] J. Wang, Z. Zeng, C. R. Weinberger, Z. Zhang, T. Zhu, and S. X. Mao, "In situ atomic-scale observation of twinning-dominated deformation in nanoscale body-centred cubic tungsten," *Nat. Mater.*, vol. 14, no. 6, pp. 594–600, 2015.

[249] L. Hacini, V. N. Lê, and P. Bocher, "Traitement de surfaces par impacts : Évaluation des contraintes résiduelles induites par martelage," in *18ème Congrès Français de Mécanique*, 2007, no. 2004, pp. 27–31.

[250] G. Bruno and B. D. Dunn, "Surface and Bulk Residual Stress in Ti6Al4V Welded Aerospace Tanks," *J. Press. Vessel Technol.*, vol. 126, no. 3, p. 284, 2004.

[251] D. Yang, G. Wang, and G. Zhang, "Thermal analysis for single-pass multi-layer GMAW based additive manufacturing using infrared thermography," *J. Mater. Process. Tech.*, vol. 244, pp. 215–224, 2017.

[252] J. Ge, J. Lin, Y. Lei, and H. Fu, "Materials Science & Engineering A Location-related thermal history , microstructure , and mechanical properties of arc additively manufactured 2Cr13 steel using cold metal transfer welding," *Mater. Sci. Eng. A*, vol. 715, no. August 2017, pp. 144–153, 2018.

[253] R. A. Felice and D. A. Nash, "Pyrometry of Materials With Changing , Spectrally- Dependent Emissivity – Solid & Liquid Metals," in *The 9th International Temperature Symposium*, 2012.

[254] H. Schöpp, A. Sperl, R. Kozakov, G. Gött, D. Uhrland, and G. Wilhelm, "Temperature and emissivity determination of liquid steel S235," *J. Phys. D Appl. Phys*, vol. 45, pp. 1–9, 2012.

[255] P. Hagqvist, F. Sikström, and A. Christiansson, "Emissivity estimation for high temperature radiation pyrometry on Ti – 6Al – 4V," *Measurement*, vol. 46, no. 2, pp. 871–880, 2013.

[256] G. C. Obasi, S. Birosca, J. Q. Fonseca, and M. Preuss, "Effect of b grain growth on variant selection and texture memory effect during a-b-a phase transformation in Ti-6Al-4V," *Acta Mater.*, vol. 60, no. 3, pp. 1048–1058, 2012.

[257] M. Boivineau, C. Cagran, D. Doytier, V. Eyraud, M.-H. Nadal, B. Wilthau, and G. Pottlacher, "Thermophysical Properties of Solid and Liquid Ti-6Al-4V (TA6V) Alloy," *Int. J. Thermophys.*, vol. 27, no. 2, pp. 507–529, 2006.

[258] D. Basak, R. A. Overfelt, and D. Wang, "Measurement of Specific Heat Capacity and Electrical Resistivity of Industrial Alloys Using Pulse Heating Techniques," *Int. J. Thermophys.*, vol. 24, no. 6, pp. 1721–1733, 2003.

[259] K. Kubiak and J. Sieniawski, "Development of the microstructure and fatigue strength of two phase titanium alloys in the processes of forging and heat treatment," *Mater. Process. Technol.*, vol. 78, pp. 117–121, 1998.

Appendix A Contact Mechanics: Rolling and MHP

Simple contact mechanics theory analyses linear elastic contact systems. This section discusses the relevant aspects to this thesis to provide theoretical explanation for the results in this thesis. Flat rolling is explained by cylindrical contact on a flat surface and can be used for the chapters 4 and 7. Ball indentation on a flat surface and can be used to explain the machine hammer peening results in the chapters 5 and 6.

Flat Rolling

Figure 138 shows the annotation of a flat roller contact with a diameter *R* and width *b* giving a penetration depth Δt and the contact length *l*.

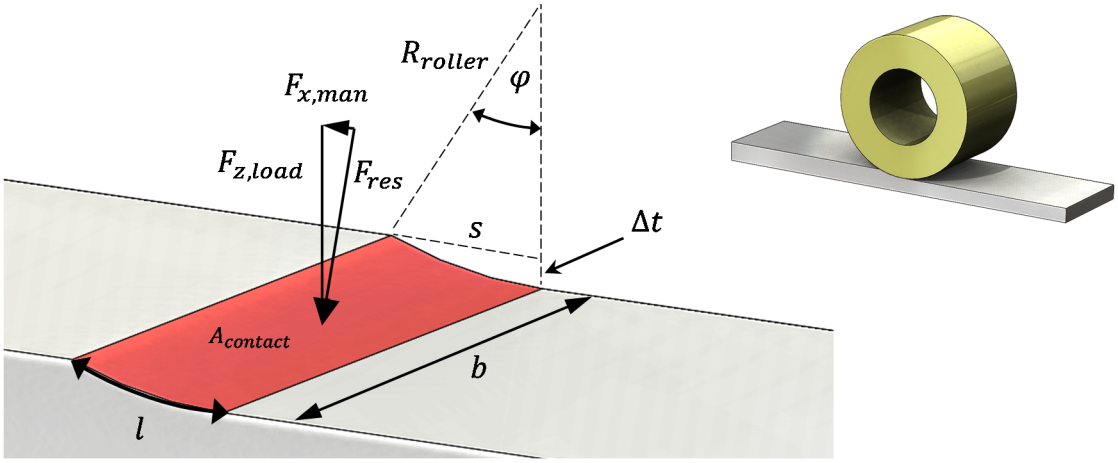

Figure 138: Geometry and dimensions of a flat rolling process.

The contact area *A* is calculated using eq. (38) with the projected length s from eq. (36) and the contact angle φ from eq. (37). The annotation is equivalent for the other two contact mechanic systems.

$$s = \sqrt{R\Delta t - \Delta t^2} \approx \sqrt{R\Delta t}\ for\ \Delta t \ll R \tag{36}$$

$$\varphi = \sin^{-1}\frac{s}{R} = \sin^{-1}\frac{\sqrt{2R\Delta t - \Delta t^2}}{R} \approx \sin^{-1}\sqrt{2\Delta t/R} \tag{37}$$

$$A = l * b = b * 2\pi * R\frac{\varphi}{2\pi} = bR\varphi \approx bs = b\sqrt{R\Delta t} \tag{38}$$

A larger diameter results in a larger contact area according to eq. (38), which requires a higher force to reach the same depth. For any arbitrary penetration depth Δt, the applied stress using a constant load, but different roller diameter follows eq. (39).

$$\frac{A_1}{A_2} = \frac{\sigma_2}{\sigma_1} = \sqrt{R_2/R_1} \quad for\ \Delta t \ll R\ and\ F = const. \tag{39}$$

An example is shown in Figure 139 (a), where the contact area is plotted for two roller diameters of 150 mm and 200 mm against the penetration depth Δt. The ratio of the contact area is always 86.6 % according to eq. (39). Figure 139 (b) shows that the simplified eq. (37) is acceptable to almost 10 mm penetration, as it still predicts an 86 % ratio and therefore is reasonable for all rolling processes in WAAM.

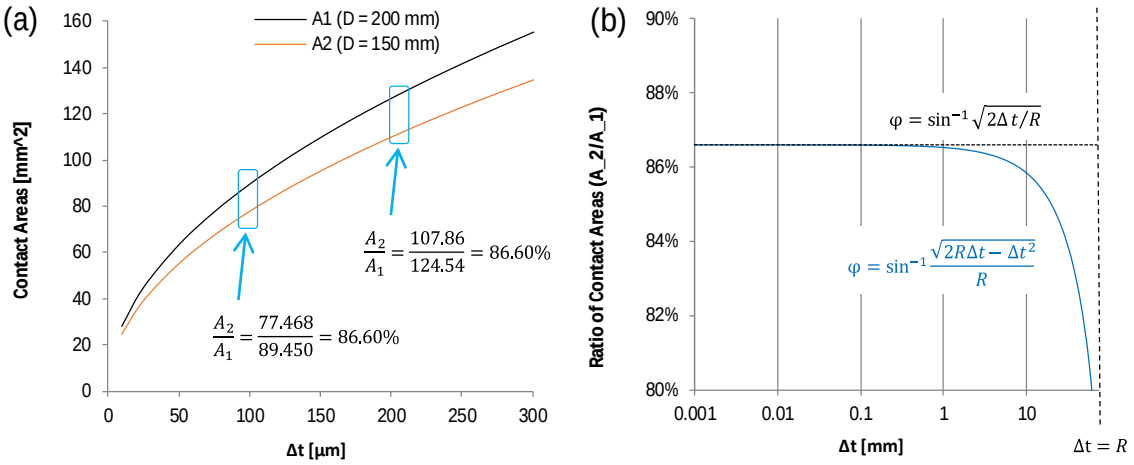

Figure 139: (a) contact area for different roller diameters vs. the penetrated depth; (b) range in which the simplified equation is valid.

Changing the rolling parameters, i.e. diameter, contact pressure, force and target penetration depth, also influences the not insignificant force required to actually manipulate the roller. The following approach investigates how the manipulation load changes with changing rolling conditions that all reach identical target penetration depths. A given rolling load F_z has to be manipulated in the rolling direction with the force F_x, which needs to overcome the rolling friction, calculated using eq. (40) and (41).

$$\sum M_i = 0 \rightarrow F_{x,man} * (R - \Delta t) = F_{z,load} * s \tag{40}$$

$$F_{x,man} = F_{z,load} * \frac{\sqrt{\Delta t(2R - \Delta t)}}{R - \Delta t} \tag{41}$$

If a certain plastic deformation Δt is targeted, then the manipulation force is inverse proportional to the square root of the roller diameter according to eq. (42). However, a smaller roller diameter results in a smaller contact area, as previously shown in eq. (38), which requires less force to achieve the same depth. The rolling load is therefore proportional to the square root of the contact radius (eq. (43)). In other words, the roller load can be decreased, if a smaller roller is used. However, smaller roller require a proportionally larger manipulation force, which ultimately neutralises the first effect. Therefore the required manipulator force F_x only depends on the penetration depth and can theoretically not be influenced by changing the roller diameter (eq. (44)).

$$F_{x,man} \sim \frac{1}{\sqrt{R}} F_{z,load} \tag{42}$$

$$F_{z,load} \sim \sqrt{R} \tag{43}$$

$$F_{x,man} = f(\Delta t) \neq f(R) \tag{44}$$

Ball Indentation

The behaviour in ball indentations into a flat surface are slightly different and as this chapter describes the theory of the penetration process during machine hammer peening, the relevant direction of travel is vertical and not along the surface. The contact force required to penetrate a flat surface to the depth Δt using a ball radius R is calculated with eq. (45), where the combined elastic modulus E' of both materials in this system is calculated using eq. (46). During the indentation process to the final depth Δt, the force increases nonlinearly. The integration of the force using eq. (45) yields the required energy to achieve the final depth (eq. (46)). Depending on whether a cold working systems provides a constant force or a certain impact energy, significantly changes penetration process. If a cold working system can provide a constant force, then $2^{1.5}$ = 2.83 times the load is required to achieve double penetration depth. If the impact energy is the tool parameter, then $2^{2.5}$ = 5.66 times the energy is required to achieve

double the depth. The influence of the ball size on the penetration depth and the plastically deformed volume using a range of quasi-static impact forces or energies is illustrated in Figure 140 (a) and (b) respectively.

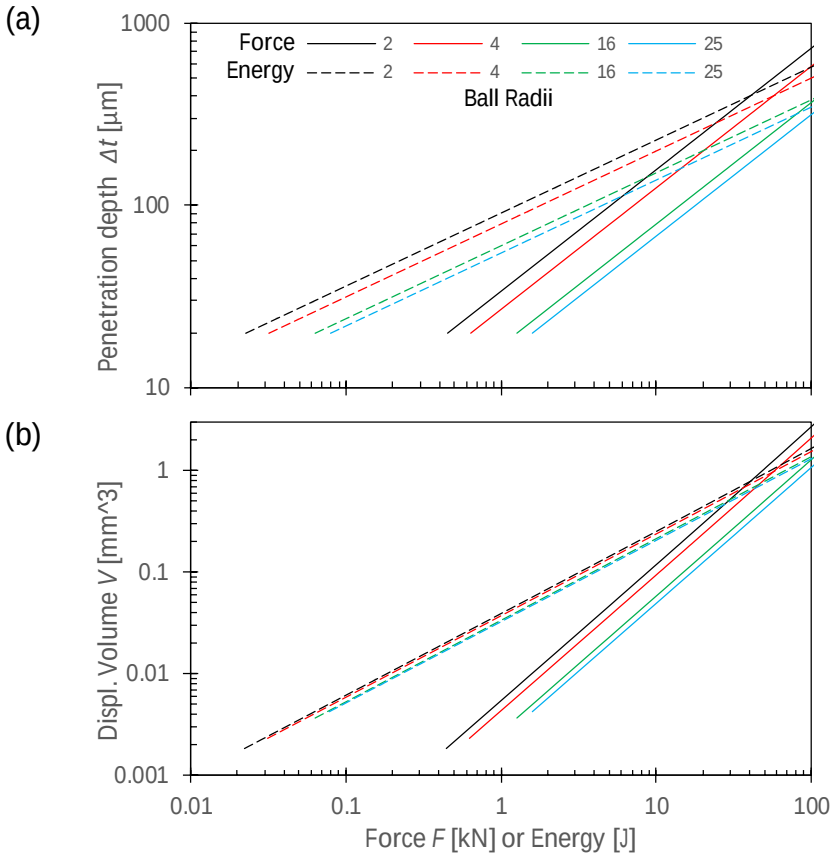

Figure 140: Theoretical (a) penetration depth and (b) displaced volume for a range of ball radii, loads and energies.

The plots show the required load or energy using ball diameters of (4, 8, 16 and 25) mm to penetrate Ti–6Al–4V with tool steel ball. This contact systems has a united elasticity of $E' = 83.8\ MPa$, using eq. (46) for standard material properties for both metals.

It can be seen that larger radii require more energy or force to achieve the same penetration. Smaller radii displace more volume at similar loads. However, the effect of the ball diameter using constant impact energies is almost negligible. The residual stress and plastic straining behaviour below the surface can vary, even if penetration depth or displaced volume are the same according to Hertz'ian pressure and different plastic stretching behaviour [198] (Figure 141). In general, it can be concluded that larger diameter can have a stress profile with a maximum stress deeper than the one of a

smaller diameter, while a smaller diameter can achieve larger plastic deformation, but less deep.

$$F = \frac{4}{3} E' \sqrt{R \Delta t^3} \tag{45}$$

$$\frac{1}{E'} = \frac{1 - {\upsilon_1}^2}{E_1} + \frac{1 - {\upsilon_2}^2}{E_2} \tag{46}$$

$$W = \int_0^{\Delta t} \frac{4}{3} E' \sqrt{R \Delta t^3}\, dz = \frac{4}{3} E' \sqrt{R} \int_0^{\Delta t} \Delta t^{\frac{3}{2}}\, dx \tag{47}$$

$$W = \frac{10}{3} E' \sqrt{R} \Delta t^{\frac{5}{2}} \tag{48}$$

Both contact mechanical theories assume linear elasticity, while the actual experiments involve large plastic deformation. The theory is therefore not suitable to describe the penetration behaviour, as well as the stress and strain distribution precisely, but it is nevertheless useful for comparing different parameters to help to explain the observations made in the experiments discussed in the chapters 4 to 6.

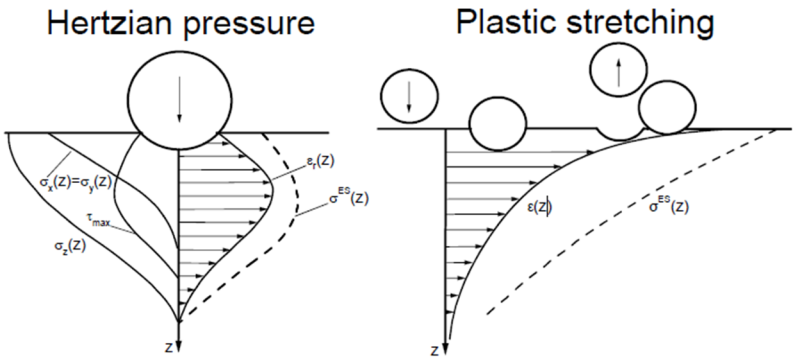

Figure 141: Governing deformation mechanisms "Hertzian pressure" and "plastic stretch" during ball contact [198]

Appendix B Crystal Structure and hcp orientation

Slip modes in hexagonal closed packed (hcp) unit cells, which ultimately determine the strength of α-titanium, were discussed in section 1.2.2.1 and the actual macroscopic strength of the lamellar microstructure of additively manufactured Ti−6Al−4V in section 1.3 in the literature review. Typical hcp unit cell orientations in the room temperature α phase and the high temperature body-centred-cubic (bcc) β phase using EBSD inverse-pole-figure (IPF) were reported by Donoghue et al. [86], who also discussed the unit cell orientation within the α-plates in respect to the neighbouring residual β-phase. These associated topics are not often discussed together. The present chapter visualises the knowledge contained in independent literature to describe the texture and anisotropic properties. Common hcp slip systems are shown in Figure 142. The preferred ones are the prismatic {1010} plane and the basal {0001} plane, both in <1120> direction, with a low critical resolved shear stresses (CRSS). The actual values change with the composition and are only available for pure titanium [63], but not the alloy. Pyramidal slip systems, such as the {1122} plane and the {1011} plane in <1123> direction can be observed as well and have a relatively high CRSS.

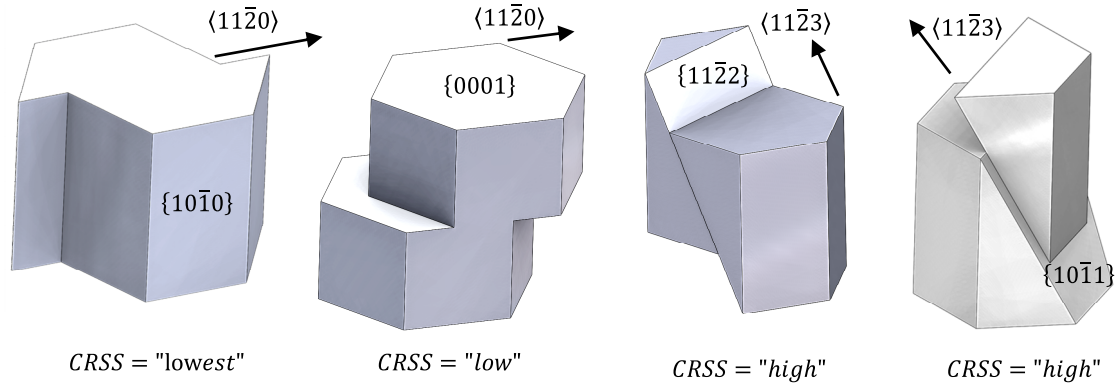

Figure 142: Four commonly observed slip systems in hcp crystals [43]**.**

The orientation of the unit cells can therefore influence the mechanical anisotropy of the macroscopic material. Donoghue et al. [86] reported a strong dependency of the bcc unit cell in respect to the build direction z, which can be reconstructed from the hcp unit cell orientation. The dominantly purple and green colouration of the IPF-z map in Figure 143 (a) indicates an alignment with either the {1012} or the {1120} plane to the z-direction. Both orientations originate from a single bcc phase of the parent β-phase,

as shown in Figure 143 (b), which is entirely aligned with the basal {100} plane normal to the z-axis. The dependency and appearance of dominantly purple and green colour of the α-IPF-z map can be explained with BOR, visualised in Figure 144. According to BOR, the basal {0001} plane of the hcp unit cell transforms on the {110} plane of the bcc unit cell, which has 6 variants.

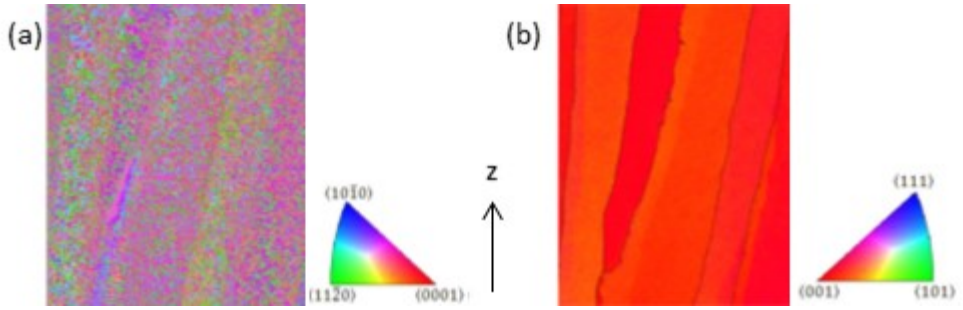

Figure 143: IPF-z maps of (a) the α-phase and (b) the reconstructed parent β-phase in Ti–6Al–4V WAAM material [86]**.**

Since the basal plane of the bcc cell is always normal to the build direction z, all six variants have only limited possible orientations, as shown in Figure 144 (a). Four of the six variants of the {110} plane appear with a 45° angle to the z-axis and the other two are in-plane with it. The only two possible hcp orientations are therefore the ones shown in IPF-z colours in Figure 144 (b).

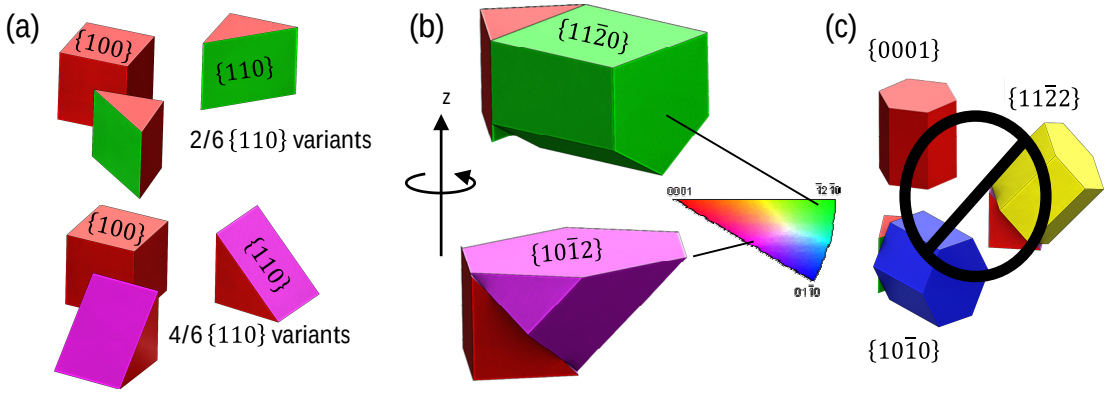

Figure 144: (a) possible variants of the {110} plane in the aligned bcc unit cell, ob which the hcp transforms on according to BOR [48]**; (b) possible and (c) the theoretically impossible orientations of the IPF-z coloured hexagon after phase transformation.**

In theory two-thirds of the hcp cells align with the {1012} plane normal to the z-direction (transformation mode 1) and one-third with the {1120} plane (Transformation mode 2). This is because four of the six variants of the $\{110\}_{bcc}$ plane are in 45 °C angle and the

other two are in-plane with the z-axis. Other orientations, such as the ones in Figure 144 (c) can theoretically not occur respecting BOR, as the parent bcc unit cell would have to be inclined. The dominantly purple coloured IPF-z with green as secondary colour in the measured EBSD scans (Figure 143 (a)) support both, the theory and likelihood of phase transformation. The hcp unit cells have limited macroscopic orientations, and therefore so do the slip systems. The growth of an hcp lattice is shown in Figure 145 also showing the preferred slip direction <1120>, in which the {1010} plane is either aligned with the normal z-axis or in a 60° angle with it for the transformation mode 1. In the transformation mode 2 it is the basal {0001} plane that aligns with the preferred slip direction at 38° with the normal z-direction. This is only to mention the two most preferred slip systems, which are both close to 45° to the normal z-direction, facilitating slipping and thereby decreasing the strength, but increasing the ductility due to the highest slip length (along the entire α-plate). The non-random orientation yields the anisotropic macroscopic material behaviour of additively manufactured Ti–6Al–4V. The free rotation around the z-axis results in no preferred hcp oriantation in respect to both other directions.

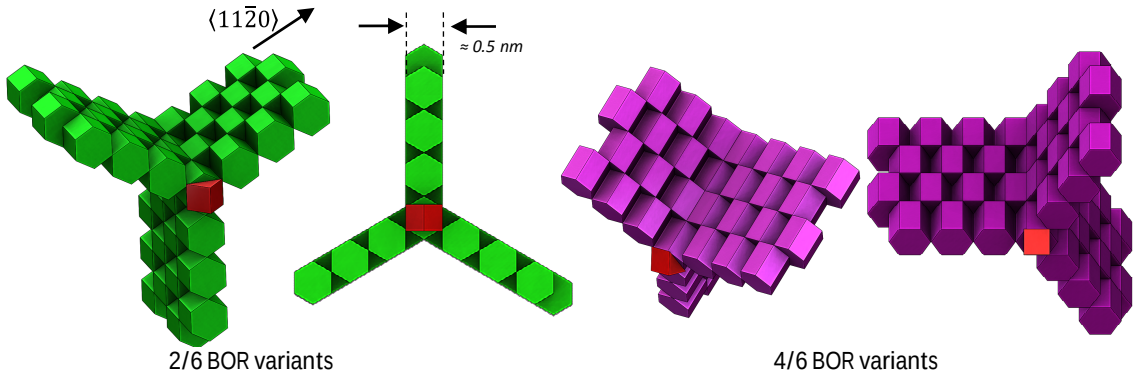

Figure 145: growth direction and global orientation of unit cells and slip systems of both transformation modes.

Eriksen [78], Mathisen et al. [65] and Lütjering [43] report the typical orientation of the hcp unit cell within the microscopically long, wide and flat α-plates (for example 20 x 20 x 1 µm in size) in respect to the surrounding residual β-phase, as shown in Figure 13 and 14 in the literature review: The {1010} plane coincides with the border of the α-plate. In turn, the limited parent β orientation determines the microscopic orientation of the α-plates too, as shown in Figure 146. The typical growth of these

α-plates aligns with the preferred slip systems longitudinal to the length of the plate. The result is a preferred system aligned with the longest slip length in the α-grain. Several parallel α-plates form so-called α-colonies that further increase the ductility of this configuration. Strength increase can be achieved by avoiding preferred orientations and by decreasing α-plate dimensions and the number of plates in one colony to ideally one. For this extreme case of only individual plates, the microstructure appears in a basket-weave fashion and is typically referred to as Widmanstätten microstructure.

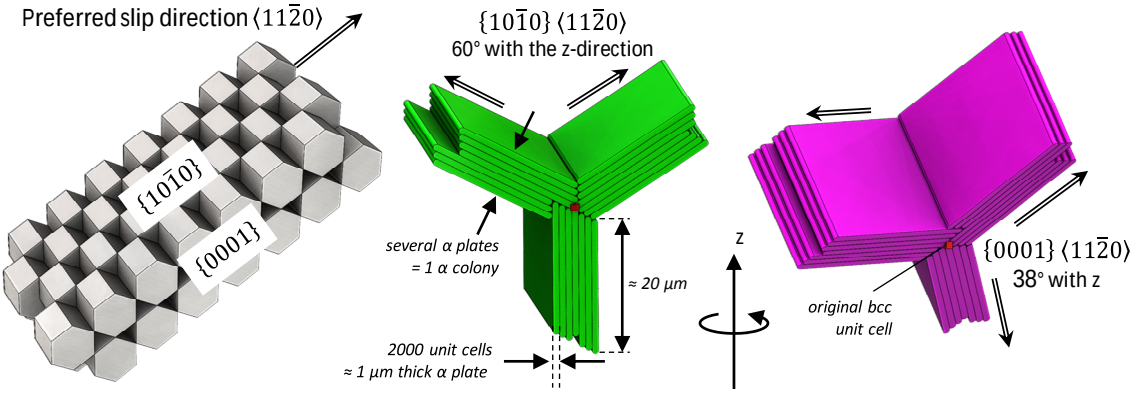

Figure 146: Slip systems in the hcp lattice and the orientation within α-plates and colonies according to [43], [62], [63], [65], [78]**.**

How micrographs and EBSD scans originate from the β-texture illustrates Figure 147. Even though the α-plates and the unit cell orientations appear random in Figure 147 (a), they follow the previously described development of the α-texture. When a cross section is cut, polished and etched, the α-plates appear like plates. In Figure 147 (b), where the α-plates are plotted in IPF-z colours, it is illustrated how identical α-plates can appear as α-plates of different size, which is only due to the orientation of the α-plate.

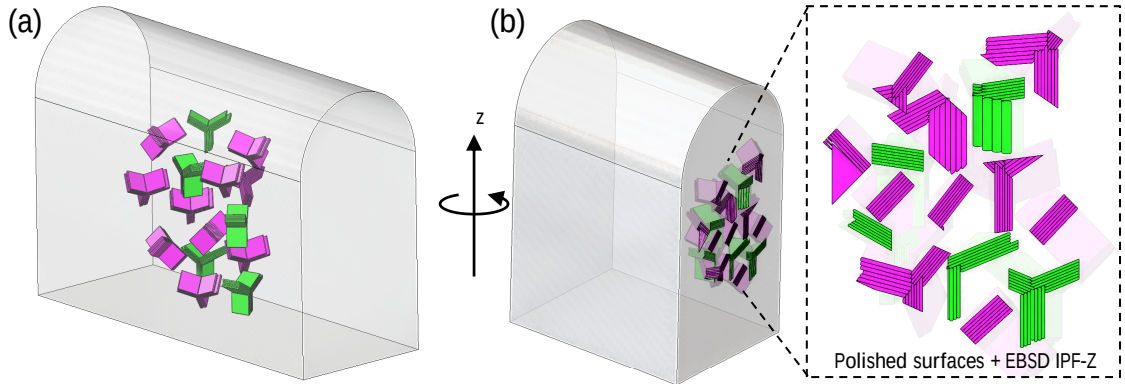

Figure 147: (a) both preferred α-orientations in respect to the z-axis and (b) EBSD IPF-z coloured cross-sectional schematic of the α-plates.

The random z-rotation of the plates causes the randomly appearing microscopic orientations of the α-plates in the cross-section. Both transformation modes and therefore the entire material offers a preferred slip system with a long slip length that is aligned close to 45 ° with the z-direction, resulting in the high ductility and reduced strength in this direction.

Appendix C EBSD Investigation of Strain Distribution in a Rolled WAAM Component

UNIVERSITY OF MANCHESTER

Alistair Ho

3rd July 2017

Aim of Investigation

The aim of this investigation is to determine the extent of rolling strain on a rolled WAAM specimen. Techniques such as Electron Back Scatter Diffraction (EBSD) and β reconstruction software developed by Davies and Wynne [244] have been used to construct the strain map.

β Reconstruction Technique

It is possible to establish the high temperature β phase (prior β grain structure) in titanium alloys through measurements of the α EBSD pattern as the two phases are

linked by the Burgers Orientation Relationship (BOR). The BOR shows that each β grain can form into 12 possible α orientations upon cooling through the β transus; each α plate can also have transformed from 6 possible prior β orientations. Therefore by using the BOR, it is then possible to determine the parent β orientation from the misorientation of grains that have similar α variants originating from the same α grain. BOR is given by:

$$\{110\}_\beta \parallel \{0002\}_\alpha;\ \langle 111\rangle_\beta \parallel \langle 11\bar{2}0\rangle_\alpha \quad (49)$$

The procedure for β reconstruction operates in 4 distinct steps [72]:

1. Identification of neighbouring points that belong to the same α variant

This operates by limiting the maximum misorientation value (2° default) that two neighbouring α grains can be considered to be in the same variant.

2. Calculating possible β transformations for all α variants

The 6 possible β transformation orientations are calculated for each α variant obeying the BOR.

3. Identification of neighbouring variants that transformed from the same parent β grain.

From the BOR each grain has 12 possible transformed α variants, so there are 11 other possible neighbouring misorientations which are then compared to establish the parent β grain. The misorientation threshold value (3° default) can be altered to set the degree of misorientation allowed for each α variant to be considered part of the same parent β grain.

4. Determination of parent β orientation

The parent β orientation is determined by a number of steps. Firstly, the misorientation anaylsis gives a maximum of 3 possible solutions for the parent β orientation where a unique solution can be considered for each neighbouring α variant neighbouring another variant. If there are more than one solution of β, then these orientations are

also compared to the 6 orientations calculated in step 2, where the most frequent β solution is assigned as the parent β orientation for those α variants.

The map distribution of relative plastic strain in the microstructure can be established from the deviation of the set misorientation threshold value (Step 3) of neighbouring α variants from fulfilling the BOR in reconstructed EBSD α maps. This method is suitable for Ti alloys as plastic strain increases the average degree of rotation of neighbouring α grains away from the ideal BOR; which is much more prominent than the local variability between specific α variants. One important consideration of this method is that the map strain values are not absolute, but rather a relative distribution of strain in the material. This is useful for understanding the extent of the plastic strain introduced by rolling and also the shape profile of the strain.

Technique

An α EBSD map is first collected from Maxim CamScan MX2000 FEG-SEM with a 6μm step size and a map of 6.37mm by 4.82mm was obtained as shown in Figure 148. The EBSD map is then β reconstructed at varying misorientation threshold values (1°- 6°), as shown in Figure 149 to determine the extent of strain where 1° shows least plastic strain and 6° is the most. The β reconstructed maps of varying misorientation threshold values were then converted back into α transformed EBSD maps (Figure 150) and compiled into a strain map (Figure 151). The reference axis for the orientation and inverse pole figure (IPF) colouring maps are aligned with the main fibre direction z (IPF-z).

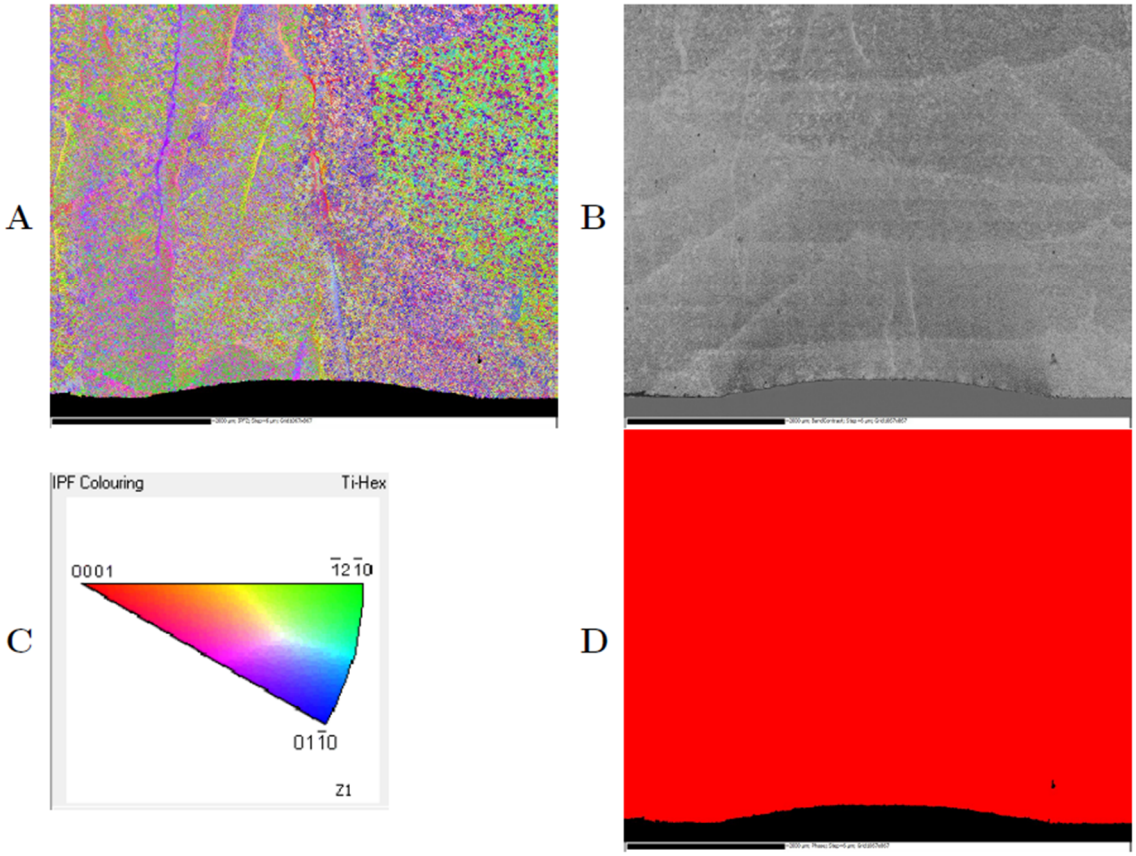

Figure 148: A – α phase IPF-Z map; B - band contrast map; C - HCP IPF colouring coordinates, D - phase contrast map where α is the red phase

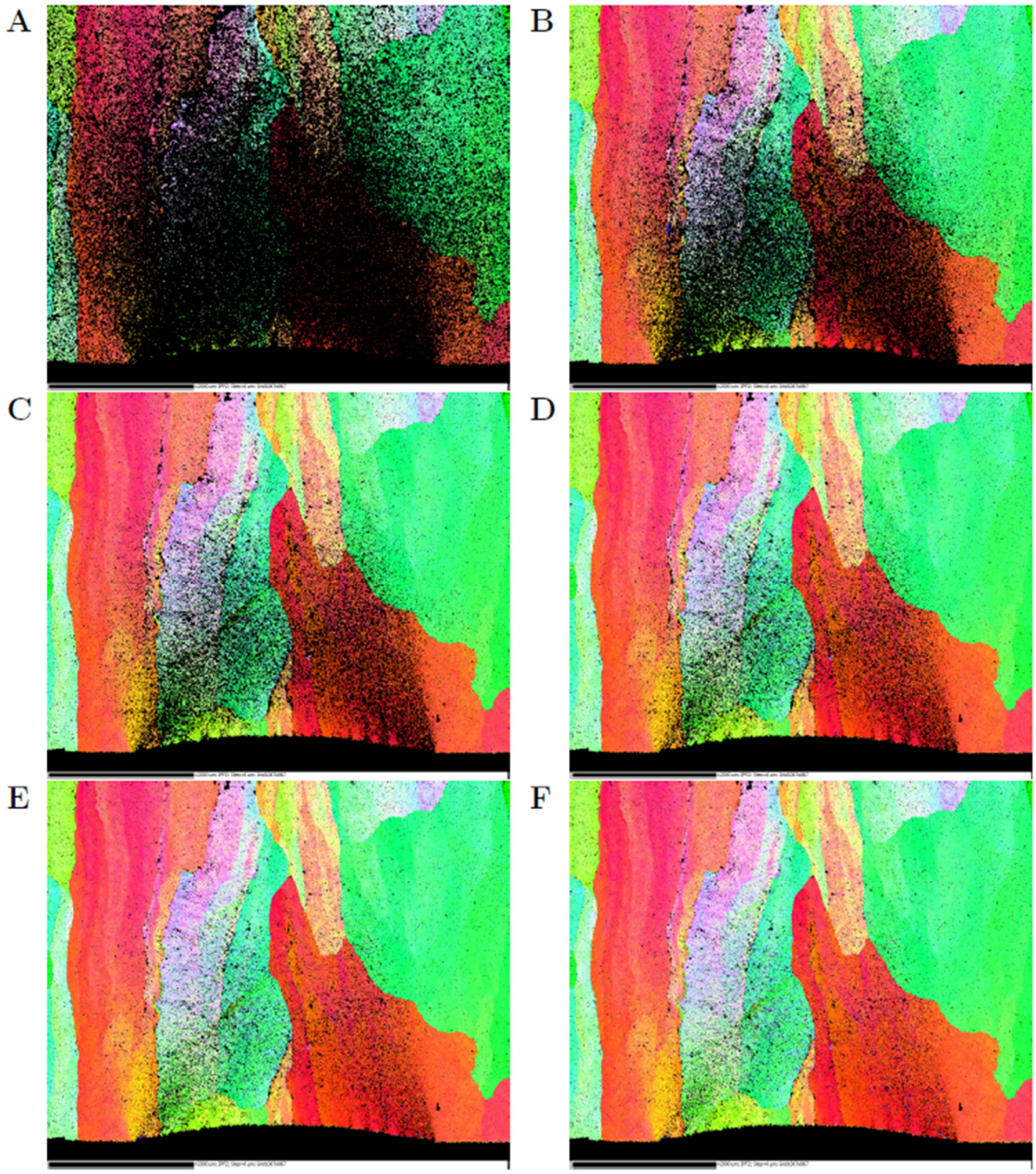

Figure 149: β reconstructed maps at different misorientation threshold values from 1° to 6° (A – F).

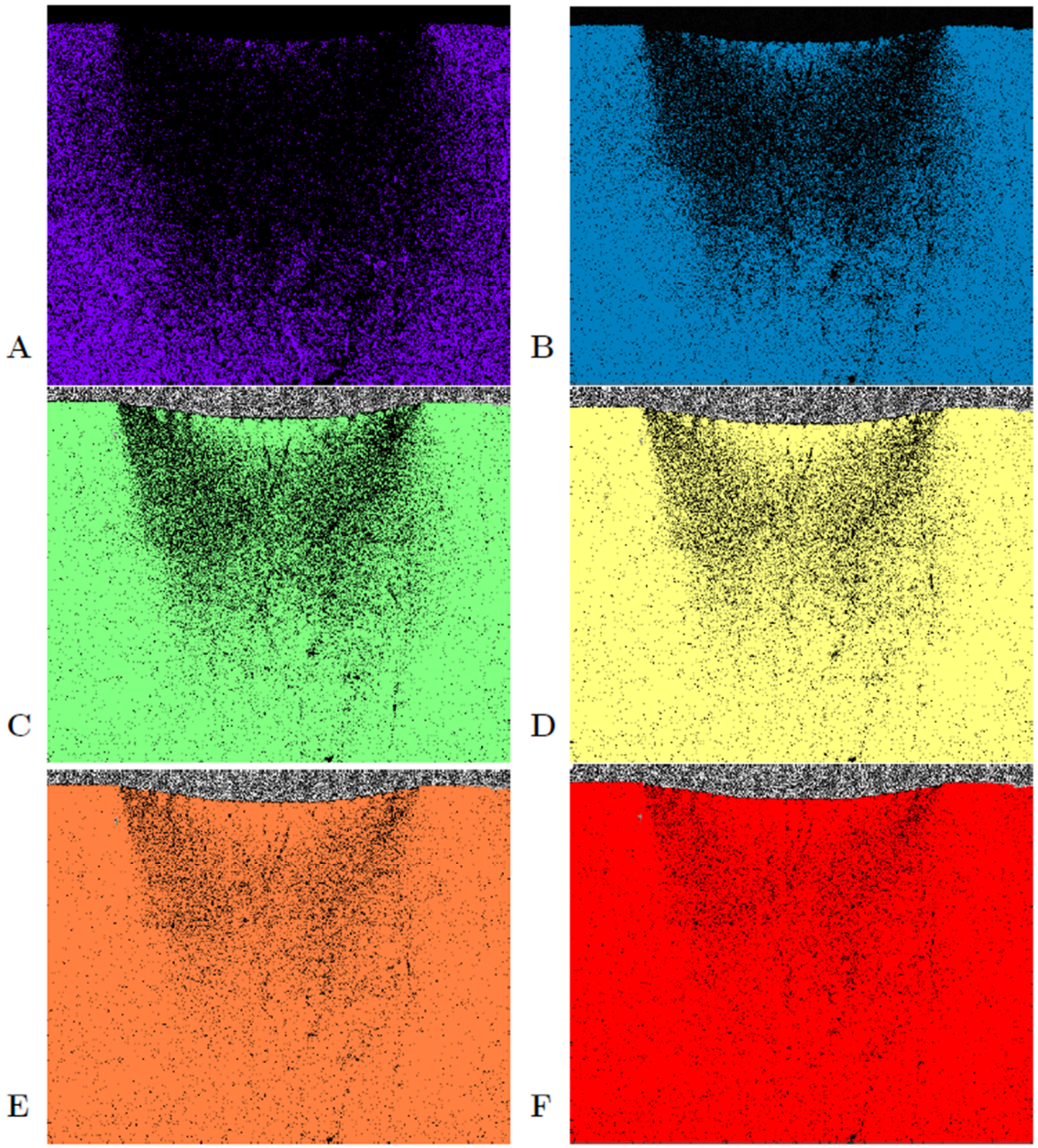

Figure 150: β reconstructed α phase maps at different misorientation threshold values from 1° to 6° (A – F). Note that figures have been rotated by 180°

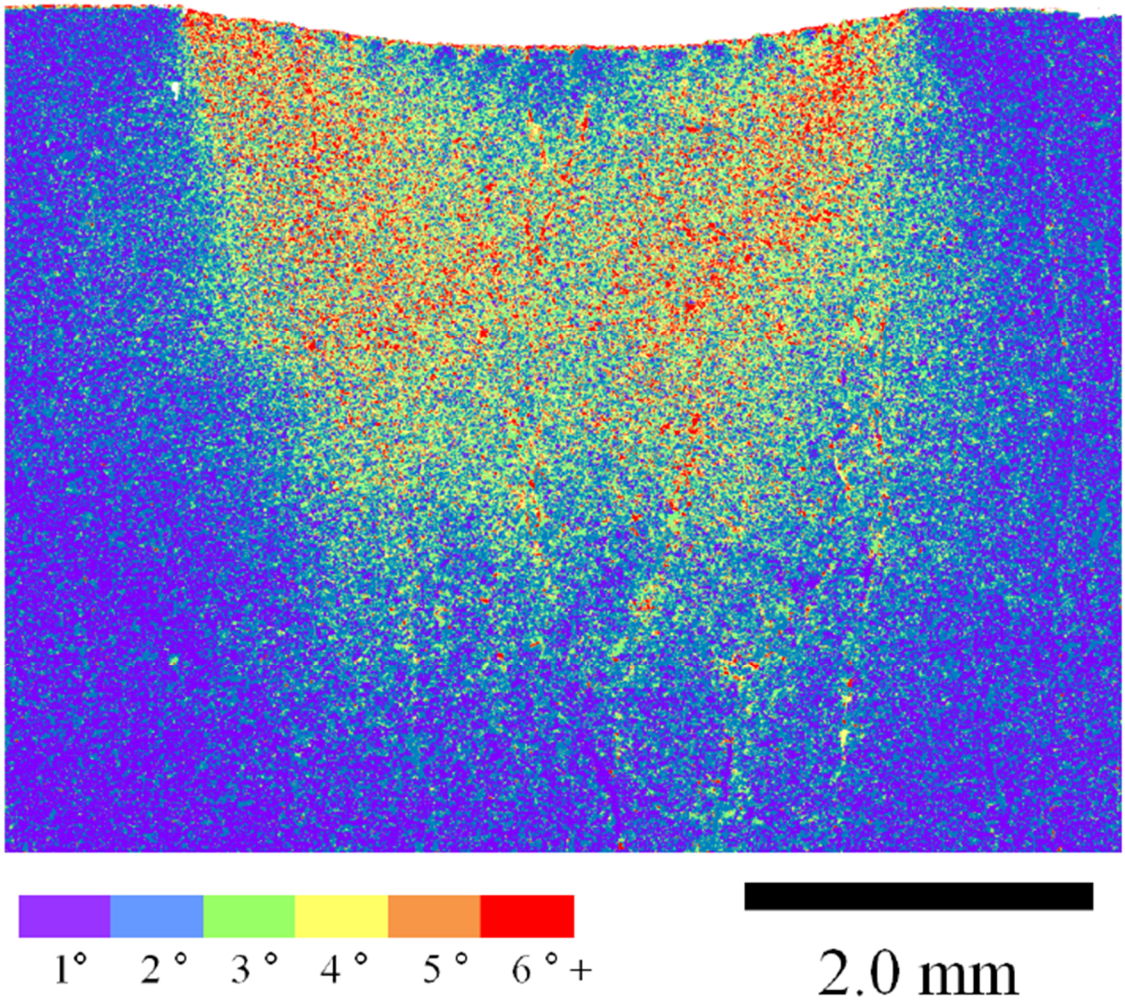

Figure 151: Reconstructed α phase maps combined to produce a relative strain map (- 1° relatively low strain, 6° relatively high strain) of Ti−6Al−4V WAAM material rolled with 90 kN using a 150 mm diameter roller with a convex profile of 3 mm radius.

Appendix D Compression test

Report

Compressive stress-strain curve of Wire+Arc Additive Manufacturing Ti–6Al–4V deposits

Geesthacht

January 18, 2018

The cylindrical compression test coupons were 10 mm in diameter and 15 mm large. For each direction six coupons were extracted from specimen #7 (taken from the WAAM wall in chapters 5 and 6), according to Figure 152. The coordinate system represents the one from the WAAM wall, where x- is the longitudinal direction, y is the transverse and z is the normal direction. Three of the six coupons were tested, for which the compressive stress/strain curves are shown in Figure 153.

Figure 152: LASIMM – Entnahmeplan f. Ti (?)-Druckproben

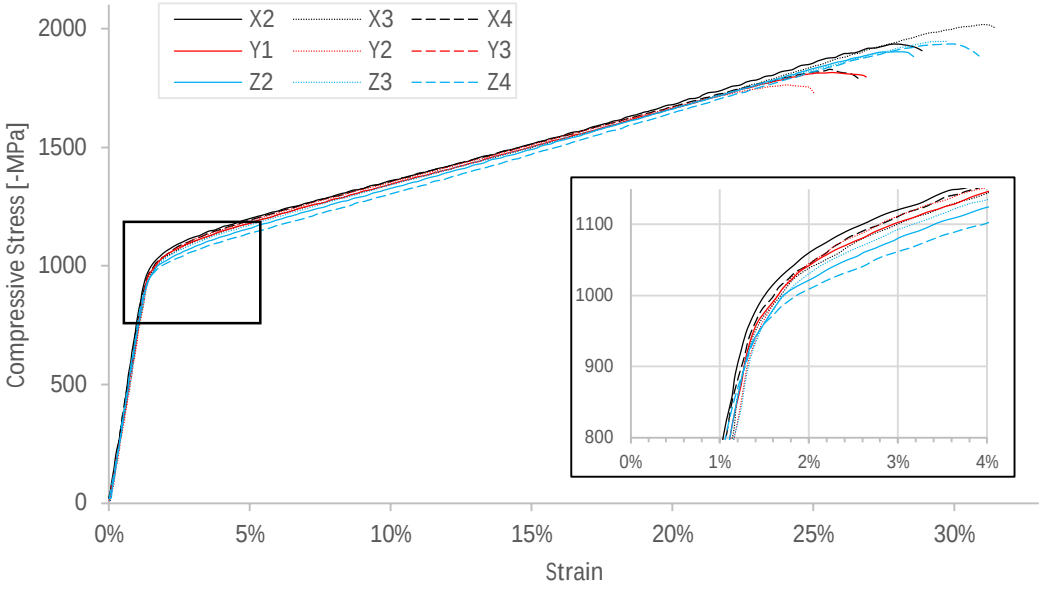

Figure 153: Results compression tests

Appendix E Inter-pass Rolling Trials

Colegrove et al. [111] showed that rolling every four layers only had the same effect as rolling every layer on reducing RS & D in steel WAAM. The effect on the microstructure was not discussed and neither was the effect on Ti–6Al–4V deposits.

A preliminary study was conducted with five walls using the welding parameters from Table 10. One wall remained completely unrolled for 20 layers. The other four were rolled with 50 kN every layer, every second layer, every third and every fourth layer. The resulting microstructures are shown in Figure 154. It can clearly be seen that reducing the number of intervals also decreased the effect on the grain refinement.

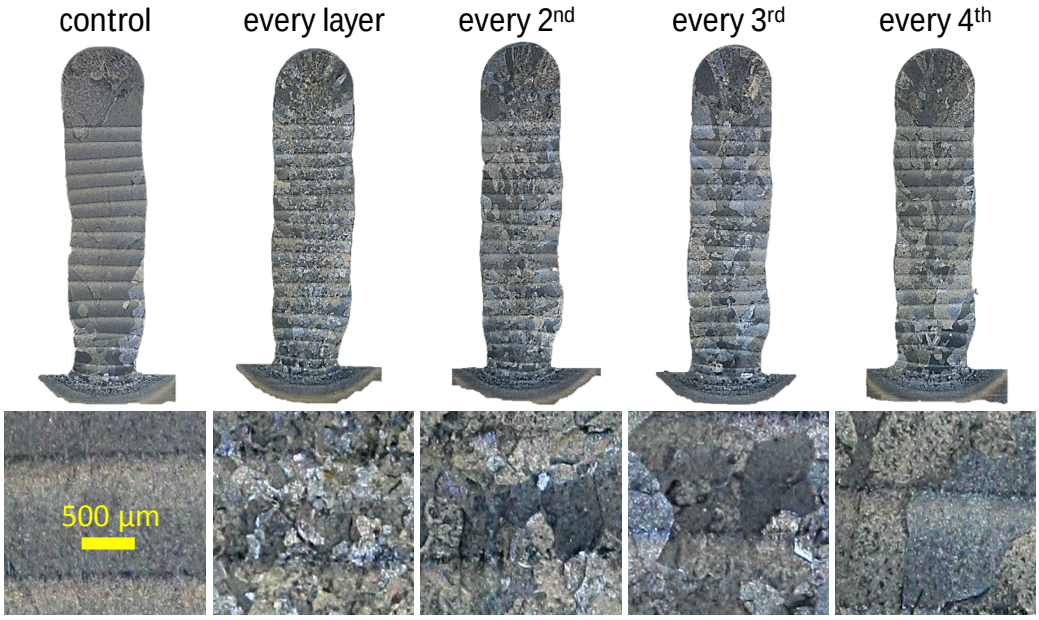

Figure 154: Control Microstructure vs. Rolled microstructure in Ti–6Al–4V WAAM.

When performing inter-pass rolling, the region that is thermo-mechanically cycled travels with the wall. Eventually the material could be further refined, if cycled multiple times. A second preliminary study investigated therefore applied inter-pass rolling but without adding extra wire to make sure that the same region is thermo-mechanically cycled over and over again. 20 layers were deposited using the same parameters without inter-pass rolling. The control is shown in Figure 155 (a). Then rolling was performed using a profiled roller and 50 kN rolling load. After running the torch with the same parameters, but without adding wire refined the microstructure slightly, and

another rolling + heat treatment step further refined the microstructure finally to a very small grain size, as shown in Figure 155 (b) and (c) respectively. However, Figure 155 (d) shows that additional thermo-mechanical cycles do not further refine the microstructure.

(a) as-deposited (b) after 1 cycle (c) after 2 cycles (d) after 3 cycles

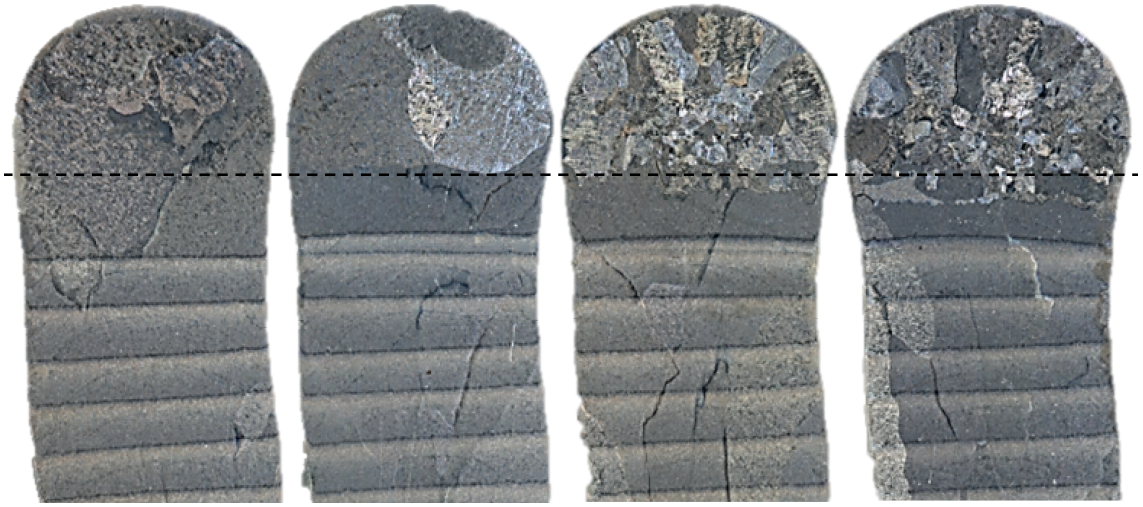

Figure 155: Control Microstructure vs. Rolled microstructure in Ti–6Al–4V WAAM.